Four Dimensional Analysis of Submillimetre Observations to Untangle Dust Properties and Structure in Nearby Starforming Regions

Alexander D. P. Howard

A Thesis submitted to
Cardiff University
for the degree of
Doctor of Philosophy

May 2020

"'It isn't light. It's Dust.'
Something in the way he said it made Lyra imagine Dust
with a capital letter, as if this wasn't ordinary Dust."
Philip Pullman, *His Dark Materials*,
Book One, *The Northern Lights*.

Acknowledgements

This thesis represents the culmination of not just the last four years of work, but of a 19 year dream kindled in the heart of the Everglades by a great flash of fire, a tremendous wall of sound, and a pillar which rose to connect the Earth and Heavens. This odyssey was not undertaken alone, however, and I would like to express my deepest gratitude to just a few of those who have helped me along the way. To any not mentioned here, please forgive a tired mind its momentary forgetfulness.

Firstly I would like to thank my fantastic supervisors, Matt Griffin and Ant Whitworth, and to PPMAP's creator Ken Marsh, who have tirelessly guided me through this process. Their constant support throughout the arduous moments, and the freedom they let me have to explore new and exciting avenues have made all of this possible. I would also like to thank Sarah Ragan and Derek Ward-Thompson for making an already stressful examination, undertaken in strange and frightening circumstances, a truly enjoyable experience.

I am deeply indebted to those postdocs and more advanced students into whose midsts I was thrust so suddenly. Olly, Andy, Zeinab and Emily were always free with their wisdom, and their laughter, never making me feel lesser. Seamus, Sarah, Rachael, Gwen and Camilo took me under their wings, and made me part of something bigger. You were far more than colleagues; you were tea buddies and pizza pals, pub mates and conference comrades, explorers of castles and temples and the darkest reaches of both space and humour, and most importantly, very dear friends. This extends further to the Cardiff Astronomy Group as a whole, to Paul and Sarah, to Ana and Niko, to Matt, to Tim, to Chris, to all of you. Thank you from the bottom of my heart.

I must reserve a special thank you for the *iocorum raeda*: Liz, Tom, Jeni and Eve. Starting their PhDs at the same time as I did, they have been a continual source of utter joy, a guiding constellation when times were dark. And to those others of my intake, defending their theses in these trying times, I tip my hat and raise my glass to my fellow Plague Doctors.

I cannot continue without mentioning the Tewkes of Hazzard. Ryan, Jack, Becca, Chris, David and Gareth have always provided an often needed escape, whether that is to a magical fantasy world, an action packed virtual one, or simply to Stroud, I could not have done this without you all.

And now I come to those closest to my heart. To my partner, Zoe, who has stuck by me through thick and thin, and without whose love and support I do not believe I could have finished this. Your unwavering support, even in the face of your own struggles, has been an inspiration to me which I can hardly describe. And to

Mum and Dad who nurtured my curiosity, fed the flame of discovery, never once making me doubt your love and commitment. The virtues and passions you instilled in me have been my North Star, and forever will be. And to my brother, Sam. Words cannot express how much of a hero you are to me.

Thank you, everyone.

Finally, I would like to dedicate this thesis to my grandparents. To Nanny and Grandad, whose continued belief in me drives me to ever greater deeds, and to Grandma and Grandpa, with their love of learning and exploration in all its forms, and who are dearly missed.

Abstract

The analysis of far infrared and sub-millimetre observations of filamentary structures within star forming regions has relied upon single temperature modified black body fitting techniques. While these procedures are simple to execute, they require a number of unphysical assumptions regarding the properties of the dust in the target molecular cloud, such as assuming that the dust temperature is uniform along the line of sight, and that the dust opacity index does not vary across the cloud. Furthermore, the observations are commonly degraded to the coarsest common resolution, leading to data loss.

The Bayesian fitting procedure, PPMAP, is able to overcome these limitations by utilising multi-band dust continuum observations at their native resolutions to produce high accuracy models of H_2 column density distributed into multiple discrete dust temperature and dust opacity index bands along the line of sight. In this thesis I present the results of a number of tests of PPMAP with synthetic data, and use the algorithm to analyse local star forming regions.

By constructing model filaments, I produce synthetic far infrared and sub-millimetre observations which I use to test the capabilities of the PPMAP algorithm. I show that PPMAP is able to more accurately estimate the total mass of a filament than a conventional modified black body fitting technique. I also determine that PPMAP is capable of lifting the dust temperature and dust opacity index degeneracy commonly seen in modified black body results. This allows PPMAP to probe line of sight variations in the dust properties. I also determine that PPMAP is able to estimate the contribution to the final model of each of the input observations equally well or better than conventional modified black body fitting techniques.

I apply PPMAP to *Herschel* and SCUBA-2 dust continuum observations of the main filament in the Taurus L1495/B213 star forming complex. I produce a length averaged profile of the B211/B213 filament and fit this profile with a Plummer-like function. I find it has a FWHM $\approx$0.087 pc and a Plummer-like exponent, $p \approx 1.88$. The FWHM is nearly half the characteristic width reported in Arzoumanian et al. (2011) and other studies when adjusted for differences in fitting technique, while p is consistent with previous studies. By instead fitting multiple Plummer-like functions at different positions along the length of the filament, I determine that the filament is better approximated by a $p = 4$ Plummer-like exponent, though I still recover a narrow filament width. The shallower function attributed to the length averaged profile is likely to be a consequence of smoothing over areas of resolved sub-structure along the filament. Therefore, I conclude length averaged fitting should be avoided. The ability of PPMAP to distinguish dust emitting at different temperatures, and

thereby to discriminate between the warm outer layers of the filament and the cold inner layers near the spine, leads to a significant reduction in the column density through the filament, and hence in the line-density, μ. If we assume a gas temperature of 10 K, and thus a critical line density, $\mu_c \approx 16\,\mathrm{M_\odot\,pc^{-1}}$, then the B211/B213 is, on average, trans-critical, with $\widetilde{\mu} = 17.8\,\mathrm{M_\odot\,pc^{-1}}$. The locations of pre-stellar cores agree well with segments of the filament that are locally super-critical.

I also apply PPMAP to *Herschel* and SCUBA-2 dust continuum observations of the Ophiuchus L1688 and L1689 sub-regions. I identify a network of filamentary structures in both regions. As with the B211/B213 filament in Taurus, I determine that the widths of the dense filaments in L1688 and L1689 are also significantly narrower than the canonical characteristic filament width. I find that the filaments in L1688 and L1689 have a median line density of $(43 \pm 13)\,\mathrm{M_\odot\,pc^{-1}}$, and hence are super-critical assuming a gas temperature of 10 K. However, both regions are strongly heated by feedback from the Upper Scorpius OB association, which may raise the gas temperature enough that the filaments are globally trans-critical. By examining the distribution of mass, I determine that while L1688 contains twice as much material with $A_V \geq 7$ as L1689, the proportion of that material which is associated with starless cores and dense, compact clumps is similar in the two sub-regions.

In addition, I present an analysis of the dust properties as revealed by PPMAP. The variations in dust opacity index in both the Taurus and Ophiuchus regions exhibit broadly similar properties. The more diffuse medium surrounding the networks of filaments and cores is generally composed of dust with opacity indices ≥ 1.5. In contrast, the dense structures harbour reservoirs dust with opacity indices ~ 1.0. This may be indicative of grain growth in the densest regions of star forming clouds.

Contents

Chapter 1
An Introduction to Molecular Clouds and Dust

For millennia, people have wondered at the make-up of what we can see in the night sky. The classical treatise *Meteorologica* (Aristotle c. 350 BCE) derides the early philosopher, Democritus (450-370 BCE), for believing that the light from the Milky Way comes from distant stars. Instead, Aristotle puts forward the theory that it is due to a large collection of burning gasses given off by the most luminous stars. We now know that not only was Democritus closer to the truth, but that all the stars visible to the naked eye, and our own solar system, are part of the same collection. The bright band stretching across the sky (as they would have seen it, see Figure 1.1) is simply the disc of our parent galaxy seen edge on, and from within. However, Aristotle was not completely wrong either. In addition to stars, there is a large amount of gas distributed throughout the space between the stars. Furthermore, dark dust-obscured lanes can be seen cutting through the plane of the galaxy, obscuring the light from the stars behind. These components, along with a halo of dark matter, govern the dynamic processes of the galaxy at scales from kilometers to kiloparsecs.

Our understanding of stars has grown enormously over the intervening centuries. We now know that stars can be roughly broken into two broad categories. Low mass stars are on the order of a few tenths to a few times the mass of our Sun. They are the most populous stars, with lifespans of billions or even trillions of years. High mass stars are on the order of ten solar masses ($M_\odot$). While much fewer in number, they are much more luminous than low mass stars, and often dominate the luminosity from star forming regions. Massive stars only survive a few million years, and drive powerful stellar winds and turbulent motions which sweep up the surrounding gas into dense clouds while their intense radiation greatly heats the gas and dust

Figure 1.1. Astrophotography image of the Milky Way taken over the Pinnacles, Australia, altered to appear as close as possible to what the human eye would observe from the same spot. While taken from a different hemisphere, the sight would have been similar to the one visible to the ancient Greek philosophers, with the hazy, white "gasses" and the dark lanes both clearly visible. Image credit Dobson (2015).

in their local region. They then die in violent explosions, enriching the environment with heavy elements.

Despite our understanding of stellar life and death, many questions remain regarding the formation of stars. Stellar nurseries have historically proven to be difficult to observe, as they lie at the hearts of dense, dust rich clouds which obscure ultra-violet, visible, and near infrared radiation. It is only with recent advances in far infrared and sub-millimetre astronomy that we have begun to probe these clouds in which protostars are formed, and thus to build an understanding of the processes that govern their formation. Thus, while Democritus was correct as to the source of light in the Milky Way, it is with Aristotle's gasses between the stars that the field of star formation is most concerned.

1.1 The Interstellar Medium

The Interstellar Medium (ISM) is the term given to the non-dark matter component of the Galaxy which permeates the space between the stars. The ISM makes up approximately 10-15% of the visible mass of the Milky Way (Tavakoli 2012; Roman-Duval et al. 2016), and comprises mostly hydrogen (70% by mass), with trace amounts of helium (28%) and metals (2%, Spitzer 1978). However, studies of molecular line emission have shown that many of the refractory metals (elements with condensation temperatures greater than 1300 K) appear to be depleted from the gas phase (e.g. Morton et al. 1973; Jenkins 1987; van Steenberg and Shull 1988). Dwek (1998) suggests that this indicates that a significant fraction of these elements is instead bound up in solid dust grains. This dust accounts for approximately 1% of the ISM.

The ISM is a multi-phase medium. While McKee and Ostriker (1977) originally proposed a three phase gas model for the ISM, it is now generally considered that it is composed of at least five distinct gas phases. The first of these phases is the Hot Ionised Medium (HIM), made up of ionised hydrogen atoms with temperatures exceeding 10^6 K, and number densities of $10^{-4}\,\mathrm{cm}^{-3}$ to $10^{-2}\,\mathrm{cm}^{-3}$. The gas is likely heated by supernova shocks and other energetic processes. Estimates of how much of the ISM is taken up by the HIM vary. McKee and Ostriker originally assumed it was the largest component, occupying as much as 70% of the volume. However, its volume filling factor may be as low as 20% (Ferriere 1998).

The Warm Ionised Medium (WIM) is also mostly composed of ionised hydrogen, though at lower temperatures. It is typically found in HII regions and in a diffuse network of galactic scale loops, clouds and filaments. The WIM is heated by Lyman continuum radiation from OB stars, with the HII componant reaching 6000 K

and the diffuse loop network reaching as much as 9000 K (Reynolds, Sterling, and Haffner 2001). The WIM is denser than the HIM, with number densities ranging from $0.2\,\mathrm{cm}^{-3}$ to $0.5\,\mathrm{cm}^{-3}$

The next component of the gas in the ISM is the Neutral Atomic Medium, which is composed of mainly neutral atomic hydrogen and is itself split into two phases: the Warm Neutral Medium (WNM), with an estimated temperature range of 6000 K to 10 000 K and a number density of $0.2\,\mathrm{cm}^{-3}$ to $0.5\,\mathrm{cm}^{-3}$, and the Cold Neutral Medium (CNM), with temperatures from 50 K to 100 K and number densities of $20\,\mathrm{cm}^{-3}$ to $50\,\mathrm{cm}^{-3}$ (Dickey, Terzian, and Salpeter 1978; Kulkarni and Heiles 1987). While it is two orders of magnitude hotter, the WMN is also two orders of magnitude less dense than CNM, which suggests the two phases are in approximate pressure equilibrium. Both the warm and cold neutral medium are likely to be heated by the same process: low energy cosmic rays. The difference in temperature is due to different cooling mechanisms, with more efficient cooling only possible at higher densities (Field, Goldsmith, and Habing 1969).

The Molecular Medium (MM), which is mostly H_2 gas, is the smallest fraction of the ISM by volume ($< 1\%$), but makes up 30% of the ISM by mass (Stahler and Palla 2005). This is because it is significantly colder and more dense than the other phases, with temperatures <30 K and number densities of $10^2\,\mathrm{cm}^{-3}$ to $10^6\,\mathrm{cm}^{-3}$.

The gas in the ISM is continually transitioning between these different phases. Supernovae, radiation from massive stars, and other energetic processes heat cold material, dissociating molecules and replenishing the HIM and WIM. Warm material cools and condenses, becoming optically thick and shielding molecules from dissociation. These molecules then provide even more effective mechanisms for cooling, leading to condensation of molecular clouds and the formation of stars.

1.1.1 Molecular Clouds

Molecular clouds are dense regions of atomic and molecular gas which condense out of the warmer phases of the ISM. They are thought to form when supersonic flows driven by massive stellar winds, expanding HII bubbles, and supernova explosions sweep up large amounts of the Neutral Medium (see McCray and Kafatos 1987; Vazquez-Semadeni, Passot, and Pouquet 1995). Where the flows converge, the column density of the gas increases. When it exceeds $\sim 1 \times 10^{21}\,\mathrm{cm}^{-2}$, the interiors of the clouds become shielded from the UV radiation from the interstellar radiation field (ISRF, van Dishoeck and Black 1988; van Dishoeck and Blake 1998). The increase in density enables rapid production of molecules on the surfaces of dust grains, and

prevents those molecules from being dissociated (Hollenbach and Salpeter 1971).

The molecular gas within the clouds comprises mostly H_2, but also contains trace amounts of other molecular species, such as CO and NH_3. These molecules help to further reduce the temperature of the cloud through various cooling mechanisms, allowing the gas to cool to temperatures between between 10 K and 20 K (Bergin and Tafalla 2007). This further aids in the production of molecular hydrogen and other species. Due to the collisional processes involved, and the high rate of molecular gas production, molecular cloud formation is thought to be very rapid, occurring on the timescale of a few Myr (Hartmann, Ballesteros-Paredes, and Bergin 2001).

Molecular clouds vary greatly in size, with masses ranging from $10^2\,M_\odot$ to $10^7\,M_\odot$, and diameters from 1 pc to 100 pc. Molecular clouds with a total mass exceeding $10^4\,M_\odot$ are called giant molecular clouds, or GMCs.

It is hard to directly observe the H_2 in molecular clouds, as it is a non-polar molecule with a low moment of inertia, leading to weak rotational transitions with high excitation energies. Instead, observers use other tracers of the dense gas. One method is to use molecular line emission from the polar molecular species present in the cloud. Polar molecules are excited to high rotational states via thermal collisions. When they de-excite, they release a specific wavelength of light. Basic properties such as total cloud mass and gas temperature can be inferred from the intensity of the emitted radiation (assuming a fixed ratio between the number density of the observed molecule and the number density of H_2), while other properties such as infall, outflow and turbulence can be examined through Doppler-induced effects on the spectral line features (e.g. Ballesteros-Paredes 2006; Ragan et al. 2014; Hacar et al. 2018).

An alternative method to estimate the total cloud mass, temperature, and other physical properties is to use thermal emission from the dust grains, and to assume a uniform ratio between the mass of molecular hydrogen and the dust mass. This method is explained in more detail in Section 1.2.1.

As mentioned previously, molecular clouds are not uniform, but are highly sub-structured complexes. They have been observed to contain networks of filaments (André et al. 2010), dense clumps, and starless and star-forming cores (Motte, Andre, and Neri 1998). This substructure is thought to arise from turbulent motions within the clouds. The turbulence is driven by gravity, accretion, local feedback such as young stellar winds and expanding HII regions (Leitherer, Robert, and Drissen 1992; Gritschneder et al. 2009; Drabek-Maunder et al. 2016), and larger scale energetic processes such as supernova explosions, and galactic flows and sheer forces (Heitsch et al. 2008; Dib et al. 2009; Klessen and Hennebelle 2010).

Despite their large sizes, individual molecular clouds do not persist for very long. Instead they disperse on the order of a few freefall times (Elmegreen 2000; Ballesteros-Paredes 2006). While initially believed to be gravitationally bound, it is now thought that molecular clouds can be unbound structures (Clark and Bonnell 2004). The high densities observed, coupled with a high degree of sub-structure and turbulent motions promote fragmentation on small scales within the clouds (Clark et al. 2005), which drives filament growth and rapid star formation.

1.1.2 Interstellar Filaments

Interstellar filaments are dense, dusty structures with high aspect ratios, and are composed primarily of molecular gas. They have been found to dominate the mass budgets of some molecular clouds and GMCs (e.g. Schisano et al. 2014; Könyves et al. 2015). While they have long been thought to play a role in the star forming process (Barnard 1910; Schneider and Elmegreen 1979), it was not until the advent of the *Herschel* Space Observatory (Pilbratt et al. 2010), and the subsequent revelation that filaments are an ubiquitous part of star forming environments, that their importance was established (e.g. Men'shchikov et al. 2010; Hill et al. 2011; Wang et al. 2015). Further observations have shown that filaments are well correlated with sites of core formation (e.g. Marsh et al. 2016).

Several methods of filament formation have been proposed. Gravitationally unstable, spheroidal molecular clouds will collapse preferentially along their shortest axis, forming a comparatively thin "sheet" of material. Sheets may also be produced through the collision of two or more molecular clouds or on the surface of expanding bubbles, which sweep up diffuse material into denser shells. Gravitational instabilities within these sheets give rise to perturbations with characteristic length scales several times thicker than the sheets themselves. The aspect ratios of these perturbations increases with time, preferentially driving fragmentation to form filamentary structures (Miyama, Narita, and Hayashi 1987; Whitworth 2016).

Filaments can also form through the collision of two or more sheets. Where sheets intersect with one another, material can flow within the sheets into the potential well generated along the line of intersection, thus forming a filament along this axis, as shown in Figure **??** (see Shimajiri et al. 2019).

Additionally, numerical simulations have shown that filaments can form through the collisions of turbulent streams of material within clouds (Ballesteros-Paredes, Hartmann, and Vazquez-Semadeni 1999; Bonnell, Bate, and Vine 2003; Clarke et al. 2017). When turbulent motions, which can be modelled as plane waves, interact, they

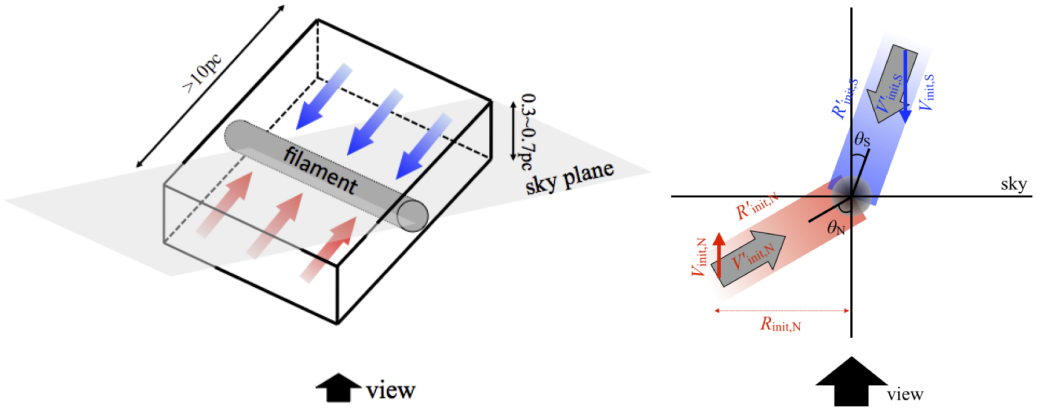

Figure 1.2. Schematics of the proposed formation method of the Taurus B211/B231 filament as an intersection between two sheets, as shown in Shimajiri et al. (2019).

will constructively and destructively interfere with one another. The nodes that form at the sites of destructive interference will be elongated along the line of intersection. These linear nodes act as stable points within which gas can gather as it moves with the wave fronts. Turbulence can also drive shear forces which can pull structures out into elongated shapes (Hennebelle 2013). Shear forces due to galactic rotation strongly affect objects on galactic scales in this way (Dobbs 2015; Duarte-Cabral and Dobbs 2017).

Magnetic fields are also thought to play a significant role in filament formation. Palmeirim et al. (2013) observe low density striations aligned parallel with the magnetic field lines in the Taurus L1495/B213 complex, while the dense main B211/B213 filament in the same region is aligned perpendicular to the magnetic field. This trend was later observed in many other environments (Planck Collaboration et al. 2016a; Planck Collaboration et al. 2016b), with many fields exhibiting a systematic shift from low density structures parallel with the magnetic field, to high density structures perpendicular to the field lines (e.g. Soler 2019). This may be an indication that the field lines funnel material onto the filament, helping it to accrete mass. This accretion would also help to prevent filaments from collapsing radially to form very narrow spindles by injecting turbulent energy into the system (Heitsch, Ballesteros-Paredes, and Hartmann 2009; Klessen and Hennebelle 2010). On smaller scales, within dense filaments themselves, observations indicate that the magnetic field direction changes again, to lie parallel to the primary axis of the structure (e.g. Pattle et al. 2018). Such internal, longitudinal fields may also aid in supporting the filaments against collapse.

Filaments range from a few parsecs to tens of parsecs long (Beuther et al. 2015; Arzoumanian et al. 2019), with the longest filaments spanning approximately 100 pc in projection (Wang et al. 2015; Wang et al. 2016). However, recent studies with

Gaia have indicated that projected length might be only a fraction of total length (Großschedl et al. 2018).

Ostriker (1964) showed that an infinitely long isothermal filament in hydrostatic equilibrium has a radial density profile described by

$$n_{\mathrm{H_2}} = n_0 \left\{ 1 + \left(\frac{r}{r_0} \right)^2 \right\}^{-2} \tag{1.1}$$

where n_0 is the volume density of hydrogen molecules on the spine of the filament. r_0 is a factor such that for $r \ll r_0$, the density is approximately uniform, while for $r \gg r_0$, the density falls off as r^{-4}. Such isothermal cylinders can be supported against gravity by internal thermal pressure alone if their line density, μ, is below a critical value given by

$$\mu_{\mathrm{C}} = \frac{2c_s^2}{G}, \tag{1.2}$$

where c_s is the isothermal sound speed of the gas (Ostriker 1964). This sound speed is given by

$$c_s = \left(\frac{k_B T}{\bar{m}} \right)^{1/2}, \tag{1.3}$$

where k_B is the Boltzmann constant and $\bar{m}$ is the mean mass associated with a gas molecule. For molecular gas with a solar composition at a temperature of 10 K, this equates to $c_s = 0.19\,\mathrm{km\,s^{-1}}$, and therefore $\mu_{\mathrm{C}} \approx 16\,\mathrm{M_\odot\,pc^{-1}}$. Filaments with line masses greater than this value should, in theory, undergo rapid radial collapse into a thin spindle.

In reality, thermal pressure is not the only supporting mechanism. Clarke et al. (2017) generalised equation 1.3 to include support from turbulent motions by replacing c_s with $c_{eff} = \sqrt{c_s^2 + \sigma_{1D}^2}$, where σ_{1D} is the one dimensional gas velocity dispersion. Internal magnetic fields aligned parallel to the long axes of filaments are also thought to contribute to support, by restricting the flow of material inward across the field lines. The majority of prestellar and protostellar cores are found in filaments with a line density greater than μ_{C} (Polychroni et al. 2013; Könyves et al. 2015; Marsh et al. 2016).

Whitworth and Ward-Thompson (2001) generalised equation 1.1, introducing a variable Plummer-like exponent, p, which produces

$$n_{\mathrm{H_2}}(r) = n_0 \left\{ 1 + \left(\frac{r}{r_0} \right)^2 \right\}^{-p/2} . \tag{1.4}$$

The filament column density profile is then

$$N_{\mathrm{H_2}}(b) = N_0 \left\{ 1 + \left(\frac{b}{r_0} \right)^2 \right\}^{-(p-1)/2} , \tag{1.5}$$

where N_0 is the column density through the filament spine, and b is the impact parameter, or projected radius of the filament. Observations of nearby filaments with the *Herschel* Space Observatory have indicated that, when averaged along their length, filaments are well described by this Plummer-like profile, with an exponent of $p \approx 2$ (Arzoumanian et al. 2011; Palmeirim et al. 2013; Arzoumanian et al. 2019). $p \approx 2$ values have also been seen in simulations (Gómez and Vázquez-Semadeni 2014; Smith, Glover, and Klessen 2014). There have been several explanations for why observed and synthetic filaments exhibit Plummer-like exponents of $p \approx 2$ rather than $p \approx 4$. Fischera and Martin (2012) show that a $p \approx 2$ value can be obtained in the case where filaments are radially confined by an external pressure. Alternatively, Federrath (2016) suggests that if filaments form from colliding shocked sheets, then the density of the filament will go as $n_{\mathrm{H_2}} = l^{-2}$, where l is the thickness of the sheet.

In probing many varied environments, dust observations from the *Herschel* Gould Belt Survey (HGBS, André et al. 2010) have shown that filaments seem to present similar widths. Gaussian profiles fitted to the inner portions ($b \lesssim r_0$) of length-averaged profiles of filaments in many nearby regions show a narrow distribution of FWHM centred on 0.1 pc (Arzoumanian et al. 2011; Palmeirim et al. 2013; Arzoumanian et al. 2019). This result has also been shown to be true for filaments found outside local molecular clouds (André et al. 2016). However, recent work has called this result into question. Panopoulou, Psaradaki, and Tassis (2016) found that the narrow distribution of widths is a consequence of fitting to a length-averaged radial profile for each filament. Furthermore, Panopoulou et al. (2017) are unable to find a characterising length scale when analysing the HGBS filaments in Fourier space, a result which echoes the findings of Miville-Deschênes et al. (2010) who also observed no features at 0.1 pc when analysing the power spectrum of the Polaris Flare. In response, Roy et al. (2019) show that the area filling factor and the contrast between filaments and background emission in *Herschel* observations is likely to be too low for a characteristic length scale corresponding to filament widths to be detectable in Fourier space, even if one is present. Simulations of filamentary structures have

struggled to robustly reproduce the 0.1 pc width seen in observations. Hennebelle (2013) was able to produce filaments with 0.1 pc widths in magneto-hydrodymanic simulations, and suggested that the well defined width is a product of ion-neutral friction, which operates on a similar length scale. However, they note that if this is the case, then poorly shielded filaments and clumps on the edges of molecular clouds would be much narrower, a relation which is not seen in observations. Heitsch (2013a) was instead able to produce filaments with a 0.1 pc width via continual accretion processes, though if the ram pressure of the infalling material is taken into account, then this relation is destroyed in all but a few cases (Heitsch 2013b). Both Heitsch (2013b) and Smith, Glover, and Klessen (2014) note that the width recovered from a filament is highly dependent on the fitting parameters.

In molecular line observations, the 0.1 pc width is not observed. Instead, Panopoulou et al. (2014) identify a broad distribution of filament widths peaked at 0.4 pc when observing ^{13}CO in the Taurus region. This peak shifts to 0.2 pc when limiting observations to structures with coherent velocities, indicating that line of sight confusion may be broadening width estimates in both dust emission and integrated line emission. This interpretation is consistent with the high degree of sub-structure now known to be present within filaments. Hacar et al. (2013) show that the Taurus B211/B213 filament is composed of bundles of velocity coherent fibres. This has since been shown to be the case across several other regions (Henshaw et al. 2017; Hacar, Tafalla, and Alves 2017; Hacar et al. 2018). Simulations have also shown that what is observed as a 2D filament is often made up of a network of smaller 3D sub-filaments, though the 3D sub-filaments and the velocity coherent fibres do not necessarily trace the same structures (Clarke et al. 2018).

1.1.3 Fragmentation into Cores

Filaments are thought to be an intermediate step between molecular clouds and the formation of stars. 75% of pre- and protostellar cores are observed to be located along filaments (Könyves et al. 2015; Marsh et al. 2016). Therefore, understanding how filaments fragment into cores is vital for building a clear picture of core formation.

Models of equilibrium filaments have shown that filaments experience global collapse on longer timescales than equally dense spheres (Pon, Johnstone, and Heitsch 2011), which gives time for turbulent perturbations to grow. In equilibrium, the fasting growing mode has a wavelength equal to four times the diameter of the filament (Inutsuka and Miyama 1992). For filaments that are undergoing accretion, and that are also influenced by turbulent processes, the wavelength of the fastest growing mode

is instead given by

$$\lambda_{fragment} = 2\tau_{\rm C} c_{eff}, \tag{1.6}$$

where $\tau_{\rm C}$ is the time required to produce a thermally critical filament via accretion (Clarke, Whitworth, and Hubber 2016; Clarke et al. 2017). This gives rise to two scenarios. In gravity-dominated filaments, the largest perturbation breaks the filament into a series of widely spaced dense clumps. As the clumps grow in mass and become gravitationally unstable, they themselves fragment at the scale of the Jeans length: the length below which a spherical body is stable against gravitational collapse. The Jeans length is given by

$$\lambda_J \sim \frac{c_s}{\sqrt{G\rho}}, \tag{1.7}$$

where ρ is the mean density (Jeans 1928).

In contrast, turbulence-dominated filaments "fray and fragment" into sub-filaments (Tafalla and Hacar 2015; Clarke et al. 2017). Simulations have shown that either sub-filaments themselves undergo fragmentation, spawning cores along their lengths similar to the gravity-dominated filaments, or that intersections between multiple sub-filaments act as hubs for core formation (Clarke et al. 2017; Clarke et al. 2018). This turbulent model has been corroborated by recent, high resolution observations of several star forming regions (Hacar, Tafalla, and Alves 2017; Hacar et al. 2018).

The dense cores formed by either of these processes are the direct progenitors of stars. Cores have diameters from 0.01 pc to a few tenths of a parsec (Andre, Ward-Thompson, and Barsony 2000; Lomax, Whitworth, and Cartwright 2013), and range in mass from $0.1\,{\rm M}_\odot$ to tens of solar masses. They are much denser than typical molecular clouds, with central molecular hydrogen densities often exceeding $10^5\,{\rm cm}^{-3}$. The high density means their interiors are also well shielded from the ISRF. Thus cores are initially very cold ($\sim$10 K).

The initial phase of core evolution is the starless core, which can be gravitationally bound or unbound. By considering a sphere of radius $r_J = \lambda_J$, it is possible to derive the mass above which the sphere will collapse due to gravity, termed the Jeans Mass:

$$M_J \sim \left(\frac{4\pi}{3}\right)\rho r_J^3 = \left(\frac{4\pi}{3}\right)\frac{c_s^3}{G^{3/2}\rho^{1/2}}. \tag{1.8}$$

where ρ is the average mass volume density of the core. Starless cores with masses greater than the Jeans mass are bound, and are called pre-stellar cores, as they will collapse to form protostars at their centres. Starless cores with masses less than the Jeans mass, or which have additional mechanisms to support themselves against

gravitational collapse, are unbound. Unbound cores which are not pressure confined will disperse on a time scale given by

$$t_d \approx \frac{r}{\sigma}, \tag{1.9}$$

where σ is the internal velocity dispersion of the core (Ward-Thompson and Whitworth 2015).

Protostars are classified into several observationally distinct Classes from 0 to III (Lada 1987; Andre, Ward-Thompson, and Barsony 1993). Class 0 is the earliest type of protostar and has features comparable with a modified black body spectrum at $\sim$30 K. Physically, it is believed to have most of the core mass still contained in the core envelope. Class I cores are those whose infrared spectrum can be well described by a power law with a spectral index, $\alpha > 0.3$, when measured between 2.2 µm and 20 µm. The physical transition from Class 0 to Class I is thought to take place when the fraction of the core mass contained within the central protostar exceeds 50%. However, as the protostar is still deeply embedded, Class 0 and Class I sources share many physical and observational properties and are difficult to tell apart observationally. Therefore, they are often grouped together as Class 0/I sources. Class II cores have a spectral index $-0.3 > \alpha > -1.6$. The steepening slope is due to the lost their envelopes through a combination of accretion onto the protostar, excavation with bipolar outflows, and other dispersive processes, leaving them with just the circumstellar discs surrounding the central objects. Class III stars have lost all circumstellar material, and are considered pre-main sequence stars. They exhibit $\alpha < -1.6$.

While theoretical work has allowed some physical understanding of the state of protostars associated with different Classes, observational nature of the Class system can lead to confusion and misidentification of cores in different geometries. For example, a Class II protostar viewed edge on might exhibit the same infrared spectrum as a Class I source, as the thick, circumstellar disk behaves like an envelope, obscuring the central object. It is sometimes beneficial to refer to protostellar Stages (Robitaille et al. 2006; Robitaille et al. 2007; Robitaille 2017), which are derived from the physical parameters of protostars in simulations. The mass budget of Stage 0/I protostars is dominated by an infalling envelope, while Stage II protostars have very tenuous envelopes but optically thick circumstellar discs. Stage III protostars have lost most or all of their discs. Synthetic observations of these protostellar models reveal that in most cases, a Stage is analogous to a Class of the same order. However, they also indicate how viewing angle can change the observational appearance, and

thus Class, of a protostar. As protostars are not the main focus of this thesis, and I am simply concerned with their observational properties, I utilise the Class system throughout.

During the initial contraction of a prestellar core, gravitational potential energy is converted into inward radial kinetic energy and thermal kinetic energy of the gas and dust. In the early stages of collapse, cores are generally optically thin. This allows the thermal energy to be radiated away via emission. As long as this holds true, the contraction will approach freefall collapse, with a timescale given by

$$t_{ff} = \left(\frac{3\pi}{32G\rho}\right)^{1/2}. \tag{1.10}$$

As the density of the protostellar core increases, the gas and dust become increasingly optically thick. This reduces the efficiency with which thermal energy is radiated away from the interior of the core, leading to an increase in temperature. The protostar is first observable as a deeply embedded point source in the centre of a gas- and dust-rich envelope when the central object has reached a temperature between 20 K and 40 K. This corresponds to a peak wavelength of between 160 µm and 70 µm (PACS Bright Red Sources, Stutz et al. 2013). As the protostar continues to warm, its emission peak shifts to shorter wavelengths.

Eventually, the density of the protostellar core increases to the point where thermal energy is unable to be radiated away from the core interior faster than it is generated through conversion of gravitational potential energy. This halts the collapse and forms the First Hydrostatic Core (FHC) in the centre of the envelope. The FHC is heated by accretion shocks and the Kelvin-Helmholtz contraction, and this allows it to shrink, becoming a Class 0 protostar.

Mass continues to accrete from the envelope onto a circumstellar disc, and then onto the protostar itself. When the mass of the protostar exceeds the mass of the remaining envelope, it becomes a Class I protostar. As the temperatures continue to rise, the molecular hydrogen within the protostar dissociates, and it undergoes another rapid collapse towards the Second Hydrostatic Core (SHC). Continued accretion onto the SHC eventually raises the density and temperature to the point where fusion processes begin to occur, and the remaining envelope is dispersed (Larson 1969a; Larson 1969b; Masunaga and Inutsuka 2000; Commerçon et al. 2011; Bate, Tricco, and Price 2014).

These processes describe the formation of low- and intermediate-mass stars. The formation process of high-mass stars is less certain. One theory proposes high-mass stars form from high-mass cores, in much the same way as low-mass stars.

These cores, which greatly exceed the Jeans mass, are supported through high internal turbulent pressures. On very short timescales (typically on the order of a single freefall time), the turbulence dissipates and the core collapses monolithically, rapidly forming a high-mass protostar. This "turbulent core" model was first proposed by **McKee2002**. A second theory suggests that high-mass stars begin as low-mass cores, that are continually fed material as they collapse at a rate equivalent to the matter being accreted. Such models (**Vazquez-Semadeni2009**; **Vazquez-Semadeni2017**) is based on the earlier "competitive accretion" model (**Smith2009**), and requires that the parent cloud is arranged in such a way as to funnel material towards the core. Such a system is believed to be present in hub-and-spoke filament networks, where several filaments converge on a central, dense region. Observational evidence for either scenario is proving difficult to obtain, due to the small number of high-mass stars to low-mass stars, and due to the short timescales involved (**Motte2007**; **Tige2017**; **Motte2018**). Eventually, the intense radiation from the massive central protostar drive the formation of an ionised HII bubble, which, together with stellar winds and other processes, stall further accretion and excavate a cavity within the parent cloud. This transition begins to occur when the core exceeds $8\,M_\odot$.

1.1.4 The Gould Belt and the Radcliffe Wave

John Herschel (1847) first noted a large number of bright stars visible from the Southern Hemisphere that appeared to form a coherent structure inclined to the Galactic Plane by $\sim 20^\circ$. Benjamin Gould (1879) produced the first detailed study of this structure, finding that the stars formed a complete ring on the sky. The structure was therefore given his name: the Gould Belt. Shapley (1919) further confirmed that the Gould Belt was not part of the Galactic Plane by determining that the stars which made up the belt were much closer to the solar system ($<600\,pc$) than the clusters found within the rest of the Galaxy. Later studies linked the Gould Belt not just with stars, but also sites of active star formation (Taylor, Dickman, and Scoville 1987; Porras et al. 2003).

The Gould Belt is believed to be a 50 pc thick, elliptical structure, inclined between 16° and 22° to the galactic plane, with semi-major and semi-minor axes of $\sim 350\,pc$ and $\sim 250\,pc$ respectively. The Sun is estimated to be 40 pc from the line connecting the two nodes of the ellipse, placing it slightly off centre (Bobylev 2014). Many theories have been proposed for creating such a ring, including an expanding bubble driven by stellar feedback (Poppel 1997), the impact of a high velocity cloud with the galactic disc (Comeron and Torra 1994), and the collision of a GMC with

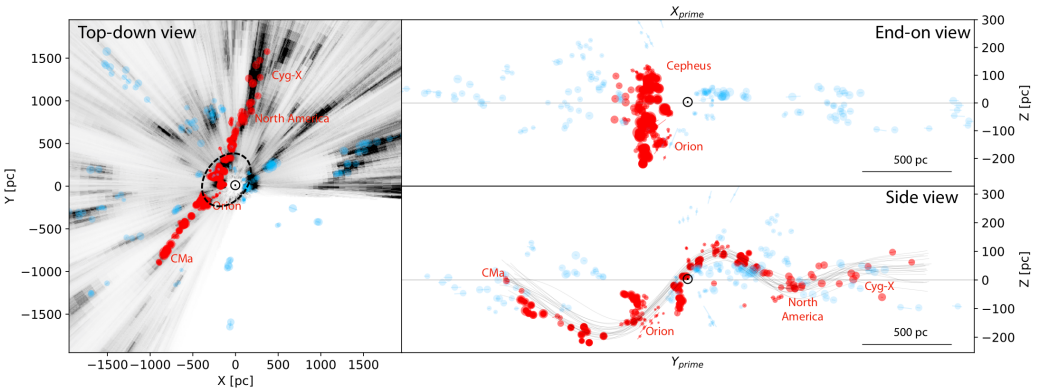

Figure 1.3. A diagram of the star forming clouds surrounding the solar system. A coherent, elongated structure is clearly visible in red. This structure appears to form a wave consistent with a damped harmonic oscillator when viewed in the yz plane. Diagram taken from Alves et al. (2020). I have added the black dashed ring to indicate the approximate location of the Gould Belt. The ring passes through several clouds that are considered part of the Radcliff Wave, as well as a cluster of clouds that are not part of the wave . The position of the ring is taken from Perrot and Grenier (2003).

a rogue, dark matter dominated cloud (Bekki 2009). Despite this, no one theory has been able to fully explain the observed structure. However, a recent study has indicated that this may be because the Gould Belt is not a single structure. *Gaia* Data Release 2 measurements of the distances and velocities of stars associated with molecular clouds have shown that the star forming regions that make up one half of the Gould Belt may belong to a much larger density wave spanning >2.5 kpc (see Figure 1.3) called the Radcliffe Wave (Alves et al. 2020).

This finding suggests that the Gould Belt did not form as a ring, but is instead only the coincidental projection of several star forming regions. Nevertheless, the Gould Belt remains a useful name for grouping the nearest star forming clouds. These clouds are of great importance, as they allow us to examine the star formation processes with unparalleled spatial resolution across a number of environments, informing our understanding of cloud collapse, filament formation, core fragmentation, low and high mass star formation and feedback processes.

1.2 Dust

As highlighted previously, dust is an important component of the ISM, making up $\sim 1\%$ its mass. However, the origin of dust still remains a mystery. While dust is produced by stars in the red giant or red supergiant phase, and given off in stellar winds (Ferrarotti and Gail 2006; Sargent et al. 2010), the observed production rate is insufficient to produce all the dust seen in the ISM (Matsuura et al. 2009; Dunne

et al. 2011). Large quantities of dust have also been observed in young supernova remnants, indicating that they are significant factories of dust (Dwek and Scalo 1980; Dunne et al. 2003; Matsuura et al. 2011), but much of that dust is thought to be destroyed by the supernova reverse shock. Dust could also form *in situ* through reactions in the diffuse ISM, though no viable chemical pathways have so far been identified. Regardless of its formation, however, the presence of dust in the ISM, and its importance to galactic processes is without dispute.

Most of the interstellar dust grains in the Milky Way are between 10 nm and 10 µm in diameter (Kim and Martin 1994). Such grains scatter and absorb a significant fraction (30%) of all light in the universe in a process called extinction (Popescu and Tuffs 2002; Viaene et al. 2016; Bianchi et al. 2018). Shorter wavelength radiation (e.g. UV or blue light) is more strongly extincted than longer wavelength radiation (e.g. red and infrared) as the strength of the effect has a $\sim \lambda^{-1}$ dependence. This is further compounded at wavelengths comparable to the size of the dust grains, where the dependence on the scattering goes as λ^{-4}. Therefore, extinction produces a reddening effect on sources seen through dust clouds. During the absorption process the energy of the absorbed photons is not lost, but is re-emitted at longer wavelengths. This effect helps to regulate the thermal balance of the ISM, and is particularly important for removing thermal energy from dense, star forming cores, allowing them to collapse.

Dust grains are also important molecular factories, with H_2 and other, more complex, molecules forming on the surfaces of the grains. The grains then aid in shielding those molecules, preventing them from becoming dissociated by UV radiation. Dust grains also form the building blocks for planet formation.

In most situations, the dust is dynamically coupled to the gas, and thus is concentrated in molecular clouds. While it is therefore a good indicator of molecular cloud position, the dust blocks optical and UV emission which makes it difficult to observe the structures and processes in the cloud interiors. This is a problem for understanding the star formation that takes place within these dense, dark clouds. However, it is possible to examine the effects of dust itself, and use it as a tracer for these deeper structures.

One method is to observe dust through extinction. Radiation from stars behind dense clouds of dust and gas is attenuated by the dust grains due to scattering and absorption. As mentioned previously, shorter wavelength radiation is more attenuated than longer wavelength radiation, which leads to a reddening of the observed light. This reddening can be used to compare stellar magnitudes in different optical bands, such as the blue magnitude (B) and red magnitude (R). By modelling the

stars, it is possible to compare the observed colour difference $(B-V)$ to the the theoretical colour difference from the unattenuated stars, $(B-V)_0$, and thus determine the degree of reddening

$$E(B_V) = (B-V) - (B-V)_0 \tag{1.11}$$

This is often converted to an absolute extinction, $A_V = RE(B-V)$, where R is the ratio of total to selective extinction; in the diffuse ISM, $R \sim 3.1$ (Cardelli, Clayton, and Mathis 1989).

Unfortunately, A_V is difficult to measure for dense molecular clouds due to the high opacity meaning they are nearly completely opaque to optical wavelengths. Instead, near infrared extinction (A_K) is often used (Lada et al. 1994; Lombardi and Alves 2001). This is determined via the same procedure, but utilises near infrared observing bands. A_K can be converted to an equivalent A_V (e.g. Rieke and Lebofsky 1985), and then into an estimate of H_2 column density (e.g. Bohlin, Savage, and Drake 1978). It can therefore be used to track changes in column density across the cloud, and to measure the total cloud mass and the masses of the smaller sub-structures. However, it gives no information on the dust temperature or variations in the dust opacity properties.

An alternative method of using dust as a tracer of the gas in molecular clouds is to directly observe the thermal emission from the dust grains. At the typical temperatures of molecular clouds, this emission is in the far infrared and sub-millimetre wavebands. The emission mechanism and methods for estimating H_2 mass, temperature, and opacity index are described in the following Sections.

1.2.1 Dust Emission as a Tracer of Molecular Cloud Mass

The first thorough analysis of far infrared and sub-millimetre dust emission as a good tracer for the mass of molecular clouds was performed by Hildebrand (1983). The mass estimation begins by considering the emission and transmission of radiation itself. From a generalised observational perspective, the transmission of radiation through a medium to an observer is governed by the equation of radiation transport (e.g. Chandrasekhar 1960),

$$\frac{\mathrm{d}I_\lambda}{\mathrm{d}s} = -\alpha_\lambda I_\lambda + j_\lambda, \tag{1.12}$$

where I_λ is the specific intensity of radiation at a given wavelength, λ, s is a position in space along the line of sight between the observer and the emitting object, α_λ is

a coefficient that describes the absorption properties of the medium, and j_λ is the emission coefficient. By defining an optical depth, τ_λ such that $\mathrm{d}\tau_\lambda = \alpha_\lambda \mathrm{d}s$, and by assuming that the emission term is independent of this optical depth, the solution of equation 1.12 is

$$I_\lambda = I_0 e^{-\tau_\lambda} + S_\lambda(T)\left(1 - e^{-\tau_\lambda}\right), \tag{1.13}$$

where $S_\lambda(T)$ is the source function, and is in turn given by j_λ/α_λ. T is the temperature of the source, and I_0 is the unattenuated emission from the medium though which the radiation propagates. In the case where the observed radiation is far infrared and sub-millimetre emission from an interstellar dust cloud which is in thermal equilibrium, the source term is given by the Planck function*

$$S_\lambda(T) = B_\lambda(T) = \frac{2hc^2}{\lambda^5}\frac{1}{\exp\left(\frac{hc}{\lambda k_\mathrm{B} T}\right) - 1}. \tag{1.14}$$

Furthermore, when the background intensity is negligible ($I_0 \sim 0$) the solution to equation 1.12 then becomes

$$I_\lambda = \left(1 - e^{-\tau_\lambda}\right) B_\lambda(T), \tag{1.15}$$

which can be further simplified in optically thin environments ($\tau_\lambda \ll 1$) to

$$I_\lambda \approx \tau_\lambda B_\lambda(T). \tag{1.16}$$

In the case of a molecular cloud, where the radiation is due to thermal emission from a population of uniform, spherical dust grains at a temperature T_D, the optical depth is directly related to the properties of the emitting dust within the cloud by the equation

$$\tau_\lambda = \sigma_{grain} N_\mathrm{D} Q_\lambda, \tag{1.17}$$

where σ_{grain} is the cross section of a dust grain, N_D is the column density of the dust grains, and Q_λ is an efficiency coefficient which describes the ratio between the power emitted by a dust grain at wavelength, λ, and the power emitted by a black body with

*A peculiarity of far infrared and sub-millimetre dust astronomy is that specific intensity is often quoted in units of some multiple of janskys per unit solid angle (e.g. $\mathrm{MJy\,sr^{-1}}$ for *Herschel* SPIRE observations), while observation bands are quoted in terms of wavelength. The jansky is a measure of power per unit area per unit frequency with $1\,\mathrm{Jy} = 10^{-23}\,\mathrm{erg\,s^{-1}\,cm^{-2}\,Hz^{-1}}$. Therefore, while the formalism in this thesis is to present all analysis in terms of wavelength, care is taken to ensure quantities are correctly converted to maintain the correct dimensionality.

the same effective temperature at the same wavelength. The value of Q_λ is related to the physical absorption and emission properties of the individual dust grains. In the regime where the dust grains are much smaller than the wavelength of emitted light (which holds true for dust in molecular clouds radiating in the far infrared and sub-millimetre), Q_λ can be related to the emission wavelength by considering the Mie (1908) approximation to Maxwell's equations. This gives the relation

$$Q_\lambda \propto \lambda^{-\beta}, \tag{1.18}$$

where β is the dust opacity index[†]. The spectral luminosity of dust grains in an observed dust cloud with surface area A_{cloud} is given by

$$L_\lambda = 4\pi A_{cloud} N_{\mathrm{D}} \sigma_{grain} Q_\lambda B_\lambda(T_{\mathrm{D}}). \tag{1.19}$$

The specific intensity is recovered by considering the surface area of a sphere centred on the cloud and through the observer, over which the luminosity from equation 1.19 is spread and noting that the solid angle subtended by the cloud is $\Omega = A_{cloud}/D^2$, where D is the distance to the cloud from the observer. The specific intensity is therefore given by

$$I_\lambda = \sigma_{grain} N_{\mathrm{D}} Q_\lambda B_\lambda(T_{\mathrm{D}}). \tag{1.20}$$

As the emission has a form similar to that of a black body radiator, it is often referred to as a grey body, or modified black body (MBB). It is common to replace the column density of dust, N_{D}, with the column density of hydrogen molecules, $N_{\mathrm{H_2}}$, by assuming a dust to gas ratio, R_{D2G}. Thus, equation 1.20 can also be expressed as

$$I_\lambda = \sigma_{grain} N_{\mathrm{H_2}} R_{D2G} Q_\lambda B_\lambda(T_{\mathrm{D}}). \tag{1.21}$$

As, in reality, the dust in a molecular cloud is not formed from uniform, spherical grains, σ_{grain} is poorly constrained. Similarly, the value of Q_λ depends on the physical properties of the grains such as size, mass, heat capacity and chemical composition which are often exceedingly difficult or impossible to determine accurately. It is, therefore, convenient to group these terms, along with the dust to gas ratio, such that

[†]the terms "opacity index" and "emissivity index" are both used to describe β in published works. I choose to use "opacity index" to remain consistent with Marsh, Whitworth, and Lomax (2015), which introduces the PPMAP algorithm.

$$\sigma_{grain} Q_\lambda R_{D2G} = \bar{m}_{\mathrm{H_2}} \kappa_\lambda, \tag{1.22}$$

where $\bar{m}_{\mathrm{H_2}}$ is the mean mass associated with each hydrogen molecule when account is taken of other species, and κ_λ is the mass opacity coefficient which describes the dust opacity properties in a single parameter. For gas with solar composition, in which all the hydrogen is molecular, $\bar{m}_{\mathrm{H_2}} \approx 4.77 \times 10^{-24}$g.

As with equation 1.18, in the small grain regime, the wavelength dependence of κ_λ can be expressed by a power law:

$$\kappa_\lambda = \kappa_0 \left(\frac{\lambda}{\lambda_0} \right)^{-\beta}, \tag{1.23}$$

where κ_0 is the reference mass opacity coefficient, which has units of area per unit mass, at wavelength λ_0.

The reference mass opacity coefficient is typically found to have uncertainties of at least a factor 2 due to the underlying uncertainty in the values of σ_{grain} and Q_λ. Throughout this thesis, I use a reference mass opacity at 300 µm, $\kappa_{300\,\mu\mathrm{m}}$, of $0.1\,\mathrm{cm^2\,g^{-1}}$, which is the value adopted by the *Herschel* Gould Belt Survey team, and is consistent with the observationally derived reference opacity at 1.3 mm commonly used for dense, prestellar cores and clumps (e.g. Preibisch et al. 1993; Andre, Ward-Thompson, and Motte 1996; Motte, Andre, and Neri 1998). This value is very close to the opacity proposed by Hildebrand (1983), and is consistent with a gas to dust ratio of 100 (i.e. $R_{D2G} = 0.01$).

Once κ_0 is fixed, variations in the dust emission properties can be expressed as changes to the opacity index, β. Through observation and experiment (e.g. Dunne and Eales 2001; Smith 2013; Demyk et al. 2013), β has been found to take a value close to 2, while Planck Collaboration et al. (2014) estimates a median opacity index value within the Milky Way of 1.76, with a standard deviation of 0.08.

It has been suggested that high values of the opacity index ($\beta \approx 2$) indicate the presence of metallic or crystalline dust grains, while lower values of the opacity index ($\beta \approx 1$) are indicative of small (<300 nm) amorphous grains (Tielens and Allamandola 1987). However, grains made of layered silicate structures have been found to complicate this relationship, as linking between the layers produces $\beta > 1$. Additionally, while grain growth and ice mantle formation has been found to significantly alter the value of the opacity index (Testi et al. 2014), the relationships refer exclusively to grains typically found in proto-planetary discs, which are larger than interstellar grains (>10 µm). Furthermore, Agladze et al. (1996) found that the value of β changes significantly with increasing temperature over the range 1.2 K

to 30 K for 0.1 µm to 1 µm amorphous iron silicate grains when observed between 700 µm and 2900 µm, though similar cryogenic analyses of the dust opacity index of other compounds are sparse, and few focus on the far infrared and sub-millimetre wavebands. Thus, while dust opacity index variations are likely to be a good tracer of changes in dust properties, the precise nature of those changes remains uncertain.

By substituting equation 1.22 and equation 1.23 into equation 1.21, I obtain a MBB with the form

$$I_\lambda = N_{\mathrm{H_2}} \bar{m}_{\mathrm{H_2}} \kappa_0 \left(\frac{\lambda}{\lambda_0}\right)^{-\beta} B(T_\mathrm{D}). \tag{1.24}$$

The mass column density is often represented by a single parameter, $\Sigma_{\mathrm{H_2}}$, where $\Sigma_{\mathrm{H_2}} = N_{\mathrm{H_2}} \bar{m}_{\mathrm{H_2}}$.

The hydrogen column density along a given line of sight can be obtained by rearranging equation 1.24 to produce

$$N_{\mathrm{H_2}} = \frac{I_\lambda}{\bar{m}_{\mathrm{H_2}} \kappa_0 \left(\frac{\lambda}{\lambda_0}\right)^{-\beta} B(T_\mathrm{D})}, \tag{1.25}$$

and the cloud total mass can then be derived by integrating over the surface area of the cloud to give

$$M_{\mathrm{H_2}} = N_{\mathrm{H_2}} \bar{m}_{\mathrm{H_2}} A_{cloud} = \frac{I_\lambda}{\kappa_0 \left(\frac{\lambda}{\lambda_0}\right)^{-\beta} B(T_\mathrm{D})} A_{cloud}. \tag{1.26}$$

1.2.2 Fitting a Spectral Energy Distribution

While, in theory, equation 1.25 can be used to obtain the H_2 column density along a sight line from a single measurement of specific intensity, it would require known values of the line of sight dust temperature and opacity index. These values are, however, very difficult to determine independently. Instead, targets are typically observed at multiple wavelengths. This makes it possible to fit a spectral energy distribution (SED) consisting of one or more MBBs to the observations. If there are enough independent data points, the total H_2 column density, the dust temperatures and opacity indices of each constituent MBB along a given line of sight can be treated as free parameters, and thus are estimated simultaneously. It is common to assume that the emission can be modelled as a by single MBB (this is called the MBB fitting technique to distinguish it from other, more complex SED models) with constant line of sight dust temperature and dust opacity index.

Although MBB fitting is simple and quick to perform, it does have significant pitfalls. To accurately estimate H_2 column density, MBB fitting requires that the observations accurately capture all the emission from along the line of sight. Therefore, the target must be optically thin. Otherwise self absorption of emission within the target will lead to an underestimate of the column density. Fortunately, this condition is expected to hold true for far infrared and sub-millimetre emission in all but the densest protostellar cores. As stated previously, a single MBB fit assumes that the dust along the line of sight has a single, fixed temperature and opacity index. This assumption is clearly a gross simplification due to the highly sub-structured nature of molecular clouds and filaments, which are subject to heating from the ISRF at their surfaces, cooling though dust and molecular line emission, and feedback effects from protostellar objects and young massive stars.

Figure 1.4 shows the effect of changing dust temperature and dust opacity index on a modified black body function. The intensity of each of the displayed MBB curves has been normalised for convenience. Comparing the MBB curves shows that by lowering the temperature from 20 K (black curve) to 16 K (red curve), the peak of the MBB is shifted to longer wavelengths. However, a similar shift in the peak position can be achieved by keeping temperature fixed, and instead lowering the value of the opacity index, β, from 2 (black curve) to 1 (blue-dashed curve). Only in the longer wavelength Rayleigh-Jeans tail can the two effects be disentangled. This effect has been well noted as an observed temperature and opacity index anti-correlation (**ShettyA2009**; **ShettyB2009**). Therefore, to accurately fit both parameters, we require observations that well sample both the peak and the tail of the function.

For warm targets (dust temperature >25 K), this is not typically much of an issue. However, for colder targets (dust temperature <25 K), such as molecular clouds, this can be difficult to achieve. Ground based observatories that are capable of imaging at longer wavelengths (λ >500 µm) struggle to produce observations of extended structure due to the filtering required to remove atmospheric effects. Long wavelength space observatories are limited by the poorer angular resolution inevitable with smaller telescopes, while space observatories with high resolution have not carried instruments capable of observing beyond 500 µm (because of the competition for such observations from ground-based facilities).

Therefore, in most studies of molecular clouds the dust opacity index is not only assumed to be constant along the line of sight, but is also typically fixed at a single value across the entire region or even multiple regions. The commonly assumed value of opacity index for molecular clouds within the Gould Belt is 2 (see André et al. 2010; Könyves et al. 2010), which is consistent with Hildebrand (1983).

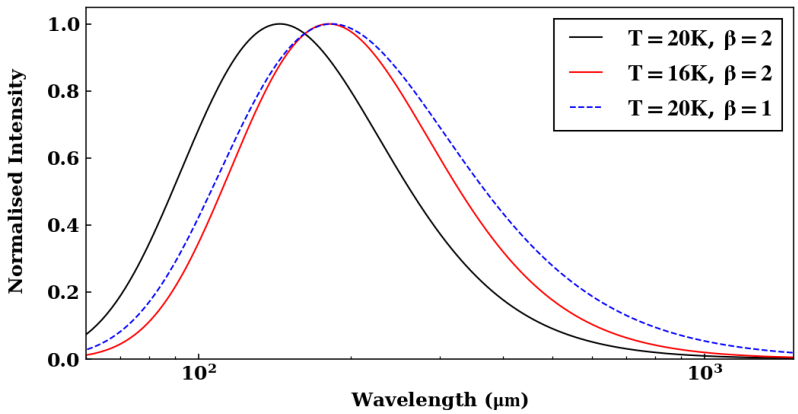

Figure 1.4. The effect of variable dust temperature (red curve) and variable dust opacity index (blue-dashed curve) on the shape of a MBB (black curve). Comparison of the red and blue-dashed curves reveal that the effect on the MBB peak of a drop in dust temperature can be reproduced by a drop in dust opacity index. In contrast, the two variations can be distinguished by their effect on the Rayleigh-Jeans tail at longer wavelengths. The intensity of the MBB functions has been normalised for easy reference.

A further requirement of SED fitting is that the observations all share a common resolution. This is typically achieved by convolving the observations with the beam profile of the observation with the coarsest resolution. This degrades the image quality of the other observation bands, leading to information loss. A few common techniques, such as the one presented in Palmeirim et al. (2013), are able to recover some of the lost angular resolution through careful comparison of low-resolution, high-accuracy column density maps produced from all available observations, and higher-resolution, lower-accuracy column density maps made from a subset of the observations after excluding those with the coarsest resolutions. However, the recovered resolution comes at the expense of an increased level of noise.

1.3 Thesis Outline

Accurate measurements of the properties of environments surrounding star forming filaments, and the structure of the filaments themselves, are vital to understand their role in star formation. However, attempts to measure these properties from observations of dust emission suffer from the limitations of fitting MBBs noted above. The recently developed PPMAP algorithm provides a method of estimating H_2 column density and dust properties without having to resort to the simplified assumptions of standard MBB fitting techniques.

Using the superior diagnostic capabilities of PPMAP, I analyse two of the closest star forming regions within the Gould Belt, using multiband mapping by the

Herschel PACS and SPIRE cameras, and ground-based sub-millimetre maps from the James Clerk Maxwell Telescope (JCMT): the Taurus L1495/B213 complex, and the Ophiuchus L1688 and L1689 sub-regions. These are the closest regions of active star formation to the Sun, lying at a distance of ∼140 pc. This enables very high spatial resolution mapping, sufficient to resolve the filamentary structure that mediates star formation. In both regions, I identify the main filamentary structures and analyse the filament properties, with a particular focus on determining variations in width and line density along the lengths of each of the filaments. I also use PPMAP to investigate both the line of sight and plane-of-sky variations in the dust temperature and dust opacity index within each region. I then link both the filament properties and dust properties to sites of active core formation to build a picture of how these variations affect, or are affected by, the star formation processes.

This analysis reveals several key findings:

- I show for the first time that the main Taurus B211/B213 filament is better fit by a $p = 4$ Plummer-like profile than by the standard $p = 2$ profile.
- I determine that the main Taurus B211/B213 filament is globally thermally trans-critical, and areas of active core formation are only locally super-critical.
- In the Ophiuchus L1688 and L1689, I identify several filaments and perform the first large scale analysis of their properties.
- In both the Taurus and Ophiuchus regions, I find the filaments are approximately half as wide as previously reported, and that the conventional width of 0.1 pc is likely to be a result of single MBB fitting techniques misidentifying the warm, diffuse dust in the outer portions of filaments as colder, denser material.

1.3.1 Thesis Structure

In Chapter 2, I give an overview of the main instruments and techniques involved in producing and reducing the observational data for this thesis. Chapter 3 describes the mathematical underpinnings for the PPMAP algorithm, and explains its implementation. In Chapter 4, I present the results of a number of tests I have performed to test the capabilities of the PPMAP algorithm. Chapter 5 presents my analysis of the results of the application of PPMAP to far infrared and sub-millimetre observations of the Taurus L1495/B213 complex, and compares the findings with previous observational work conducted by Palmeirim et al. (2013). In Chapter 6, I discuss the results of my application of PPMAP to far infrared and sub-millimetre

observations of the Ophiuchus L1688 and L1689 star forming sub-fields. Within this Chapter, I present the first analysis of the properties of filaments within the fields. In Chapter 7, I summarise the main conclusions from this thesis, and outline my future plans to expand upon these analyses.

Chapter 2
Instrumentation and Data Reduction

The observations analysed in this thesis are taken in far infrared and the sub-millimeter wavebands. The presence of water vapour in the Earth's atmosphere means that it is effectively opaque at many of these wavelengths. To combat this, ground based telescopes must be located at high altitudes, where there is very little water content. This opens transmission windows through which certain wavelength bands can be observed. Figure 2.1 (Casey, Narayanan, and Cooray 2014) shows that transmission rates of 80% can be obtained at the summit of the extinct, Hawaiian volcano, Mauna Kea, for precipitable water vapour (PWV) content of 0.5 mm (very good conditions). This is the site of the James Clerk Maxwell Telescope (JCMT), which provided data for part of this thesis.

Another way to overcome poor atmospheric transmission is to locate the telescope in space. Additionally, space operation avoids other unwanted effects such as thermal radiation from the atmosphere in the observing band, which can increase noise. In this thesis, data have been used from primarily the *Herschel* Space Observatory, with supplemental data from the Infrared Astronomy Satellite (*IRAS*) and *Planck* Surveyor missions. *IRAS* was stationed in a geocentric, Sun-synchronous low-Earth orbit, while *Herschel* and *Planck* operated from orbits around the second Lagrangian point of the Sun-Earth system (L2).

Another source of noise is the thermal emission from the telescope structures and instruments. Together with atmospheric thermal emission, these effects are called photon noise. With modern bolometric and photo-conducting detectors, it is these thermal fluctuations that provide the ultimate limit on sensitivity. As such, detectors and optics are often cooled to temperatures a few tenths of a degree above absolute

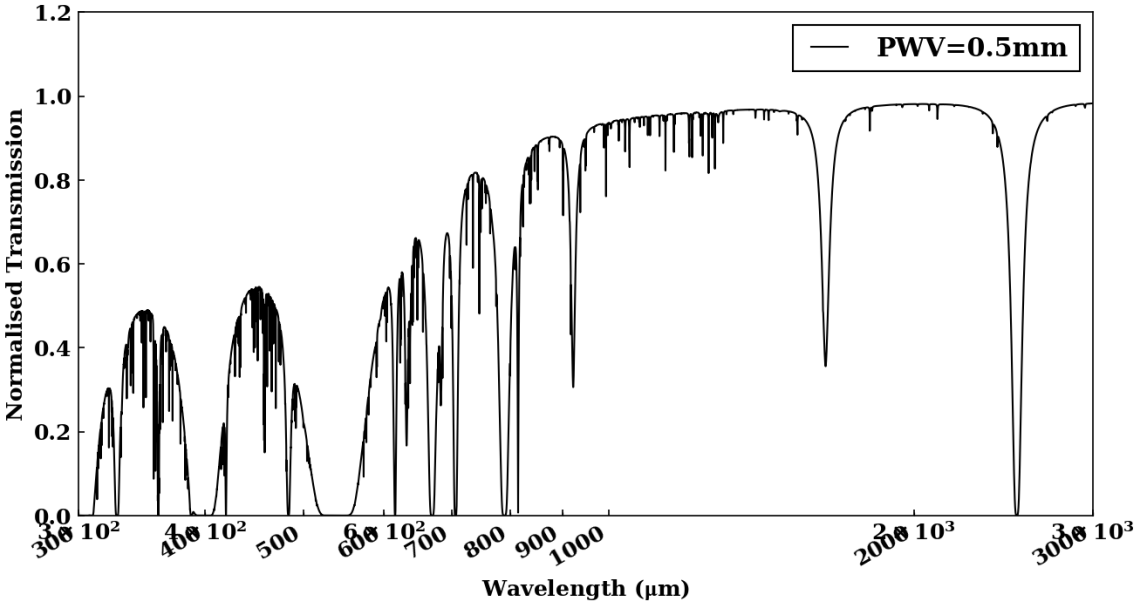

Figure 2.1. Atmospheric transmission of sub-millimetre and millimetre wavelengths, atop Mauna Kea, for a Precipitable Water Vapour (PWV) level of 0.5 mm. Reproduced from Casey, Narayanan, and Cooray (2014), with permission.

zero. The placement of telescopes in space allow for the entire system to be cooled, rather than just the focal plane.

Observations in this work are photometric, though the spectroscopic capabilities of each telescope are briefly discussed.

2.0.1 *Herschel*

The *Herschel* Space Observatory (Pilbratt et al. 2010), was a far infrared and sub-millimetre space telescope operated by the European Space Agency (ESA), covering a wavelength range of 55 µm to 671 µm. It was launched in May 2009, and placed in a quasi-halo orbit around the Sun-Earth second Lagrangian point (L2). As a far infrared/sub-millimetre telescope, it was highly sensitive to photon noise, which typically dominates over the range of wavelengths *Herschel* was designed to observe. L2 provides a stable platform for telescope operations as the orientation of the Sun-Earth-satellite system prevents the temperature of the satellite from fluctuating greatly. In turn, this reduces thermo-elastic fluctuations which could degrade the pointing precision during observing runs. Further advantages of L2 over low-Earth orbit are to reduce the angular size of the Earth, allowing for a greater observable region at a given time, and to minimise the effects of the Earth acting as a thermal radiator, which could limit the degree of cooling possible for a telescope. Satisfying

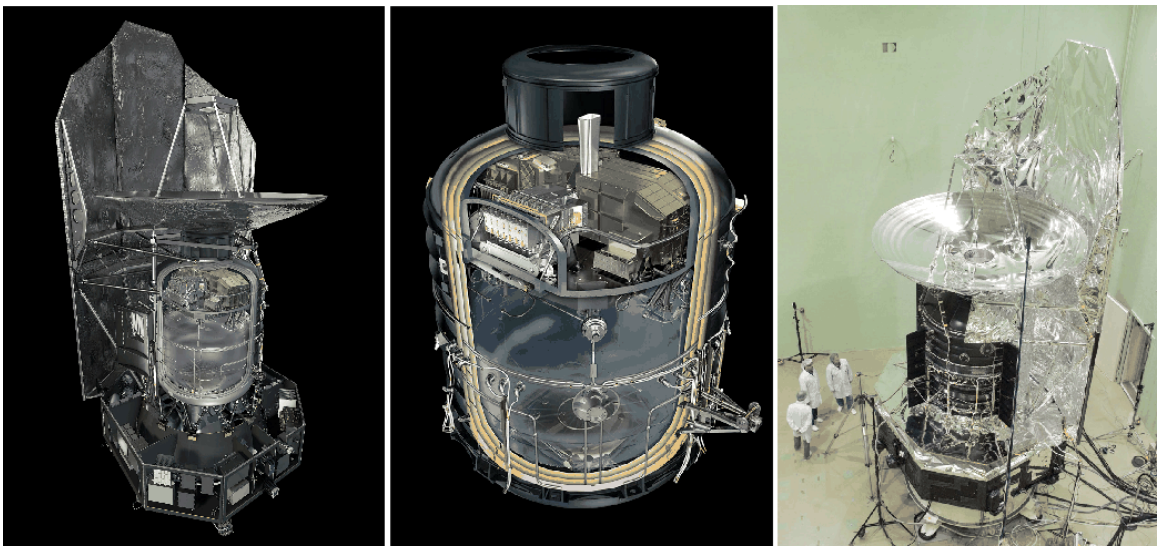

Figure 2.2. Digital models of the full spacecraft (left), comprising the PLM, SVM and sunshield, and of the cryostat (middle), showing the instruments placed on top of the helium tank. The final panel (right) displays *Herschel* being prepared for acoustic testing. Image credit Pilbratt et al. (2010).

these conditions was vital for ensuring *Herschel's* outstanding sensitivity.

Figure 2.2 shows a diagram of the *Herschel* spacecraft (left), in which its components are clearly visible. As with many scientific satellites, *Herschel* was divided into a Payload Module (PLM), a Service module (SVM), and a sunshade to protect from direct solar radiation. Solar arrays to power the craft were situation on the back side of the sunshade, which was directed to face the Sun at all times during operation.

The PLM was comprised of the primary and secondary mirrors, and a liquid helium cryostat for cooling the instruments. *Herschel*'s 3.5 m diameter primary mirror was the largest primary mirror of any space astronomy telescope to date. The secondary mirror was slightly undersized to ensure that the insturments could not see thermal emission from the spacecraft itself. This limited the effective telescope diameter to 3.28 m.

Directly below the primary mirror is the cryostat, with a capacity of 2200 l. This contained the liquid helium coolant at a temperature of 1.7 K, with the instruments mounted on an optical bench above the helium tank. A diagram of the cryostat can be seen in the middle panel of Figure 2.2.

The space-facing side of *Herschel* was painted black to maximise the rate at which the telescope could be cooled. This, and further passive cooling techniques, maintained the telescope itself at ∼80 K. The liquid helium was boiled off through a series of pipes to cool the instruments to ∼5 K, which were thermally insulated from the telescope by a series of nested shields. Finally, the PACS and SPIRE bolometers

(described below) were cooled by internal refrigerators to 0.3 K.

The SVM, situated below the PLM, housed the computers, telemetry equipment, and other systems vital for operating the spacecraft. The SVM was kept thermally isolated from the PLM by low-thermal conductance support struts, as the SVM had an operating temperature of 300 K.

Although *Herschel*'s primary mirror was large for space telescopes, it was still much smaller than ground-based observatories dedicated to comparable wavebands (e.g. JCMT's 15 m dish). This was due to restrictions on the size and mass of the Ariane 5 rocket which carried it into orbit. The 3.28 m effective diameter of the primary determined the diffraction-limited beam size of the *Herschel* bands. This beam size is given by

$$\text{FWHM} \sim \frac{\lambda}{3.28\,\text{m}}, \tag{2.1}$$

where the observation wavelength, λ, is given in metres. This beam size varied between $\sim$5.5″ at 70 µm at the slowest scan speed, and 36.6″ at 500 µm for the fastest scan speed.

Herschel had three science instruments, HIFI, PACS, and SPIRE, capable of observing the universe through spectroscopy and photometry. The instruments were designed to compliment each other, providing spectroscopy and photometry across the full wavelength coverage of the observatory. These instruments are discussed below, with particualr emphasis on PACS and SPIRE, which provided much of the data used in this thesis.

Herschel maintained a high operating efficiency, observing for an average of $\sim$21 hours per day, with the remaining time utilised for cooler recycling and data transmission. After expending the last of its liquid helium coolant, *Herschel* was unable to continue observations due to photon noise from the craft dominating the observing bands. It was deactivated in June 2017. While a proposal was made for placing it on a lunar collision course, intended to generate a large plume of ejecta which could be analysed from the ground, it was eventually decided to place *Herschel* into a safe heliocentric orbit, which ensured it will not interact with the Earth again for thousands, if not millions of years.

2.0.1.1 *Herschel* Spectroscopy and Photometry

As previously stated, *Herschel* was capable of observing the universe through both sub-millimetre spectroscopy and sub-millimetre photometry. Spectroscopy is sensitive to the emission or absorption of particular wavelenghts of light by molecules or atoms. In the sub-millimetre regime, this occurs when small polar molecules are

thermally excited to higher rotational states. The molecules then decay to lower energy states, releasing excess energy in the form of mono-chromatic light. Another pathway for sub-millimetre line emission is hyper-fine splitting, where bound electrons are encouraged to change spin state, leading to the splitting up of single emission or absorption lines into closely grouped multiples. Both forms of transition are typically collisionally motivated. It is possible to infer the total mass in a region by observing the intensity of individual lines, and the intensity ratios between lines from different molecules, though this requires assumptions regarding e.g. optical depth, molecular abundance, coupling to other molecules, and excitation populations.

As spectral emission lines are often nearly monochromatic, and occur at precisely known wavelengths in a rest frame, they are highly susceptible to shifts in frequency due to the Doppler effect. The frequency of an observed molecular emission line, $\nu_{\rm Obs}$, is related to its rest emission frequency $\nu_{\rm Em}$ by

$$\nu_{\rm Obs} = \left(1 + \frac{\Delta v}{c}\right) \nu_{\rm Em}, \tag{2.2}$$

where Δv is the velocity of the molecule along the line of sight. By observing these shifts in emission frequency, it is possible to determine the kinematics of the gas. The velocity shifts can occur due to random thermal motions, turbulence within the gas, and systematic motions, such as gas infall/outflow or large scale motion towards or away from the observer.

Photometry is the recording of the total amount of power received within a broad waveband. Generally photometry is concerned with recording the continuum emission of the source. This often involves sampling its spectral energy distribution (SED). As stated in Chapter 1, at far infrared and sub-millimetre wavelenghts, this emission is largely from interstellar dust grains at temperatures typically between 10 K and 100 K, which have been heated by a release of gravitational potential energy, or by reprocessing of short wavelength emission into longer wavelength emission. If the emitting source is optically thin, the intensity is directly related to the amount of emitting material, and again assumptions can be made to estimate the total mass of dust and gas within the source.

Bolometers are the favoured detectors for continuum observations in the far infrared and sub-millimetre. Bolometers function as temperature-sensitive resistors, which are heated by the absorption of radiation over a very broad band. When cooled to very low temperatures, bolometers can achieve a sensitivity limited only by the photon noise.

The PACS and SPIRE instruments were designed for large area observing.

This required scanning the telescope across areas of sky much larger than the instrument fields of view, often several square degrees. These observations were susceptible to drifts and low frequency variations, called $1/f$ noise, which manifest as slow increases in detector output over the course of an observation. In turn, this can be seen in output observations as "stripes" of high and low intensity, alternating with each scan leg. $1/f$ noise is characterised by a knee frequency (the frequency at which the noise has increased by a factor of $\sqrt{2}$) which translates to artefacts with a particular angular scale during the scanning process. Sources of $1/f$ noise include atmospheric effect, which are the limiting factor for many ground based observatories, and fluctuations in the temperature of the detectors. Locating *Herschel* at L2 eliminated the contribution to the noise from the atmosphere, though detector temperature remained as a noise source. The PACS and SPIRE $1/f$ noise limits, and strategies for artefact removal, are discussed in the PACS and SPIRE instrument Sections below.

2.0.1.2 HIFI

The dedicated high-resolution spectrometer aboard *Herschel* was the Heterodyne Instrument for the Far-Infrared (HIFI, de Graauw et al. 2010). It contained two observing bands at 157 µm to 212 µm and 240 µm to 625 µm, with a spectral resolving power of 10^7. The spectral resolving power, R, can be determined from both the smallest observable wavelength change in a given waveband, and by the change in velocity of the source relative to the speed of light,

$$R = \frac{\lambda}{\Delta\lambda} = \frac{c}{\Delta v}. \tag{2.3}$$

Thus HIFI was sensitive to velocity shifts as small as $0.03\,\mathrm{km\,s^{-1}}$. The instrument utilised superconducting mixers as detectors, and had only a single pixel on the sky, designed for single point spectral analysis rather than wide area scan mapping. This, in addition to HIFI being designed to examine spectral lines for astrochemistry rather than examine continuum emission from interstellar dust, meant that I did not use data from the instrument in this thesis.

2.0.1.3 PACS

Unlike the *Herschel* HIFI instrument, the Photometric Array Camera and Spectrometer (PACS, Poglitsch et al. 2010) instrument contained both an integral field unit (IFU) spectrometer, and an imaging photometer (i.e., a camera).

An IFU allows a spectrometer to obtain spatially resolved spectra of astronomical fields, allowing for more rapid mapping of extended regions. The PACS IFU, based on a grating spectrometer and an image slicer, covered a range of wavelengths

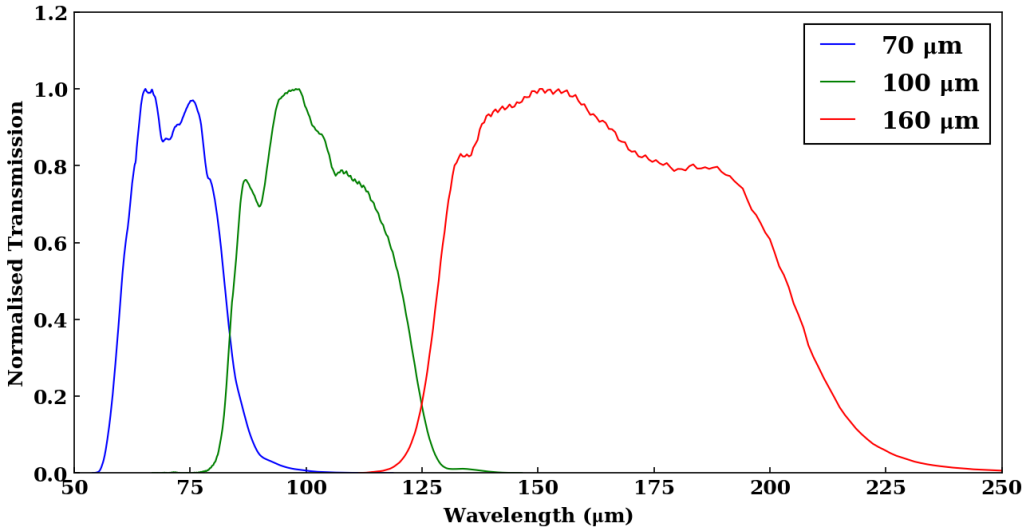

Figure 2.3. Normalised response functions for the three PACS bands, centred on 70 µm, 100 µm and 160 µm. Data from Müller, Okumura, and Klass (2011).

from 55 µm to 210 µm, and covered a $47'' \times 47''$ field of view. The spectral resolving power of 1000 to 4000 allows PACS to be sensitive to velocity changes (Δv) between $75\,\mathrm{km\,s^{-1}}$ to $350\,\mathrm{km\,s^{-1}}$. As with HIFI, the aims of this thesis did not facilitate the use of data from the PACS spectrometer.

The PACS photometer covered three broad wavebands with $\lambda/\Delta\lambda > 2$; 68 µm to 85 µm, 85 µm to 130 µm, and 130 µm to 210 µm. The wavebands are referred to by their relative colour or central wavelength; the "blue" 70 µm band for 68 µm to 85 µm, the "green" 100 µm band for 85 µm to 130 µm, and the "red" 160 µm band for 130 µm to 210 µm. The filter transmission profiles of these wavebands are shown in Figure 2.3. Only two bands, viewing the same area of sky, could be observed at once. Instead, emission in the "red" band was always recorded by a rectangular detector composed of two 16 × 16 filled silicon bolometer arrays operating at 0.3 K, while a mechanism was used to select either the "blue" or "green" band, which was then projected onto a 4×2 block of 16×16 bolometer arrays. While each 16×16 bolometer array was completely filled, small gaps were present between arrays. These gaps were compensated for by various scanning techniques (covered in Section 2.0.1.5). The PACS bolometers had a field of view of $3.5' \times 1.75'$.

In this thesis, PACS observations were taken in the PACS/SPIRE parallel mode. Therefore, it is appropriate to quote the 1σ sensitivities that could be achieved in this mode for a 1 square degree field observed for 1 hour. The PACS/SPIRE parallel mode 1σ sensitivities quoted for the "blue" and "red" PACS bands by Poglitsch et al. (2010) are 19.8 mJy and 116 mJy, respectively, for a 4 square degree field observed

Table 2.1. 1σ sensitivity values for the PACS and SPIRE instruments operating in the PACS/SPIRE parallel mode for a 1 square degree field observed over 1 hour. Sensitivities are derived from from Poglitsch et al. (2010) and Griffin (2007).

Band	Sensitivity (mJy)
PACS 70 µm	17.1
PACS 160 µm	44.0
SPIRE 250 µm	4.8
SPIRE 350 µm	5.3
SPIRE 500 µm	6.3

over 3 hours. While it is a simple task to rescale the sensitivities to the correct field size and observation time, the quoted "red" sensitivity is dominated by confusion. A confusion-less sensitivity can be estimated by comparing the ratio in the "blue" band between the PACS/SPIRE parallel mode uncertainty, and the 5σ uncertainty for the smaller scan mapping mode (3.7 mJy for a 150 square arcminute field observed for 30 hours). This ratio can then be used to scale the "red" band uncertainty for the smaller scan mapping mode (9.5 mJy), which is not dominated by confusion. This produces a 1σ uncertainty of 50.8 mJy for a 4 square degree field observed for 3 hours. By rescaling for a 1 square degree field observed for 1 hour, the 1σ uncertainties for the "blue" and "red" PACS bands operating in PACS/SPIRE parallel mode are 17.1 mJy and 44.0 mJy, respectively. In practice, the uncertainty in observations of fields within the Galaxy is likely to be dominated by emission from cirrus objects, leading to source confusion. The PACS 1σ uncertainties are summarised in Table 2.1.

PACS had a relatively large $1/f$ knee of between 1 Hz to 5 Hz. Careful selection of scanning methods could not be used to overcome this degree of noise, and "de-striping" algorithms were needed to remove the resulting artefacts. The algorithms work by modelling the intensity shifts present in the scan legs, which then allows the signal to be corrected.

The process to convert from bolometer output to a value of surface brightness (i.e. MJy/sr) requires accurate flux calibration and knowledge of the instrument beam profiles. For PACS, this was achieved through scans of well-understood point sources. These comprised a selection of standard stars and asteroids with high accuracy thermophysical models. It was found that the PACS beams were heavily dependent on the scanning speed, and were distorted for most observations. This was due to the detector response speed being too slow in relation to the beam crossing time, particularly at higher scan speeds. The beam properties, including the degree of distortion, are given in Table 2.2 for the SPIRE/PACS parallel scanning mode, while azimuthally averaged radial beam profiles are shown in Figure 2.6.

2.0.1.4 SPIRE

As with PACS, the Spectral and Photometric Imaging REceiver (SPIRE, Griffin et al. 2010) was able to observe both spectroscopically and photometrically.

SPIRE's spectroscopic capabilities came in the form of an imaging Fourier-Transform Spectrometer, with a circular field of view of 2.6′. It covered two separate wavebands, 194 µm to 313 µm and 303 µm to 671 µm. In addition, it had two resolution modes. The high resolution mode allowed for a spectral resolving power of 370-1300, equating to a Δv of 230 km s^{-1} to 810 km s^{-1}, while the Low resolution mode had a resolving power between 20 and 60, with a corresponding Δv of 5000 km s^{-1} to 15 000 km s^{-1}. As stated before, spectroscopic data was not utilised as part of this thesis.

The SPIRE photometer, like the PACS photometer, had three bands, commonly referenced by their nominal wavelength: 250 µm, 350 µm, and 500 µm, with each waveband having a width characterised by $\lambda/\Delta\lambda \sim 3$. The SPIRE filter relative response functions are shown in Figure 2.4. Unlike PACS, SPIRE was able to observe simultaneously in all three photometric bands, as each had a dedicated detector array. The arrays were comprised of doped germanium "spider web" bolometers, coupled to the incident lightby conical feedhorns with a circular entrance aperture. The feedhorns were hexagonally close-packed, and the three arrays cover the same 4′×8′ field of view. While the PACS filled array detectors directly measure all radiation incident on the arrays, the SPIRE feedhorns act as an antenna, coupling directly to the telescope beam. This reducing the collection of stray light. The feedhorns had a diameter of $\sim 2\lambda/D$, but had a beam size of $\sim \lambda/D$, resulting in gaps between the beams on the sky. This was by design, and was compensated for by the design of the scanning techniques. This is discussed in more detail in Section 2.0.1.5. A diagram of the feedhorn arrays is shown in Figure 2.5. The 250 µm array contained 139 detectors, the 350 µm array 101 detectors, and the 500 µm array 43 detectors.

The SPIRE sensitivities presented in Griffin (2007) are given in terms of the time required to observe a 1 square degree field to a 1σ uncertainty limit of 3 mJy. It is, therefore, trivial to estimate the 1σ sensitivity that would be achieved for an observation time of 1 hour. For the SPIRE 250 µm, 350 µm and 500 µm, the associated PACS/SPIRE parallel mode 1σ uncertainties limit for a 1 square degree field observed for 1 hour are 4.8 mJy, 5.3 mJy and 6.3 mJy, respectively. These uncertainties are summarised in Table 2.1. As with the PACS instrument, uncertainties for observations of galactic objects are likely to be dominated by cirrus confusion.

The $1/f$ knee for SPIRE was much lower than that of PACS at 1 mHz to

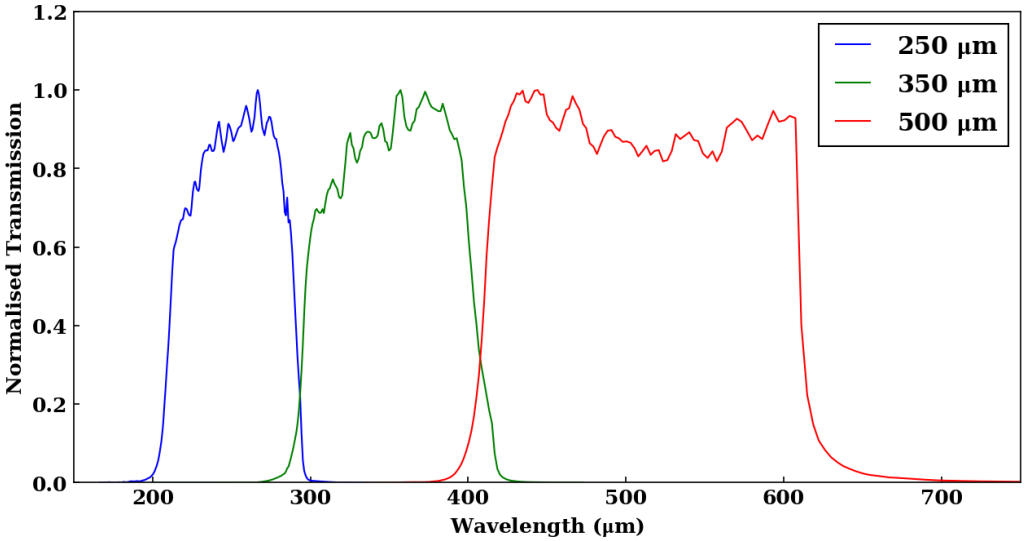

Figure 2.4. Normalised response functions for the three SPIRE bands, centred on 250 µm, 350 µm and 500 µm. Data from Valtchanov (2017).

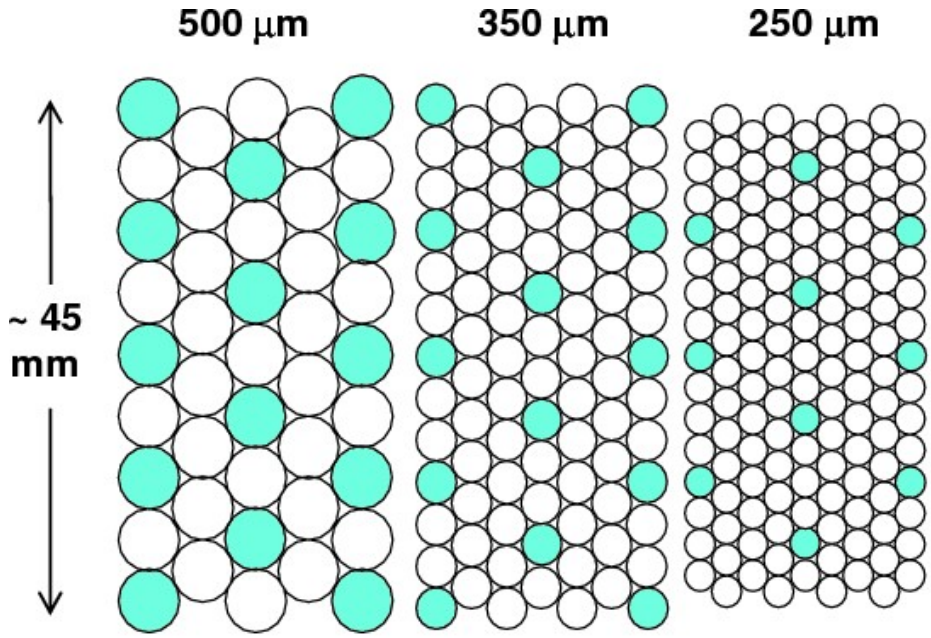

Figure 2.5. Diagrams of the three SPIRE bolometer arrays, showing overlapping detectors. Image credit Griffin et al. (2010).

3 mHz, allowing for removal of $1/f$ noise simply by rapidly scanning large regions of the sky.

The primary flux calibration souce for the SPIRE photometer was Neptune, which has a well-understood spectrum and appeared as a point source for SPIRE, with a $2''$ angular size. Unlike PACS, the beams were not greatly affected by the scan speed, and thus are known to a great degree of accuracy. As above, the beam properties are given in Table 2.2, and azimuthally averaged radial beam profiles are shown in Figure 2.6.

2.0.1.5 PACS and SPIRE Observing Modes

In order to appropriately observe objects of various sizes, *Herschel* was capable of several mapping techniques, including scan mapping for both PACS and SPIRE, and jiggle mapping for SPIRE.

SPIRE jiggle mapping procedures were designed to obtain fully-sampled maps of sources smaller than the array field of view. Once the telescope had be oriented to point at a target, small motions would be made to "jiggle" the detector array over the source, enabling any unfilled areas of the feedhorn arrays to be compensated for. Ultimately, jiggle mapping was rarely used, as the SPIRE scan mapping proved to have exceptional sensitivity over all spacial scales, even for compact objects. Furthermore, jiggle mapping was not possible when *Herschel* operated in Parallel mode (see below).

Scan mapping was intended to allow the *Herschel* instruments to fully sample large fields. As stated previously, while the PACS bolometer arrays are filled, small gaps in coverage exist between adjacent arrays, leading to incomplete sampling, and the SPIRE feedhorn arrays under-sampled the sky by design.

The telescope scans were orientated so that the detector arrays moved across the target field, with any single point being sampled by multiple individual detectors. Although the scan areas were fully sampled (even with one scan) to ensure the highest quality data and enhance sensitivity any single scan (termed the nominal scan) was also complemented with a second perpendicular cross scan (the orthogonal scan). For PACS, these two opposing scans could be combined to help in circularising beams that were distorted by the scanning process. In addition, this technique also served to double the number of observations in an area, thus reducing noise and improving sensitivity. A diagram of the cross scan orientation for *Herschel* SPIRE can be seen in Figure 2.7.

Scans of large areas were conducted by slewing the telescope across the target area in long, parallel strips, as shown in Figure 2.8. These strips were spaced such

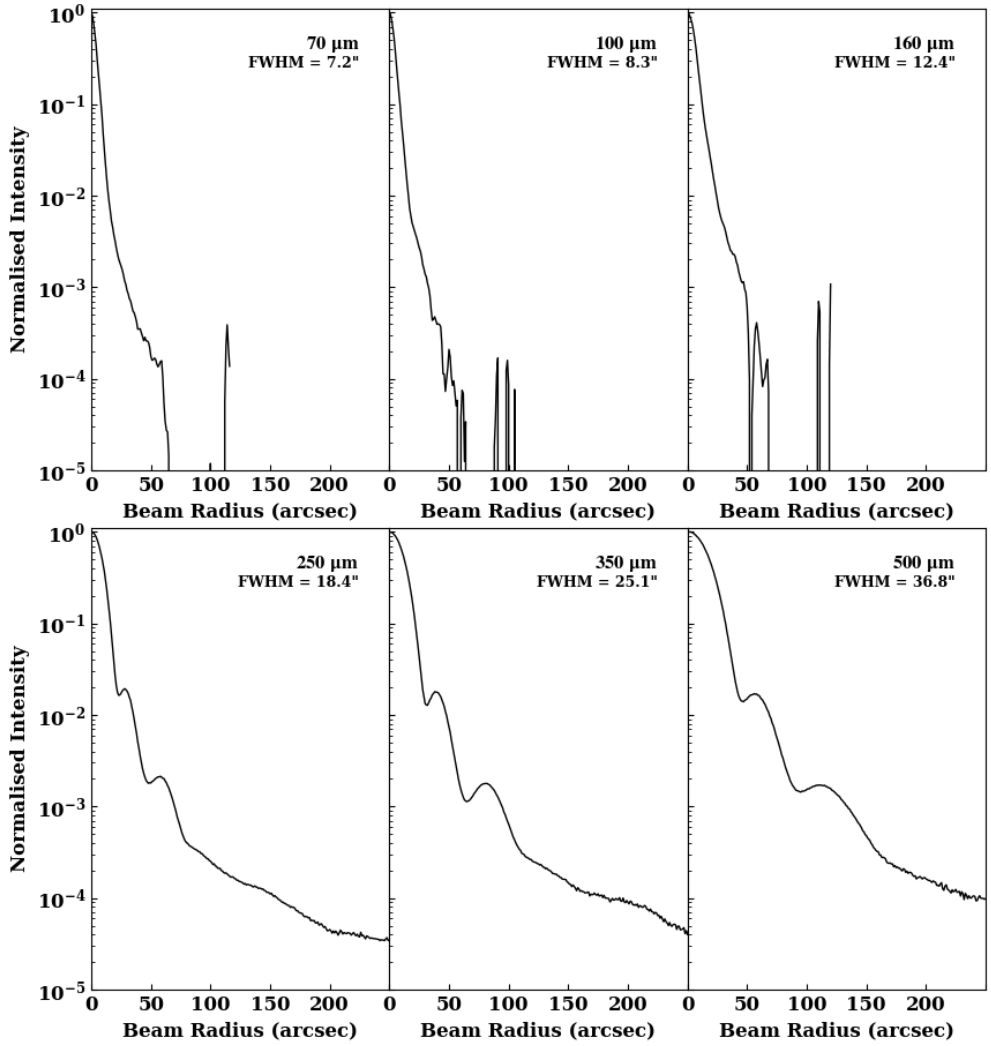

Figure 2.6. Radial beam profiles for the *Herschel* PACS 70 µm, 100 µm and 160 µm bands, and the SPIRE 250 µm, 350 µm and 500 µm bands. The beams have been modelled as azimuthally averaged profiles and do not account for smearing due to scanning speed. The FWHMs of the beams are given in the top right of each plot axis. Due to instrumental noise, the PACS beams contain areas of < 0 relative intensity, which appear as breaks in the profile. The PACS images are known to a radius of $116''$ for the 70 µm and 100 µm bands, and $120''$ for the 160 µm band. The SPIRE beams are modelled to much larger radii. The profiles presented here are produced from data published by Geis and Lutz (2010) for the PACS instrument, and from the Herschel Science Archive for the SPIRE instrument.

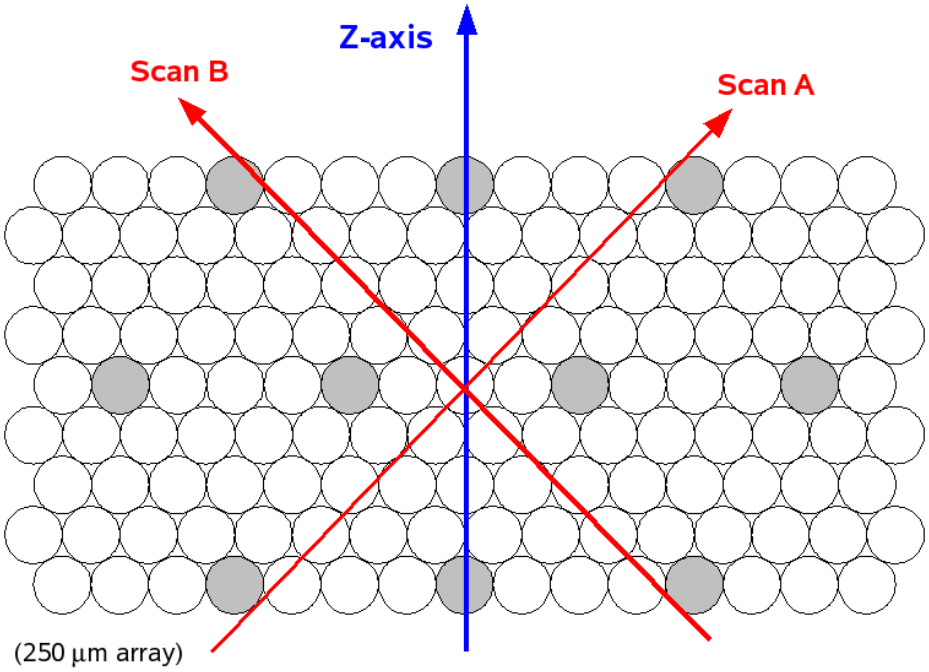

Figure 2.7. Diagram of Nominal and Orthogonal scan directions across a SPIRE bolometer array. The scan directions are optimised so every path is seen by at least two different feed horns. Image credit Valtchanov (2017)

that the instrument FOV caused a small overlap between adjacent scan legs. One set of nominal legs was completed for an entire observable region before the orthogonal scans were conducted.

Scan speeds were optimised to allow regions to be mapped without being affected by significant temporal or thermal drifts in detector noise during operation, and to minimise beam smearing. As the telescope had to accelerate to the required scanning speed before beginning a leg, and decelerate at the end of a leg before turning and slewing back in the opposite direction, a larger area than required was observed. This ensured that the entire target area was completely observed at the optimal scanning speed, and provided additional data around the field.

The PACS and SPIRE instruments could be operated together, providing simultaneous coverage with all three SPIRE bands, the PACS 160 µm band, and one of the two other PACS bands, in an observing mode known as the SPIRE/PACS Parallel mode (Müller, Cesarsky, and AOT WG 2011). A diagram of a typical Parallel mode scan is shown in Figure 2.9. The spacing of adjacent scan legs was determined by the $47'' \times 47''$ FOV of the PACS instrument, which was smaller than the SPIRE $4' \times 8'$ FOV, and thus required a closer spacing to fully sample a target area. This led to a greater degree of spatial oversampling for SPIRE, which further reduced noise. Conversely, the angle of scan was optimised for the SPIRE detectors, to ensure the gaps

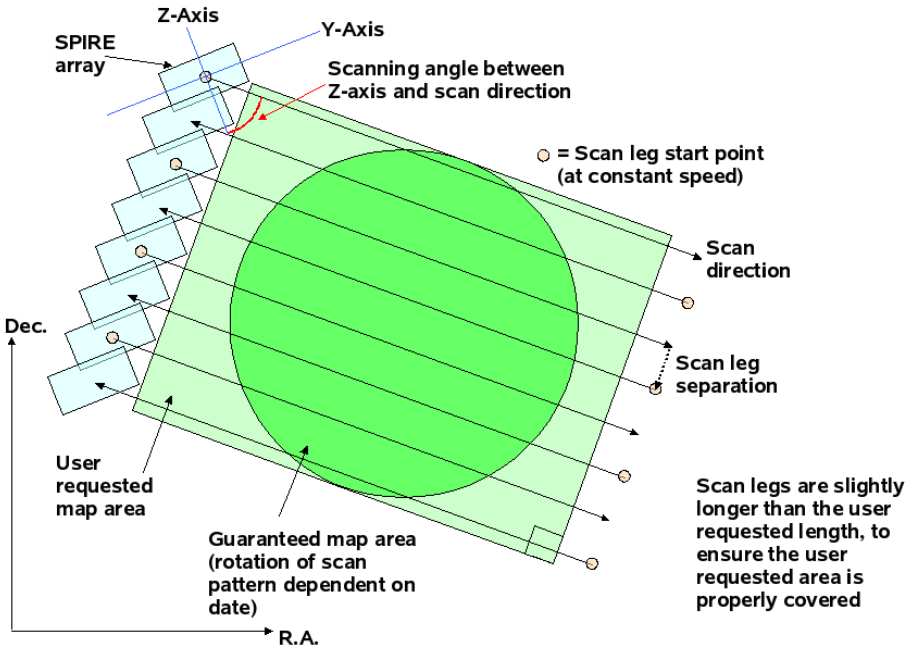

Figure 2.8. Diagram of SPIRE scan directions relative to bolometer array. Scan angle is chosen to achieve maximal coverage for the detector arrays, while scan leg separation is chosen for the array field of view. The scan images an area larger than that requested to account for telescope acceleration and deceleration at the begininning and end of each run. Image credit Valtchanov (2017).

between the SPIRE detector beams were efficiently filled. As the PACS and SPIRE instruments had viewing angles separated by $21'$, the telescope scanned a much larger area than the target field to ensure that both instruments sampled the required area.

Parallel mode was carried out with one of two available scanning speeds: $20''\,\mathrm{s}^{-1}$, and $60''\,\mathrm{s}^{-1}$. The faster scan speed was well suited for SPIRE, and enabled large regions to be mapped quickly. However, the PACS beams were greatly elongated at this speed, essentially producing a coarser resolution than that of the slower scan speed. The lower speed was used for producing high quality maps of small areas. All *Herschel* data utilised in this thesis are from observations of large fields, and were taken with the faster scan speed of $60''\,\mathrm{s}^{-1}$.

2.0.2 JCMT

The James Clerk Maxwell Telescope (JCMT, Phillips 2002) is a ground-based sub-millimetre telescope located at an altitude of 4.1 km near the summit of the Mauna Kea dormant volcano on the Big Island of Hawaii. While completion was delayed due to high seas piracy shortly before it was scheduled to be offloaded, it nevertheless began operations in 1987, under the command of the Joint Astronomy

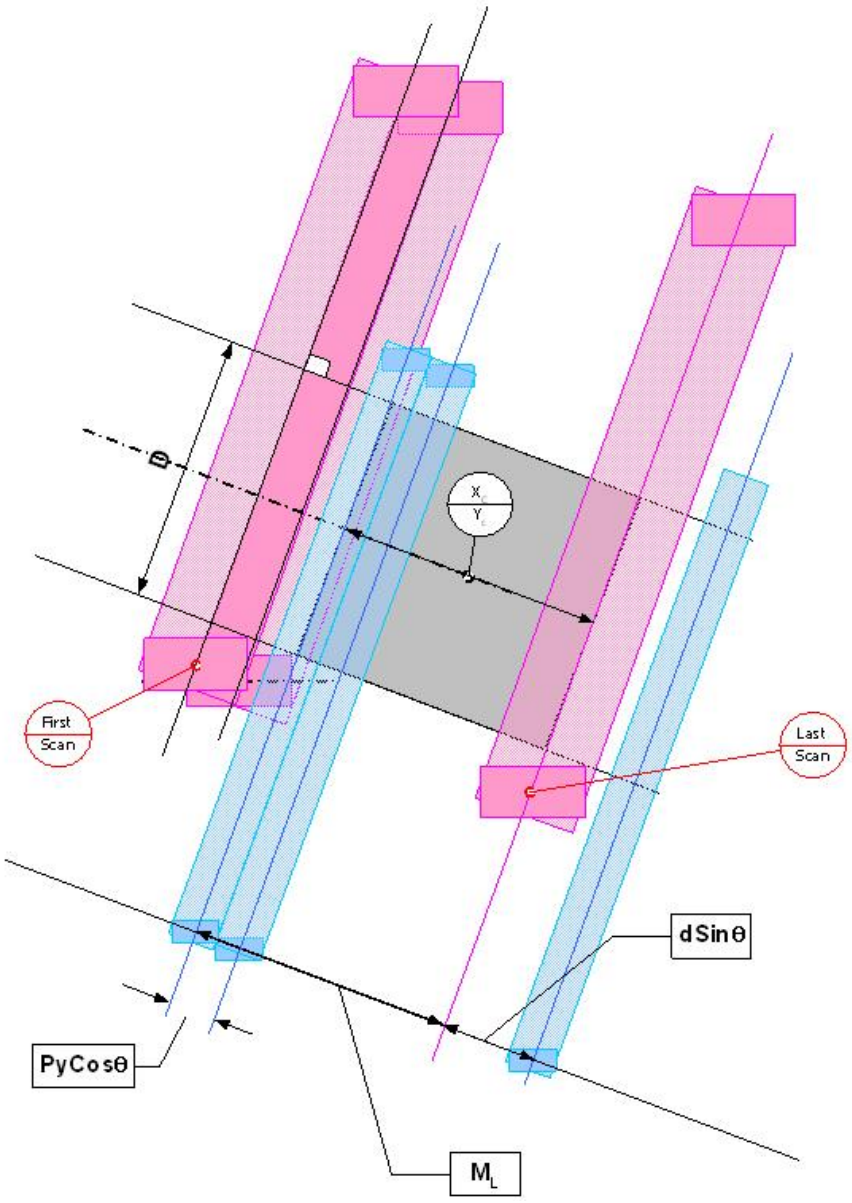

Figure 2.9. Diagram of scanning with SPIRE/PACS Parallel mode, showing extra observed area to compensate for SPIRE and PACS offsets, and narrower scan leg separations, optimized for PACS, leading to a greater degree of oversampling for the SPIRE arrays. Image credit Müller, Cesarsky, and AOT WG (2011)

Table 2.2. Beam properties for the *Herschel* PACS and SPIRE instruments during SPIRE/PACS Parallel Mode operations. The FWHM of the distorted PACS and SPIRE beams are given by their semi-minor and -major axes. As the SPIRE beams exhibit a small distortion, their orientation angle was not recorded. The beams are given for a scan speed of $60\,''\,s^{-1}$. Beam properties from Valtchanov (2017) and Exter (2017).

Band	Beam FWHM (″)	Beam Orientation (°)
PACS 70 µm	5.86×12.16	63.0
PACS 100 µm	6.98×12.70	63.0
PACS 160 µm	11.64×15.65	53.4
SPIRE 250 µm	18.3×17.0	n/a
SPIRE 350 µm	24.7×23.2	n/a
SPIRE 500 µm	37.0×33.4	n/a

Centre (JAC), a multinational collaboration between Canada, the Netherlands, and the UK. The telescope was initially funded up to February 2015. JCMT is the largest dedicated sub-millimetre telescope in the world. Its altitude places it above the usual cloud base, and above 97% of atmospheric water vapour. This ensures a high degree of sub-millimetre transmission, as shown in Figure 2.1.

Figure 2.10 shows the telescope features. The dome houses the telescope and provides protection against severe weather. The telescope itself is an azimuthally mounted Cassegrain, with a 15 m primary mirror, providing a diffraction limited beam FWHM of 14.3″. A Gore-Tex sheet is normally deployed in front of the primary mirror during operation. The sheet, which is 97% transparent to millimetre and sub-millimetre wavelenghts, protects the telescope from damage from wind and dust, while allowing, in principle, 24 hour operation. A rotating tertiary mirror directs incident light to different instruments.

The instruments currently operating on the JCMT are the Heterodyne Array Receiver Program (HARP), which has a set of 4×4 detector beams on the sky and operates with the Auto Correlation Spectral Imaging System (ACSIS)to form a 325 GHz to 375 GHz spectrometer, and the Submillimetre Common-User Bolometer Array 2 (SCUBA-2), a continuum camera that is discussed in detail below.

When JAC funding ceased in 2015, the East Asian Observatory (EAO) took up operations, which it continues at the present time.

2.0.2.1 SCUBA-2

SCUBA-2 (Holland et al. 2013) is a 10,000 pixel bolometer array capable of observing dust continuum emission at 450 µm and 850 µm, with narrow filter bands matched to the atmospheric windows giving $\lambda/\Delta\lambda$ of 14 and 10 respectively. The response functions for the 450 µm and 850 µm bands are presented in Figure 2.11.

Figure 2.10. Image of the JCMT, showing the telescope dome and primary mirror. A Gore-Tex sheet can be manoeuvred in front of the mirror to allow for continuous day and night observations, while protecting the telescope from wind and particulate damage. Image credit East Asian Observatory (2017).

The two wavebands are observed simultaneously. As with *Herschel* PACS, SCUBA-2 uses filled bolometer arrays (four for each waveband) without the use of feedhorns. These arrays are butted together with a small spacing between them. Thus, various scanning modes need to be employed to ensure full coverage of an observational target. The bolometer arrays have a 45′ field of view.

The SCUBA-2 detectors are transition edge superconducting (TES) bolometers, which are cooled to ∼0.1 K by a dilution refrigerator. As with other ground based instruments, SCUBA-2 is not limited to a pre-determined finite lifespan, and is not restricted by mass or size, as space telescopes are. The cooling system can operate for up to a year with continuous use, after which it requires servicing.

Sensitivity limits for SCUBA-2 are presented in Table 2.3 for a number of different scanning modes. The sensitivities are given as the value of the 3σ noise level after one hour of integration time (in mJy). Despite the large uncertainties, SCUBA-2 can achieve similar sensitivities to its predecessor with scanning speeds between 100 and 150 times greater. This is due to the increase in bolometer count between the two instruments.

The 1/f knee is at the high value of 0.7 Hz, which led to the development of scanning modes that ensured multi-pixel sampling of a source with high scan speeds.

Table 2.3. SCUBA-2 sensitivities for different scanning modes. The sensitivities are given as the value of the 3σ noise level after an integration time of one hour. Data from Dempsey et al. (2013).

Observing Mode	450 µm (mJy)	850 µm (mJy)
DAISY	39.0	5.6
PONG900	85.0	11.9
PONG1800	166.0	23.0
PONG3600	361.0	49.0
PONG7200	732.0	98.0

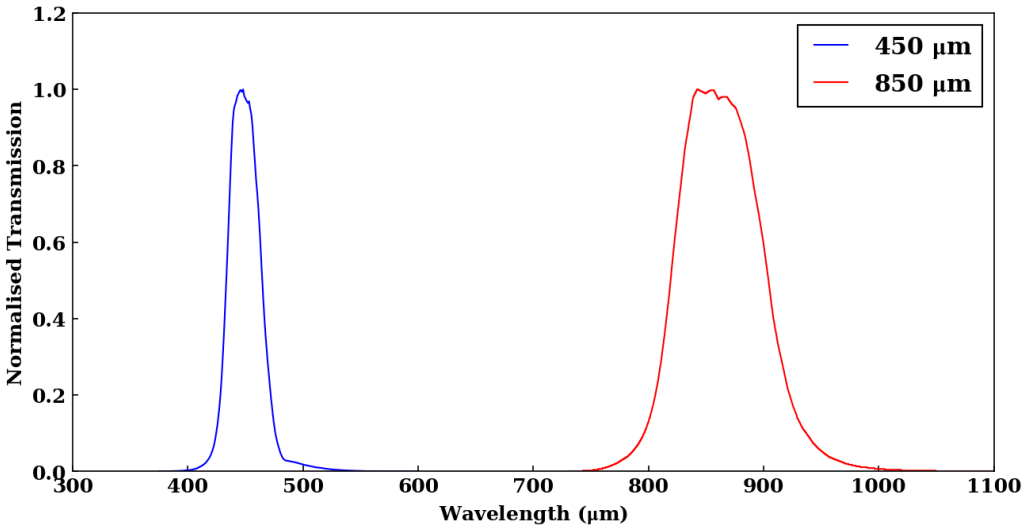

Figure 2.11. Response functions for the SCUBA-2 450 µm and 850 µm bands. Under typical operating conditions, both response functions would be reduced by the atmospheric transmission. Data accessed from East Asian Observatory (2010).

Table 2.4. Parameters of the Gaussian functions used to fit the SCUBA-2 450 µm and 850 µm beam profiles. Data from Dempsey et al. (2013).

	450 µm	850 µm
FWHM Main Beam ($\theta_{\rm MB}$)	7.9″	13.0″
FWHM Secondary Component ($\theta_{\rm S}$)	25.0″	48.0″
Relative Amplitude Main Beam (α)	0.94	0.98
Relative Amplitude Secondary Component (β)	0.06	0.02

In addition, a high-pass filter with an edge frequency of ∼0.1 Hz to 1.0 Hz is used to remove residual noise, and sky noise not removed by background subtraction (Chapin et al. 2013). Unfortunately, this destroys large scale structures in observations. At typical scanning speeds of 600″ s^{-1}, this translates to objects with length scales larger than ∼10′.

Flux calibration for SCUBA-2 was initially performed on Mars and Uranus (Dempsey et al. 2013). The planets were observed and the instrument output (in pW) was compared to surface planetary models (in Jy) to produce a Flux Conversion Factor (FCF). The FCF is checked nightly against secondary calibrators.

The SCUBA-2 beam profiles were determined from observations of Uranus, and both wavebands can be well fit by a double Gaussian approximation. This approximation is composed of a narrow main Gaussian, and a wider secondary Gaussian. The two beams are related by the sum of the two Gaussian profiles by the equation

$$G_{\rm Total} = \alpha G_{\rm MB} + \beta G_{\rm S}. \tag{2.4}$$

Here α and β are the relative powers of the two profiles. The parameter values for the SCUBA-2 beams are given in Table 2.4. The total FWHMs of the beam profiles are well approximated by the FWHMs of the main components. Figure 2.12 shows the beam SCUBA-2 beam profiles produced from equation 2.4.

2.0.2.2 SCUBA-2 Scanning Modes

SCUBA-2 employs a number of different scanning modes. These can be subdivided into two groups: "DAISY" scans, for smaller regions, and "PONG" scans, for larger areas. "DAISY" scans are typically used when the observable field has a smaller angular size than the instrument field of view. The telescope tracks a roughly circular path at a constant velocity, keeping the target within the bounds of the detector arrays, as shown in the top left panel of Figure 2.13. After a single rotation of the "DAISY" pattern, the telescope is rotated and the scan is repeated, offset from the original scan, to increase integration time, thus reducing noise, and to improve multi-pixel coverage. The effects of this are shown in the top right of Figure 2.13.

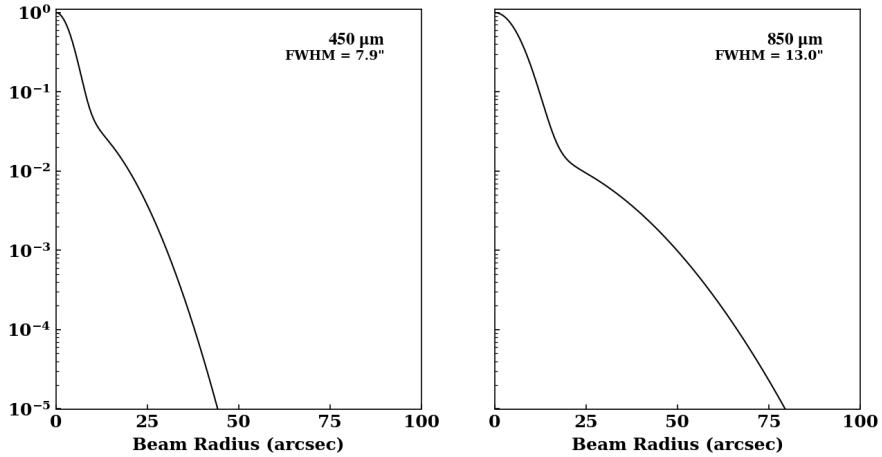

Figure 2.12. SCUBA-2 beam profiles for the 450 µm and 850 µm wavebands, produced from the models provided by Dempsey et al. (2013).

The "PONG" scanning modes allow for observation of areas larger than the instrument field of view, and can reach sizes up to 1 square degree. "PONG" paths are constructed by defining a square box around the target region, and slewing the telescope across it. Where the telescope pointing encounters the edge of the box, it is "bounced" onto a different trajectory, much like the classic arcade game "Pong" from which the scanning mode derives its name. An example of a single rotation of a "PONG" scan is given in the bottom left panel of Figure 2.13. Once the box has been well covered, the area is rotated, and a second "PONG" scan takes place. These rotated scans build to form the roughly circular pattern observed in the bottom right panel of Figure 2.13. As above, this rotation is intended to improve sensitivity by lowering noise and cross-linking neighbouring detector pixels.

There are several "PONG" scans of varying angular sizes. They are defined by their diameter in arcseconds: "PONG900", "PONG1800", "PONG3600" and "PONG7200".

In order to ensure the telescope acceleration remains roughly constant during a single scan, the "bounces" performed at the edges of the target box are typically rounded, producing a modified scanning mode called "CURVY PONG". SCUBA-2 data used in this thesis were taken in the "CURVY PONG1800" mode.

2.0.3 *IRAS*

The InfraRed Astronomical Satellite (*IRAS*, Neugebauer et al. 1984) was launched in January 1983, as a joint effort by the United States, the UK, and the

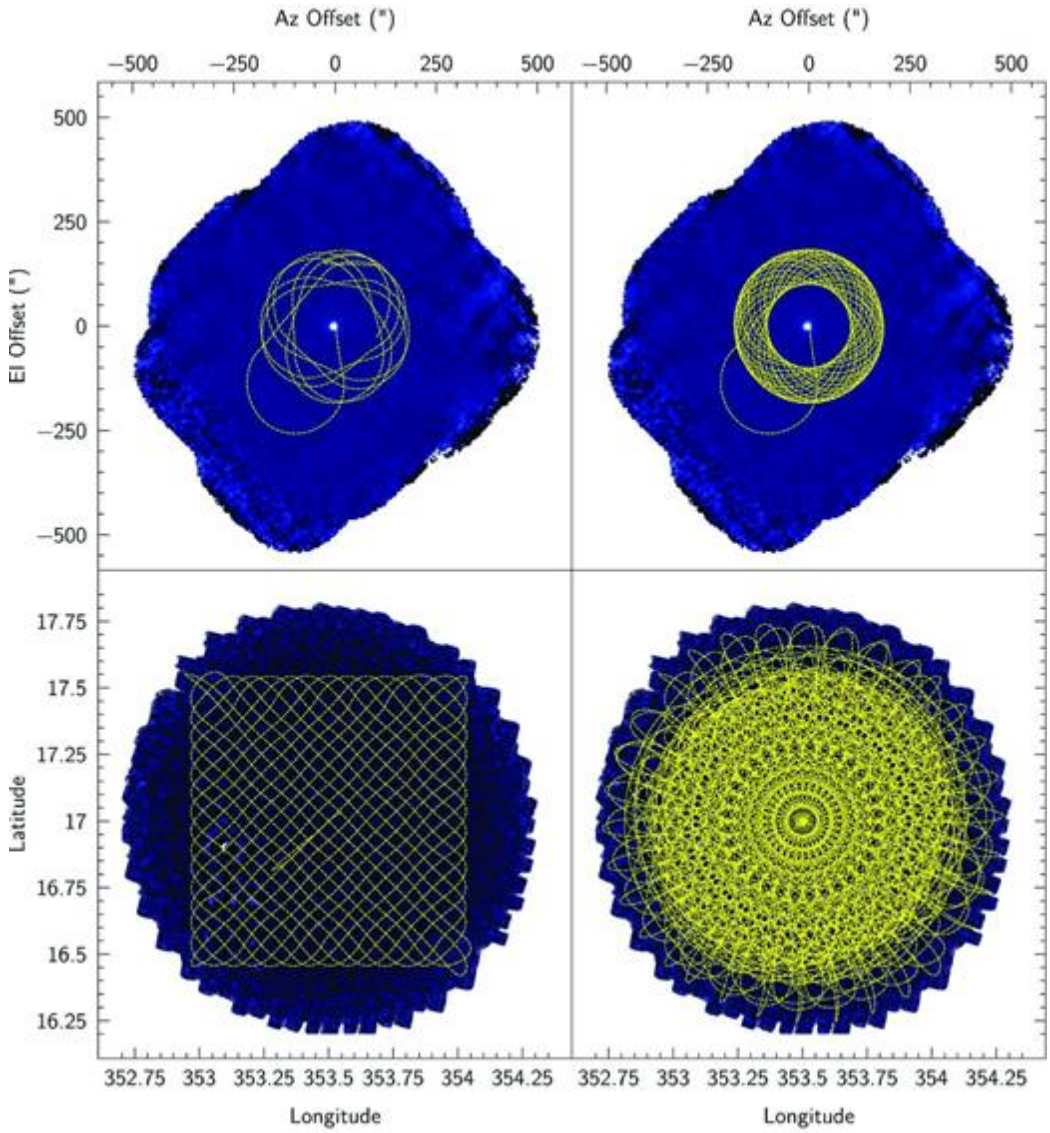

Figure 2.13. Diagrams of the SCUBA-2 "DAISY" (top), and "PONG" (bottom) scanning modes. The images show how a single rotation of each mode (left) can be enhanced by combining multiple rotations (right) to achieve better coverage. Image credit Holland et al. (2013).

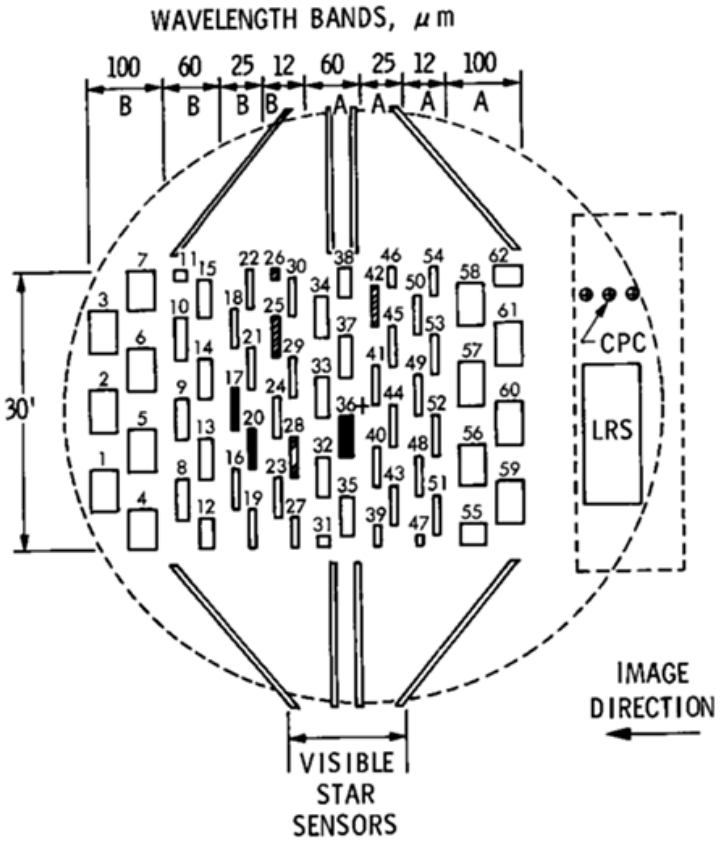

Figure 2.14. A diagram of the *IRAS* focal plane, showing the band detectors in the centre, the spectrometer on the right of the plane, and the visible star sensors as slits to the top and bottom. Solid black rectangles indicate dead detectors. Image credit Beichman et al. (2002a).

Netherlands. Placed in a Sun-synchronous polar Earth orbit, *IRAS* was designed to produced an unbiased infrared survey of the entire sky over four wavebands; 12 µm, 25 µm, 60 µm and 100 µm. *IRAS* also had a low resolution spectrometer (LRS), and a chopped photometric channel (CPC), for analysis of individual sources.

The 0.57 m mirror was cooled to <10 K, and the detectors to <2 K, by a liquid helium cryostat (Beichman et al. 2002b). The mirror and detectors were protected from solar and ambient radiation by a Sun shield and baffle. The position of the detectors on the focal plane are shown in Figure 2.14.

For the sky survey 62 detectors were subdivided into eight modules, with two modules for each of the four filter bands. These were arranged such that any source passing over the detectors was imaged by at least two detectors in each of the four bands. The detector characteristics are summarised in Table 2.5.

Table 2.5 presents the 1σ sensitivities for the IRAS detectors after five minutes of observation. The band filter profiles are shown in Figure 2.15.

Table 2.5. *IRAS* field detector characteristics. Data from Beichman et al. (2002a).

Detector (µm)	Field of View (′)	Waveband (µm)	1σ Sensitivity (mJy)
12	0.75×4.5	$8.5 - 15$	105
25	0.75×4.6	$19 - 30$	125
60	1.5×4.7	$40 - 80$	170
100	3.0×5.0	$83 - 120$	580

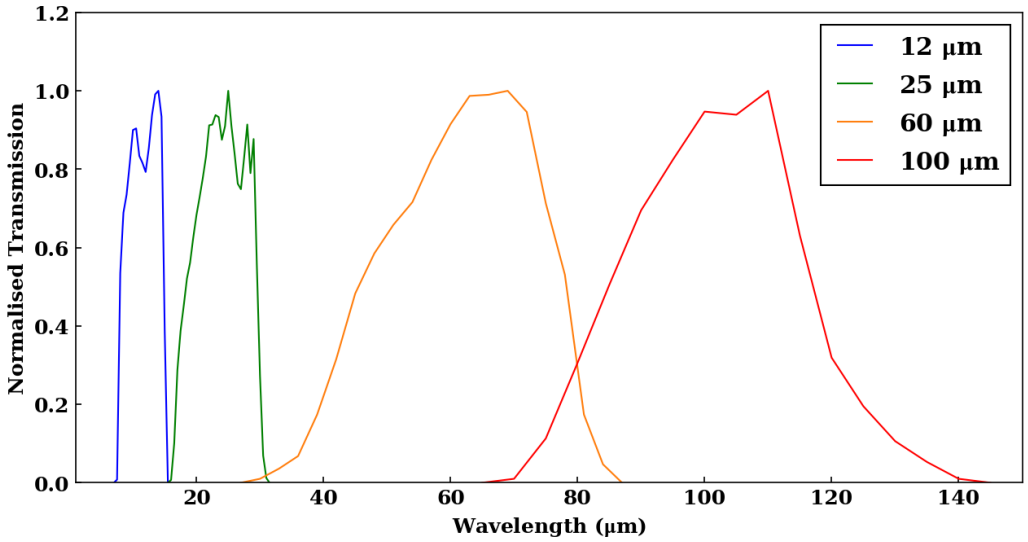

Figure 2.15. Normalsied response functions for the *IRAS* detectors. Data from Beichman et al. (2002a).

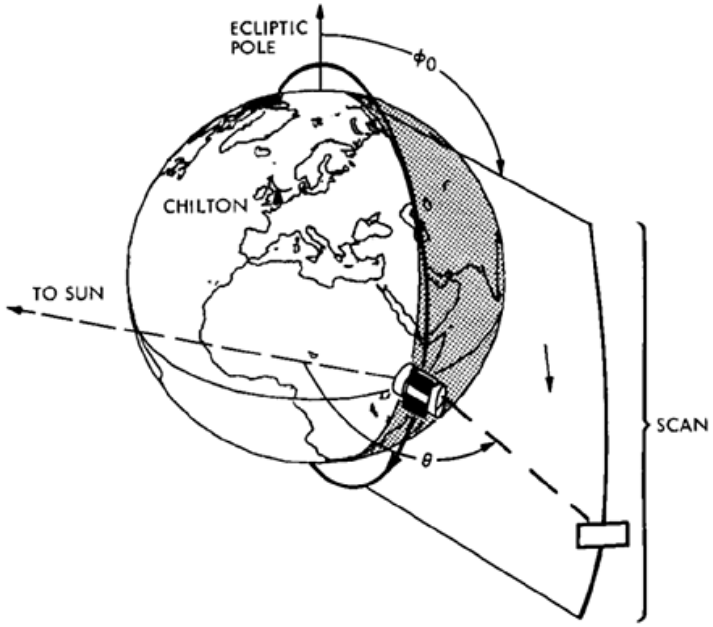

Figure 2.16. A diagram of the polar *IRAS* orbit. The schematic shows how *IRAS* maintains a constant angle to the Sun, and uses its rotation around the Earth to map vertical strips of the sky. Rotation of the Sun-Earth system would, over time, cause the vertical strips to pass over nearly the entire sky, allowing for a full survey. Image credit Beichman et al. (2002a).

Flux calibration of the field detectors was achieved by using the 12 µm band to observe the star α Tauri, and compare the detector output with SEDs obtained from ground based observations. Once the 12 µm band had been calibrated, it could be used to calibrate the other bands through observations of asteroids for which reliable thermal models were available. The flux calibration for point sources was absolute, but extended emission calibration was only relative.

The *IRAS* spacecraft was decommissioned after a 10 month operation, having surveyed more than 96% of the sky in all four bands.

2.0.3.1 *IRAS* Observing Mode

Unlike *Herschel* and JCMT, *IRAS* was not designed to point at specific targets. Instead, *IRAS* utilised its orbit around the Earth, and the orbit of the Earth around the Sun, to continuously map the full sky. Figure 2.16 gives a diagram of the observation mode. *IRAS* maintained a fixed angle relative to the Sun, ensuring its instrumentation was always protected by the Sunshield. It then took observations in vertical strips as it passed around the Earth. This produced an effective scan speed of $3.85\,''\,\mathrm{s}^{-1}$.

The visible star sensors shown in Figure 2.14 were used to identify known stars in visible wavelengths, allowing for adjacent scans to be stitched together to

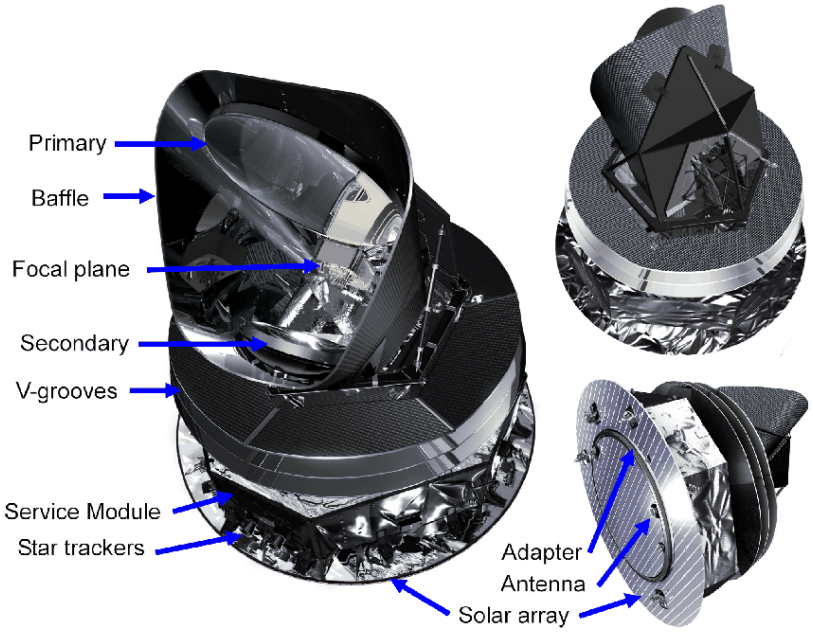

Figure 2.17. A diagram of the *Planck* satellite. The solar array is clearly visible at the base, indicating that *Planck* was kept at a constant angle to the Sun. The V-grooves act as a thermal insulator and radiator between the warm service module and the cold telescope. The baffles help to reduce contamination from ambient radiation. Image credit Tauber et al. (2010).

form coherent maps, and provide cross scan capabilities which allowed for higher sensitivity.

2.0.4 *Planck*

The ESA *Planck* satellite was carried to L2 on the same rocket as *Herschel*. At the end of the launch sequence, the two spacecraft were injected into separate trajectories that propelled them into different halo orbits around L2. *Planck* carried two instruments covering a broad range of wavelengths from 350 µm to 10 mm. Although in many ways a direct successor to *IRAS*, *Planck* was not intended to observe the infrared emission of the sky as a primary aim, but instead to map the small anisotropies of the cosmic microwave background (CMB) radiation. However, *Planck* needed to produce highly accurate all-sky maps of foreground sub-millimetre dust emission and longer wavelength synchrotron emission to enable accurate subtraction of foreground astrophysics and derive the CMB signals. It is these observations that make *Planck* of particular interest to this thesis.

As seen in Figure 2.17, *Planck* comprised a passivly cooled telescope module, thermally separated from the uncooled service module by low conductance structs and thermal shields, and protected from solar radiation by a sunshield (Tauber et al. 2010). *Planck* was kept at a constant orientation to the Sun as it performed its

observations, and a large solar panel on the Sun side of the sunshield provided power. The telescope contained an elliptical primary mirror, with semi-major and -minor axes of 1.9 m×1.5 m, set at an angle such that in projection it behaved as a circular mirror with radius 1.5 m.

The Low Frequency Instrument (LFI) had three bands with central wavelenghts of 10 mm, 6.8 mm and 4.3 mm. LFI was cooled to 20 K. Data from the LFI is not used in this thesis.

The High Frequency Instrument (HFI) contained 52 spider-web bolometers split between six wavebands centred at 3000 µm, 2098 µm, 1382 µm, 850 µm, 550 µm and 350 µm (Lamarre et al. 2010). Bands at 3000 µm, 2098 µm, 1382 µm and 850 µm contained two orthogonally positioned groups of four bolometers each, and were capable of detecting polarized emission. Additional bands at 2098 µm, 1382 µm and 850 µm, as well as the bands at 550 µm and 350 µm, contained four bolometers each, and were insensitive to linear polarization. The bolometer arrays were coupled to the incident radiation via conical feedhorns.

Due to the cold (40 K) telescope and the need for long wavelength observations, the sensitivity requirements for HFI were more stringent than those for *Herschel*-SPIRE, and required cooling the bolometers to 0.1 K. This cooling was provided by a complex cryogenic system involving passive cooling to ∼40 K, a pulse-tube cooler stage to achieve ∼18 K, a further mechanical cooler to reach ∼2 K, and a liquid helium dilution cooler to reach 100 mK.

The sensitivities of the *Planck* instruments are not presented in the same form as those of *Herschel* or SCUBA-2. The longer wavelength bands, which primarily observed temperature and polarisation fluctuations in the CMB, had their sensitivity estimates quoted in terms of noise equivalent temperature fluctuation level (NEΔT) in µK. This is the temperature change observable above the 1σ noise level over the full mission. The two shortest wavelenghts had their sensitivities recorded in Noise Equivalent Flux Density (NEFD) in $\mathrm{kJy\,sr^{-1}}$ °. These sensitivities are given in Table 2.6. The sensitivities were computed for a square pixel with side length 1° (Planck Collaboration 2018a). The *Planck* sensitivity curves for each band are displayed in Figure 2.18.

The HFI beam profiles were estimated through scans of Jupiter and Saturn, with validation of the beams carried out using scans of Mars (Planck Collaboration 2016a). Initial relative flux calibration of the 350 µm and 550 µm bands was conducted through observations of Uranus and Neptune, and comparison with thermal models of the planets as point-like sources. Temperature calibration of the longer wavelength HFI bands was done by measurements of the CMB dipole. This is described in detail

Band Wavelength (µm)	Sensitivity (µK deg)	Beam FWHM (arcminute)
3000	1.29	9.66
2098	0.55	7.22
1382	0.78	4.90
850	2.56	4.92
(µm)	(kJy sr^{-1} deg)	(arcminute)
550	0.78	4.67
350	0.72	4.22

Table 2.6. Sensitivities and beam profile angular sizes of the HFI bands.

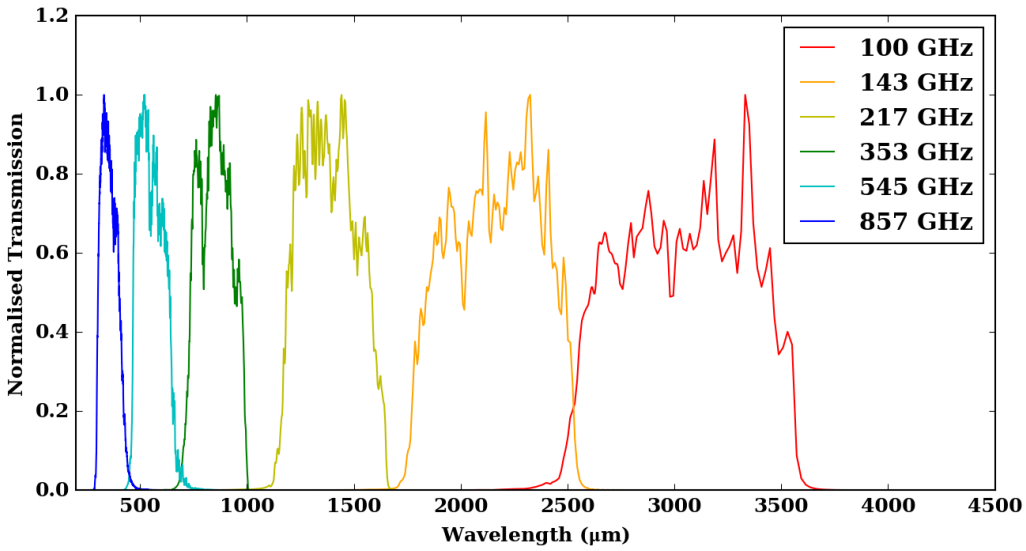

Figure 2.18. Normalised response functions for the six HFI bands. Data from Planck Collaboration (2018b).

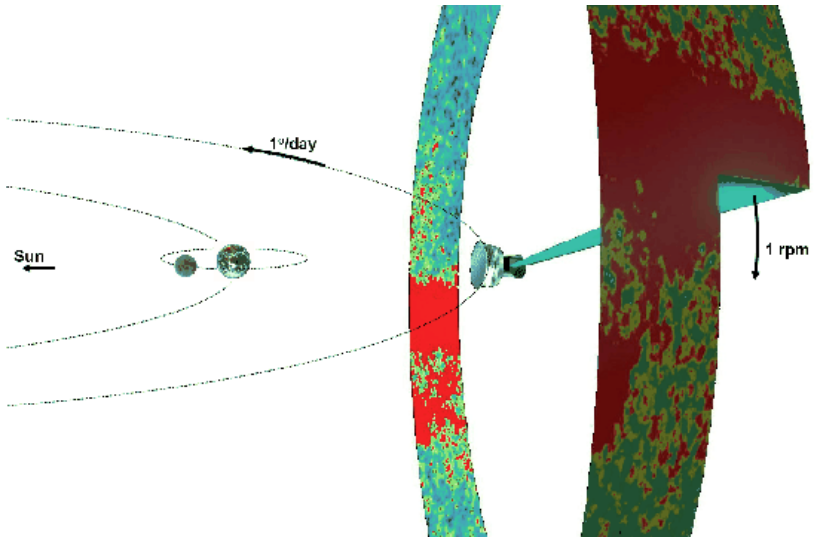

Figure 2.19. Diagram of *Planck* scanning mode, indicating how the telescope was kept at a constant angle away from the Sun. The rotation at a speed of 1 rpm enabled *Planck* to scan a circular strip, while its orbit around the Sun ensured that it would view the entire sky approximately once every six months, due to the 1 °/day angular velocity. Image credit Tauber et al. (2010).

in Planck Collaboration (2016b).

The lifetime of *Planck* was limited by its supply of helium for the dilution refrigerator, and it ceased operating in October 2013, after which it was deactivated and placed in a heliocentric orbit, moving it away from L2.

2.0.4.1 *Planck* Observing Mode

Much like *IRAS*, *Planck* was designed to survey the full sky autonomously. Figure 2.19 shows that *Planck* maintained a position where its solar panels continually faced the Sun. The telescope, therefore, had a fixed viewing angle offset from the *Planck*-Sun system by 85°.

The spacecraft rotated continuously around this axis at a rate of 1 rpm, tracing an almost complete great circle with each revolution. As *Planck* orbited the Sun, its view of the sky is shifted by approximately 1° every 24 hours. This ensured that the entire sky was observed twice every six months. The high rate of rotation allowed *Planck* to repeatedly image the same region of the sky, providing redundancy in the data and building up integration time.

A benefit of this continuous rotation is that *Planck* observed the galactic poles once each revolution. These regions contain very little dust emission, and thus comparison with COBE-FIRAS data, which provide absolute flux values, allowed for the *Planck* data to be corrected for zero flux emission.

2.1 Observations and Data Reduction

This Section will discuss the observations and general data reduction for the products utilised in this thesis. The *Herschel* observations formed the primary data source for the project, and were reduced utilising the latest pipelines to take account of improved calibration scripts. Thus, a detailed description of the reduction process is provided in Section 2.1.2. Ancillary data, including the SCUBA-2 observations were retrieved as final products from their respective archives, and only a general overview of the reduction processes for each data set is presented.

2.1.1 The *Herschel* Gould Belt Survey

The *Herschel* observations for this project come from the *Herschel* Gould Belt Survey (HGBS, André et al. 2010). This survey with PACS and SPIRE aimed to tackle questions regarding the origins of the stellar initial mass function by taking a census of pre- and protostellar cores in the star forming regions contained within the Gould Belt.

Herschel observations were organised with a mix of guaranteed time (GT), set aside for use by the PI consortium, and open time (OT), which could be applied for by anyone. GT made up approximately 32% of the total allotted observing time. Observing proposals were chosen by the Herschel Observing Time Allocation Committee, and all *Herschel* data became public after a short propitiatory period. The HGBS formed one of the GT Key Projects of the *Herschel* program, and required extensive use of both PACS and SPIRE in the SPIRE/PACS parallel observing mode.

The HGBS concentrated on the most nearby star-forming molecular clouds, achieving spatial resolution as small as 0.01 pc. Its combination of sensitivity and angular resolution was vital in establishing the ubiquity and importance of filamentary structures in the formation of pre-stellar objects.

2.1.2 *Herschel* Data Products

Before they could be viewed as useful observational maps, *Herschel* data had to be run though an extensive data reduction process. This is because the raw data from the instruments are not images, or even a series of images strips forming individual scan legs, but are simply lists of voltage time series from the bolometers, each with a corresponding time for the reading. These time sequences, along with telemetry data indicating the pointing location of the telescope at the time of the

observation, form a *Herschel* Level-0 data product*. To reach the point where the data is useful for analysis, the Level-0 data must be processed through standard reduction pipelines, before being uploaded to the *Herschel* Science Archive (HSA). This is typically achieved through a series of automated scripts in the *Herschel* Interactive Processing Environment (HIPE). HIPE is also available for users who wish to manually reprocess observations from low level products, either to make use of updated pipeline procedures that were not part of the available archive data pipelines at a given time, or to use modified pipeline procedures for specific tasks.

The first step in data reduction is to process the Level-0 voltage time series data into time series given in physical units, creating Level-1 data. This is done in such a way as to make the data, in principle, instrument independent. Level-2 is the designation for data which have been converted into a true image map of adjacent scans of a region for a single scan direction. At this stage, the data are nominally ready for analysis. However, as discussed above, optimal coverage and sensitivity for the *Herschel* instruments is obtained by combining nominal and orthogonal scans into a single map. This intermediate step denotes Level-2.5 data. Finally, Level-3 data products are formed when neighbouring regions are mosaicked together to form larger coherent maps.

Prior to 2017, *Herschel* products available in the HSA, and the then release version of HIPE 14, utilised older models and scripts during data reduction. However, the final build of HIPE (version 15) was released in December 2016, and all products on the HSA were reprocessed by February the following year. This took advantage of improved models for the PACS photometric beam profiles, and an improved script for background flux calibration for the SPIRE observations. All analysis in this thesis utilised data products obtained from HIPE 15.

For PACS observations, I opted to produce higher level data products myself, utilising HIPE 15, rather than simply retrieve the Level-2.5 data present on the HSA. This was initially due to the complicated scan nature of the Taurus region, which is discussed in Section 5, and was repeated for the Ophiuchus region for consistency. I used a modified version of the `JScanam` script, provided by Matt Smith, to take the Level-1 data and process it into usable Level-3 data in an automated fashion. The `JScanam` script combines a map maker, mosaicking script, and de-striping algorithm into a single action. As discussed above, post-processed de-striping of PACS data is required due to the high $1/f$ noise knee of the instrument.

Data reduction was simpler for the SPIRE data, though it still required some manual reduction of lower level products, again due to the unusual scan pattern of

*`http://herschel.esac.esa.int/hcss-doc-15.0/index.jsp`

the target regions. Without the need for de-striping due to a much lower 1/f knee, I opted to retrieve the Level-2 products, and utilise the HIPE 15 `mosaic` task to co-add nominal and orthogonal scans, and join adjacent regions into finalised Level-3 data.

2.1.3 The JCMT Gould Belt Survey Data Reduction

The JCMT Gould Belt Legacy Survey (GBS, Ward-Thompson et al. 2007) was designed to survey star forming regions contained within the Gould Belt using a combination of three instruments: SCUBA-2 for dust continuum emission, HARP for molecular line emission, and SCUBA-2's ancillary polarimeter, POL-2, for determining the dust polarisation of each region. All SCUBA-2 observations were taken between 2012 and 2014 while JCMT was under the control of the JAC. An archive of all GBS data is maintained by the Canadian Astronomy Data Centre (CADC)[†].

All SCUBA-2 data reduction for the GBS followed the same routine. Individual pointings, taken with the "PONG1800" mapping mode, are reduced with an iterative map making process in the Sub-Millimetre User Reduction Facility (SMURF, Chapin et al. 2013). First, the pointings are resampled to 6″ at 850 µm, a process which essentially acts as a low-pass filter to remove noise while resolving structure on the scale of the beam profile. An initial iterative map making pass is conducted on the resampled pointings to define a signal-to-noise mask of the region, which is used to identify useful emission. This mask is then used to inform a second reduction pass, with the results being mosaicked together to produce the completed map.

To reduce the effect of $1/f$ noise, the map making process applies a 10′ spatial filter in Fourier space. Tests with synthetic data have shown that flux from Gaussian sources with FWHM <2.5′ is largely unaffected by the filter, while sources with FWHM between 2.5′ to 7.5′ have both their flux and their angular size underestimated as a result. Structures with angular scales larger than 7.5′ are often largely removed from the filtered maps. This presents a problem for this thesis, which aims to examine the properties of extended structure. However, large scale emission can be recovered from the SCUBA-2 maps through a technique described in Section 2.1.7.

2.1.4 IRIS

The *IRAS* extended emission maps were first published as part of the SkyFlux Atlas in 1984. The *IRAS* Sky Survey Atlas (ISSA) was released in 1992, and featured

[†]`http://www.cadc-ccda.hia-iha.nrc-cnrc.gc.ca/en/search/?collection=JCMT&noexec=true`. This research used the facilities of the Canadian Astronomy Data Centre operated by the National Research Council of Canada with the support of the Canadian Space Agency.

reprocessed maps constructed with a better understanding of the instruments, and a rudimentary destriping method (Wheelock et al. 2002). In addition, new zodiacal light models allowed for better flux correction across the fields. While ISSA boasted a factor five sensitivity increase over the SkyFlux Atlas, significant glitches and striping remained.

A new catalogue of cleaned, destriped and zero-calibrated *IRAS* fields was released in 2005, termed the Improved Reprocessing of the *IRAS* Survey (IRIS, Miville-Deschênes and Lagache 2005). In the first step, small scale glitches and point sources were identified, and removed or masked respectively. The cleaned fields were then subject to a wavelet analysis which removed large scale variation, before a fast Fourier transform was applied to identify the striping. Once the striping had been removed in Fourier space, the inverse transform was then added to the original field. Figure 2.20, taken from Miville-Deschênes and Lagache (2005), shows the effect of this destriping on one of the ISSA tiles.

With the striping removed, the fields could then be recalibrated for each band. This was done to take account of improved models of the instruments. By comparison with the DIRBE instrument on the COBE satellite, which provided an absolute flux calibration, the response of each band at differing scales and brightnesses could be estimated and corrected for. A final comparison with DIRBE at large scales allowed for zero level calibration of the IRIS products.

This process was applied to each field from both complete surveys (hour confirmation, HCON, 1-2) and those of the incomplete survey (HCON-3). Cleaned fields were then coadded to further improve sensitivity. Each IRIS tile is $12.5^\circ \times 12.5^\circ$ in size, with a $1.5'$ pixel resolution. All the IRIS fields are publicly available from the IRIS Data Collection Atlas[‡].

2.1.5 *Planck* All-Sky Dust Models

To complete its mission to produce high-sensitivity maps of the CMB anisotropies, *Planck* results needed to be corrected for contribution from the foreground emission. This is because over much of the sky, galactic emission, especially near the plane of the Milky Way, dominates at wavelengths sensitive to the variations in the CMB. As such, the *Planck* consortium needed to produce highly detailed models of dust foreground emission.

The *Planck* all-sky dust models were constructed from a combination of *Planck* HFI 350 µm, 550 µm and 850 µm thermal dust maps, with the addition of modified

[‡]`https://irsa.ipac.caltech.edu/data/IRIS/`

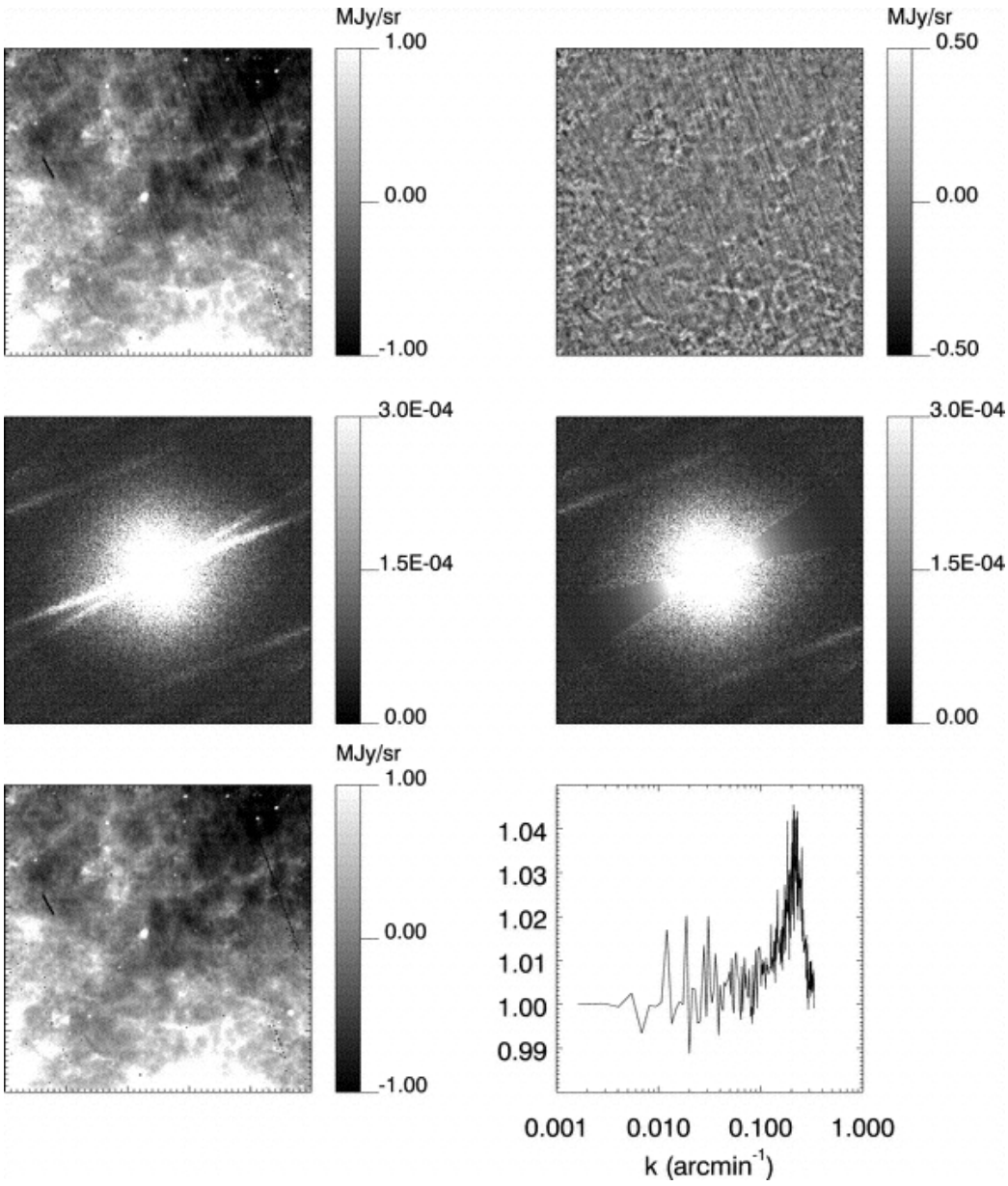

Figure 2.20. The figure shows the effect of the IRIS destriping algorithm on an ISSA tile (top left) at 60 µm. The wavelet filtered tile (top right) is passed through a fast Fourier transform (middle left) where the directional stripes are identified and removed (middle right). The inverse transform is then added back to the original image (bottom left) to remove the striping. The bottom right panel shows the ratio of the power spectrum between the striped and destriped images. Figure taken from Miville-Deschênes and Lagache (2005).

IRAS 100 µm data (Planck Collaboration 2016d). Initially, the raw temperature sky maps from all nine *Planck* bands are treated to remove contamination from zodiacal light (Planck Collaboration 2014) by fitting them to the COBE/DIRBE zodiacal models (Kelsall et al. 1998). For data at 100 µm, the *IRAS* IRIS tiles were combined with the low resolution, large-scale map produced by Schlegel, Finkbeiner, and Davis (1998).

The maps were then cleaned by removing point sources identified in the *Planck* Catalogue of Compact Sources (Planck Collaboration 2016c). The masked regions were filled using a spline interpolation of neighbouring pixels.

A foreground dust map produced through the Generalized Needlet Internal Linear Combination (GNILC, Remazeilles, Delabrouille, and Cardoso 2011) technique. This enables removal of anisotropic contribution to the foreground emission by the Cosmic Infrared Background (CIB) by applying a series of spherical wavelets of varying radii to all observation bands, and comparing components at different spatial scales in both Fourier and real space. The result of the GNILC technique can be seen in Figure 2.21. Here the raw 850 µm image (top left) is stripped of CMB emission (top right), and fitted with a MBB to produce a dust model (bottom left). The result of the GNILC algorithm being applied to the dust model is shown in the bottom right panel. This process is repeated for all nine bands.

Once foreground dust emission maps had been produced, maps of dust temperature, dust opacity index, and optical depth could be estimated with a simple MBB with three free parameters, fit to the 350 µm, 550 µm and 850 µm and modified 100 µm data. The MBB function is given by the equation

$$I_\nu(p) = \tau_0(p) \left(\frac{\nu}{\nu_0}\right)^{\beta(p)} \mathrm{B}_\nu(T(p)), \tag{2.5}$$

where $I_\nu(p)$ is the intensity in band ν and at pixel p, τ_0 is the dust optical depth at the reference frequency 350 GHz (850 µm, $\beta(p)$ and $T(p)$ are the dust opacity index and dust temperature at pixel p, and $\mathrm{B}_\nu(T)$ is the Planck function. The parameters were fit simultaneously at 5′ resolution.

The dust model maps can be accessed publicly from the *Planck* Public Data Release 2 archive[§].

[§]`https://irsa.ipac.caltech.edu/data/Planck/release_2/all-sky-maps/ysz_index.html`

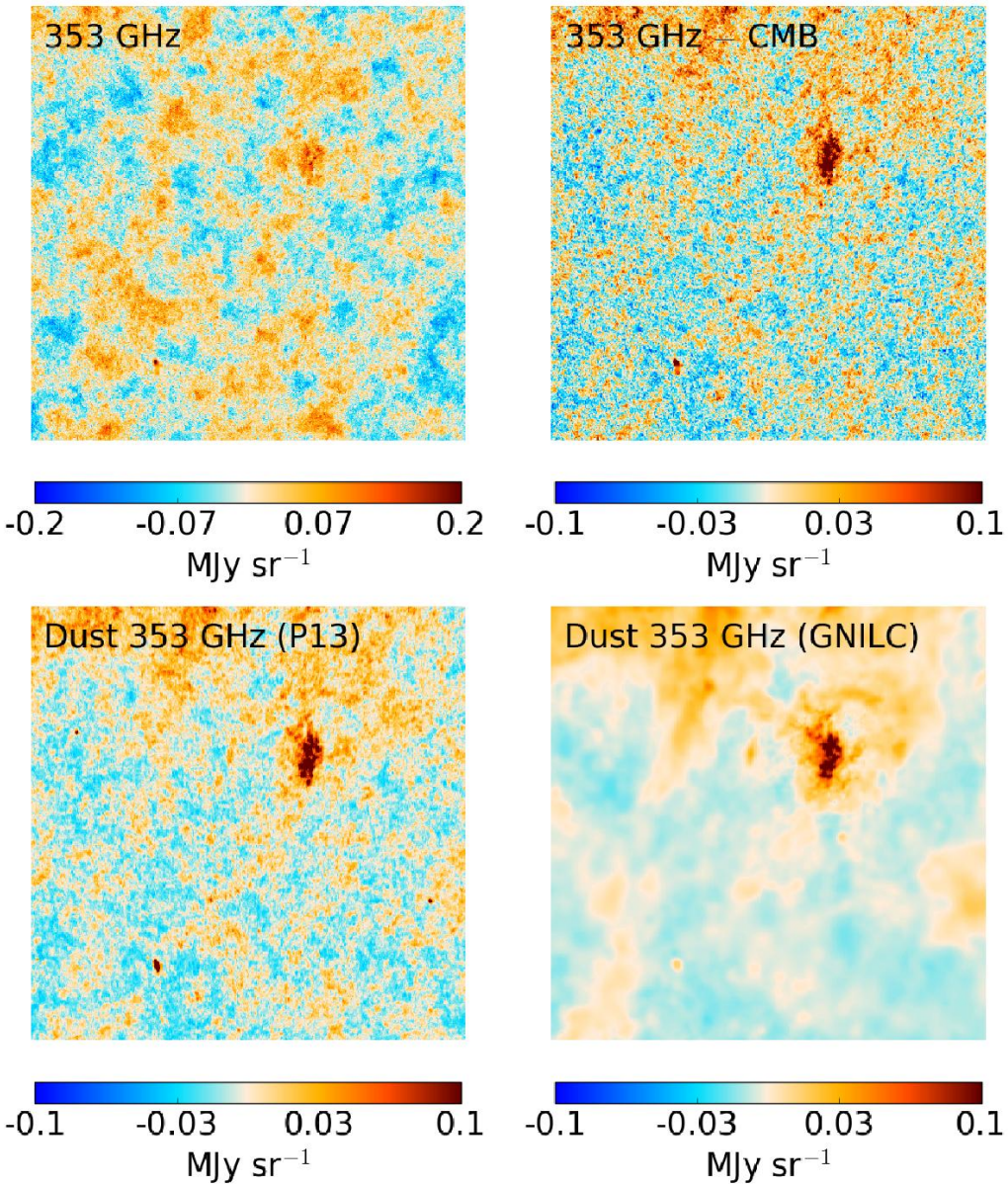

Figure 2.21. Images showing the steps to produce *Planck* foreground dust emission maps. The panels show: the *Planck* 850 µm emission map (top left); the 850 µm map with CMB removed (top right); dust model produced from MBB fitting of the CMB subtracted map (bottom left); the GNILC foreground dust emission map (bottom right). Wavebands are given in frequency as per *Planck* Collaboration convention. In each case, the mean intensity has been subtracted. Image taken from Planck Collaboration (2016d).

2.1.6 Zero-Point Corrections

As the photometric backgrounds (from the telescope in the case of *Herschel*, and from the atmosphere and telescope in the case of SCUBA-2) are far larger than the astrophysical signals, the observations do not provide a measurement of the absolute astronomical sky brightness. The lack of a reference point for zero flux introduces a systematic error because an area of sky with zero emission cannot be recorded as such by the arrays. This zero point error has to be corrected before any analysis can take place.

The Constant-Offset Technique was first described in Bernard et al. (2010), and further expanded upon in other works, e.g. Lombardi et al. (2014) and Abreu-Vicente et al. (2017). It involves the use of the *Planck* all sky surveys and IRIS tiles to produce synthetic, zero-point calibrated observations at the *Herschel* wavelengths, which can then be used to compare with the true observations. SPIRE zero-point correction is carried out as a standard procedure in the HIPE data pipeline.

However, PACS and post-feathering SCUBA-2 observations must be calibrated manually. The process to accomplish this is described below.

2.1.6.1 PACS and SCUBA-2

I took sections of the *Planck* all-sky models of dust opacity index, β, temperature, and optical depth at 850 µm, τ_{λ_0}, located around my target region. From these, I constructed a series of synthetic, monochromatic observations at 250 µm, 350 µm, 500 µm and 850 µm through the equation

$$I_\lambda = \mathrm{B}_\lambda(\lambda, T) \cdot \tau_{\lambda_0} \left(\frac{\lambda}{\lambda_0} \right)^{-\beta}. \tag{2.6}$$

At typical temperatures for dusty, star forming regions, these monochromatic observations tightly constrain the Rayleigh-Jeans tail of the Planck function, and provide good reference points for calibrating SPIRE and SCUBA-2 observations. However, PACS wavebands lie around the black body peak, or in the Wien's regime, which is poorly constrained with these observations alone. To counter this, I took the IRIS 100 µm tile that spanned my region of interest, and convolved it with the 5′ *Planck* beam profile. This allowed me to construct an SED at every point in my target region that was well constrained across all *Herschel* bands.

I then finely sampled this SED over both PACS wavebands, and convolved the resultant fluxes with the *Herschel* response functions to produce synthetic PACS observations, albeit at 5′ resolution. I will term these $\mathrm{Obs}_{\mathrm{Planck}}$, with surface brightness S_{Planck}.

I then convolved the true PACS observations, $\mathrm{Obs_{PACS}}$, with the 5′ *Planck* beam profile, and performed a linear fit between $\mathrm{Obs_{Planck}}$ and $\mathrm{Obs_{PACS}}$,

$$S_{\mathrm{PACS}} = m \cdot S_{\mathrm{Planck}} + c. \tag{2.7}$$

The gradient of the fit, m, should return a value close to 1.0, indicating good relative flux calibration of the PACS instrument. The offset c is then the average surface brightness value by which the $\mathrm{Obs_{PACS}}$ is lower than the $\mathrm{Obs_{Planck}}$. The negative of c is, therefore, the value of the offset that must be applied to the *Herschel* PACS observations to correctly zero-point correct them.

As the *Planck* and PACS observations are sensitive to emission at different size scales, in regions with bright, extended sources, it was sometimes necessary to limit fitting to background regions. I achieved this by defining a background flux level in each set of observations and masking regions in both images that exceeded this level.

The process to zero-point correct the feathered SCUBA-2 observations is, in principle, simpler. This is because the 850 µm band is already well constrained by just the *Planck* bands. However, as the combined *IRAS*/*Planck* SED had already been constructed, I used an identical pipeline to the one described above to perform the offset. Equation 2.7 then becomes

$$S_{\mathrm{SCUBA-2}} = m \cdot S_{\mathrm{Planck}} + c. \tag{2.8}$$

Thus, the offset can be identified and applied as before.

2.1.7 Ground Based Observation Extended Emission Recovery

As discussed in Section 2.1.3, the 10′ Gaussian filter, applied to reduce the effect of $1/f$ noise, also removes much of the emission from extended sources with an angular size greater than 7.5′. Conversely, the *Planck* 850 µm HFI band does not need to contend with $1/f$ noise contribution from the atmosphere, but cannot resolve structures smaller than 5′.

Planck and SCUBA-2 850 µm maps of the same area can be combined in Fourier space to produce observations with the resolution of SCUBA-2, and the extended structure of *Planck*. First, the *Planck* observation, $\mathrm{Obs_P}$ is resampled at the same pixel scale as the SCUBA-2 observation, $\mathrm{Obs_S}$. A 2D Gaussian filter, $\mathrm{Obs_G}$, with FWHM 5′ is also generated at the centre of a pixel grid with the same dimensions and sample rate as the observations. A 2D fast Fourier transform (FFT) is then

performed to produce $\mathcal{F}\{\mathrm{Obs_S}\}$, $\mathcal{F}\{\mathrm{Obs_P}\}$, and $\mathcal{F}\{\mathrm{Obs_G}\}$. Fourier Transforming the images places them into the frequency domain, which allows objects of a certain spacial scale to be identified. $\mathcal{F}\{\mathrm{Obs_G}\}$ is renormalised to ensure it has a peak amplitude of 1. It is then applied to the observations, and the resultant images are combined, such that

$$\mathcal{F}\{\mathrm{Obs_{SG}}\} = \mathcal{F}\{\mathrm{Obs_S}\} \cdot (1 - \mathcal{F}\{\mathrm{Obs_G}\}) \tag{2.9}$$

$$\mathcal{F}\{\mathrm{Obs_{PG}}\} = \mathcal{F}\{\mathrm{Obs_P}\} \cdot \mathcal{F}\{\mathrm{Obs_G}\} \tag{2.10}$$

$$\mathcal{F}\{\mathrm{Obs_{SP}}\} = \mathcal{F}\{\mathrm{Obs_{SG}}\} + \mathcal{F}\{\mathrm{Obs_{PG}}\}, \tag{2.11}$$

where $\mathcal{F}\{\mathrm{Obs_{SG}}\}$ and $\mathcal{F}\{\mathrm{Obs_{PG}}\}$ are the Fourier combinations of the Gaussian filter with the SCUBA-2 and *Planck* observations, respectively, and $\mathcal{F}\{\mathrm{Obs_{SP}}\}$ is then the Fourier combination of the two filtered observations. By applying the filter in this way, the SCUBA-2 image has objects with angular size $<5'$ partially suppressed, reducing the effect of small scale stochastic noise, which structures in the *Planck* observations much larger than the filter scale are similarly suppressed. This allows for a seamless combination of the images based on the spatial scales of the observed structures, which would be prohibitively difficult to achieve in the image plane. The inverse FFT is then taken of $\mathcal{F}\{\mathrm{Obs_{SP}}\}$ to produce the final combined observation, $\mathrm{Obs_{SP}}$. This process does not automatically apply the *Planck* zero point correction, which has to be performed via the method described in Section 2.1.6.

The algorithm used to combine SCUBA-2 and *Planck* observations for the analysis in this thesis was constructed by Matt Smith (in prep.), and is based on the CASAfeather algorithm (McMullin et al. 2007).

2.2 Colour Corrections

Many of the detectors described in this chapter are calibrated assuming that an observed source has a spectrum that remains constant across the entire observing band. In particular, both the *Herschel* PACS and SPIRE instruments use an assumed source function of

$$\lambda I_\lambda = const. \tag{2.12}$$

While this approximation holds true for narrow observation bands (e.g. those

of the SCUBA-2 instrument), this is not true for the wide bands of *Herschel*, especially when observing emission from cold dust, which can vary significantly across a single observing band due to the band covering the peak of the modified black body spectrum.

Thus the intensity reported by the detecting instrument is often offset from the true intensity of the source. This effect can be corrected for by generating a series of colour correction factors. The factors are calculated by comparing the estimated intensity a detector would produce if observing a modified black body, with the true intensity of that source

$$K(T, \beta, \lambda_0) = \lambda_0^{-\beta} \mathrm{B}(T, \lambda_0) \left[\frac{\int_{band} \lambda R(\lambda) \mu(\lambda) \Omega(\lambda) d\lambda}{\int_{band} \lambda^{-\beta} \mathrm{B}(T, \lambda) R(\lambda) \mu(\lambda) \Omega(\lambda) d\lambda} \right]., \tag{2.13}$$

where T and β are the dust temperature and opacity index respectively, λ_0 is the central wavelength of the waveband for which the colour correction factors are being generated, $\mathrm{B}(T, \lambda)$ is the Planck function, $R(\lambda)$ is the value of the spectral response function for a given wavelength, $\mu(\lambda)$ is the aperture efficiency, and Ω is the solid angle of the effective beam profile. By varying the value of T and β, a series of colour correction factors can be generated for different dust conditions. Colour correction factors for a small range of temperatures and opacity indices for the *Herschel* instruments are given in Exter (2017) and Valtchanov (2017).

These corrections must be applied to all observations before accurate measurements of dust column density can be made. For conventional MBB fitting, this is often an iterative process. Typically, a fixed value of the opacity index is set to reduce the complexity of the fitting. This also limits the scope of the corrections to be applied to just those that vary with temperature. Initially, the temperature of the source is not known, and therefore the appropriate correction cannot be applied. An inaccurate estimate of dust column density and temperature is made, and therefore be used to apply an appropriate temperature-dependent colour correction to each sky location in each observation band. The fitting can then be repeated, producing a more accurate estimate of the column density and temperature, and thus allowing for a more accurate application of the colour correction factors. This process continues until convergence is reached between iterations.

The PPMAP application of colour corrections is somewhat different, and is discussed in chapter 3.

Chapter 3
PPMAP: Theory and the Algorithm

In this chapter, I introduce the PPMAP algorithm as a method of analysing hydrogen column density derived from multi-wavelength dust emission observations to determine the intrinsic properties of the dust. Initially, I introduce the mathematical concepts behind the point process method, and their specific application to PPMAP. I then describe how the theory is implemented in the code, and discuss the operation of the algorithm. Finally, I discuss the data products produced by PPMAP, and introduce several derived products that are useful for the analysis of the dust models.

3.1 Point Process Mapping

PPMAP is a Bayesian Point Process algorithm for estimating the opacity of different populations of interstellar dust by analysing multi-wavelength far infrared and sub-millimetre continuum observations, where each population can be characterised by a single representative dust temperature and dust opacity index. PPMAP was first described by Marsh, Whitworth, and Lomax (2015), although other applications of the Point Process formalism had been described earlier, by Richardson and Marsh (1987) for use in acoustic imaging, by Richardson and Marsh (1992) for the identification and tracking of moving targets in RADAR data, and by Marsh, Velusamy, and Ware (2006) for planet detection with interferometric observations. The mathematical theory behind PPMAP, and the operations of the algorithm, are described in the following sub-sections.

3.1.1 The Mathematical Theory

The Point Process method refers to the concept that nearly any system in "real space" can be approximated by a number of "points", each occupying a "single-point state space" whose extent covers all possible values of the important properties of the system. In the case of PPMAP, a "point" of the system can be thought of as a single unit of dust opacity, while the extent of "single-point state space" represents the total range of possible values in the (x, y) sky coordinates, the range of possible dust temperatures, T, and the range of potential dust opacity indices, β. The whole system is then made up of many "points" all occupying a different locations within a "multi-point state space".

To reduce the complexity of the problem, "multi-point state space" is sub-divided into a number of elements, each characterised by a characteristic value for each of the properties, with the total number of elements given by the quantity N_{states}. Therefore, one only needs to ensure that the elements are suitably spaced to characterise each parameter sufficiently well. The system can then be characterised by the set of occupation numbers, $\mathbf{\Gamma}$, for each of those elements. $\mathbf{\Gamma}$ is a vector with N_{states} dimensionality, with each element, Γ_n, containing the occupation number of the n^{th} element in "multi-point state space". A full description of how PPMAP solves for $\mathbf{\Gamma}$, and converts the output to a hydrogen column density, is given blow.

3.1.1.1 The Measurement Model

The underlying model for the PPMAP algorithm can be expressed simply as

$$\mathbf{d} = \mathbf{A\Gamma} + \mu, \tag{3.1}$$

where $\mathbf{d}$ represents an M-dimensional matrix of measurements, or observations, where the m^{th} element represents the observed intensity at location (X_m, Y_m) at wavelength λ_m. The quantity μ is a Gaussian random process, with covariance $\mathbf{C}_\mu$, and represents noise in the measurement matrix, $\mathbf{d}$. $\mathbf{A}$ is the response matrix, with dimensions $M \times N_{states}$, which links element d_m to the "points" in element Γ_n, corresponding to the "multi-point state space" spatial coordinates (x_n, y_n). Element A_{mn} measures the response of d_n to Γ_n by containing the information about the model, and can be expressed as

$$A_{mn} = H_{\lambda_m}(X_m - x_n, Y_m - y_n)K_{\lambda_m}(T_n)B_{\lambda_m}(T_n)\kappa(\lambda_m, \beta_n)\Delta\Omega_m, \tag{3.2}$$

where $H_{\lambda_m}(X_m - x_n, Y_m - y_n)$ is the emission spread over the beam profile for the observations taken at wavelength λ_m when it is centred on, and convolved with,

a single "point" at spatial position (x_n, y_n) in "multi-point state space"; $K_{\lambda_m}(T_n)$ is the colour correction due to finite passband width that would be applied to an observation at wavelength λ_m, due to a "point" with a dust temperature T_n; $B_{\lambda_m}(T_n)$ is the Planck function response at wavelength λ_m and temperature T_n; $\Delta\Omega_m$ is the solid angle subtended by observational element m; κ is the dust opacity law, which is given by

$$\kappa = \kappa_{300\,\mu\mathrm{m}} \left(\frac{\lambda_m}{300\,\mu\mathrm{m}} \right)^{-\beta_n}. \tag{3.3}$$

The reference opacity at 300 µm, $\kappa_{300\,\mu\mathrm{m}}$, is assumed in this work to be $0.1\,\mathrm{cm}^2\,\mathrm{g}^{-1}$, and is defined per unit mass of both dust and gas. It is consistent with a gas to dust ratio of 100.

The role of the response matrix, $\mathbf{A}$, can be further explored by considering the quantity $\mathbf{A\Gamma}$, which can be expressed by the alternative formalism

$$\mathbf{A\Gamma} = \sum_n f(\mathbf{z}_n)\Gamma_n. \tag{3.4}$$

As described above, Γ_n represents the occupation number of "points" in the n^{th} element in "multi-point state space", while $\mathbf{z}_n$ is the vector of coordinates of the n^{th} element of "multi-point state space". In the case of PPMAP, $\mathbf{z}_n$ has a dimensionality of four, corresponding the the x, y, T, and β coordinates. $f(\mathbf{z}_n)$ is then the noiseless observation of the singly occupied element (the equivalent of that element in "single-point state space"), taking into account the beam profile, colour correction, Planck function, opacity law, and solid angle appropriate to the element's position, temperature and β values, and the waveband in which it is being observed. Thus, $f(\mathbf{z}_n)\Gamma_n$ is the contribution to the noiseless observations of all the "points" in the n^{th} element, and the sum over all n builds up the full set of observations.

The initial state of the $\mathbf{\Gamma}$ vector is considered to be a Gaussian random process, with the individual elements, Γ_n, being statistically independent, with individual "points" equally likely to occupy any given x, y position, and any given value in the distribution of $\log T$. This initial distribution across all positions and temperatures is expressed as

$$P(\Gamma_n) = \frac{1}{\sigma\sqrt{2\pi}} \exp \frac{-(\Gamma_n - \eta)^2}{2\sigma^2}, \tag{3.5}$$

where $\sigma = \sqrt{\eta(1-p)}$, with p being the probability that any given element in Γ is occupied if only one "point" is present in the system, i.e. $p = 1/N_{states}$. η is the dilution parameter, defined by $\eta = N_0/N_{states}$, where N_0 is the *a priori* expectation number of "points" in the system. Therefore, η can be considered a resolution parameter, where

a low value of η will force PPMAP to construct the model with a small number of "points", relative to the number of elements in "state space".

To enable PPMAP to lift the $T - \beta$ degeneracy, the distribution of "points" across the range of opacity indices is not flat, but is itself drawn from a Gaussian distribution, with a mean value of $\bar{\beta}$, and a standard deviation, σ_β. This modifies the value of $P(\Gamma_n)$, by appending a factor derived from the probability that a given state, n, has a particular value of β.

The *a priori* distribution of states over all $\mathbf{\Gamma}$ can be obtained from

$$P(\mathbf{\Gamma}) = \prod_{n=1}^{N_{st}} P(\Gamma_n). \tag{3.6}$$

3.1.1.2 Defining the Density of Occupied States

The aim of the PPMAP algorithm is to estimate $\mathbf{\Gamma}$, given the observations, $\mathbf{d}$. This is achieved by minimising the mean square error, which ensures that the best estimate is the *a posteriori* expectation value of $\mathbf{\Gamma}$. This is given by

$$\mathrm{E}(\Gamma_n|\mathbf{d}) = \sum_{\mathbf{\Gamma}} \Gamma_n P(\mathbf{\Gamma}|\mathbf{d}). \tag{3.7}$$

The quantity $P(\mathbf{\Gamma}|\mathbf{d})$ is derived from Bayes' rule,

$$P(\mathbf{\Gamma}|\mathbf{d}) = \frac{P(\mathbf{d}|\mathbf{\Gamma})P(\mathbf{\Gamma})}{P(\mathbf{d})}. \tag{3.8}$$

$P(\mathbf{d}|\mathbf{\Gamma})$ is given by

$$\ln P(\mathbf{d}|\mathbf{\Gamma}) = -\frac{1}{2}(\mathbf{d} - \mathbf{A\Gamma})^\top \mathbf{C}_\mu^{-1}(\mathbf{d} - \mathbf{A\Gamma}) + const. \tag{3.9}$$

$\top$ denotes the transpose. $P(\mathbf{d})$ is a normalisation factor, while $P(\mathbf{\Gamma})$ is given by equation 3.6.

The expectation value of $\mathbf{\Gamma}$ is also equivalent to the density of the states,

$$\rho(\mathbf{z}_n|\mathbf{d}) \equiv \mathrm{E}(\Gamma_n|\mathbf{d}). \tag{3.10}$$

$\rho(\mathbf{z}_n|\mathbf{d})$ (hereafter, simply ρ) is termed a density as it measures the local concentration of "points" within each of the elements of $\mathbf{\Gamma}$. ρ is the quantity that the PPMAP algorithm ultimately estimates, through the procedure described below.

3.1.1.3 The Stepwise Change in ρ

The PPMAP algorithm performs the estimation of ρ using a stepwise approach in which it initially assumes an artificially high value for the noise in the model, such that the observations, $\mathbf{d}$, essentially contribute no information to the distribution of "points" in $\mathbf{\Gamma}$. The level of artificial noise is then incrementally decreased, updating the value of ρ at each step as the observations contribute information to the model. This is done until the artificial noise level reaches the true noise level in the observations. The steps of the algorithm are tracked by a "time" variable, t, which increases from $t = 0$ at the initial step, to $t = 1$ when the artificial noise level matches the true noise level, and measures the degree of conditioning of the data (i.e. how close the artificial noise level is to the true measurement noise). This measurement model at a given time is then

$$\mathbf{d}(t) = \mathbf{A}\mathbf{\Gamma}(t) + \nu(t), \tag{3.11}$$

where $\nu(t)$ represents the level of the assumed artificial noise level at time t. At $t = 1$, $\nu(1) = \mu$. Just as μ is considered to be a Gaussian random process with a covariance matrix $\mathbf{C}_\mu$, so ν is also a Gaussian random process, with covariance $\mathbf{C}_\nu$.

At a given time, t, the state of ρ can be written as

$$\rho(\mathbf{z}_n|\mathbf{d}^t) \equiv \mathrm{E}(\Gamma_n|\mathbf{d}^t) = \sum_{\mathbf{\Gamma}} \Gamma_n P(\mathbf{\Gamma}|\mathbf{d}^t), \tag{3.12}$$

where the superscript, ^{t}, denotes all times up to, but exclusive of, the current time t. Therefore, the change in ρ due to a new measurement at time $t + \Delta t$ is simply

$$\Delta\rho(\mathbf{z}_n|\mathbf{d}^t) \equiv \Delta\mathrm{E}(\Gamma_n|\mathbf{d}^t) = \sum_{\mathbf{\Gamma}} \Gamma_n \Delta P(\mathbf{\Gamma}|\mathbf{d}^t). \tag{3.13}$$

Δt is initially set to a very small value, and is updated dynamically to ensure that changes to the model between consecutive iterations are as large as they can be while remaining linear (and thus reducing the time it takes to fit a model). The term $\Delta P(\mathbf{\Gamma}|\mathbf{d}^t)$ can be defined by considering the time dependent form of equation 3.8;

$$P(\mathbf{\Gamma}|\mathbf{d}^t) = \frac{P(\mathbf{d}(t)|\mathbf{\Gamma})P(\mathbf{\Gamma})}{P(\mathbf{d}(t))}, \tag{3.14}$$

where $\mathbf{d}^t$ is the full set of all measurements up to time t, and $\mathbf{d}(t)$ is the set of

measurements at the current iteration time. $P(\mathbf{d}(t)|\mathbf{\Gamma})$ can then be expressed as

$$P(\mathbf{d}(t)|\mathbf{\Gamma}) = \prod_m \frac{1}{\sqrt{2\pi C_{\nu|m}}} \exp\left[-\frac{1}{2}\sum_m \frac{1}{C_{\nu|m}}\left(d_m(t) - \sum_n A_{mn}\Gamma_n\right)^2\right]. \quad (3.15)$$

Therefore, for the initial state where $t = 0$ equation 3.14 and equation 3.15 can be written as

$$P(\mathbf{\Gamma}|\mathbf{d}(0)) = \frac{P(\mathbf{d}(0)|\mathbf{\Gamma})P(\mathbf{\Gamma})}{P(\mathbf{d}(0))} \quad (3.16)$$

$$P(\mathbf{d}(0)|\mathbf{\Gamma}) = \prod_m \frac{1}{\sqrt{2\pi C_{\nu|m}}} \exp\left[-\frac{1}{2}\sum_m \frac{1}{C_{\nu|m}}\left(d_m(0) - \sum_n A_{mn}\Gamma_n\right)^2\right]. \quad (3.17)$$

The expression for $P(\mathbf{\Gamma}|\mathbf{d}^{t+\Delta t})$ is identical to the generic expression given in equation 3.14, with the *a priori* value of $P(\mathbf{\Gamma})$, such that

$$P(\mathbf{\Gamma}|\mathbf{d}^{t+\Delta t}) = P(\mathbf{d}(t)|\mathbf{\Gamma})P(\mathbf{\Gamma}|\mathbf{d}^t)/P(\mathbf{d}(t)). \quad (3.18)$$

Thus, the change in the conditional probability of $\mathbf{\Gamma}$ between subsequent time steps can be expressed by

$$\Delta P \equiv P(\mathbf{\Gamma}|\mathbf{d}^{t+\Delta t}) - P(\mathbf{\Gamma}|\mathbf{d}^t) \quad (3.19)$$

$$= P(\mathbf{\Gamma}|\mathbf{d}^t)\left\{[P(\mathbf{d}(t)|\mathbf{\Gamma})/P(\mathbf{d}(t))] - 1\right\}. \quad (3.20)$$

Equation 3.20 can be expanded and simplified by substituting in equation 3.15, bringing the $P(\mathbf{\Gamma}|\mathbf{d}^t)$ factor over the the left side. This is shown by

$$\frac{\Delta P}{P(\mathbf{\Gamma}|\mathbf{d}^t)} = \left(\prod_m \frac{1}{\sqrt{2\pi C_{\nu|m}}} \exp[\mathcal{E}] \Big/ P(\mathbf{d}(t))\right) - 1, \quad (3.21)$$

where $\exp[\mathcal{E}]$ is given by the expression

$$\exp[\mathcal{E}] = \exp\left[-\frac{1}{2}\sum_m \frac{1}{C_{\nu|m}}\left(d_m(t) - \sum_n A_{mn}\Gamma_n\right)^2\right] \quad (3.22)$$

$$= \exp\left[-\frac{1}{2}\sum_m \frac{1}{C_{\nu|m}}\left(d_m(t)^2 - 2d_m(t)\sum_n A_{mn}\Gamma_n + \left[\sum_n A_{mn}\Gamma_n\right]^2\right)\right] \quad (3.23)$$

$$= \exp\left[-\frac{1}{2}\sum_m \frac{d_m(t)^2}{C_{\nu|m}}\right] \exp\left[-\frac{1}{2}\sum_m \frac{1}{C_{\nu|m}}\left(-2d_m(t)\sum_n A_{mn}\Gamma_n + \left[\sum_n A_{mn}\Gamma_n\right]^2\right)\right]. \tag{3.24}$$

For most cases, where the number of states is extremely large (in practice, where $N_{states} > 20$), the value of $C_{\nu|m}$ is also very large, and thus the prefactor, $1/C_{\nu|m}$, approaches 0. In this case, $P(\mathbf{d}(t))$ is defined by a Gaussian random process with variance $\mathbf{C}_\mu$:

$$P(\mathbf{d}) \approx \prod_m \frac{1}{\sqrt{2\pi C_{\nu|m}}} \exp\left(-\frac{1}{2}\sum_m \frac{d_m(t)^2}{C_{\nu|m}}\right). \tag{3.25}$$

Applying equation 3.25 to equation **??**, and approximating the remaining exponential term with $\exp[-x] \approx 1 - x$, produces the Probability Update Equation, which is explicitly given by

$$\frac{\Delta P}{P(\mathbf{\Gamma}|\mathbf{d}^t)} \approx -\frac{1}{2}\sum_m \frac{1}{C_{\nu|m}}\left(-2d_m(t)\sum_n A_{mn}\Gamma_n + \left[\sum_n A_{mn}\Gamma_n\right]^2\right). \tag{3.26}$$

Thus, the change in state density at time t is given by

$$\Delta\rho \approx \sum_n \Gamma_n P(\mathbf{\Gamma}|\mathbf{d}^t) \sum_m \frac{1}{C_{\nu|m}}\left(d_m(t)\sum_n A_{mn}\Gamma_n - \frac{1}{2}\left[\sum_n A_{mn}\Gamma_n\right]^2\right) \tag{3.27}$$

3.1.1.4 ρ as a Truncated Hierarchy of Infinite Equations

While equation 3.27 represents the change in density of the $\mathbf{z}_n$ position in "multi-point state space" given the measurements $\mathbf{d}$ up to time t, the dimensionality of the equation is still in practice too large to compute. For even small models, the value of N_{states} can still exceed several million. This is a particular problem for the final term in the expression, which does not have a dimensionality $M \times N_{states}$, but $M \times N_{states}^2$. Fortunately, it is possible to truncate equation 3.27 to an approximately correct solution with a much lower dimensionality.

The initial step is to expand the summation terms by extracting the first order

term, such that

$$\Delta\rho = \sum_n \Gamma_n P(\mathbf{\Gamma}|\mathbf{d}^t) \sum_m \frac{1}{C_{\nu|m}} \left(d_m(t) \left[A_{mn}\Gamma_n + \sum_{n'\neq n} A_{mn'}\Gamma_{n'} \right] - \frac{1}{2} \left[A_{mn}\Gamma_n + \sum_{n'\neq n} A_{mn'}\Gamma n' \right]^2 \right) \tag{3.28}$$

$$= \sum_n \Gamma_n P(\mathbf{\Gamma}|\mathbf{d}^t) \sum_m \frac{1}{C_{\nu|m}} \left(d_m(t) \left[A_{mn}\Gamma_n + \sum_{n'\neq n} A_{mn'}\Gamma_{n'} \right] - \frac{1}{2} \left[(A_{mn}\Gamma_n)^2 + 2A_{mn}\Gamma_n \sum_{n'\neq n} A_{mn'}\Gamma_{n'} + \sum_{\substack{n'\neq n \\ n''\neq n}} A_{mn'}\Gamma_{n'} A_{mn''}\Gamma_{n''} \right] \right). \tag{3.29}$$

Equation 3.29 can be expressed in terms of $\rho(\mathbf{z}_n|\mathbf{d}^t)$, and higher order terms, by substituting in equation 3.12. This produces

$$\Delta\rho = \sum_m \frac{1}{C_{\nu|m}} \left(d_m(t) \left[\rho(\mathbf{z}_n|\mathbf{d}^t) A_{mn} + \sum_{n'\neq n} \rho(\mathbf{z}_n, \mathbf{z}_{n'}|\mathbf{d}^t) A_{mn'} \right] - \frac{1}{2} \left[\rho(\mathbf{z}_n|\mathbf{d}^t) A_{mn}^2 + 2A_{mn} \sum_{n'\neq n} \rho(\mathbf{z}_n, \mathbf{z}_{n'}|\mathbf{d}^t) A_{mn'} + \sum_{\substack{n'\neq n \\ n''\neq n}} \rho(\mathbf{z}_n, \mathbf{z}_{n'}, \mathbf{z}_{n''}|\mathbf{d}^t) A_{mn'} A_{mn''} \right] \right). \tag{3.30}$$

It is possible to further expand equation 3.30, by extracting the second order term for state n' from the summations, and to continue the expansion for all higher order terms. However, it is possible at this point to introduce the closure approximations which will allow the infinite series to be truncated at the first order expansion.

The closure approximations are given by

$$\rho(\mathbf{z}_n, \mathbf{z}_{n'}|\mathbf{d}^t) = \rho(\mathbf{z}_n|\mathbf{d}^t)\rho(\mathbf{z}_{n'}|\mathbf{d}^t) \tag{3.31}$$

$$\rho(\mathbf{z}_n, \mathbf{z}_{n'}, \mathbf{z}_{n''}|\mathbf{d}^t) = \rho(\mathbf{z}_n|\mathbf{d}^t)\rho(\mathbf{z}_{n'}|\mathbf{d}^t)\rho(\mathbf{z}_{n''}|\mathbf{d}^t). \tag{3.32}$$

There are an infinite number of closure approximations expanding the higher order forms of ρ, though for reasons that will become apparent, only the two listed above are required. The closure approximations are substituted into equation 3.30 to produce

$$\begin{aligned}\Delta\rho = \sum_m \frac{1}{C_{\nu|m}} \Bigg(& d_m(t) \left[\rho(\mathbf{z}_n|\mathbf{d}^t) A_{mn} + \rho(\mathbf{z}_n|\mathbf{d}^t) \sum_{n' \neq n} \rho(\mathbf{z}_{n'}|\mathbf{d}^t) A_{mn'} \right] \\ & - \frac{1}{2} \Bigg[\rho(\mathbf{z}_n|\mathbf{d}^t) A_{mn}^2 + 2\rho(\mathbf{z}_n|\mathbf{d}^t) A_{mn} \sum_{n' \neq n} \rho(\mathbf{z}_{n'}|\mathbf{d}^t) A_{mn'} \\ & \rho(\mathbf{z}_n|\mathbf{d}^t) \sum_{\substack{n' \neq n \\ n'' \neq n}} \rho(\mathbf{z}_{n'}|\mathbf{d}^t) A_{mn'} \rho(\mathbf{z}_{n''}|\mathbf{d}^t) A_{mn''} \Bigg] \Bigg)\end{aligned} \tag{3.33}$$

$$\begin{aligned}= \rho(\mathbf{z}_n|\mathbf{d}^t) \sum_m \frac{1}{C_{\nu|m}} \Bigg(& d_m(t) \left[A_{mn} + \sum_{n' \neq n} \rho(\mathbf{z}_{n'}|\mathbf{d}^t) A_{mn'} \right] \\ & - \frac{1}{2} \Bigg[A_{mn}^2 + 2A_{mn} \sum_{n' \neq n} \rho(\mathbf{z}_{n'}|\mathbf{d}^t) A_{mn'} \\ & \sum_{\substack{n' \neq n \\ n'' \neq n}} \rho(\mathbf{z}_{n'}|\mathbf{d}^t) A_{mn'} \rho(\mathbf{z}_{n''}|\mathbf{d}^t) A_{mn''} \Bigg] \Bigg)\end{aligned} \tag{3.34}$$

$$= \rho(\mathbf{z}_n|\mathbf{d}^t) \left\{ \sum_m \frac{1}{C_{\nu|m}} \left[d_m(t) - \sum_{n' \neq n} \rho(\mathbf{z}_{n'}|\mathbf{d}^t) A_{mn'} \right] A_{mn} \right.$$

$$- \frac{1}{2} \sum_m \frac{1}{C_{\nu|m}} A_{mn}^2 + \sum_m \frac{1}{C_{\nu|m}} \left[d_m \sum_{n' \neq n} \rho(\mathbf{z}_{n'}|\mathbf{d}^t) A_{mn'} \right. \tag{3.35}$$

$$\left. \left. - \sum_{\substack{n' \neq n \\ n'' \neq n}} \rho(\mathbf{z}_{n'}|\mathbf{d}^t) A_{mn'} \rho(\mathbf{z}_{n''}|\mathbf{d}^t) A_{mn''} \right] \right\}.$$

As the last term in equation 3.35 is independent of $\mathbf{z}_n$, it must be constant over all "multi-point state space". It can therefore be inferred that its value is equal to 0. Thus the equation simplifies to

$$\frac{\Delta\rho}{\rho(\mathbf{z}_n|\mathbf{d}^t)} = \sum_m \frac{1}{C_{\nu|m}} \left[d_m(t) - \sum_{n' \neq n} \rho(\mathbf{z}_{n'}|\mathbf{d}^t) A_{mn'} \right] A_{mn} - \frac{1}{2} \sum_m \frac{1}{C_{\nu|m}} A_{mn}^2. \tag{3.36}$$

The effect of this is to truncate the density update equation, greatly reducing the dimensionality of the problem. Equation 3.36 is equivalent to the differential equation

$$\frac{\partial\rho}{\partial t} + \phi_1 \rho = 0, \tag{3.37}$$

where ϕ_1 is the conditioning factor, given by the negative of the term on the right hand side of equation 3.36. It is then a simple procedure to numerically integrate equation 3.37 to achieve the density of "points" in a given state element, though the process remains computer intensive for large values of N_{states}. However, strategies employed during pre-processing can reduce the scale of the integration needed. These are discussed in Section 3.1.2.

When considered for all states, ϕ_1 can be expressed as

$$\phi_1 = -(\mathbf{d} - \mathbf{A}\rho)^\top \mathbf{C}_\nu^{-1} \mathbf{A} + \mathbf{b}/2, \tag{3.38}$$

where $\mathbf{b}$ is a vector formed from the diagonal elements of $\mathbf{A}^\top \mathbf{C}_\nu^{-1} \mathbf{A}$.

The initial value of ρ at time $t = 0$ is simply the *a priori* expectation value of $\mathbf{\Gamma}$, which is equivalent to the value of the dilution parameter, modified by the *a*

priori Gaussian distribution of β values,

$$\rho_{n|t=0} = \eta \times \alpha \exp \frac{-(\beta_n - \bar{\beta})^2}{2\sigma_\beta^2}. \tag{3.39}$$

The α term is a normalization constant which ensures that the mean value of $\rho_{t=0}$ over all n states remains equal to η.

3.1.2 PreMAP and the PPMAP Input Variables

For PPMAP to produce a solution for the optimal value of ρ, it requires a parameter file describing the full extent of the "state space" of the desired model, a set of far infrared and sub-millimetre observations of dust emission for the region of interest, high accuracy 2D models of the beam profiles of the systems responsible for producing the observations, and colour corrections for each of the observation wavebands, given the discrete values which define the positions of each of the elements along the dust temperature dimension of the "state space". The model, observation images, and beam profiles must all share a common sample rate (pixel size), though the observations should not be convolved to a common angular resolution, as they must for conventional MBB fitting techniques. Furthermore, the observations must be in units of $\mathrm{Jy\,pix^{-1}}$.

While each of these input variables can be manually passed to PPMAP, the preprocessing sub-routine, preMAP, simplifies the process by generating the PPMAP parameter file from a more human-readable preMAP parameter file. An image of a typical preMAP input file is given in Figure 3.1.

The `gloncent` and `glatcent` parameters specify where to position the centre of the model in world coordinates, while the `fieldsize` parameter dictates the angular size of the model. All three parameters only accept values in decimal degrees. It is assumed that the coordinates of the field centre are given in the same projection system as the input observations; either RA and Dec, or galactic latitude and longitude. The `pixel` parameter governs the angular side length of each model element in the x and y, plane of the sky dimensions. The parameter assumes values are given in arcseconds. PPMAP elements are square in the xy plane. As PPMAP models are Nyquist sampled in the xy plane, the `pixel` parameter effectively determines the angular resolution of the model, which is twice the value provided.

The `dilution` parameter represents the value of η. As discussed above, η relates to the number of "points" PPMAP has available to fit the model to the data, and can be though of as the "state space" resolution. Typical values of η range from

```
Parameter value            Name of variable         Description

246.75                          <gloncent> ; gal. long. (or RA) at centre [deg]
-24.4666666666                  <glatcent> ; gal. lat. (or Dec) at centre [deg]
1.2 0.8                         <fieldsize>; field of view dimensions [deg]
7.                              <pixel>    ; output sampling interval [arcsec]
3                               <dilution> ; a priori dilution
7000                            <maxiterat>; max no. of integration steps
0.1                             <kappa300> ; reference opacity [cm^2/g]
3                               <nbeta>    ; number of opacity law index values
1. 1.5 2.                       <betagrid> ; opacity law index values
2.0 0.25                        <betaprior>; a priori mean and sigma of beta
12                              <Nt>       ; number of temperatures
7. 50.                          <temprange>; range of temperatures [K]
6                               <nbands>   ; number of bands
70. 160. 250. 350. 500. 850.    <wavelen>  ; wavelengths [microns]
15.0 17.1 14.0 4.76 2.08 2.26   <sigobs>   ; noise of image [MJy/sr]
Herc850.txt                     <ccfile>   ; colour correction table
40                              <ncells>   ; nominal size of subfield
20                              <noverlap> ; size of subfield overlap
                                <obsimages>; list of FITS files follows:

L1688_0070.fits
L1688_0160.fits
L1688_0250.fits
L1688_0350.fits
L1688_0500.fits
L1688_0850.fits
```

Figure 3.1. A preMAP input file showing the most parameters most commonly parsed to preMAP. Where a single parameter requires two or more variables, the values are separated by white space. A small description of each parameter is given after the parameter tag.

~ 0.1 to ~ 3. η should be as small as possible while still achieving a reduced $\chi^2 \approx 1$. `maxiterat` sets the limit on the number of iterations PPMAP will perform if it does not reach convergence, or a divergent solution is detected. As with η, this value should be just large enough to ensure a reasonable fit to the data, as the model will become progressively noisier with each iteration.

The `kappa300` parameter defines the value of the reference opacity, κ_0, at the reference wavelength of 300 µm. `nbeta` gives the number discrete opacity index values PPMAP should include in the model, while `betagrid` lists the individual β values. The optional `betaprior` parameter accepts two arguments which define the mean and standard deviation of the Gaussian prior imposed on the opacity index. If `betaprior` is excluded, preMAP will parse a prior with a mean of 2, and a standard deviation of 10000; essentially a flat distribution. The `Nt` parameter specifies the number of discrete temperature values available to PPMAP. `temprange` defines the values of the lowest and highest temperature values. preMAP will then produce a logarithmically spaced array of temperatures of length `Nt`, from the lowest value of `temprange` to the highest. This array then defines the temperature values of the PPMAP model.

The `nbands` parameter indicates the total number of observational wavebands that will be supplied to PPMAP, while the `wavelen` parameter lists the wavelengths (in microns) of each band. An optional parameter, `sigobs`, provides a list of noise

estimates for the input observations. If `sigobs` is excluded, preMAP will attempt to estimate the noise present in each input observation.

`ccfile` gives the file name of a colour correction table for all of the input wavebands across a large range of finely sampled temperatures. preMAP will interpolate an array of colour correction factors for each of the temperature bands and wavebands from this file. At present, PPMAP assumes that colour corrections are not necessary for variations in opacity index.

The `ncells` and `noverlap` parameters define the side-length and linear overlap, in pixels, of the PPMAP subtiles. As discussed above, to update the value of the occupation density at a single location in "state space", PPMAP calculates the effect on that location of the current state of all other locations with the model. This is shown in equation 3.36 by the term

$$\sum_{n' \neq n} \rho(\mathbf{z}_{n'}|\mathbf{d}^t) A_{mn'}. \tag{3.40}$$

The sum over all n' states can pose a problem computationally due to the large number of states present, even for models with small angular sizes. However, the states are only coupled to each other by the observational beam profiles, with states separated from each other by an angular separation much larger than the beam size having a negligible effect on one another. Therefore, preMAP utilises the `ncells` and `noverlap` parameters to split the model in the xy plane to produce a series of smaller, uncorrelated, overlapping models, which can be fitted independently. This greatly reduces the scale of the summation. The only requirement is that the subtiles are larger than the beam sizes for the observations, and that the overlap between neighbouring subtiles is sufficient to ensure a smooth transition across the entire model when the subtiles are later recombined. The separation of the model into small subtiles also allows those tiles to be processed in parallel, further reducing runtime.

The final input parameter is `obsimages`, which is a list of the observation input files, given in the same order as the list of input wavelengths.

Once the parameters have been read by preMAP, the algorithm them produces the correctly formatted PPMAP input file. preMAP also re-samples the observations, and their corresponding beam profiles, at the same pixel scale as the defined PPMAP xy grid. This re-sampling of the data does not increase the resolution of the observations, though it does have the potential to decrease the resolution should the angular size of the pixels be larger than the beam of a given observation.

The current form of preMAP also assumes that the intensity is initially in

units of $\mathrm{MJy\,sr^{-1}}$, as most *Herschel* observations are typically processed in these units. However, as I mention above, PPMAP requires observations to be in units of $\mathrm{Jy\,pix^{-1}}$. preMAP therefore converts the intensity units of the input observations to the correct form during the re-sampling process.

The final step for preMAP is to generate a series of scripts to call PPMAP to operate on the individual sub-tiles, and then to queue and execute the scripts on the supercomputer cluster. An example PPMAP script file is shown in Figure 3.2.

3.1.3 The Operations of the PPMAP Algorithm

The initial step of the PPMAP algorithm itself, after reading in the input file generated by preMAP, and the command line parameters shown in Figure 3.2, is to set up the measurement and occupation density vectors ($\mathbf{d}$ and ρ respectively), and the response matrix, $\mathbf{A}$. In the context of the algorithm, each of the n dimensions of $\mathbf{A}$ represents the intensity produced in the m^{th} waveband when the only "point" present in the system is a single unit of column density in the n^{th} state (i.e. having position X, Y, temperature T, and opacity index β), when modified by the Planck function, colour correction, and beam profile. The constant term $\mathbf{b}/2$, defined in equation 3.38, is also generated at this point.

As shown in equation 3.11, the mathematical theory behind PPMAP assumes that at each time step, the measurement model is provided with an artificially inflated value of the observational noise, $\nu(t)$, which will approach the true value of the noise, μ, as $t \to 1$. The goal is to maintain a reduced $\chi^2 = 1$ at each iteration, which requires the density model to converge on an appropriate solution as the uncertainty decreases towards the true value. However, the implementation in the algorithm is somewhat different. Instead of injecting an artificially high uncertainty at the first iteration, PPMAP specifies an initially high threshold value for the reduced χ^2. The noise remains constant across all iterations, and is fixed to the true value parsed to PPMAP at initialization. Thus, the model is initially allowed to be poorly constrained given a small uncertainty, as opposed to the theoretical principal that the model should always be well constrained, but that the uncertainty is initially very large. The reference reduced χ^2 is then reduced in value as the algorithm progresses, forcing the model to converge to a well constrained solution.

The algorithm then begins the primary fitting loop. At each iteration, a vector of noiseless observations, $\mathbf{d}'$, is generated by multiplying $\mathbf{A}$ by the current state of the occupation density vector, ρ. The value of the reduced χ^2 between these noiseless observations and the true observations, given the fixed value of the noise, is calculated

```
#!/bin/bash --login
#SBATCH --job-name=Oph-16
#SBATCH -o Oph-16.log
#SBATCH -e Oph-16.err
#SBATCH -t 3-00:00
#SBATCH -p compute
#SBATCH -N 1
#SBATCH -n 40
#SBATCH --mail-user=<useremail>
#SBATCH --mail-type=ALL

# latest intel compilers, mkl and intel-mpi

module purge
module load compiler/intel

ulimit -s unlimited
ulimit -c 0

code=${HOME}/ppmap/ppmap
MYPATH=/scratch/<username>

NCPUS="40"

cd ${MYPATH}
start="$(date +%s)"
  for n in $NCPUS; do
      echo Running PPMAP with OMP_NUM_THREADS=$n
      export OMP_NUM_THREADS=$n
      ${code} Oph                    526   551   mosaic
      echo PPMAP finished
  done
#
```

Figure 3.2. A PPMAP script file for calling the algorithm to run on a subset of the sub-tiles. Each sub-tile is modelled independently, and so to reduce computation time, the total collection sub-tiles are grouped into smaller collections and run with different processes in parallel across multiple computer cores. The list of sub-tiles to be modelled by the process called by this script file is generated by parsing the index of the first and last sub-tile in the list as command line arguments. This script represents the last script for a particular PPMAP run, and will be scheduled to run last. Therefore, it also calls the `mosaic` sub-routine to gather all the fully modelled sub-tiles and mosaic them together to produce the full 4D data hypercube of column densities.

and compared to the reference reduced χ^2. If the current reduced χ^2 is less than, or equal to, the value of the reference reduced χ^2, then the current reduced χ^2 becomes the new reference value. Otherwise the solution is deemed divergent, and the process is terminated.

As discussed previously, $\mathbf{A}$ contains the colour corrections for each of the observations bands, which ensures that PPMAP is able to accurately calculate the χ^2 between the noiseless observations, $\mathbf{d}'$, and the true observations, $\mathbf{d}$. Unlike conventional fitting techniques, PPMAP does not apply these corrections as factors to the true observations in an iterative process, but instead directly applies the corrections as divisors to the model. As the temperature bands of the model are defined as delta functions, the corrections can be correctly applied in a single step, rather than requiring a further iterative process. PPMAP, therefore, does not correct the assumptions made about a detector source, but rather modifies the true source to match those assumptions. The outcome of both methods is identical (assuming the conventional iterative method properly converges), but this faster application method is impossible for MBB fitting techniques to perform, as the temperatures of the final output are unknown.

ϕ_1 is then generated, and ρ is updated by assuming a linear solution to equation 3.26, through

$$\rho_{t+1} = \rho_t - \epsilon\phi_1\rho_t, \tag{3.41}$$

where ϵ is a factor relating to the step size between the current and next iteration. A series of conditions allow for ϵ to be dynamically updated at regular intervals during the run. This allows for ρ to initially rapidly converge on an approximate solution, and then for smaller updates to ρ to occur to enable fine tuning the model at later iteration times.

Further conditions monitor if the current run has converged to, or diverged from, a suitable solution for ρ, or if the maximum iteration count is reached. If the algorithm detects a convergence to a solution, or the maximum iteration count has been reached, the current state of ρ is written out. However, if a divergent solution is detected, the state of ρ from the previous iteration is taken as the best distribution for the density of "points" in the current sub-tile.

The elements of ρ are then mapped to the elements of the 4D data hypercube, and are converted from number densities of "points", each representing a unit of optical depth, to a H_2 column density, assuming a mean molecular weight of 2.8, and the mass of a single hydrogen atom to be 1.6726×10^{-24} g, and that each "point" is

represented by a Nyquist Gaussian kernel with a FWHM of twice the pixel size. The sub-tile is then saved to a FITS file, with the header denoting the relative position of the sub-tile to the full field, and its reduced χ^2.

Once each of the sub-tiles have been written out, PPMAP mosaics them together into the full 4D data hypercube. A mean background column density is calculated for each sub-tile, which allows for corrections to be applied to neighbouring tiles to ensure the final model does not greatly suffer from fluctuations in column density at the boundaries of sub-tiles. A 4D uncertainty hypercube of the standard deviation to the expectation value of the column density (given by ρ) is also produced, by calculating the response to the observational data of the current model, given the uncertainty in the observations. The uncertainty calculation is based on a procedure described in Whalen (1971) to identify the variance of simultaneous estimates. To achieve this, the matrix, γ, is constructed such that

$$\gamma = \mathbf{A}^\top \mathbf{C}_\mu^{-1} \mathbf{A} + \frac{1}{\mu}\mathbf{I}, \tag{3.42}$$

where $\mathbf{I}$ is the identity matrix of order N_{states}. The elements of γ are therefore the second derivatives of the expression for the χ^2 of the model. The uncertainty is then given by the diagonal elements,

$$\sigma_n = \left[(\gamma^{-1})_{nn}\right]^{1/2}. \tag{3.43}$$

In regions of the model where the local density of "points" greatly exceeds N_0, the uncertainty calculation can diverge. When this occurs, an approximation to the uncertainty can be made by replacing the values of $(\gamma^{-1})_{nn}$ with the reciprocals of the non-inverted form, $1/\gamma_{nn}$. This is equivalent to the Cramér-Rao lower bound for the uncertainty.

Calculating the uncertainty for every position in the data hypercube would be a computationally prohibitive task. As such, the uncertainty is instead calculated for the highest value of the column density in each tile, and for the central value of the tile after it has been smoothed by a large spatial filter, providing a measure of the uncertainty of the background. Uncertainties for the remaining elements within a tile, and between neighbouring tiles, are then interpolated assuming Poisson noise.

A 2D map of the reduced χ^2 for each sub-tile is also written out, along with other 2D secondary data products. Their production, along with a more detailed overview of the structure of the 4D data hypercubes, is given in Section 3.1.4.

3.1.4 The Structure of PPMAP Data Products

As briefly described above, PPMAP outputs a number of multi-dimensional data products, designed for easy analysis. These can be considered in broad categories consisting of primary products, which provide information about the model directly, secondary or derived products, which are lower dimensionality products derived from from the primary products, or from additional information about the model, and supplementary products, which I produce from combinations of primary and secondary products. Each data product is explained in more detail below.

3.1.4.1 Primary Products

The first of the primary data products is the 4D column density hypercube, with two positional dimensions, (x_i, y_j), a dimension representing the opacity index grid, β_k, and a dimension representing the associated temperature grid, T_l. Thus, any given element of the hypercube gives the expectation value of the column density at a given position, β, and temperature.

As 4D data cubes are hard to visualise, I typically marginalise out the β or temperature dimensions in turn, producing a pair of 3D data cubes describing the distribution of column density as functions of line-of-sight temperature or opacity index, respectively. These cubes can then be viewed as a series of 2D images. To obtain a cube of the column density variations with line-of-sight temperature, I sum the column density over all discrete values of β, such that

$$N_{\mathrm{H}_2;l} = \sum_k \left\{ N_{\mathrm{H}_2;kl} \right\} . \tag{3.44}$$

Similarly, if I wish to examine the how the distribution of column densities varies with the line-of-sight β variations, I sum over the discrete values of the temperatures,

$$N_{\mathrm{H}_2;k} = \sum_l \left\{ N_{\mathrm{H}_2;kl} \right\} . \tag{3.45}$$

The next primary data product is the hypercube of the uncertainty in the column density estimates. This product is also four dimensional, providing the uncertainty in the column density estimate at every position, temperature, and β. As before, it is often useful to reduce the dimensionality of the hypercube. This is done by summing in quadrature along one axis;

$$\sigma_{l|k} = \left(\sum_{k|l} \left\{ \sigma_{kl}^2 \right\} \right)^{1/2} . \tag{3.46}$$

3.1.4.2 Secondary Products

The fist of the secondary products is the 2D map of total column density across all temperatures and opacity indices. This is produced by PPMAP by marginalising out both the temperature and β dimensions of the 4D column density hypercube, via the equation

$$N_{\mathrm{H}_2} = \sum_{k=0}^{k=n} \sum_{l=0}^{l=m} \left\{ N_{\mathrm{H}_2;kl} \right\} . \tag{3.47}$$

This map is analogous to the column density maps produced by MBB fitting algorithms.

The next two secondary products are the maps of column-density-weighted (or mass-weighted), mean line-of-sight temperature and β. These are analogous to the maps of dust temperature produced through MBB fits, though it should be noted that MBB fitting produces a flux-weighted temperature, not a column-density-weighted temperature. These products are produced through the equations

$$\bar{\beta} = \frac{1}{N_{\mathrm{H}_2}} \sum_{l=0}^{l=m} \sum_{k=0}^{k=n} \left\{ \beta_k N_{\mathrm{H}_2;kl} \right\} , \tag{3.48}$$

$$\bar{T} = \frac{1}{N_{\mathrm{H}_2}} \sum_{l=0}^{l=m} \sum_{k=0}^{k=n} \left\{ T_l N_{\mathrm{H}_2;kl} \right\} . \tag{3.49}$$

3.1.4.3 Supplementary Products

During my analysis of PPMAP data, I found it useful to construct maps of the total uncertainty, to complement the total column density maps, and maps of signal-to-noise ratio. The total uncertainty map was produced by summing in quadrature over both the temperature and β dimensions of the uncertainty hypercube with the equation

$$\sigma = \left(\sum_{l=0}^{l=m} \sum_{k=0}^{k=n} \left\{ \sigma_{kl} \right\} \right)^{1/2} . \tag{3.50}$$

From this 2D map of uncertainty, I produce a map of the Point Process Statistical Degeneracy (PPSD). The PPSD is a measure of the statistical degeneracy

inherent in the Point Process method. A large value of the PPSD indicates that there is a small number of possible "states" that reproduce the input data well, and so the expectation value has a small uncertainty. Conversely, a small value of the PPSD indicates that there is a large number of states that reproduce the input data, and hence the expectation value of the model (the estimate of the H_2 column density in the case of PPMAP) has a large uncertainty. The PPSD is calculated through the equation

$$\mathrm{PPSD} = \frac{N_{\mathrm{H_2}}}{\sigma}. \tag{3.51}$$

3.1.5 A Note on Degrees of Freedom and Unique Solutions

A common query of PPMAP is to ask how it is capable of producing a dust model with seemingly many more free parameters (the number of discrete dust temperature bins multiplied by the number of discrete dust opacity bins) than the set of input observations (typically five Herschel bands and one SCUBA-2 band)? Certainly, for conventional MBB fitting techniques where the parameters (column density, dust temperature, and potentially dust opacity index) are all fitted simultaneously, it is vitally important that there are an equal or greater number of observation bands.

The answer to this question requires a shift in perspective. PPMAP is not attempting to constrain a single underlying SED with a large number of free dust temperature and opacity index parameters at each pixel with a small number of input bands. Instead, it is creating a smooth dust model, spanning a range of theoretically continuous dust temperatures and opacity indices. This model represents the probability-weighted average (expectation) of all possible dust distributions given the current information in any given iteration. The emission from the model is compared to the input observations, and the comparison to each band is used to update the model.

The number of observation bands has an effect on the probability of the model which is analogous to the effect the diameter of a telescope mirror has on the resolution of images produced by that telescope. Increasing the number of observations more tightly constrains the likelihood of the current model, diminishing the chances that another dust distribution is responsible for the observed emission.

The division of the continuous temperature and opacity index ranges into discrete bins is, therefore, analogous to gridding the continuous emission from the night sky onto a set of pixels. Thus, increasing or decreasing the number of temperature or opacity index bands is equivalent to resampling an existing pixelated image onto a

different pixel grid. As with image resampling, care should be taken to appropriately sample the temperature and opacity index dimensions to not over- or under-sample the model.

A second concern that has been raised regarding the algorithm is that the models it produces may not be unique solutions. With so many ways to distribute dust throughout a model, there may be many configurations which could produce very similar emission maps. As with the question regarding degree of freedom, the answer here is that the models PPMAP produces are the averages of all possible models, weighted by how likely they are to occur. This expectation solution is, by definition, always unique.

Information regarding how likely other, similar distributions are to produce similar emission maps, and how well sampled the model is, are encoded in the uncertainty hypercube and supplementary maps, as well as the reduced chi squared value produced for each band.

While PPMAP has a number of metrics which help to define how well constrained a model is, application of appropriate synthetic tests can go further to ensuring that the algorithm is performing as expected. A selection of tests coving this and other aspects of PPMAP are presented in Chapter 4.

Chapter 4
PPMAP: Testing and Limitations

In this chapter, I present a series of tests that I have performed to establish PPMAP's accuracy and limitations. I demonstrate a method for recovering the input observations from PPMAP column density data hypercubes, and show that PPMAP better estimates the contribution from each of the *Herschel* observation bands to the H_2 column density than conventional MBB fitting techniques. I develop a series of synthetic observations derived from model filaments to demonstrate that PPMAP is able to accurately estimate the column density of dusty, astrophysical structures, and that it is able to lift the dust temperature and dust opacity index degeneracy observed with standard MBB fitting routines.

4.0.1 Recovery of Observed Flux Density

After producing a dust model from a multi-band set of observed maps, PPMAP provides the user with an estimate of how closely this model matches each observation band. This estimate is in the form of a mean reduced χ^2 across the entire region. However, it is important to verify the validity of PPMAP models externally to the program. This is done by producing synthetic images from the dust column density hypercube.

In this test, I utilise the equation of radiation transport to derive a value of monochromatic flux density at every sky location in the PPMAP output in a number of observation bands. Colour corrections are applied during the process, and the resultant intensity maps are convolved with appropriate instrument beam profiles before being re-sampled at rates consistent with the original input observations. This allows for a pixel by pixel comparison between the synthetic observations recovered from PPMAP, and the actual observed maps.

For a given waveband specified by its nominal wavelength, λ, the surface brightness, I_λ for at a specific sky location is given by

$$I_\lambda = \sum_{i,j}^{n} N_{H_2:T_i,\beta_j} \cdot \bar{\mathrm{m}}_{H_2} \cdot \kappa_{300\,\mu\mathrm{m}} \left(\frac{\lambda}{300\,\mu\mathrm{m}} \right)^{-\beta_j} B_\lambda(T_i) \cdot K(T_i). \tag{4.1}$$

Here $N_{\mathrm{H_2}:T_i,\beta_j}$ is the number column density of hydrogen molecules assigned to T_i and β_j, while $\bar{m}_{H_2}$ is the mean mass of a hydrogen molecule in grams. $B_\lambda(T_i)$ is the value of the Planck function in a given PPMAP temperature band T, in MJy/sr, and $K(T_i)$ is the colour correction factor for that band.

The term

$$\kappa_{300\,\mu\mathrm{m}} \left(\frac{\lambda}{300\,\mu\mathrm{m}} \right)^{-\beta_j} \tag{4.2}$$

gives the opacity of gas and dust at wavelength, λ, for a given opacity index band, β_j. $\kappa_{300\,\mu\mathrm{m}}$ is the reference opacity at 300 µm, with a value of $0.1\,\mathrm{cm^2\,g^{-1}}$.

The result is a series of surface brightness maps at the resolution of the PPMAP model, in a number of wavebands. I then convolve the synthetic images with the observation beam profiles with the Python `astropy.convolve.convolve_fft` package, before utilising the `reproject` package to resample the images to the native sample rates of their equivalent true observations.

Figure 4.1 shows the result of this process on the Taurus L1495 molecular cloud region in four *Herschel* bands from 160 µm to 500 µm. The recovered surface brightness observations are displayed in the left hand column, while the true observations used to derive the PPMAP dust model are displayed in the middle column. The PPMAP dust model is discussed in detail in Chapter 5. The synthetic observations in the rightmost column are derived from single temperature MBB estimates of column density. Their generation is discussed in Section 4.0.1.1. It can be clearly seen that the reproduction of *Herschel* observations from the PPMAP dust model is very faithful to the real observations in all displayed bands, indicating that PPMAP produces a model that is an extremely good fit to the input data. By comparison, the MBB fitting technique overestimates the flux contribution from shorter wavelength bands by a large factor. These differences are assessed quantitatively in the following Sections.

4.0.1.1 Flux Recovery from MBB fitting

It is important to verify that not only can accurate surface brightness maps be recovered from PPMAP column density models, but that these recovered surface

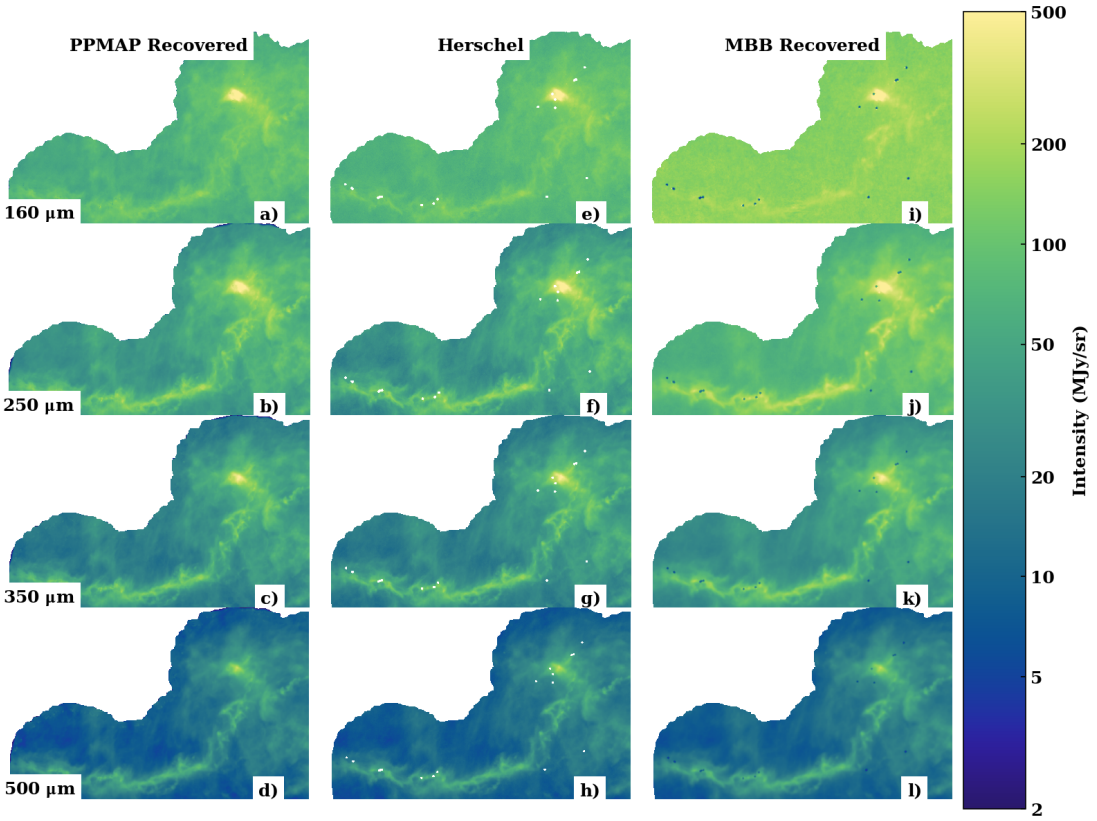

Figure 4.1. A comparison of recovered surface brightness from PPMAP dust models, presented as synthetic observations, (left) with the true *Herschel* observations used to derive the model (middle). A further comparison with surface brightness recovered from a MBB fitter (right) provides a reference point for standard fitting techniques. The images are compared across four wavebands from 160 µm (top) to 500 µm (bottom). All images share a common surface brightness colour scale. The observations recovered from the PPMAP model (left) are clearly visually very similar to the true *Herschel* observations (middle) across all bands. In contrast, the MBB recovered observations clearly greatly overestimate the surface brightness of the 160 µm and 250 µm bands, though they are a good match to the longer wavelength observations.

brightness maps are better than those recovered from leading MBB fitting techniques.

The process to produce synthetic maps from MBB estimates of H_2 column density and dust temperature is simpler than the one for PPMAP. The MBB fitting process produces a single value of column density and temperature at each sky location, and does so for a single fixed value of β. Thus, Eq. 4.1 becomes

$$I_\lambda = N_{H_2} \cdot \bar{m}_{H_2} \cdot \kappa_{300\,\mu\mathrm{m}} \left(\frac{\lambda}{300\,\mu\mathrm{m}} \right)^{-2} B_\lambda(T) \cdot K(T). \tag{4.3}$$

This equation is equivalent to Eq. 4.1 for a model with a single line of sight temperature and β value. As before, the synthetic flux density maps derived from Eq. 4.3 are then convolved with the appropriate *Herschel* beam profiles, and reprojected to the sample rate of the true observations.

4.0.1.2 The Goodness of Fit Parameter

While the maps of synthetic flux density shown in Figure 4.1 allow one to qualitatively compare flux recovered from different fitting techniques in different observational bands, they are not able to show, quantifiably, which technique produced superior fits, or which bands prove difficult to recover. To that aim, we produce a "goodness of fit" parameter, $\mathcal{G}$, which is given by the expression

$$\mathcal{G} = \left(\frac{\sum_{\mathrm{PIXELS}} \left\{ I_{\mathcal{B},\mathrm{true}}^{-1} \left(I_{\mathcal{B},\mathrm{synth}} - I_{\mathcal{B},\mathrm{true}} \right)^2 \right\}}{\sum_{\mathrm{PIXELS}} \left\{ I_{\mathcal{B},\mathrm{true}} \right\}} \right)^{1/2}. \tag{4.4}$$

Here, $I_{\mathcal{B},true}$ is the true observed surface brightness in band $\mathcal{B}$, while $I_{\mathcal{B},synth}$ is the synthetic flux density in the same band. Therefore, $\mathcal{G}$ is the root mean square fractional difference between the synthetic and true maps of any given band, with the contribution from each pixel weighted by the true flux density within that pixel. Smaller values of $\mathcal{G}$ indicate smaller deviations between the synthetic and true observations, with a value of $\mathcal{G} = 0$ indicating an exact match.

Table 4.1 gives the $\mathcal{G}$ values for the bands shown in Figure 4.1 for synthetic observations recovered from both the PPMAP algorithm and the MBB fitting technique described in Palmeirim et al. (2013). In all bands, synthetic observations recovered from PPMAP models are a closer fit to the true observations than those recovered from the MBB fitting technique. This is particularly evident in both the 160 µm and 250 µm bands.

Table 4.1. Goodness of fit, $\mathcal{G}$ values for the synthetic observations shown in Figure 4.1, recovered from modles produced by PPMAP and the MBB fitting technique described in Palmeirim et al. (2013) for the L1495 molecular cloud. Lower values of $\mathcal{G}$ indicate a better fit to the true observations in each band.

Band (µm)	$\mathcal{G}_{PPMAP}$	$\mathcal{G}_{MBB}$
160	0.23	1.05
250	0.11	1.02
350	0.08	0.37
500	0.08	0.09

The L1495 synthetic observations and $\mathcal{G}$ values are further discussed and expanded upon in Section 5, while observations and values for the Ophiuchus field are analysed in Section 6.

4.0.2 Accurate Column Density and Temperature Estimation

While testing that accurate synthetic observations can be recovered from PPMAP dust models helps to ensure the fidelity of the results, it is also important to verify that PPMAP can correctly recover known dust column density and temperature results when given observations of a synthetic filament. This is because while a dust model may produce a good fit to the input observations, this many not be a unique solution. Generally, when fitting dust column density and temperature, the two variables are partially degenerate, and lower estimates of the dust mass can be compensated for by an increase in temperature, or vice versa. Here I present the results of a series of tests to determine whether the PPMAP dust model is accurate. As the introduction of a variable dust opacity index, β, brings another degeneracy, a fixed value of $\beta = 2$ was utilised throughout the tests. An investigation into PPMAP's ability to lift the temperature-β degeneracy is presented in Section 4.0.3.

For this test, I construct a synthetic filament with a Plummer-like density profile given by

$$n_{\mathrm{H_2}}(r) = 10^4 \mathrm{H_2 cm^{-3}} \left\{1 + (r/0.04\mathrm{pc})^2\right\}^{-1}, \tag{4.5}$$

and an inverse Plummer-like temperature profile given by

$$T(r) = 10\mathrm{K} \left\{1 + (r/0.04\mathrm{pc})\right\}^{0.125}. \tag{4.6}$$

I choose the outer radius of the filament to be 0.4 pc, an order of magnitude

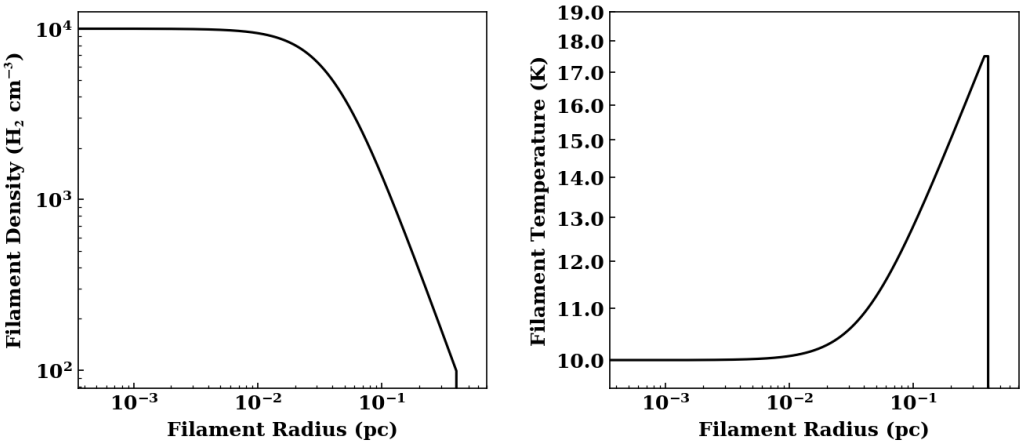

Figure 4.2. The synthetic filament number density (left) and temperature (right) models. From these continuous models, the local density and temperature of the filament could be calculated, and thus the contribution to the line of sight column density, mass weighted mean temperature, and surface brightness. These parameters were determined with a stepwise integrator for a range of impact parameters.

larger than the inner radius. The filament is placed in a diffuse cloud with a uniform column density of $1 \times 10^{20}\,\mathrm{H_2\,cm^{-2}}$, and a uniform temperature of 17.5 K. The background extends out to 1 pc to either side of the filament. The filament is axially symmetric and is placed at a nominal distance of 140 pc. Figure 4.2 shows the filament density and temperature profiles as a function of radius.

I construct a stepwise integrator to perform simple radiation transport, assuming an optically thin regime. The integrator determines the surface brightness, $I_\lambda(b)$ for a given position at a given impact parameter, b in a particular observational wavelength through the equation

$$I_\lambda(b) = \int_{s=0.40\mathrm{pc}}^{s=-0.40\mathrm{pc}} N_{\mathrm{H_2}}(s)\bar{m}_{\mathrm{H_2}}\kappa_0 \left(\frac{\lambda}{\lambda_0}\right)^{-2} \{B_\lambda(\lambda, T(s)) - I_\lambda(s)\}\, ds \qquad (4.7)$$

where $N_{\mathrm{H_2}}(s)$ is the molecular hydrogen column density at position s along the line of sight, which is then added to the background column density. κ_0 is the PPMAP reference opacity at 300 µm, and $T(s)$ is the dust temperature at position s. This process is then repeated for all values of the impact parameter, b. A diagram of how s relates to the impact parameter, b, and the filament radius, r, is shown in Figure 4.3.

This produces an array of surface brightness values spanning an impact parameter range from $b = 0$pc to $b = 0.40$ pc, with $1''$ resolution. To produce a filament-like structure, the array is mirrored around $b = 0$ pc, and duplicated to elongate the structure parallel to the filament axis. The resultant filament is 0.80 pc in diameter, and

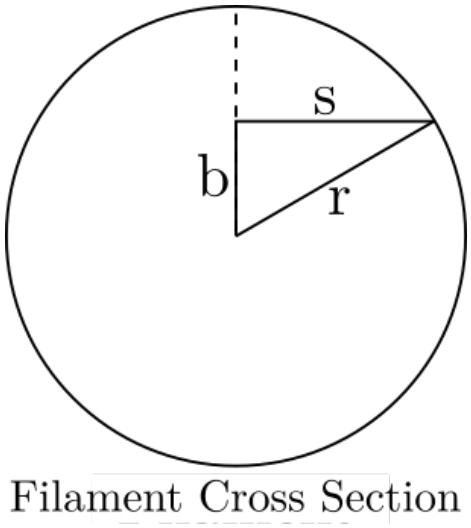

Figure 4.3. The relation between s, denoting a position within the filament as measured along the line of sight to the observer, the impact parameter, b, and the filament radius, r.

0.80 pc long.

Synthetic *Herschel* observations were then produced from monochromatic 1″ surface brightness maps at 70 µm, 160 µm, 250 µm, 350 µm and 500 µm, by convolving them with the appropriate beam profiles, and resampling them to the standard sample rates of PACS and SPIRE observations. I added Gaussian noise to the observations such that the standard deviation was equal to a peak signal-to-noise ratio of 100.

These observations were run through PPMAP. The input parameters are given in Table 4.2. While PPMAP can, in principle, super-sample the input observations at any resolution given good signal-to-noise, in practice PPMAP is limited by the highest resolution observation (70 µm at ∼14″ for *Herschel* fast scan speeds). In addition, as the 70 µm band generally contains relatively little information about a system emitting between 10 K to 20 K, it is often beneficial to ensure that the PPMAP resolution is equal to or coarser than the two finest observations. As such, a resolution for the final dust model of 16″ (with 8″ Nyquist sampled pixels) was chosen, as this is equivalent to the 160 µm resolution. The total mass of the model filament and background within the chosen PPMAP field of view is 17.8 $M_\odot$.

Figure 4.4 compares the PPMAP estimated model with the true distribution of the synthetic filament, split into the ten PPMAP temperature bands. PPMAP performs well, recovering column density in each band close to the true distribution, with the exception of the bands between 7.0 K to 10.7 K. In the lower three of these bands, PPMAP distributes ∼1.7 $M_\odot$ of material in a region along the filament spine, where there is no dust present in the true model. A further ∼1.6 $M_\odot$ of material is then attributed to the fourth band, a quantity significantly lower than the ∼3.8 $M_\odot$

Table 4.2. The PPMAP input parameters for the column density test. Parameters with list values are shown here separated by commas, but are to be separated by whitespace when running PPMAP. A description of each parameter is given in Chapter 3. The Herschel.txt colour correction table is given in Appendix A.

Parameter	Value
`gloncent`	0.0
`glatcent`	0.0
`fieldsize`	0.5, 0.5
`pixel`	8
`dilution`	0.3
`maxiteration`	10000
`distance`	140.0
`kappa300`	0.1
`nbeta`	1
`betagrid`	2.0
`betaprior`	2.0, 2.5
`Nt`	10
`temperature`	7.0, 25.0
`ncells`	40
`noverlap`	20
`ccfile`	Herschel.txt
`nbands`	5

present in the fourth temperature band of the model. However, the total contribution to the mass of the filament is approximately the same, as can be seen in the cumulative mass function shown in Figure 4.5. PPMAP estimates $\sim 7\%$ more total mass than that present in the model when summed over all bands.

A small, square artefact can be seen to the right hand side near the spine of the filament in the PPMAP model. This can be explained by interference fringing produced when PPMAP resamples the observations, creating minor variations in the exact location of the filament spine in each one, relative to the model grid. These variations are propagated to individual PPMAP tiles, and artefacts appear in tiles where the observations and the model grid are most misaligned. This is unlikely to happen with observations of true astrophysical structures as the underlying shape of the structures is unlikely to be aligned with the pixel grid.

Figure 4.6 and Figure 4.7 compare the model filament total column density and mass weighted mean line of sight temperature with PPMAP. It is important to present both total column density and mass weighted mean line of sight temperature in addition to the temperature dependent column density cube as they are most similar to the outputs of traditional modified black body fitting routines. Here we can see the total PPMAP column density accurately predicts the high density central

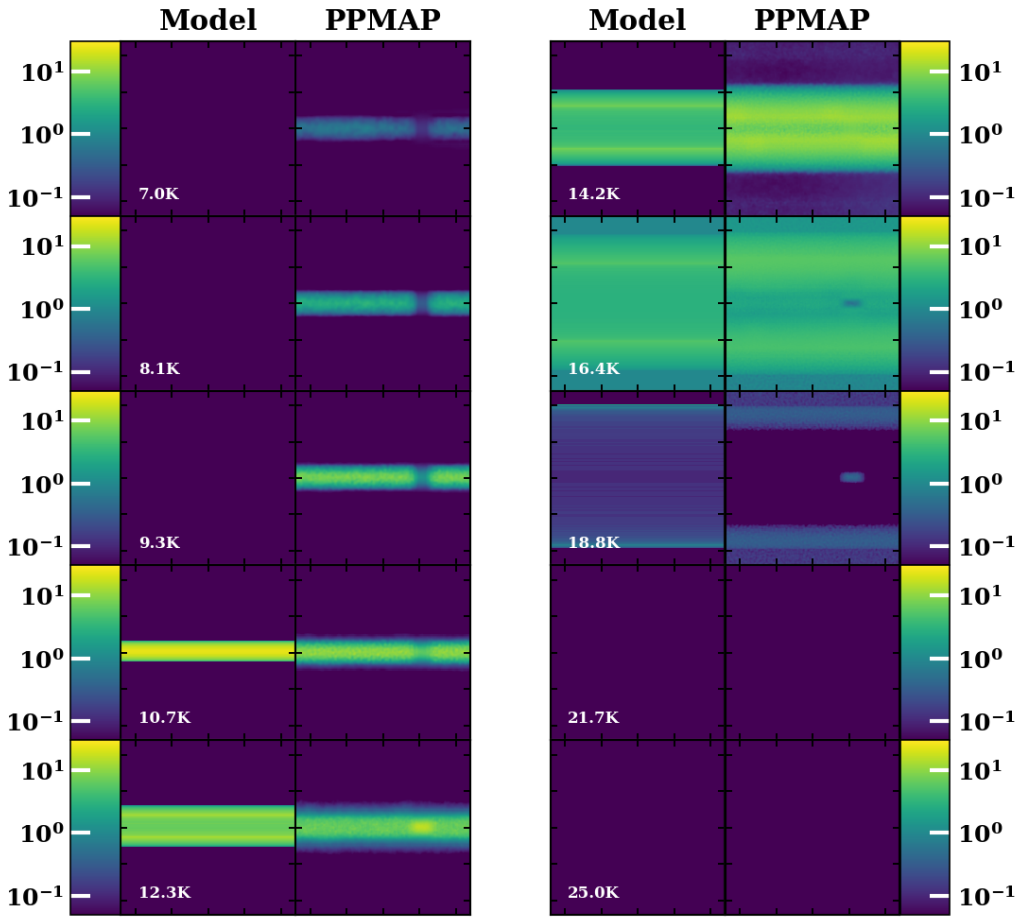

Figure 4.4. The 10 panel column density cube for the model filament compared with the estimated dust model cube produced by PPMAP. PPMAP has populated the lowest three temperature bands where the model contains no column density, and has a reduced column density in the fourth band with respect to the model. However, Figure 4.5 indicates that this has not greatly affected the total mass distribution.

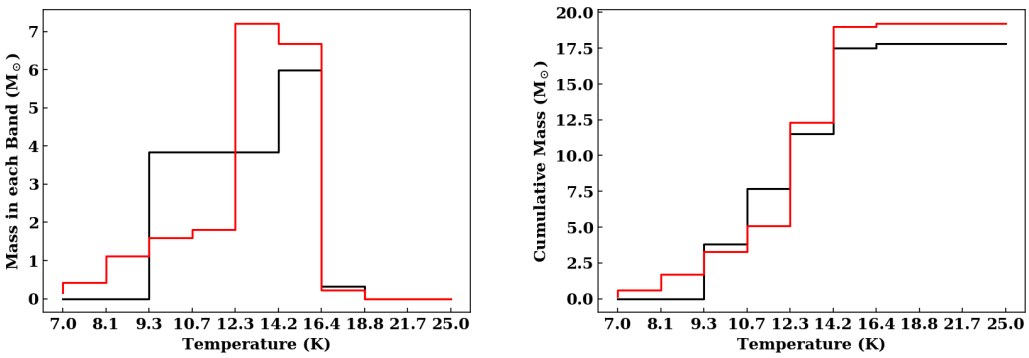

Figure 4.5. The mass and cumulative mass functions of the model filament (black) and the PPMAP estimated dust model (red) in each of the ten temperature bands, given in solar masses. The PPMAP overestimation in the first three bands is largely offset by the underestimation in the fourth band. PPMAP recovers a total mass just 7% more than the model.

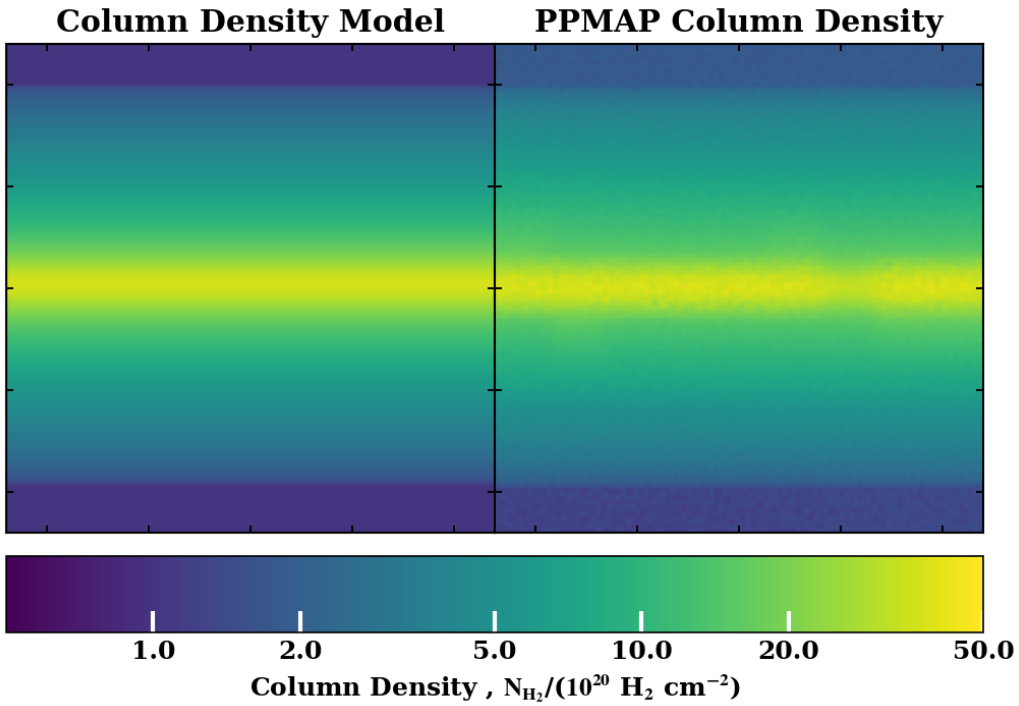

Figure 4.6. The total column density of the model (left) and of the PPMAP estimated dust model (right). It is clear here that there is very little difference between the true model and the PPMAP output.

filament, and replicates the profile of the column density from spine to edge. In addition, it is able to predict accurately the background column density. This is also true of the mass weighted mean line of sight temperature map.

4.0.2.1 Column Density Estimation with a MBB Fitting Routine

Not only should PPMAP be tested to ensure it can accurately predict column densities and temperatures from a known synthetic filament, but it is important to verify that it can do so at least as well as conventional MBB fitting techniques. To verify this, I pass the synthetic observations described above to an algorithm derived from the techniques described in Palmeirim et al. (2013). This technique fits a single temperature modified black body to the 160 µm, 250 µm, 350 µm and 500 µm *Herschel* bands, and uses spatial filtering to recover the 18″ resolution of the 250 µm band. As with many *Herschel* MBB fitters, it excludes the 70 µm observations.

The resulting column density and flux weighted mean line of sight temperature maps are shown in Figure 4.8 and Figure 4.9 respectively. The algorithm recovers $\sim 70\%$ of the column density in the spine of the filament, and has difficulty distinguishing the diffuse outer regions of the filament from the background, leading to a

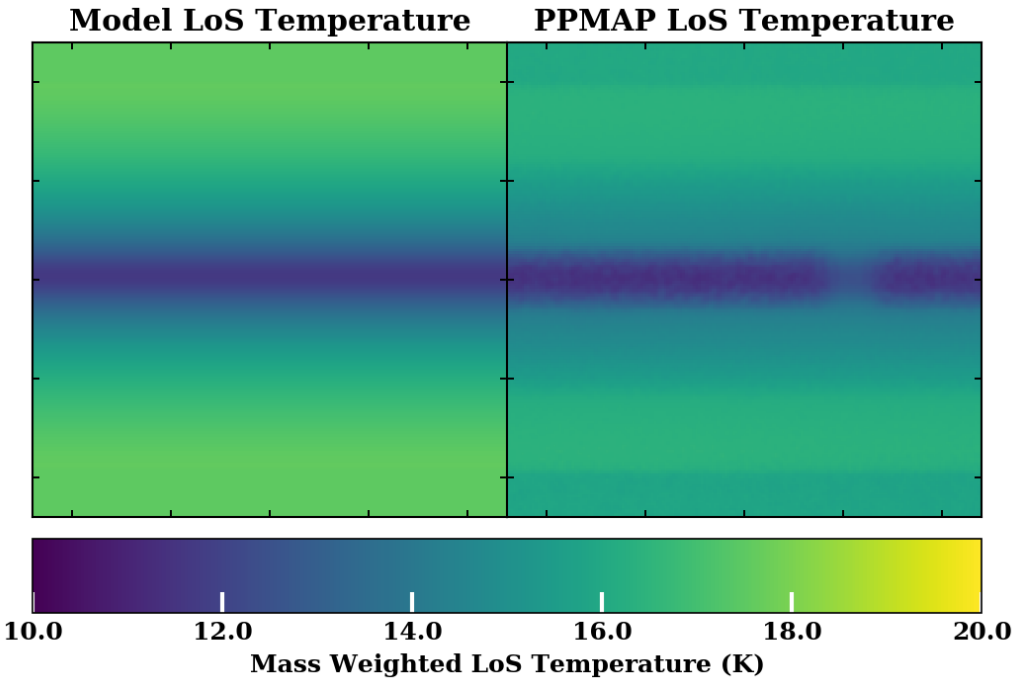

Figure 4.7. The mass weighted mean line of sight temperature of the model (left) and of the PPMAP estimated dust model (right). Here, too, the temperature maps match well.

much narrower profile. The background itself has very little column density associated with it. This is likely due to the exclusion of the 70 µm observation, which contains information about the warmer medium in the filament wings and surrounding medium.

In contrast, the temperature estimation is accurate in the filament wings and background, but is several degrees too high at the filament spine. However, it should be noted that the temperature maps produced by MBB fitting techniques are flux weighted, and so are more sensitive to brighter, warmer regions, and not mass weighted, which would tend to favour the denser, colder environments.

4.0.3 β and Temperature Correlations

PPMAP is designed to break the apparent anti-correlation between the effects of changes in temperature and β seen in *Herschel* observations at 10 K to 20 K.

To verify this, I construct a test composed of two axially symmetric filaments, with Plummer-like density profiles given by

$$n_{\mathrm{H_2}}(r) = 10^4 \mathrm{H_2 cm^{-3}} \left\{1 + (r/0.04\mathrm{pc})^2\right\}^{-1} \tag{4.8}$$

as above, and linear temperature profiles given by

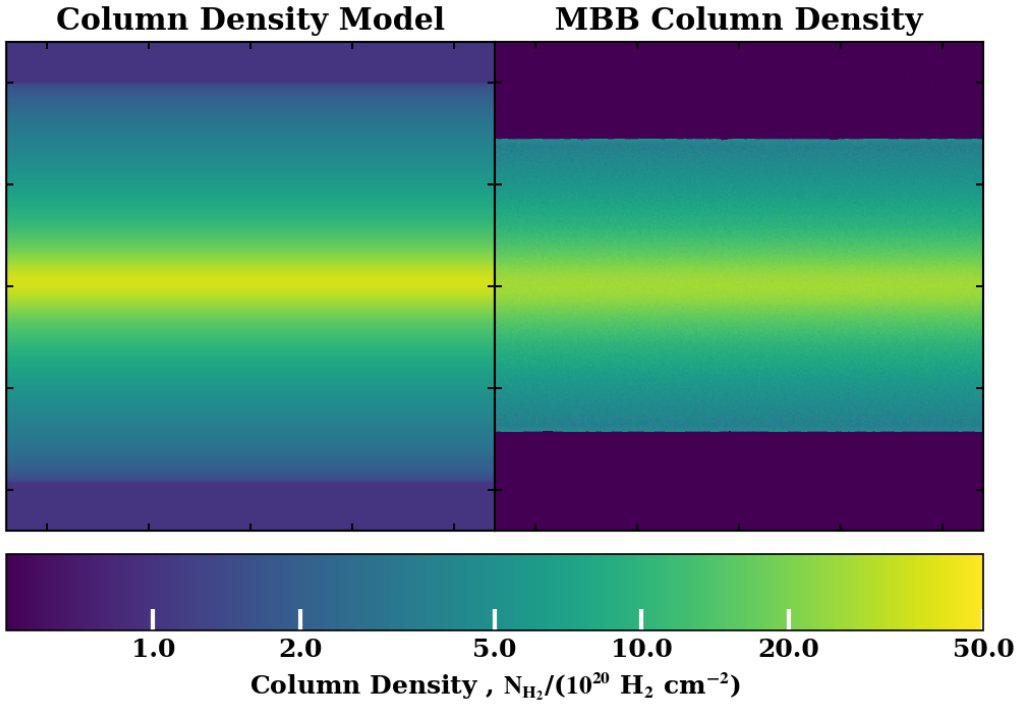

Figure 4.8. The total column density of the model (left) and of the column density estimate produced by a leading MBB fitting routine (right). While much of the filament is well reproduced, the column density through the central spine estimated by the MBB fitter is just $\sim 65\%$ of central column denisty of the model. In addition, the MBB fitting routine failed to differentiate the less dense regions of the filament from the surrounding background, and also failed to fit the background at all, leading to poor estimates of the column density. This is likely due to missing information otherwise provided by the 70 µm emission, which is not taken into account with traditional MBB fitters.

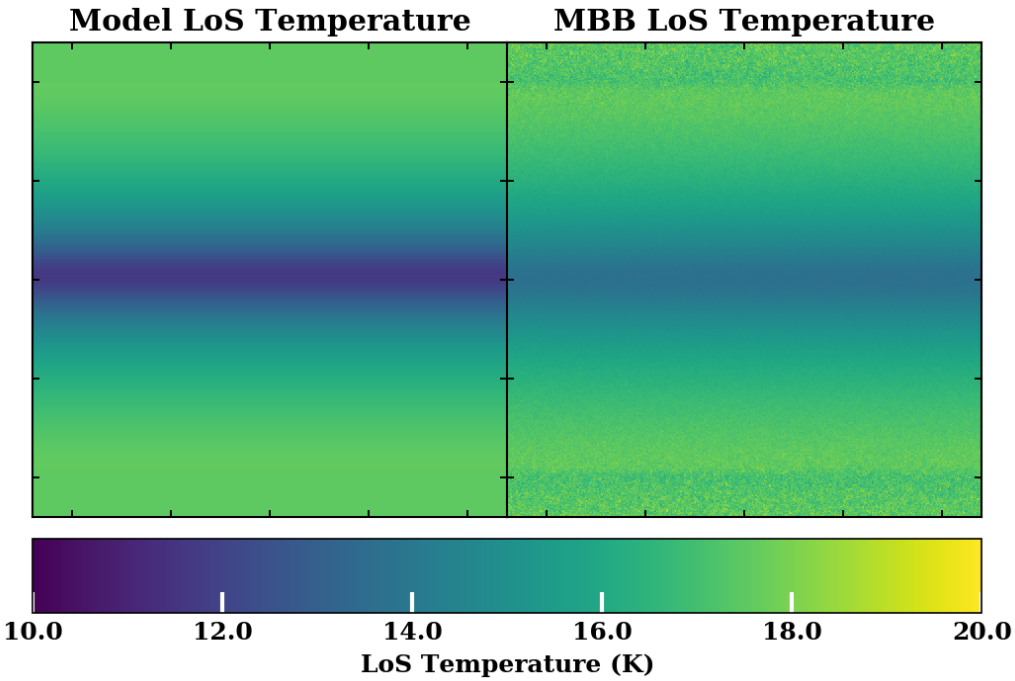

Figure 4.9. The mass weighted mean line of sight temperature of the model (left) and of the flux weighted mean line of sight temperature produced by a leading MBB fitting routine (right).

$$T(r) = 10\text{K} + 10\text{K}(r/0.40\text{pc}). \tag{4.9}$$

One of the filaments, the "correlated" filament, is given a positive linear β profile

$$\beta(r) = 1 + (r/0.40\text{pc}) \tag{4.10}$$

while the second filament, the "anti-correlated" filament, has a negative linear β profile

$$\beta(r) = 2 - (r/0.40\text{pc}). \tag{4.11}$$

The model profile is then imposed on a diffuse background with a column density of $1 \times 10^{20}\,\text{H}_2\,\text{cm}^{-2}$, an opacity index of 1.0 in the anti-correlated case, an opacity index of 2.0 in the correlated case, and a temperature of 20 K. The background extends out to 1 pc from the filament centre.

Radiation transport is employed to calculate the surface brightness of the filaments, assuming an optically thin regime. This surface brightness at a given impact parameter, b, is given by

$$I_\lambda(b) = \int_{s=0.40\mathrm{pc}}^{s=-0.40\mathrm{pc}} N_{\mathrm{H}_2}(s)\bar{m}_{\mathrm{H}_2}\kappa_0 \left(\frac{\lambda}{\lambda_0}\right)^{-\beta(s)} \{B_\lambda(\lambda, T(s)) - I_\lambda(s)\}\, ds \qquad (4.12)$$

where $N_{\mathrm{H}_2}(s)$, $\beta(s)$, and $T(s)$ are the hydrogen column density, β, and temperature of dust in the filament at a given distance, s, along the line of sight from the centre of the filament. The angular resolution of the radiation transport routine is set to $1''$.

As above, this produces an array of surface brightnesses spanning an impact parameter range from $b = 0\,\mathrm{pc}$ to $b = 0.40\,\mathrm{pc}$. To produce a filament-like structure, the array is mirrored around $b = 0\,\mathrm{pc}$, and duplicated to elongate the structure to left and right. The resultant filaments are 0.80 pc in diameter, and 0.80 pc long. Synthetic *Herschel* observations are produced as for the column density test. An additional synthetic band at 850 µm is produced in a nearly identical manner, but is convolved with the appropriate beam from the JCMT SCUBA-2 instrument. I add Gaussian noise to the observations such that the peak signal-to-noise was 100.

4.0.3.1 Tests with the five *Herschel* bands

These synthetic observations were passed through PPMAP, with input parameters given in Table 4.3, in the column marked "Cold". The results were then analysed by taking a Gaussian kernel density estimate (KDE) of the column density-weighted, line of sight mean dust temperature and β maps for both the "correlated" and "anti-correlated" filaments. These KDEs are shown in Figure 4.10. Performing a Pearson Correlation Test on the data gave a quantitative review of the degree of correlation in each case.

PPMAP performs well at identifying the "correlated" filament, but poorly at picking out an anti-correlation between β and temperature. I believe this is because for the "correlated" case, the true correlation works to weaken the degeneracy inherent in the *Herschel* bands at low temperatures, producing synthetic images with observational anti-correlations that are weaker than those produced by a model with no physical correlation. The only way PPMAP can achieve a good response to such observations is with a strongly correlated dust model.

However, in the "anti-correlated" filament, the effects of the degeneracy are reinforced observational anti-correlations which could be the result of either an anti-correlated model, or an un-correlated model. PPMAP becomes unable to produce a model that is a good fit to the available data. A positive correlation is observed in the Gaussian KDE, covering a very narrow range of temperatures and β values, clustering near the mean value of the β prior.

Table 4.3. The PPMAP input parameters for the correlated β and temperature tests. Parameters with list values are shown here separated by commas, but are to be separated by whitespace when running PPMAP. Parameters in brackets are for tests including the 850 µm band. A description of each parameter is given in Chapter 3. The Herschel.txt and Herc850.txt colour correction tables are given in Appendix A.

	Cold	Hot
Parameter	Value	
`gloncent`	0.0	0.0
`glatcent`	0.0	0.0
`fieldsize`	0.5, 0.5	0.5, 0.5
`pixel`	8	8
`dilution`	0.3	0.3
`maxiteration`	10000	10000
`distance`	140.0	140.0
`kappa300`	0.1	0.1
`nbeta`	5	5
`betagrid`	0.9, 1.2, 1.5, 1.7, 2.1	0.9, 1.2, 1.5, 1.7, 2.1
`betaprior`	1.5, 0.25	1.5, 0.25
`Nt`	13	13
`temperature`	9.0, 21.0	19.0, 31.0
`ncells`	40	40
`noverlap`	20	20
`ccfile`	Herschel.txt (Herc850.txt)	Herschel.txt (Herc850.txt)
`nbands`	5 (6)	5 (6)

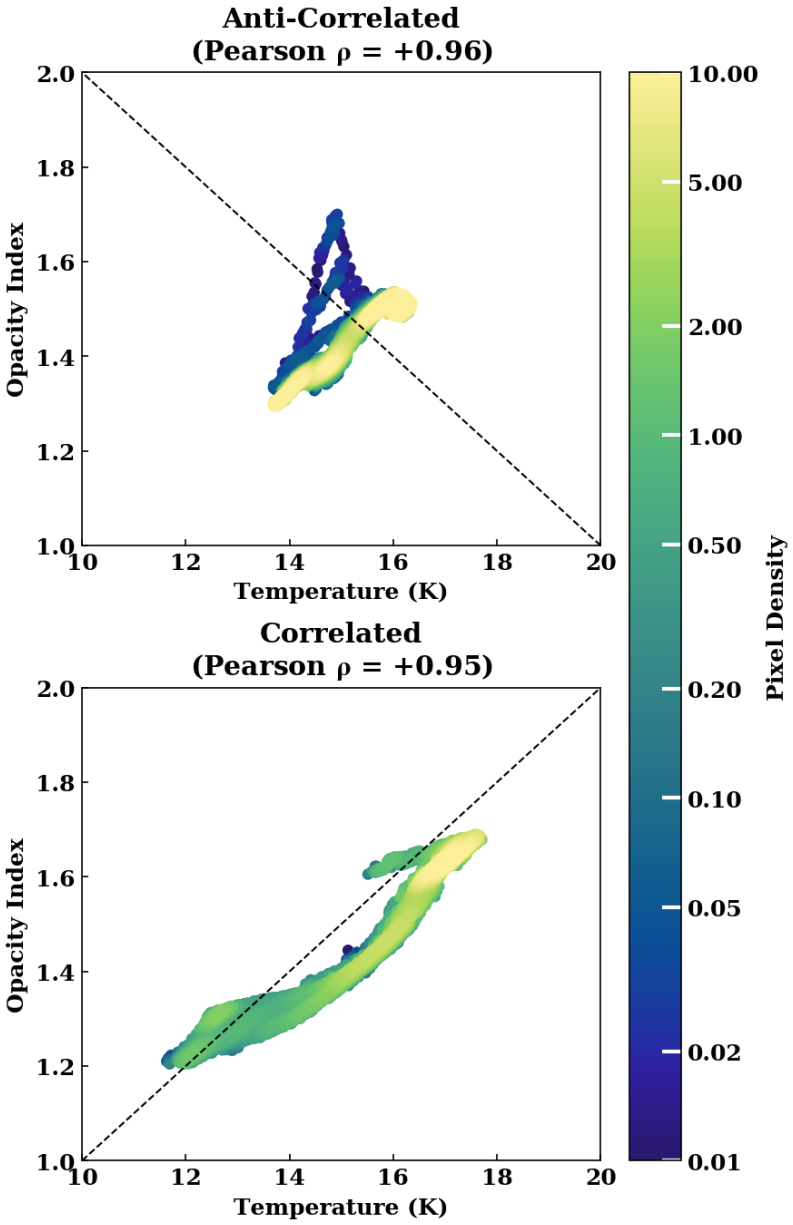

Figure 4.10. 2D KDE of the measured correlations between temperature and β estimates for the T_{cold} synthetic filament observed only with five synthetic *Herschel* bands. The colour scale gives the estimated density of pixels corresponding to a given value of temperature and β, derived from the KDE. The Pearson p value is vanishingly small.

To test this hypothesis, I produce a second set of filaments with identical density and β profiles, but with higher temperatures, given by the profile

$$T(r) = 20\mathrm{K} + 10\mathrm{K}(r/0.40\mathrm{pc}). \tag{4.13}$$

This shifts the observations far into the Rayleigh-Jeans tail of the modified Planck function, where values of β are better encoded, and the observational degeneracy is naturally broken. The production of synthetic observations was identical to that described above, and the PPMAP input parameters were identical, save for a different range of temperatures, given in Table 4.3 by the "Hot" column. As before, a KDE of the column density-weighted, line of sight mean dust temperature and β maps for both the "correlated" and "anti-correlated" filaments is given in Figure 4.11.

PPMAP finds a stronger positive correlation in the "correlated" case. Unlike the cold test, however, PPMAP is now able to recover a strongly anti-correlated model. The bulge towards low temperatures and opacity indices in the "anti-correlated" case is due to confusion between the filament and the background at the filament boundary.

Thus I conclude that PPMAP is able to determine the presence of structures that are positively correlated in temperature and opacity index in most cases with only the five *Herschel* bands, and can correctly determine the presence of anti-correlations in cases where β is strongly encoded in the observations. This occurs at temperatures in excess of 20 K.

4.0.3.2 Tests including the SCUBA-2 850 µm band

In the tests previously discussed, variations in the opacity index are well encoded in the Rayleigh-Jeans tale of the Planck function. As PPMAP can accept continuum observations from any waveband given colour correction tables and accurate beam profiles for the correct instrument, I expand the tests to include synthetic SCUBA-2 850 µm observations. Even at temperatures below 20 K, 850 µm lies far from the peak of the Planck function on the Rayleigh-Jeans tail.

I rerun PPMAP on the cold "correlated" and "anti-correlated" observations with the parameters listed in Table 4.3, expanding to include all five *Herschel* bands, and the synthetic 850 µm band. The Gaussian KDEs of the column density-weighted, line of sight mean temperature and opacity index maps for both the "correlated" and "anti-correlated" case are shown in Figure 4.12.

The additional opacity index information encoded in the 850 µm observations has tightened the relation in the "correlated" test, and has reversed the relation, recovering a strong anti-correlation in the "anti-correlated" filament. I note, however,

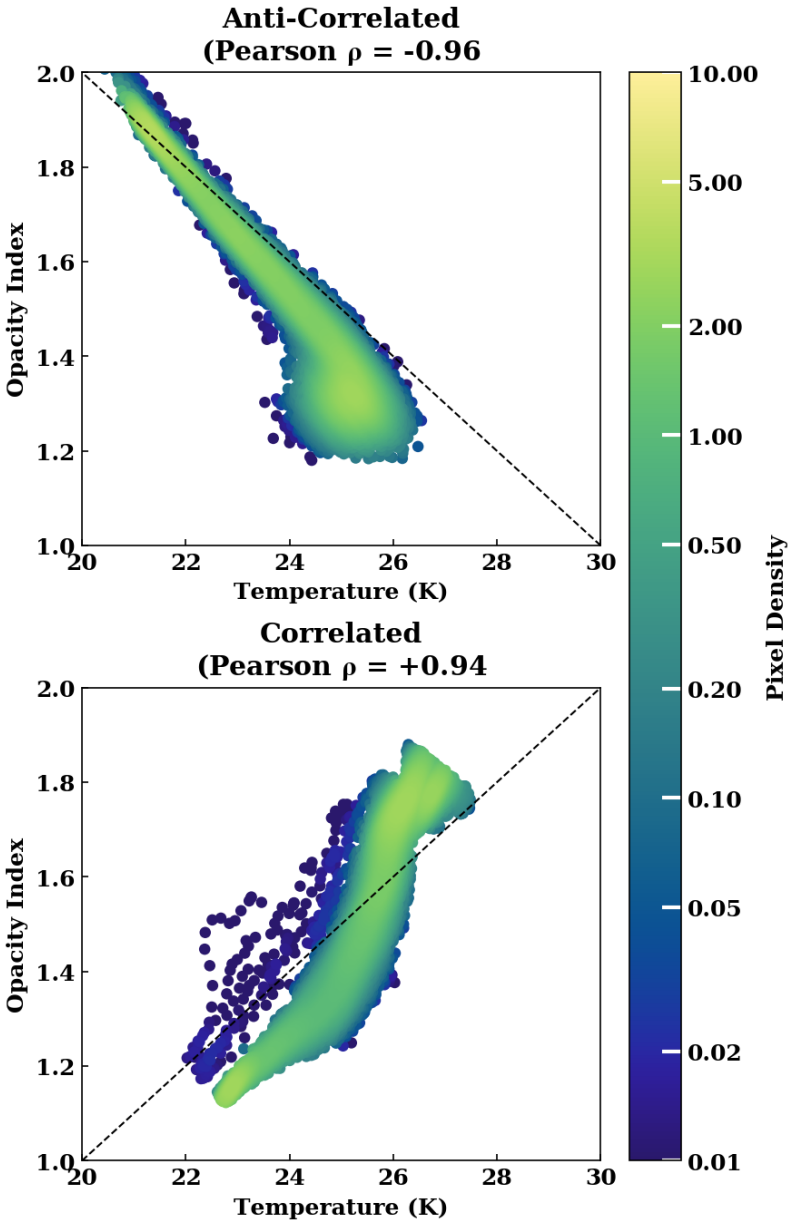

Figure 4.11. 2D KDE of the measured correlations between temperature and β estimates for the T_{hot} synthetic filament observed only with five synthetic *Herschel* bands. The colour scale gives the estimated density of pixels corresponding to a given value of temperature and β, derived from the KDE. The Pearson p value is vanishingly small.

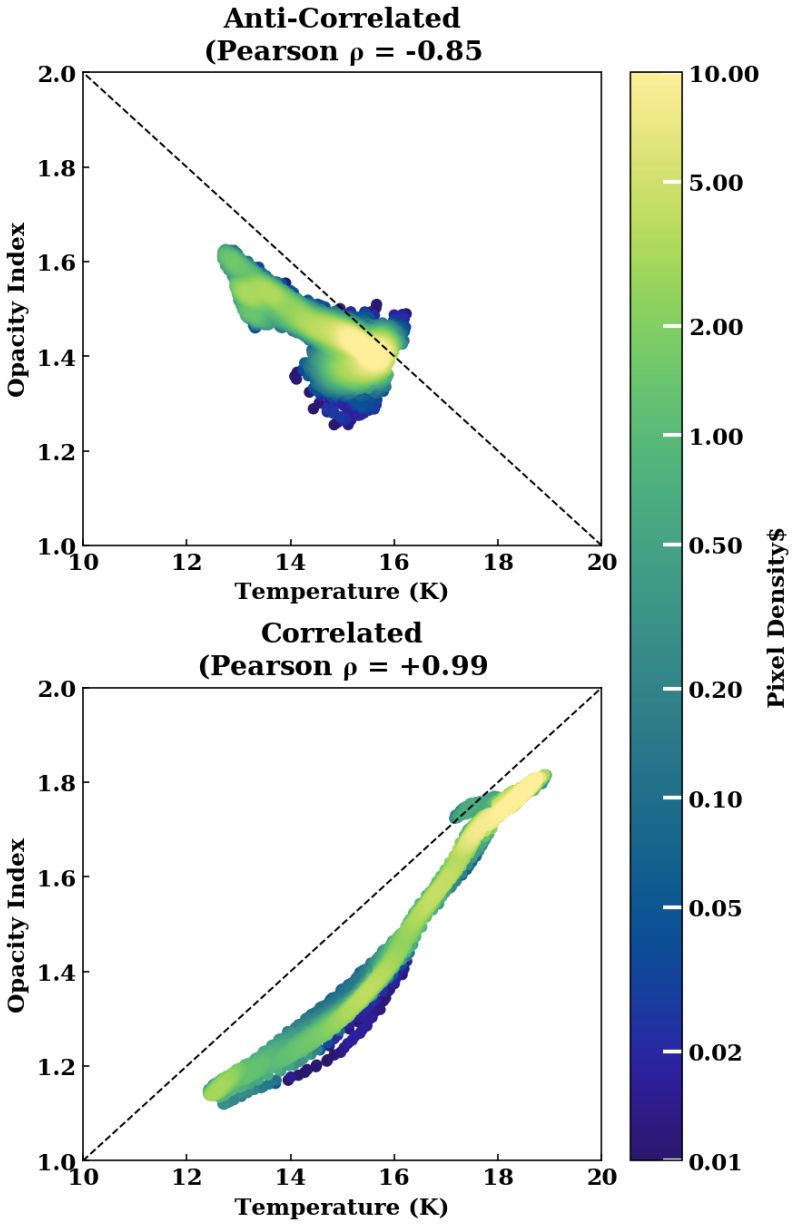

Figure 4.12. 2D KDE of the measured correlations between temperature and β estimates for the T_{cold} synthetic filament observed with synthetic *Herschel* and SCUBA-2 850 µm bands. The colour scale gives the estimated density of pixels corresponding to a given value of temperature and β, derived from the KDE. The Pearson p value is vanishingly small.

that the spread of values in the "anti-correlated" test is still limited to a small subset of the full range of temperatures and opacity indices.

I also repeat the 20 K to 30 K "correlated" and "anti-correlated" tests with an 850 µm component, and present the results in Figure 4.13.

As before, the correlations are narrower in both cases when compared with the same model without the 850 µm observations. The low temperature and low opacity index bulge in the "anti-correlated" case is more extended, which appears to weaken the Pearson correlation coefficient, ρ. This is due to a better fitting of the background temperature and opacity index.

Thus I conclude that inclusion of observations longward of 500 µm is important for correctly identifying relations between temperature and opacity index in the temperature range 10 K to 20 K. Wavelengths >500 µm are still helpful in constraining these relations at temperatures above 20 K, but are not strictly necessary.

As many dense star-forming regions are assumed to contain dust with temperatures from ∼10 K to ∼50 K, inclusion of SCUBA-2 850 µm observations with five *Herschel* bands should be considered a minimum requirement for applying PPMAP with both temperature and opacity index as free parameters.

4.1 Point-Source Artefacts

While PPMAP is able to avoid many of the unphysical assumptions that must be taken when performing MBB fitting on sub-millimetre observations, it is still limited by the need for the emission in each band to be from optically thin environments. This assumption holds true for most structures in star forming environments, particularly when observed at longer wavelengths. However, *Herschel* 70 µm observations of dense regions do become optically thick, thus violating this assumption. This most commonly occurs for young, deeply embedded protostars. Such regions violate the underlying PPMAP model, and lead to the creation of ring-like artefacts around bright, dense, 70 µm point sources. An example of these artefacts can be seen in Figure **??**.

I performed a number of investigations into the precise source of these artefacts in an attempt to derive a method for their correction or removal. As the artefacts appear only around sources which are optically thick in shorter wavelength bands, it is logical to assume that removal of the optically thick observations would lead to a PPMAP model free of the artefacts. However, removal of both the 70 µm and 160 µm bands had very little effect on the artefacts. I found that the rings appear to have similar diameters (approximately 40″), which might suggest they are somehow linked

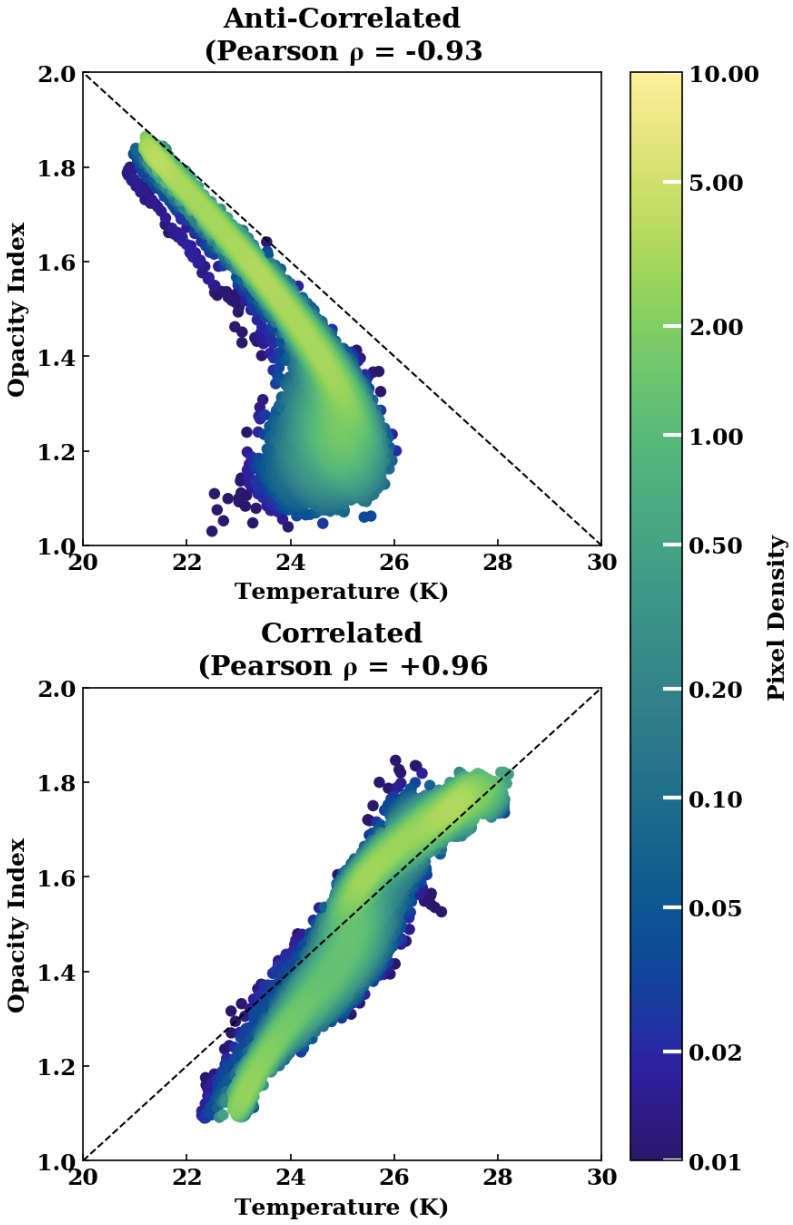

Figure 4.13. 2D KDE of the measured correlations between temperature and β estimates for the T_{hot} synthetic filament observed with synthetic *Herschel* and SCUBA-2 850 µm bands. The colour scale gives the estimated density of pixels corresponding to a given value of temperature and β, derived from the KDE. The Pearson p value is vanishingly small.

to the 500 µm beam model (with a FWHM of $\sim$36″), although tests without the 500 µm band also failed to impact the rings. I do note that the intensity of the ring itself is directly related to the relative intensity of the central point source to the background, with fainter sources producing fainter rings. Based on this finding, the decision was made to proceed by producing an initial PPMAP model for a target field, analyse the severity of the artefacts, and their potential impact on further analysis and, if deemed necessary, mask out any bright 70 µm sources in the observations, before creating a final "clean" model. This procedure was utilised for both of the regions discussed in the following chapters.

Chapter 5
The Taurus L1495/B213 Complex*

In this chapter I present the results of applying the PPMAP column density estimation procedure to *Herschel* and SCUBA-2 observations of the L1495/B213 star forming complex in the Taurus molecular cloud. I discuss variations in the dust properties as revealed by PPMAP. I identify a large filamentary structure and discuss its physical properties, such as its width and its line mass. I explore how these properties vary dependent on location within the filament, and how they relate to the distribution of pre- and protostellar cores.

5.1 An Overview of the Taurus Molecular Cloud

The Taurus molecular cloud is situated 140 pc away (Elias 1978; Galli et al. 2018; Zucker et al. 2019). In optical wavelengths, the region consists of a series of dark nebulae, due to extinction. It was first identified by Barnard (1927) in his *Catalogue of 349 dark objects in the sky*. Much of the region was later reclassified by Lynds (1962) as the L1495 complex, combining many of the smaller dark regions into a singular entity. Figure 5.1 presents a finding chart for various regions within the L1495/B213 complex.

Due to its close proximity to the Earth, and its large angular size (2° by 2°), the L1495/B213 complex has been extensively studied as a site of low- and intermediate-mass star formation (Shu, Adams, and Lizano 1987; Strom and Strom 1994; Nakamura and Li 2008; Hacar et al. 2013; Palmeirim et al. 2013; Seo et al. 2015; Tafalla and Hacar 2015; Marsh et al. 2016; Ward-Thompson et al. 2016; Punanova et al. 2018).

*The work presented here is published in Howard et al. (2019)

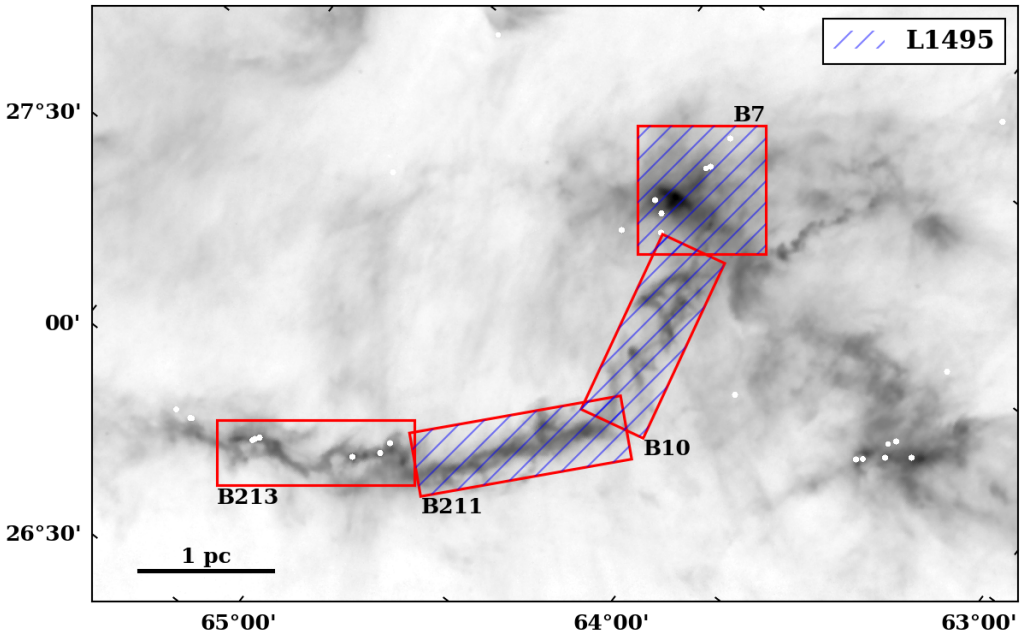

Figure 5.1. A finding chart of the Taurus L1495/B213 complex, indicating the different regions associated with the Barnard (1927, regions in red boxes, codified B#) and Lynds (1962, blue hatched region, L1495) catalogues of dark nebulae.

Previous studies by Palmeirim et al. (2013), and by Arzoumanian et al. (2019), have used *Herschel* observations of thermal dust emission and MBB fitting techniques to estimate the global properties of the filament. They find that the B211/B213 filament agrees well with the general picture of a thermally super-critical filament having an approximately 0.1 pc wide central region. There are several pre-stellar cores (e.g. Onishi et al. 2002; Marsh et al. 2016) and protostellar objects (e.g. Motte and André 2001; Rebull et al. 2010) embedded in the L1495 filament, suggesting that it has fragmented along its length. However, Schmalzl et al. (2010) point out that the B211 filament section contains no protostellar cores.

5.2 Observations of the Taurus Molecular Cloud

The primary observations for this investigation of the L1495 complex are five SPIRE/PACS Parallel observations, taken as part of the *Herschel* Gould Belt Survey in the PACS 70 µm and 160 µm and SPIRE 250 µm, 350 µm and 500 µm bands. The observations comprise 17 individual scans, covering the areas shown in Figure 5.2.

Due to the high aspect ratio and large angular size of the L1495 complex, the scans are not taken in the standard form of one nominal and one orthogonal scan for each pointing. Instead, a single nominal scan is taken parallel to the long axis of the L1495/B213 complex (shown in red), and two orthogonal scans are overlaid parallel to

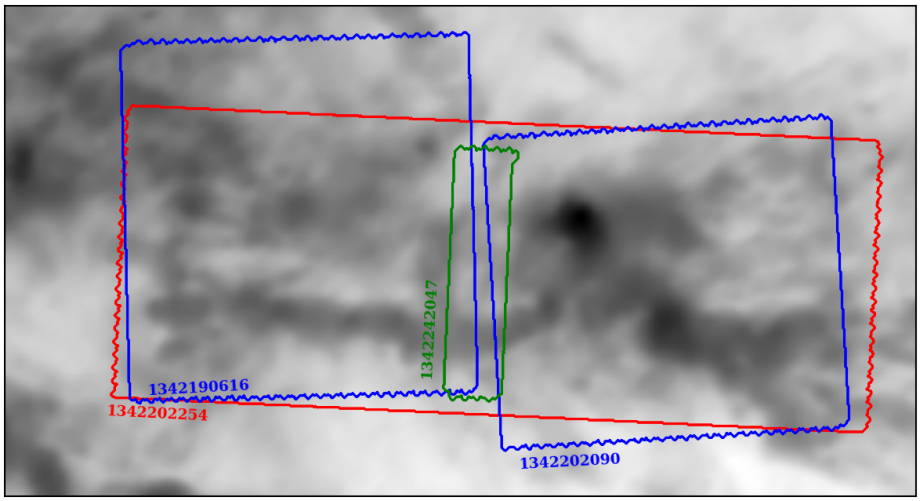

(a) PACS scan areas.

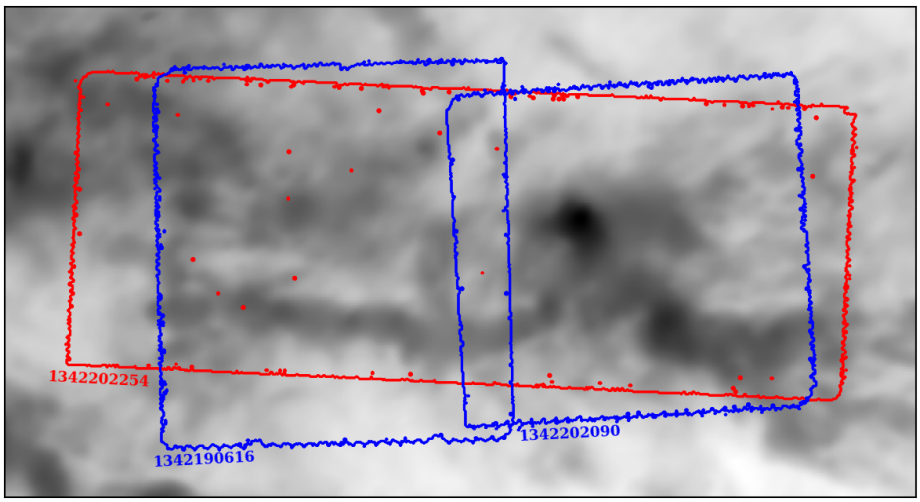

(b) SPIRE scan areas.

Figure 5.2. *Herschel* scan areas for the PACS and SPIRE observations. Both images show nominal (red box, ObsID 1342202254), and orthogonal (blue boxes, ObsID 1342190616, 1342202090) scans. Due to the fixed field of view offset between the PACS and SPIRE instruments, a supplementary orthogonal scan (green box, ObsID 1342242047) was made to fill in an area of missing data in the PACS observations. Background image taken from the *Planck* optical depth model of the region, at 5′ resolution (Planck Collaboration 2016d).

the short axis (depicted in blue). For the SPIRE bands, these scans overlap. However, due to the difference in field of view between the PACS and SPIRE instruments, as discussed in Chapter 2, Section 2.0.1.5, the PACS orthogonal scans are separated by a small angular distance. To rectify this, a supplementary scan in the same direction is taken to fill in the missing data, and is shown in green on the diagram. The observation identifiers, or ObsIDs, and their observation dates, are given in Table 5.1.

Table 5.1. The ObsIDs of the *Herschel* PACS and SPIRE scans of L1495, and their observation dates.

Scan Direction	ObsID	Date
PACS and SPIRE		
Nominal	1342202254	08/08/2010
Orthogonal	1342190616	03/08/2010
Orthogonal	1342202090	08/08/2010
PACS only		
Supp. Orthogonal	1342242047	20/03/2012

The data reduction follows the procedure outlined in Chapter 2, Section 2.1.2. Once the observations have been mosaicked , the zero-point corrections for the PACS bands are generated using the method described in Chapter 2, Section 2.1.6. The derived offsets for PACS, and those already applied to the SPIRE Level 2 products, are given in Table 5.2.

Table 5.2. Zero-Point Offsets and global Gaussian noise estimates for PACS, SPIRE and SCUBA-2 observations of the L1495/B213 complex. I obtained the PACS and SCUBA-2 offsets through the procedure described in Chapter 2, Section 2.1.6, while SPIRE offsets were applied as part of the archive data reduction process to obtain Level 2 products. Gaussian noise was estimated through manual inspection of each band, as described below.

Band	Offset (MJy/sr)	Noise (MJy/sr)
PACS 70 µm	4.3	5.62
PACS 160 µm	69.2	3.55
SPIRE 250 µm	34.3	1.42
SPIRE 350 µm	21.4	0.67
SPIRE 500 µm	9.4	0.41
SCUBA-2 850 µm	-5.2	2.27

The SCUBA-2 850 µm supplementary observations were first published by Buckle et al. (2015), and have been supplied pre-reduced by Emily Drabek-Maunder. The observations are part of the JCMT Gould Belt Survey, and consist of seven 30′

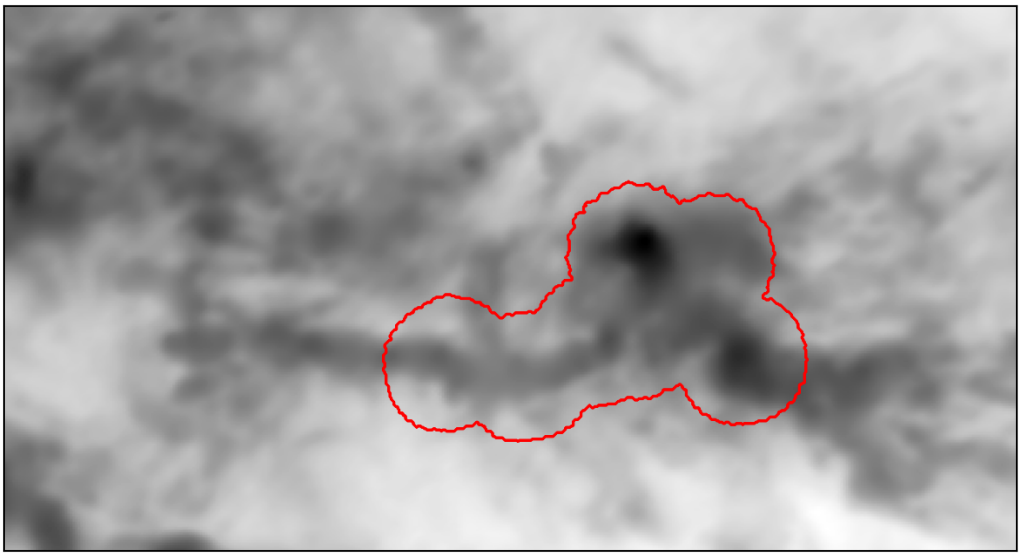

Figure 5.3. JCMT SCUBA-2 850 µm scan area for the composite observation of the L1495/B213 complex. The observations, taken as part of the JCMT Gould Belt Survey, were first published by Buckle et al. (2015), and were supplied pre-reduced by Emily Drabek-Maunder. Background image taken from the *Planck* optical depth model of the region, at 5′ resolution (Planck Collaboration 2016d).

diameter pointings, taken in the PONG1800 mapping mode. Reduction then follows the procedure described in Chapter 2, Section 2.1.3, with specific details published by Buckle et al. (2015). The reduced pointings are then mosaicked together into a continuous region, the coverage of which is shown in Figure 5.3.

As discussed in Chapter 4, Section 4.1, PPMAP produces circular ring-like artefacts around optically thick, bright 70 µm protostars. To combat this, I mask the locations of these objects in the observations, before running PPMAP. I first identify the locations of the sources with the FellWalker algorithm (Berry 2015). FellWalker identifies peaks in an emission map by locating a random pixel, and "walking" up positive intensity gradients until it reaches a maximum point; These peak positions are recorded. The key properties for the FellWalker run are provided in Table 5.3. Protostellar cores are then identified from the distribution of peaks by visual inspection, to avoid masking bright regions of extended emission. I then apply a circular mask with an angular diameter of 72″ to each remaining location. These appear as white circles in on Figures like Figure 5.4.

Figure 5.4 shows the reduced observations for the five *Herschel* bands (70 µm, 160 µm, 250 µm, 350 µm and 500 µm), and the SCUBA-2 850 µm band. The observations are restricted to a 2.8° by 1.8° region, centred on $04^{\mathrm{h}}19^{\mathrm{m}}04.95^{\mathrm{s}}$, +27°54′36.84″ (64.770 631 33°, +27.910 232 62°), at an angle of −38° to North.

For PPMAP to properly estimate the column density of a region, accurate

Table 5.3. The key parameters for the FellWalker algorithm used to identify bright protostellar cores in the 70 µm *Herschel* observations so they could be masked prior to running PPMAP.

Parameter	Value
RMS[a]	20
NOISE[b]	40
MINPIX[c]	7
MINHEIGHT[d]	40
MINDIP[e]	40
MAXJUMP[f]	4

a: The global root mean square noise level of the observation. In this instance, RMS is required by the script, but made redundant by the NOISE parameter. **b**: Absolute value of the noise in the image - no walk will start from a pixel below this value. **c**: The smallest number of pixels a clump can contain. **d**: Not considered a clump unless the peak is larger than this value. **e**: Two neighbouring peaks are considered part of the same clump, and are merged, if this value is greater than the difference of clump peaks and the minimum between them. **f**: The radius around a peak, in pixels, that the algorithm checks to establish if it is only a local maximum.

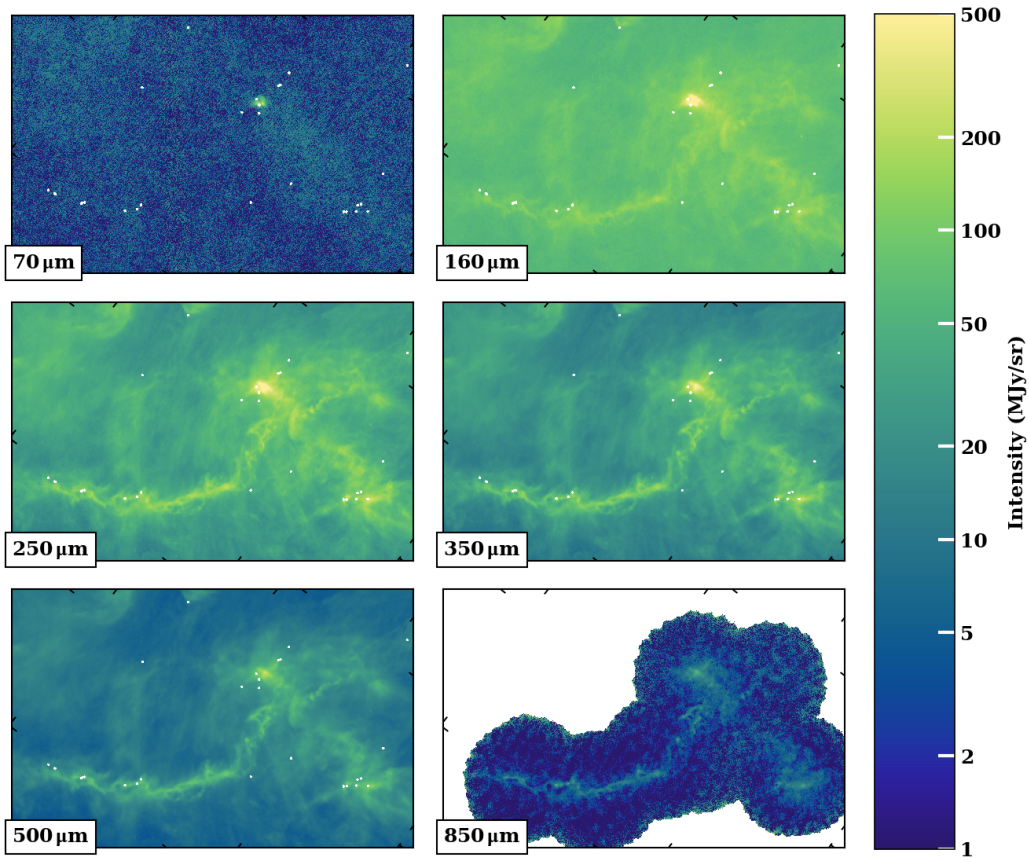

Figure 5.4. *Herschel* PACS 70 µm and 160 µm and SPIRE 250 µm, 350 µm and 500 µm observations, and JCMT SCUBA-2 850 µm observations of the L1495/B213 complex. White circles are masked regions centred on bight 70 µm sources identified using FellWalker.

Gaussian noise levels need to be given for each observation band. At present, this is best achieved by manual estimation. In each observation I select circular regions away from the bright structure, and take the standard deviation of the surface brightness. The circular regions have an angular radius $\sim 5'$. The noise estimates for each band are presented in Table 5.2.

5.3 PPMAP Analysis of the L1495/B213 Complex

Initially, I have run PPMAP with a $12''$ resolution ($6''$ Nyquist sample rate), utilising just the *Herschel* observations. However, I later opt for an $18''$ resolution ($9''$ Nyquist sample rate) to better compare with existing publications (see e.g. Palmeirim et al. 2013; Arzoumanian et al. 2019). I also add the longer wavelength SCUBA-2 observations, which help to provide a tighter constraint on the value of the opacity index, β. While all the analysis is conducted at this $9''$ pixel scale, the spine of the filament has been identified on the earlier, higher resolution results, leading to a spine point spacing of $6''$; this super-sampling has no effect on the results, and is discussed in greater detail in Section 5.3.2.

I choose 12 logarithmically spaced temperature bins, 7.0 K, 8.2 K, 9.6 K, 11.3 K, 13.2 K, 15.5 K, 18.1 K, 21.2 K, 24.9 K, 29.1 K, 34.1 K and 40.0 K. Each bin represents the dust temperature in a small range around the given value, i.e. the 7.0 K bin encompasses dust with temperatures between 6.5 K and 7.6 K. The temperature range from 7.0 K to 40.0 K is chosen to adequately sample the distribution of dust temperatures within the L1495/B213 complex. The complex is well known as a site of low mass star formation, and thus not subject to heating from internal OB stars. I choose four linearly spaced values of β, 1.0, 1.5, 2.0, 2.5, and utilise the standard PPMAP Gaussian prior on β, with a mean value of 2.0, and a narrow standard deviation of 0.25, to aid in lifting the temperature/β degeneracy. The range of β values is chosen to broadly cover the range of expected values. The full PPMAP input parameters are shown in Table 5.4.

The L1495/B213 results are produced by running PPMAP on the Cardiff University Advanced Research Computing Facility (ARCCA) Raven super computer.

5.3.1 Basic PPMAP products

As I discuss in Chapter 3, Section 3.1.4.1, it is difficult to present the full results of the 4D hypercube of column densities that PPMAP produces. Therefore, I choose to marginalise out first the β dimension, and then the temperature dimension.

Table 5.4. The PPMAP input parameters for the L1495/B213 field. Parameters with list values are shown here separated by commas, but are to be separated by whitespace when running PPMAP. A description of each parameter is given in Chapter 3. The Herc850.txt colour correction table is given in Appendix A.

Parameter	Value
`gloncent`	64.77063133
`glatcent`	27.91023262
`fieldsize`	2.8, 1.8
`pixel`	9.0
`dilution`	0.3
`maxiteration`	10000
`distance`	140.0
`kappa300`	0.1
`nbeta`	4
`betagrid`	1.0, 1.5, 2.0, 2.5
`betaprior`	2.0, 0.25
`Nt`	12
`temperature`	7.0, 40.0
`ncells`	40
`noverlap`	20
`ccfile`	Herc850.txt
`nbands`	6

Figure 5.5 shows slices from the resultant cube of column densities in different line-of-sight temperature bins when the hypercube is summed along all β. The colour bar is the same for all slices, and gives the column density of molecular hydrogen, assuming a gas-to-dust ratio of 100, and a mean molecular weight of H_2 of 2.8. However, I again stress that the model PPMAP produces is one that traces optical depth derived from thermal dust emission.

Figure 5.5 indicates that dust within the filament is cold ($\leq$15.0 K). The coldest dust ($\sim$8.2 K) is concentrated in a narrow region close to the centre of the filament. The temperature bin centred at 7.0 K contains very little dust, except for a few dense knots located along the filament. The model contains very little dust in the filament spine at $\geq$18.1 K. This view is consistent with results from the Green Bank Ammonia Survey (GAS) observations, which estimate the kinetic gas temperature of the L1495-B213 filament to be between 8 K and 15 K (Seo et al. 2015).

In contrast, the more diffuse regions surrounding the filament have large quantities of dust between 11.3 K and 18.1 K. This indicates that the surrounding cloud is warmer than the filament itself. Due to the high pass filtering and critical density thresholds required, GAS estimates of the temperature of material in the surroundings are not available. An area of much higher temperature ($\sim$25 K) is present around the

Herbig Ae/Be star V892 Tau, marked by the red star marker. This object is known to be producing X-ray flares (Giardino et al. 2004), and is presumably a source of local heating.

The temperature split between cold material (<16 K) and warm material (>16 K) may suggest that a two temperature SED model could be used to estimate the column density, temperature and opacity index of L1495, rather than a PPMAP model. However, the two estimates of temperature for each pixel that would be returned would still suffer from similar issues as a single temperature MBB fitting algorithm; these temperatures would be line of sight averages, and all other information regarding temperature variations would be lost. In particular, the granularity of being able to see the central spine of the filament grow through adjacent temperature slices would not be achievable. Furthermore, a two temperature SED model is flux weighed rather than mass weighted as PPMAP's results are. The effects of such a distinction are discussed in Chapter 7. Finally, a two temperature SED would seek to fit four variables (column density, two temperature values, and an opacity index) from six data points at each pixel, leading to a very few degrees of freedom, and increasing the chances of overfitting the model. PPMAP is able to somewhat circumvent the degrees of freedom problem, as discussed in Chapter 3, Section 3.1.5.

While PPMAP does reveal substructure within the filament that is otherwise not visible in the maps presented by Palmeirim et al. (2013), the resolution of this model is too coarse to draw a direct comparison with the fibres identified by Hacar et al. (2013). Furthermore, the dust temperature slices are too widely spaced and too sparse to perform a search for temperature coherent structures analogous to velocity coherent fibres.

When I instead marginalise out the temperature dimension, leaving only the distribution of column densities in different β slices, I produce the four images shown in Figure 5.6. As with Figure 5.5, the colour bar gives the derived H_2 column density for all four panels, shown on the same scale. From this, I deduce that the surrounding medium has a higher mean opacity index, with $\bar{\beta} \gtrsim 1.7$, while dust near the filament spine has a value of $\bar{\beta} \lesssim 1.5$. Only a very few dense regions contain dust in the $\beta = 1.0$ slice.

Almost no dust is found in the highest, $\beta = 2.5$ slice, apart from a small region around V892 Tau. The dust here may be undergoing physical changes due to the strong local radiation field. The straight-edged shapes present in this slice arise because, in tiles where the input data contains insufficient information, PPMAP adopts a nearly uniform column density. The column density discontinuities are not statistically significant (above the 1σ uncertainty level).

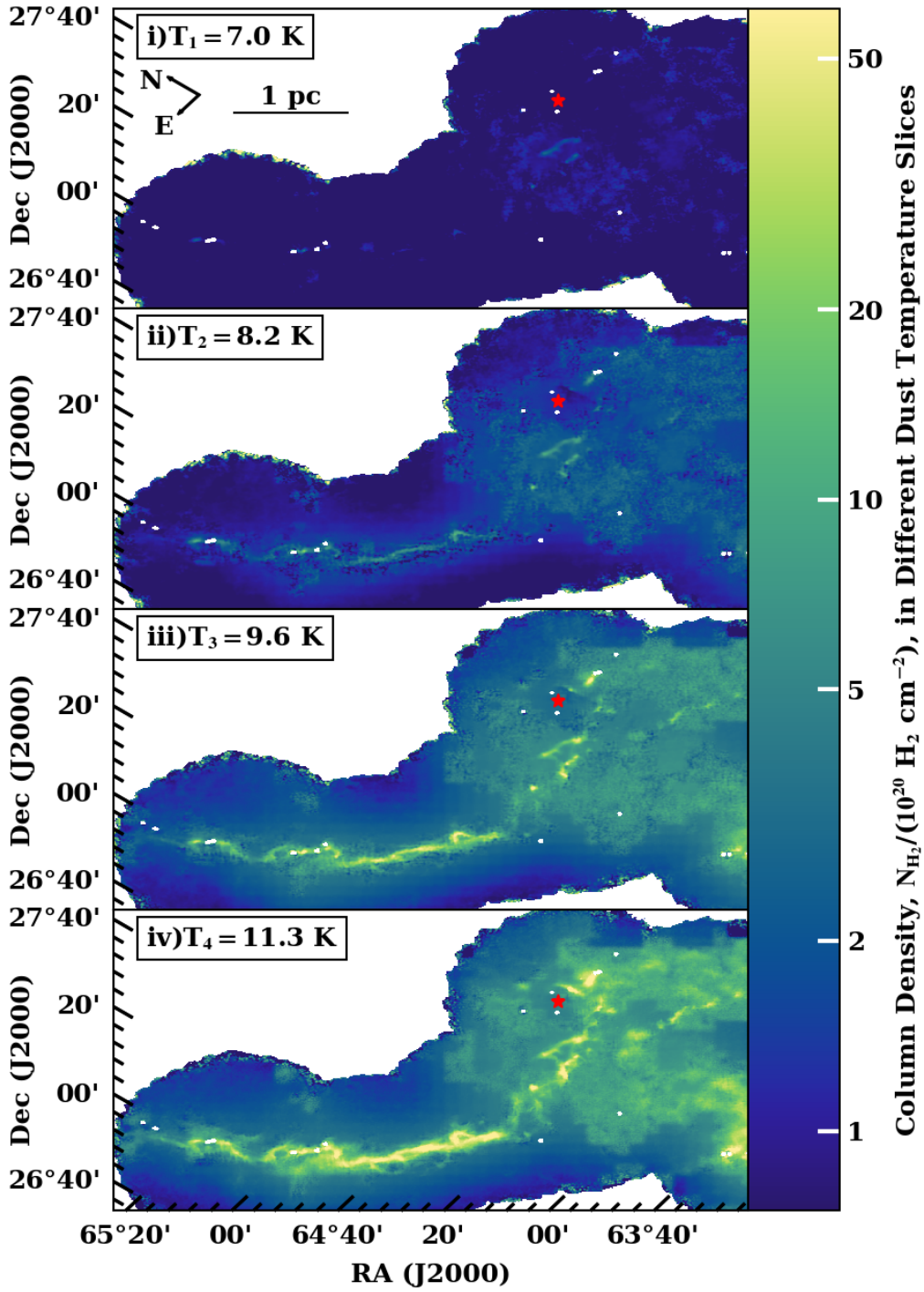

Figure 5.5. The distribution of dust, converted to H_2 column densities, in 12, logarithmically spaced line of sight temperature bins for the L1495/B213 complex. These maps are obtained by marginalising out the opacity index dimension of the PPMAP hypercube. The red star marker indicates the position of the Herbig Ae/Be star, V892 Tau.

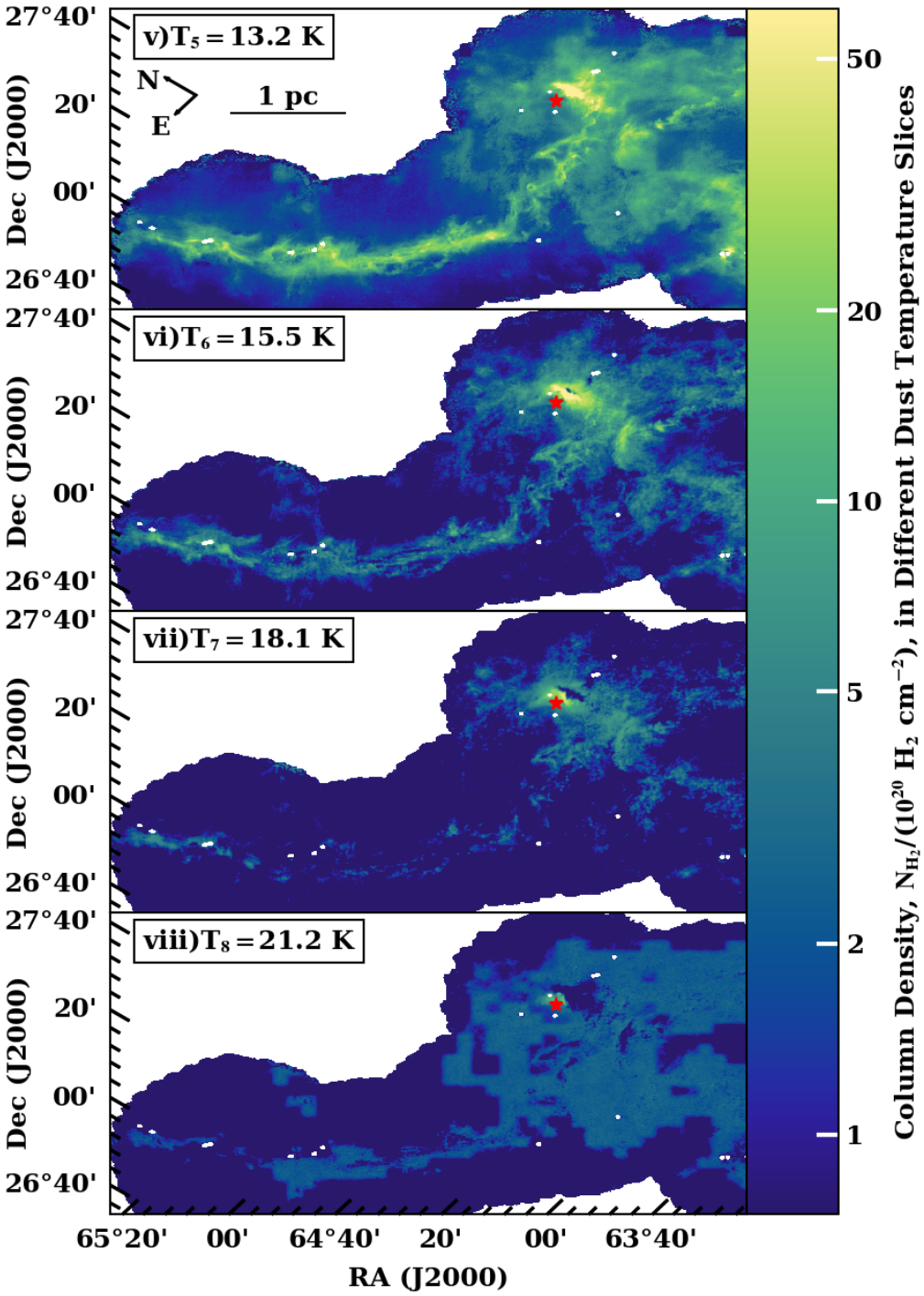

Figure 5.5 (cont.). The distribution of dust, converted to H_2 column densities, in 12, logarithmically spaced line of sight temperature bins for the L1495/B213 complex. These maps are obtained by marginalising out the opacity index dimension of the PPMAP hypercube. The red star marker indicates the position of the Herbig Ae/Be star, V892 Tau.

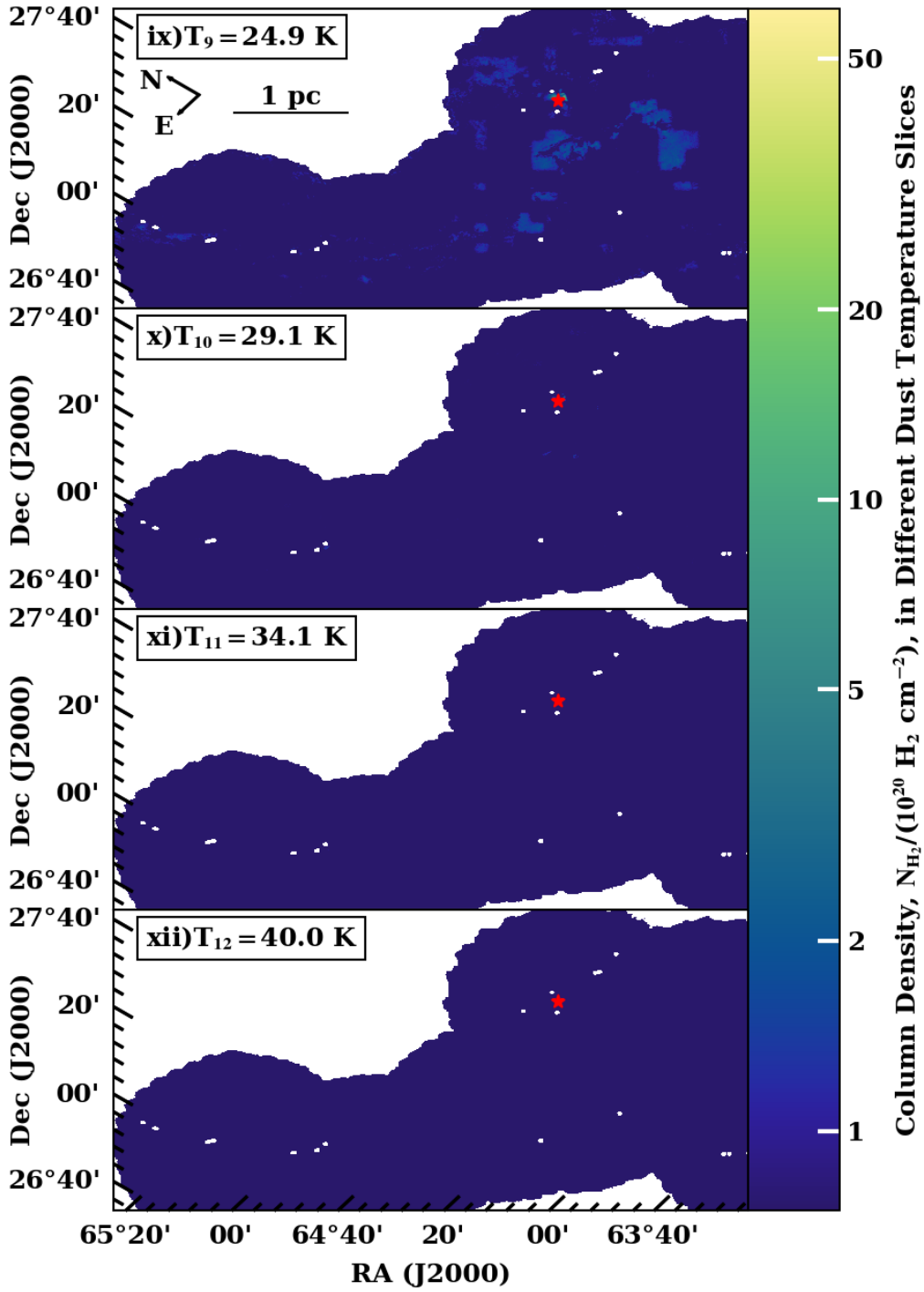

Figure 5.5 (cont.). The distribution of dust, converted to H_2 column densities, in 12, logarithmically spaced line of sight temperature bins for the L1495/B213 complex. These maps are obtained by marginalising out the opacity index dimension of the PPMAP hypercube. The red star marker indicates the position of the Herbig Ae/Be star, V892 Tau.

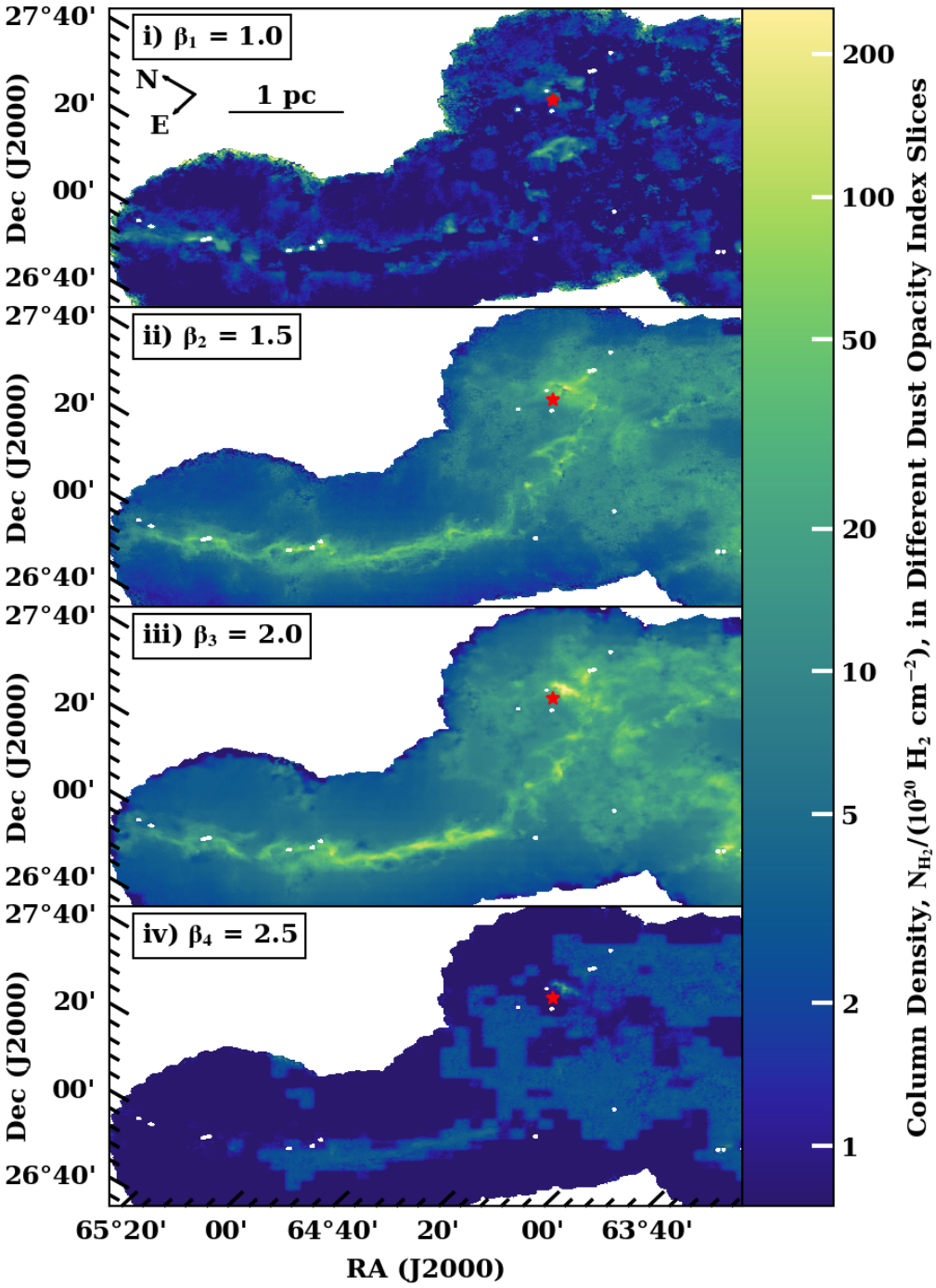

Figure 5.6. The distribution of dust, converted to H_2 column densities, in 4 linearly spaced line of sight opacity index bins for the L1495/B213 complex. These maps are obtained by marginalising out the temperature dimension of the PPMAP hypercube. The red star marker indicates the position of the Herbig Ae/Be star, V892 Tau.

Figure 5.7 is the total column density map I obtain by marginalising out both the temperature and β dimensions. "Marginalising out" is the process of lowering the dimensionality of a distribution by summing the distribution along one or more of its dimensions in order to reduce the complexity of the data. The underlying mathematical process of marginalising out dimension from PPMAP models is discussed in Chapter 3, Section 3.1.4. I identify the spines of the B213 and B211 filaments with the DisPerSE algorithm (Sousbie 2011; Sousbie, Pichon, and Kawahara 2011), and plot them as the red and blue lines, respectively. I adopt a persistence threshold of $40 \times 10^{20}\,\mathrm{H_2\,cm^{-2}}$, and utilise the SKELCONV option to join the smaller sub-spines into larger structures. For this, I choose a smoothing length of 5 pixels, and trim branches with values below $45 \times 10^{20}\,\mathrm{H_2\,cm^{-2}}$. I enable the ASSEMBLE option with an acceptance angle of 60°. I manually combine the spines into a single structure, and use an algorithm provided by Sümeyye Suri to trace the spine from one end to the other, placing the points in a sequence that followed the full length of the filament. The spine is identified with a $6''$ sample rate because this is the resolution at which earlier results from PPMAP have been analysed, and around which many of my analysis tools have been constructed. The $18''$ ($9''$ Nyquist sampled) results are resampled to $6''$ in order to identify the spine, so that the tools continue to work. This is only important for locating the spine points, and the remainder of the analysis is conducted at the $9''$ sample rate. While this oversamples the number of points along the filament, none of the results presented here depend upon a physical distance along the spine.

Figure 5.8 shows the associated Point Process Statistical Degeneracy (PPSD) for the L1495/B213 complex. The spine and inner region of B211/B213 filament, and the head of L1495, have a PPSD ≥ 5. This indicates that these regions are well constrained. The background regions are less well constrained, with a PPSD ~ 1.

Figure 5.9 and Figure 5.10 show maps of the line-of-sight mean dust temperature and opacity index, respectively. These are produced via the method outlined in Chapter 3, Section 3.1.4.2. They show that the mean temperature decreases sharply towards the spine of the filament, while β shows a more shallow decrease. While the sharp temperature decrease is almost certainly due to attenuation of the ambient radiation field, the shallow β decrease suggests another process has been at work. This might be due to processes occurring in the accretion shock at the filament boundary. Palmeirim et al. (2013) provide evidence for such a shock, noting that they found infall velocities between $0.5\,\mathrm{km\,s^{-1}}$ and $10\,\mathrm{km\,s^{-1}}$, and a sound speed of just $0.19\,\mathrm{km\,s^{-1}}$. This implies a Mach number between 2.6 and 5.3.

Figure 5.9 also indicates that the temperature is lower on the southern side

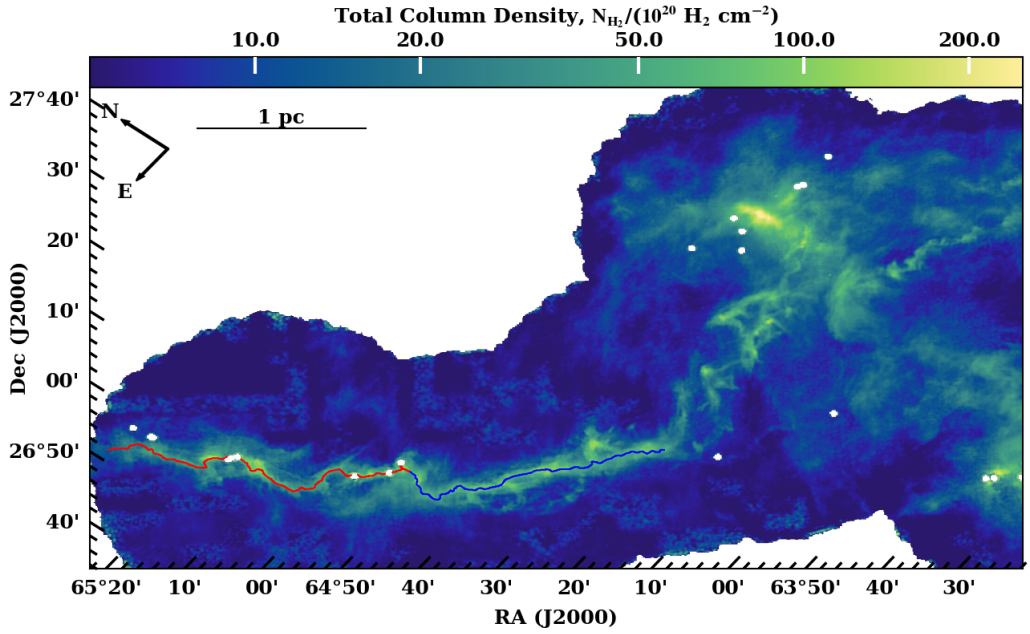

Figure 5.7. Total H_2 column density, derived from the PPMAP dust model. This map is obtained by marginalising out both the temperature and opacity index dimensions. The red and blue lines denote the spines of the B213 and B211 sub-filaments, respectively.

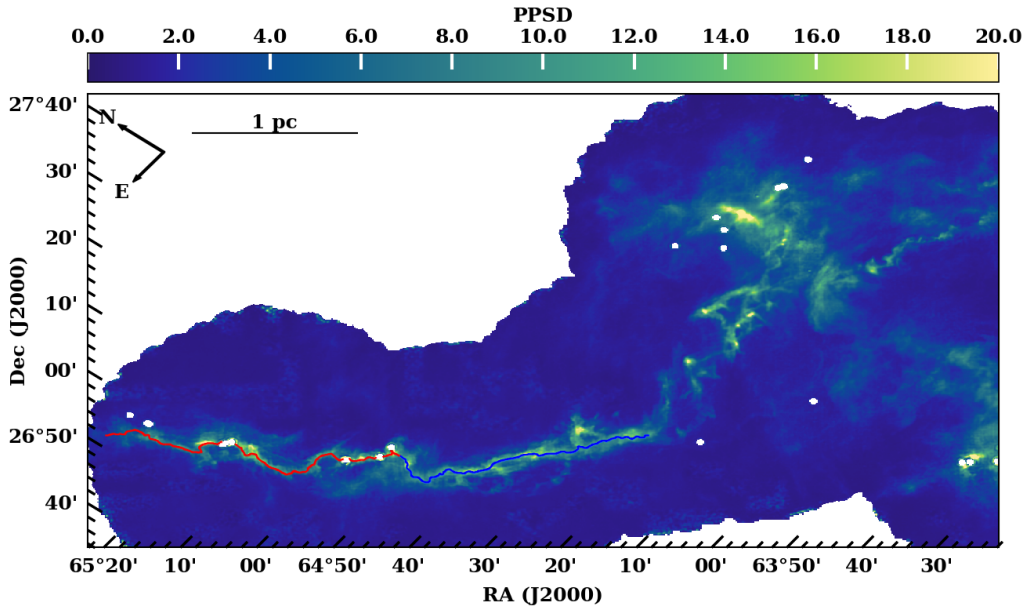

Figure 5.8. Map of the Point Process Statistical Degeneracy (PPSD, see Chapter 3, Section 3.1.4.3) for the L1495/B213 complex. The uncertainty hypercube used to derive the map of PPSD is shown in Appendix B.

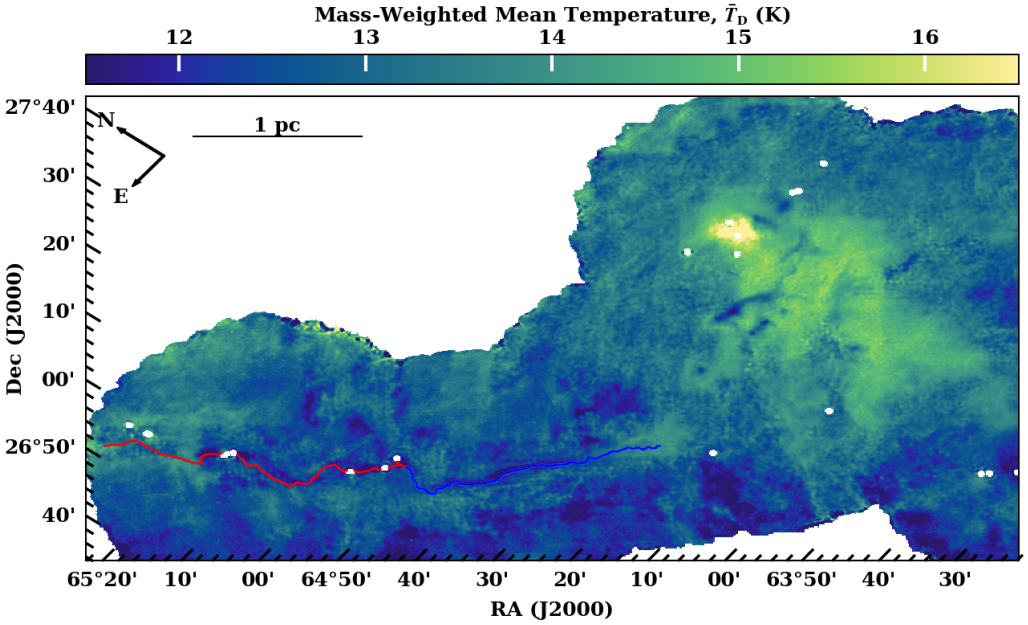

Figure 5.9. The mean line of sight dust temperature, $\bar{T}_{\rm D}$ at every pixel, obtained by marginalising out the opacity index dimension and then taking a weighted average of the temperature bins of the hypercubes, with the H_2 column density in each bin as the weighting factor.

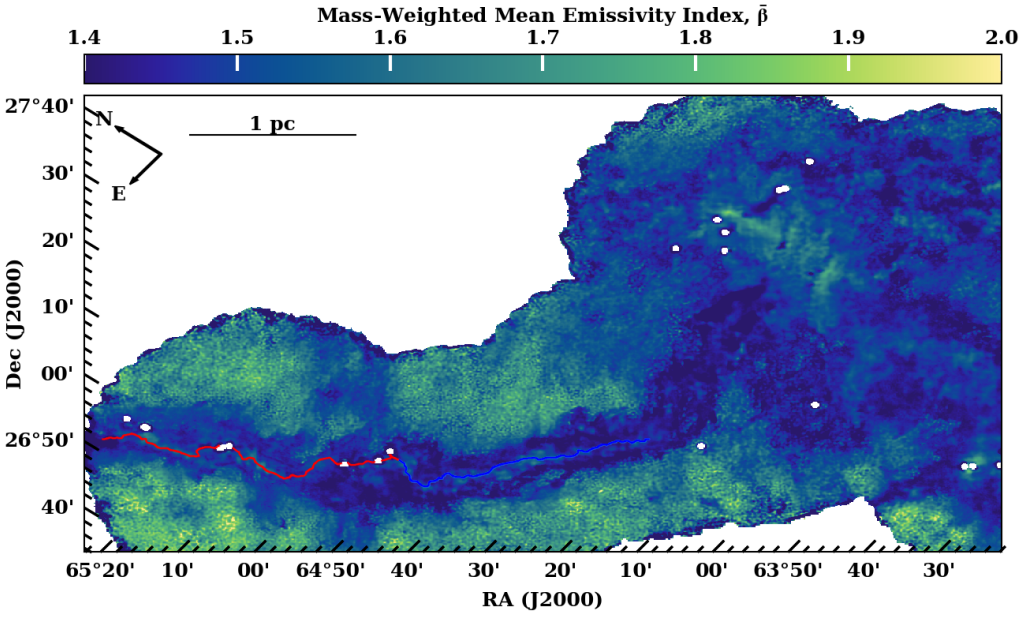

Figure 5.10. The mean line of sight dust opacity index, $\bar{\beta}$ at every pixel, obtained by marginalising out the temperature dimension and then taking a weighted average of the opacity index bins of the hypercubes, with the H_2 column density in each bin as the weighting factor.

of the filament when compared with the northern side. This may point towards a difference in the strength of the ambient radiation field. If I take $T_D \propto U_{RAD}^{1/(4+p)}$, where U_{RAD} is the density of the ambient radiation field, and $p \approx 2$, then $U_{RAD;South} \sim 0.67 U_{RAD;North}$.

5.3.2 Analysis of B211/B213

Once I define and order the spine of the filament, I analyse the filament structure in a more quantitative way. I take all 1100 discrete spine points, each separated from the neighbouring points by approximately 0.004 pc, and use them to fit a cubic spline to the filament. This allows me to identify the local tangent at each point.

I then sample the column density, along a line orthogonal to the local tangent of each spine point, at discrete values of the impact parameter, b. The sample rate is set to that of the PPMAP maps (9″, or ∼0.006 pc), out to a distance of 1 pc either side of the spine. Thus, for each spine point, I produce an array of 329 column densities corresponding to a 2 pc-long cut across the filament.

I exclude 68 cuts which contain poor or missing data due to the protostellar masking, or which run off the edge of the model, and thus contain regions with edge effects. This leaves 1032 cuts, which are used to analyse the filament.

5.3.2.1 Global Median Profile

To better compare with established literature (e.g., Arzoumanian et al. 2011; Palmeirim et al. 2013; Arzoumanian et al. 2019), I first produce an average cut across the filament by taking the median column density at each impact parameter over all 1032 cuts to produce a single cut of median values at each value of b. I also produce an array of the Median Absolute Deviation (MAD, analogous to the standard deviation for a mean), and divide it by the square root of the number of cuts to produce the error on the median ($\mathrm{MAD}_{\widetilde{N_{\mathrm{H_2}}(b)}} = \mathrm{MAD}/\sqrt{n_{cut}}$, where $n_{cut} = 1032$).

I choose to use a model of a cylindrically symmetric filament with the H_2 column density at impact parameter, b, from the spine of the filament given by a Plummer-like profile

$$N_{\mathrm{H_2}}(b) = N_0 \left\{ 1 + \left(\frac{b}{r_0} \right)^2 \right\}^{-(p-1)/2} + N_{\mathrm{B}}, \tag{5.1}$$

$$N_0 = n_0 r_0 \mathcal{B}\left(\frac{1}{2}, \frac{p-1}{2} \right) \sec i. \tag{5.2}$$

Table 5.5. Values of the fitted parameters and their uncertainties produced by fitting Equation 5.1 to the cut of median column densities for L1495.

Parameter	North	South
$N_0/(1 \times 10^{21}\,\mathrm{H_2\,cm^{-2}})$	6.38 ± 0.09	
$r_0/(0.01\,\mathrm{pc})$	2.80 ± 0.14	1.67 ± 0.06
p	2.02 ± 0.05	1.73 ± 0.02
$N_\mathrm{B}/(1 \times 10^{21}\,\mathrm{H_2\,cm^{-2}})$	0.28 ± 0.03	0.13 ± 0.04

N_0 represents the column density value on the spine of the filament, N_B is the background column density, $\mathcal{B}$ is the Euler Beta Function (Casali 1986), and i is the inclination of the filament to the plane of the sky, assumed in this case to be 0°.

I apply this function to the median column density cut using the LMFIT Python package (Newville et al. 2014), with $\mathrm{MAD}_{\widetilde{N_{\mathrm{H_2}}(b)}}$ as a constraint on the error of the sample. To account for variations in the filament between the north and south side, I choose to fit two values of each parameter r_0, p, and N_B; one set is fit using data from the north side of the filament, while the other uses data from the south side. I note, however, that the function I apply is continuous across both sides of the spine, and produces a single value of N_0 at the central spine point. Following Palmeirim et al. (2013), I constrain my fitting to sample points $\leq$0.4 pc to either side of the spine.

Table 5.5 gives the fitting parameters and their uncertainties. Figure 5.11(a) shows the cut of median column densities with impact parameter as light blue and pink circles for the north and south side of the filament, respectively. The yellow error bars represent the MAD at each impact parameter; the $\mathrm{MAD}_{\widetilde{N_{\mathrm{H_2}}(b)}}$ is too small to visualise on the plot. The dashed blue and red lines represent the fitted profile extending to the north and south of the filament.

Figure 5.11 (b) and (c) show the median filament profiles of the line-of-sight mean dust temperature and line-of-sight mean β. I shall refer to these quantities $\widetilde{T_\mathrm{D}}(b)$ for the median profile of mean dust temperatures, and $\widetilde{\beta}(b)$ for the median profile of mean β values. The profiles are produced from the maps shown in Figure 5.9 and Figure 5.10 in the same way as the median column density cuts. Both $\widetilde{T_\mathrm{D}}(b)$ and $\widetilde{\beta}(b)$ decrease as $b \to 0$. However, $\widetilde{T_\mathrm{D}}(b)$ decreases much more steeply, and with a much narrower minimum, than $\widetilde{\beta}(b)$. Therefore, while they exhibit similar general trends, the two quantities are not significantly correlated. The rise in values of $\widetilde{\beta}(b)$ immediately around $b = 0$ is not statistically significant, and is likely due to PPMAP being unable to break the observed temperature/β degeneracy in the coldest, densest parts of the filament, which are not as well sampled in the Rayleigh-Jeans regime.

I estimate the width of the median filament profile, by taking the FWHM of the fitted Plummer-like profile. I refer to this quantity as $\mathrm{FWHM_{PMP}}$, where the PMP

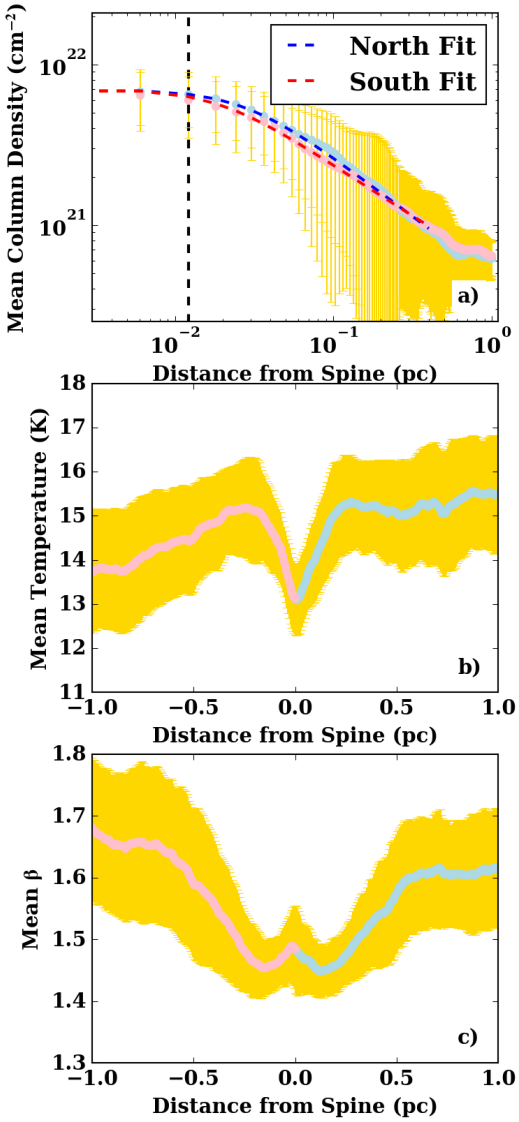

Figure 5.11. Median profiles of the (a) column density, $N_{\mathrm{H_2}}(b)$, (b) mean line of sight dust temperature, $T_{\mathrm{D}}(b)$, and (c) mean line of sight dust opacity index, $\beta(b)$, for the L1495/B213 complex. These parameters are given as a function of impact parameter from the spine of the filament, b.

subscript is an acronym of "Plummer-like Median Profile", i.e., the Plummer-like fit to the median cut of column densities. The FWHM of a generic Plummer-like profile is given by the equation

$$\text{FWHM} = 2r_0\sqrt{0.5^{-2/(p-1)} - 1}. \tag{5.3}$$

I take the average of the north and south values of both r_0 and p (i.e. $\bar{r_0} = 0.022$pc and $\bar{p} = 1.88$) and derive a value of the FWHM_{PMP} of (0.087 ± 0.003) pc. I calculate the line density of the median profile, μ_{PMP}, by integrating the median Plummer-like fit out to $b = 0.4$ pc. The line density of an axially symmetric Plummer-like profile is

$$\mu = 2\int_{b=0}^{b=b_{max}} N_0 \left\{1 + \left(\frac{b}{r_0}\right)^2\right\}^{-(p-1)/2} db. \tag{5.4}$$

This produces a value of $\mu_{\text{PMP}} = 26.8\ \text{M}_\odot\,\text{pc}^{-1}$, assuming the value of N_0 presented in Table 5.5. $N_0 = 6.4 \times 10^{21}\ \text{H}_2\,\text{cm}^{-2}$ is a factor of ~ 2.5 less than the value published in Palmeirim et al. (2013), $N_0 = 16 \times 10^{21}\ \text{H}_2\,\text{cm}^{-2}$. Similarly, Palmeirim et al. (2013) derive a line mass of $54\,\text{M}_\odot\,\text{pc}^{-1}$, nearly double the value I recover.

However, the standard method of estimating filament widths is to calculate the FWHM of a Gaussian function which is fit to the median filament profile in a narrow region around $b = 0$ pc. Thus, to compare my results with the literature values, I convert my value for FWHM_{PMP} into an equivalent FWHM_{GMP} (where GMP stands for Gaussian Median Profile). This is done by equating second derivatives of the Plummer-like and Gaussian functions at the peak, giving

$$\text{FWHM}_{\text{GMP}} = \left(\frac{8\ln 2}{p-1}\right)^{1/2} r_0. \tag{5.5}$$

This produces a value of $\text{FWHM}_{\text{GMP}} = 0.056 \pm 0.002$ pc, which lies at the low end of the distribution of filament widths published in Arzoumanian et al. (2019), and is nearly a factor of two smaller than the width of the L1495/B213 complex presented in Palmeirim et al. (2013).

5.3.2.2 Variation Along the Filament Length

While a single, median cut defining the entire filament can provide useful global parameters, it provides no information as to the variations along the filament length. Therefore, to evaluate these variation, I returne to the 1100 individual column density cuts across L1495/B213, and utilise a modified version of the FILCHAP algorithm (Suri et al. 2019) to fit many Plummer-like models along the length of the spine. Individual cuts often have a poor signal to noise, and are not well fit by a Plummer-like

model, so FilChaP bundles adjacent cuts together, which produces a local median profile for each bundle in a similar method to deriving the global median profile above. I set the number of cuts in a bundle to 12, which means adjacent bundles are separated by $\sim$0.05 pc ($\sim$72″). At this stage, the 68 corrupted cuts are again removed. This means that some bundles contain less than 12 cuts, but, by removing the cuts after the bundling process I ensure that each bundle is spaced equally along the filament. This process produces 92 local median profiles.

Each bundle is then fit independently with a Plummer-like profile. Due to the lower signal to noise in the bundles compared to the global median profile, I fix the value of the Plummer exponent to $p = 2$. In addition, FilChaP automatically performs a background subtraction, thus setting the value of $N_{\rm B} = 0$, and does not account for variation between the north and south sides of the filament. Thus equation 5.1 becomes

$$N_{\rm H_2}(b) = N_0 \left\{ 1 + \left(\frac{b}{r_0} \right)^2 \right\}^{-1/2}, \tag{5.6}$$

where N_0 becomes $n_0 r_0 \pi \sec i$. The algorithm returns only values of N_0 and r_0 for each fitted bundle.

As before, I uses these parameters to calculate a FWHM and a line density, μ, for each bundle. Figure 5.12 (a) shows the variation in the FWHM along the filament as coloured circles placed at the central position of each of the 92 bundles. The median and MAD of the distribution of widths is $\widetilde{\rm FWHM} = 0.08 \pm 0.02$ pc, while the average uncertainty an individual width estimate is 0.005 pc. Figure 5.12(b) indicates the value of N_0 for each bundle, with a median and MAD of $\widetilde{N_0} = (4.93 \pm 1.46) \times 10^{21}$ $\rm H_2\,cm^{-2}$. As with the width estimates, the average uncertainty on individual estimates of the central column density is an order of magnitude smaller than the MAD of the distribution of all central column densities, with a value of 0.2×10^{21} $\rm H_2\,cm^{-2}$. Both these median values are consistent with the values I derive from the median filament profile.

Figure 5.12(c) gives the line density at every spine point, calculated from equation 5.4. The median and MAD of the distribution of line densities is $\widetilde{\mu} = 17.8 \pm 4.4$ $\rm M_\odot\,pc^{-1}$. I compare this value with the critical line density above which an isothermal cylinder can no longer be supported against gravity by thermal pressure alone,

$$\mu_{\rm c} = \frac{2c_{\rm s}^2}{G}, \tag{5.7}$$

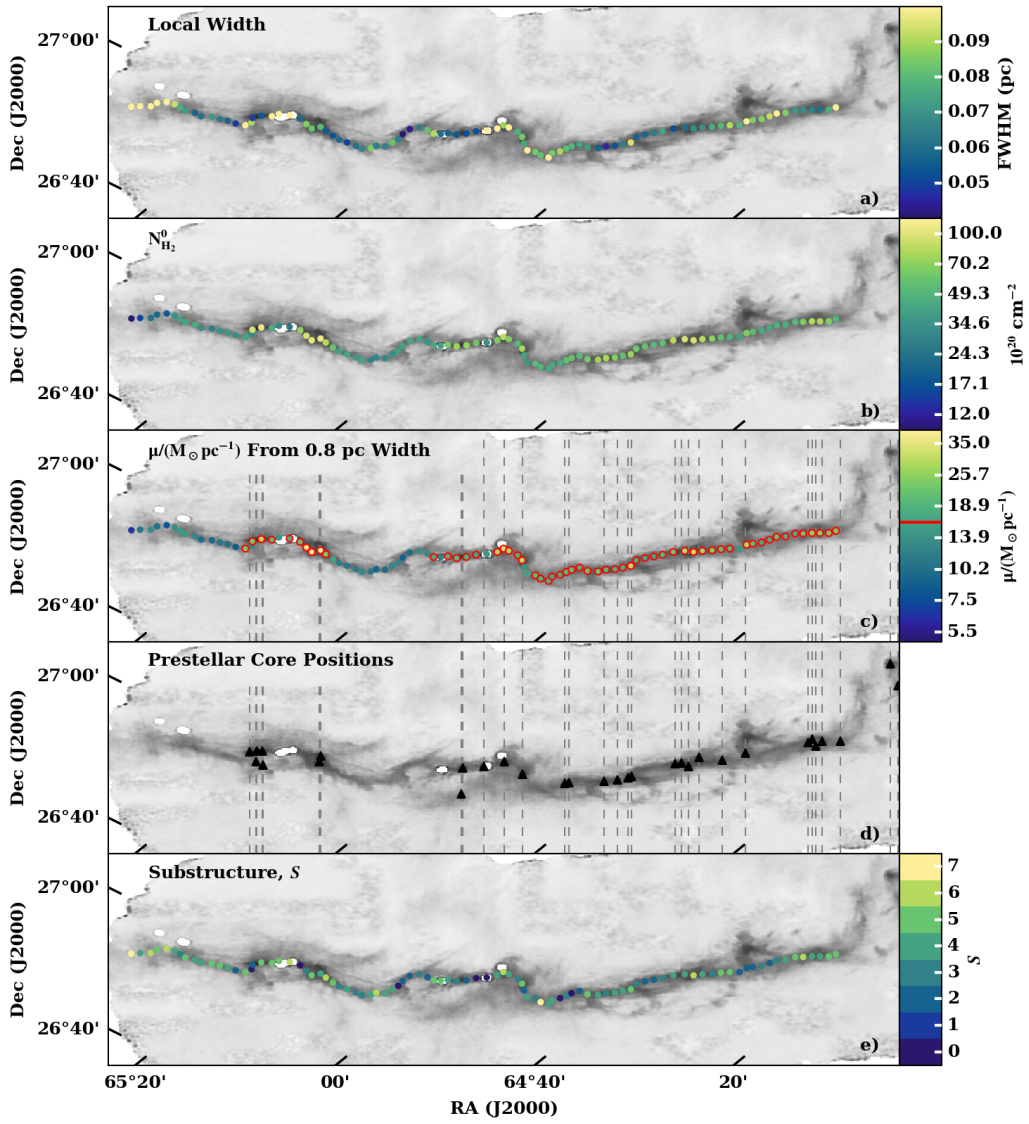

Figure 5.12. Results from using the FILCHAP algorithm to investigate variations in (a) FWHM, (b) central column density, N_0, and (c) line density, μ, along the length of the filament. The value of each parameter at the location of each FILCHAP bundle is given by the colour of each circle. Red outlines around circles in (c) indicate bundles with a line density exceeding the nominal critical value of 16 $M_\odot$ pc^{-1} for a gas temperature of 10 K. Panel (d) shows the positions of pre-stellar cores taken from Marsh et al. (2016), with vertical dashed lines in (c) and (d) highlighting the location of each core. Panel (e) indicates the degree of resolved sub-structure, $\mathcal{S}$, identified by FILCHAP.

where c_s is the isothermal sound speed. Palmeirim et al. (2013) estimate $c_s = 0.19$ $\mathrm{km\,s^{-1}}$ from CO observations, which corresponds to a kinetic gas temperature of 10 K, and hence μ_c =16.2 $\mathrm{M_\odot\,pc^{-1}}$. With these values the filament appears to be trans-critical. We note that the PPMAP estimates indicate that the mean line-of-sight mass-weighted dust temperature of the filament is ∼14 K, and is higher in the surroundings, but the gas and dust temperatures are not necessarily equal.

In Figure 5.12(c), I highlight bundles with $\mu > \mu_c$ with a red outline. There is a clear break close to the junction of the B213 and B211 sub-filaments, with the B213 filament containing far fewer super-critical bundles than B211. The median line density for bundles in the B213 filament is $\widetilde{\mu_{\mathrm{B213}}} = 13.4$ $\mathrm{M_\odot\,pc^{-1}}$, while for B211 $\widetilde{\mu_{\mathrm{B211}}} = 19.9$ $\mathrm{M_\odot\,pc^{-1}}$.

To investigate this further, in Figure 5.12(d) I plot the locations of the pre-stellar cores from Marsh et al. (2016) as black triangles, and place vertical lines on both panels (c) and (d) to mark the position of each core. There are only nine pre-stellar cores on or near the spine of the B213 sub-filament, while there are 19 on the B211 sub-filament. In addition, the positions of these cores align well with the positions of the super-critical bundles. There are 9 masked protostellar objects near the B213 filament which do not appear to match well with super-critical regions. However, in the process of masking, flux, and thus column density, is removed from the map, so I cannot draw conclusions from their positions, other than to note that B213 may be in a more advanced state of evolution.

These differences between the two sub-filaments can be explained if I consider turbulent mass accretion (Clarke et al. 2017). This suggests that the line density of the filament has never been uniform, and that some regions have reached a super-critical point before others. Fragmentation occurs in regions that become super-critical; pre-stellar cores then form, and grow to become protostellar objects. The time scale for this evolution is approximately 0.5 Myr (e.g., Enoch et al. 2008). As these cores evolve, they will deplete mass from the filament as they draw material along its length, potentially reducing the line density in neighbouring regions. Assuming an infall rate onto the filament of ∼32 $\mathrm{M_\odot\,pc^{-1}\,Myr^{-1}}$ (Clarke, Whitworth, and Hubber 2016; Palmeirim et al. 2013), the condensation time scale is comparable to the time scale for replenishment of the line density.

Thus I infer that B213 initially grew more rapidly to a super-critical state, and thus fragmented and evolved faster. It is now in a state of replenishment. Conversely, B211 grew more slowly, and is now at the stage where it is beginning to fragment into pre-stellar cores.

To further test this inference, for each of the 24 pre-stellar cores, I identify

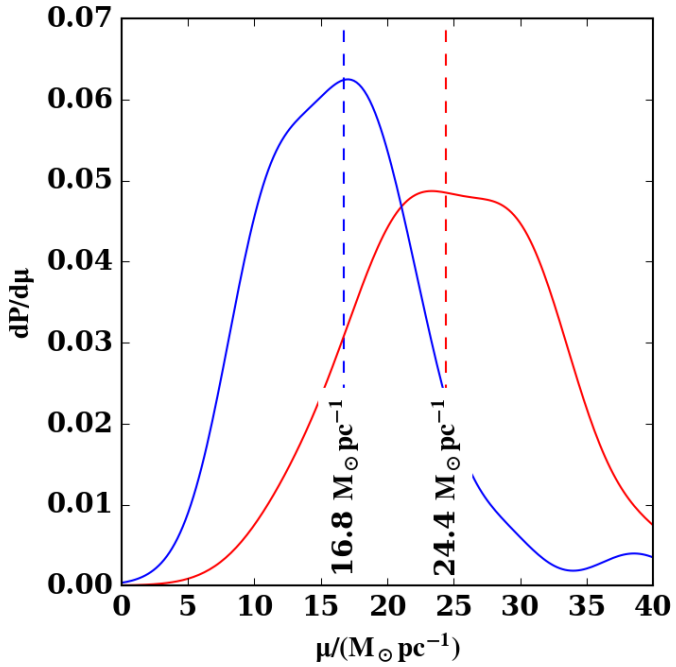

Figure 5.13. Kernel smoothed PDFs of the line masses of bundles closest to each of the pre-stellar cores that lie along the spine of the filament (from Marsh et al. 2016) in red, and of all other bundles, excluding those closest to the cores in blue. Vertical blue and red dashed lines indicate the median line density of each distribution.

the nearest bundle and note its line density. The red curve in Figure 5.13 shows the kernel-smoothed PDF of those values, and the red vertical dashed line indicates the median line density of the distribution, $\widetilde{\mu}_{\rm red} = 25.5$ M$_\odot$ pc^{-1}. Due to the positions of the cores, a single bundle is occasionally closest to two separate cores. In this instance, it is counted twice in the distribution. The blue curve shows the distribution of line densities from the remaining 72 bundles, with the blue vertical dashed line providing a median value of $\widetilde{\mu}_{\rm blue} = 16.8$ M$_\odot$ pc^{-1}. I perform a Kolmogorov-Smirnov (KS) two-sample test to determine the distance between the two distributions, and find $D_{\rm KS} = 0.58$. This indicates that the two distributions are well separated, while the probability that they are drawn from the same underlying distribution is just $p_{\rm KS} = 4 \times 10^{-6}$. Thus, I conclude that the prestellar cores lie, almost exclusively, on regions of the filament that are super-critical.

FILCHAP also returns a substructure parameter, $\mathcal{S}$, for each bundle. The algorithm obtains this by counting the number of secondary maxima and inflection points in a bundle. Thus, it is a measure of the 2D plane-of-sky resolved sub-structure. It can be assumed that some of the internal 3D sub-structure is lost due to projection effects. Figure 5.12(e) gives the substructure value of each bundle within the filament. Clarke

et al. (2018) suggests, on the basis of simulations, that internally sub-structured filaments can be supported against collapse, even as their line density increases above the critical limit due to the velocity dispersion between the sub-structured elements. This effect could appear in my analysis of the L1495/B213 complex as a correlation between $\mathcal{S}$, the bundle line density, and the bundle FWHM.

Figure 5.14 displays the relationship between each of the returned FilChaP parameters, or their derivatives. Below each plot, the Pearson correlation coefficient, $r_{\rm P}$, and Pearson p-value, $p_{\rm P}$, is given. $r_{\rm P}$ gives the degree to which two parameters are correlated, with a value of ± 1 indicating perfect positive/negative correlation, and a value of 0 indicating that the parameters are uncorrelated, while $p_{\rm P}$ is the probability that a correlation of $r_{\rm P}$ is found in a data set containing no correlation.

I find no correlation between $\mathcal{S}$ and any of the remaining parameters, and thus, I cannot determine if the resolved 2D sub-structure in the filament is supporting the structure against collapse. I also find no correlation between N_0 and FWHM, nor between μ and FWHM. However, I find a strong, positive correlation between N_0 and μ, with an $r_{\rm P} = 0.874$, and a vanishingly small $p_{\rm P}$. This indicates that the the low values of μ, when compared with the literature, are largely due to lower estimates of the central column density, N_0.

5.3.2.3 Fitting with $p = 4$

As noted in Section 5.3.2.1, and in works such as Arzoumanian et al. (2011), Palmeirim et al. (2013), and Arzoumanian et al. (2019), when fitting to the global median filament profile, a value close to $p = 2$ is often recovered. However, an isothermal cylinder in hydrostatic equilibrium, has a $p = 4$ profile (Ostriker 1964).

Plummer-like profiles can be subject to a degeneracy, with the effect of small values of p and r_0 being mimicked by large values of p and r_0 (Suri et al. 2019), if the dynamic range of the profile is limited. This is true, in general, for the L1495/B213 filament, where $N_0/N_{\rm B} \sim 20$. Therefore, while FilChaP does not allow the value of p to vary during the fitting process, I have rerun the algorithm with an imposed value of $p = 4$. The result is, on average, a much better fit, with a median reduced $\chi^2_{p=4} = 8.35$ for all bundles. This is in contrast to the much higher value of the median reduced $\chi^2_{p=2} = 29.23$ obtained with $p = 2$. This may suggest that the filament is much closer to an ideal model of a hydrostatic, isothermal cylinder than previously believed. This could be due to efficient CO cooling inside the accretion shock at the boundary of the filament, as proposed by Whitworth and Jaffa (2018).

While a $p = 4$ profile is a better fit to individual bundles, a value of $\bar{p} = 1.88$ is found on the global median profile. This result may appear to be a contradiction.

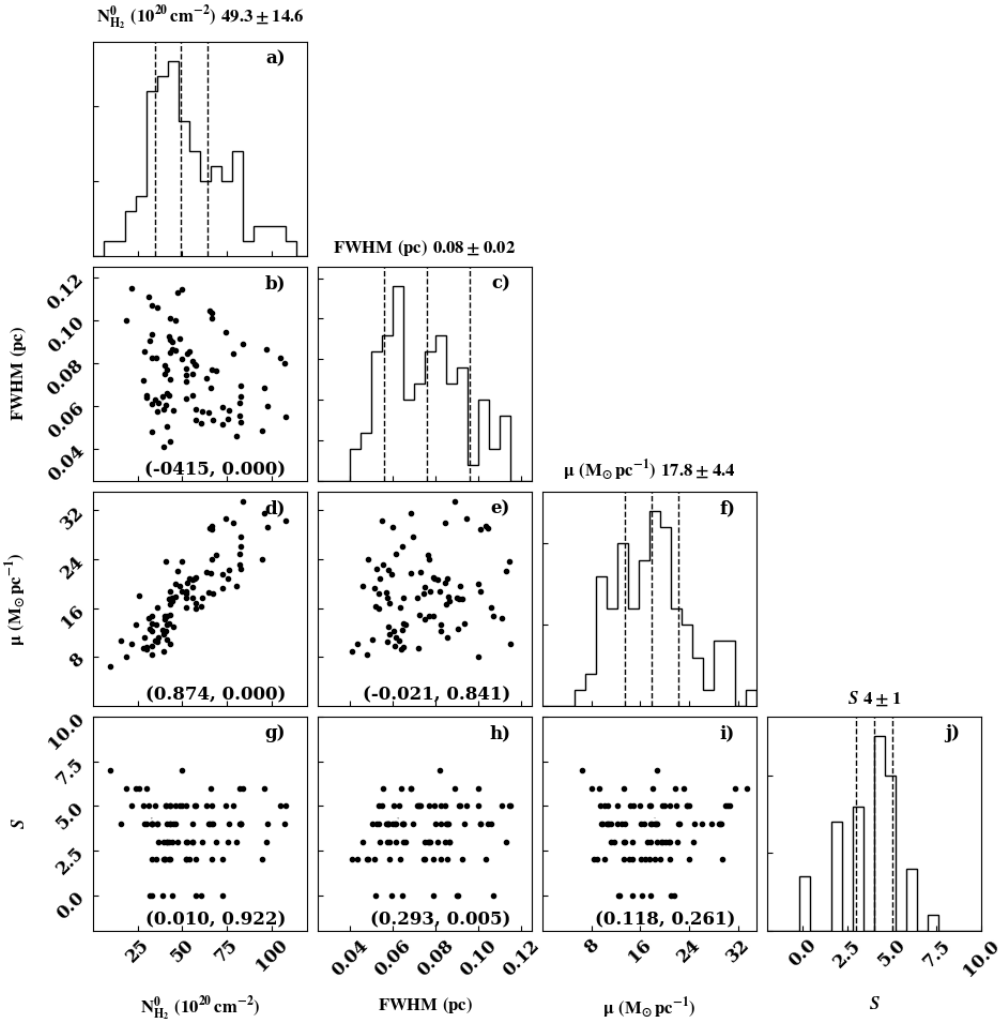

Figure 5.14. Relationship between each of the four parameters derived from the FILCHAP analysis; central column density, $N^0_{H_2}$, FWHM, line density, μ, and resolved sub-structure parameter, $\mathcal{S}$. At the top of each column, a histogram shows the distribution of each parameter, along with the median and MAD.

However, this can be explained as the global median profile is an average of all 1032 individual cuts across the filament, which will, in principal, each have their own value of N_0 and r_0. Slight variations to either side of the spine, or any resolved substructure, have the effect of broadening the profiles, and thus reducing the apparent value of p. The FilChaP bundles are much smaller regions, which individually will suffer less from this effect.

In fitting the bundles with a value of $p = 4$, I recover a value of $\widetilde{r_0} = 0.063 \pm 0.023$ pc. The larger value of the Plummer-like exponent modifies the equation for the FWHM, giving

$$\text{FWHM} = 2\left(2^{2/3} - 1\right)^{1/2} r_0. \tag{5.8}$$

The median value of the widths of the bundles is $\widetilde{\text{FWHM}} = 0.097 \pm 0.036$, which is consistent with both the values recovered from the FilChaP $p = 2$ fitting, and the global median profile fitting. This is because a $p = 4$ Plummer-like profile drops off much more steeply than a $p = 2$ profile for $r > r_0$.

5.3.3 Comparison with *Herschel* Observations

As discussed in Chapter 4, I note the importance of verifying that PPMAP produces a model that is a good fit to the observation data, both on a local, pixel-by-pixel scale, and on a global scale through the Goodness of Fit parameter, $\mathcal{G}$. I also note that it is vital to ensure that the PPMAP results are at least as good a fit, if not better, than those of a standard MBB fitting routines. To facilitate this, I first produce a column density and temperature map from a MBB routine modified with the resolution recovery technique described in Palmeirim et al. (2013). I use a fixed, global value of $\beta = 2$ as described in their work, but substitute the *Herschel* observations I use to produce my PPMAP models. This is done to produce results as close to the published work as possible, while making use of the updated HIPE pipelines, and allowing a better comparison between the PPMAP and the MBB technique.

Figure 4.1 shows the recovered *Herschel* observations for both PPMAP and the MBB fitting routine. These are produced via the method described in Chapter 4, Sec 4.0.1, for the 160 µm, 250 µm, 350 µm and 500 µm bands. I exclude the 70 µm and 850 µm bands, as they do not inform the MBB fit, and thus a comparison for those bands cannot be drawn. The left-most column shows synthetic observations derived from PPMAP. The centre column are the true *Herschel* observations, while the right-most column are the synthetic observations recovered from the MBB products.

Table 5.6. Goodness of Fit parameter, $\mathcal{G}$, for synthetic observations recovered from the models produced by PPMAP and a MBB fitting technique. Columns titled as "Whole Map" denote the values for the entire region, while columns labelled "Filament Region" provide values for a 1 pc radius strip around the B211 and B213 sub-filaments.

	Whole Map		Filament Region	
Band	$\mathcal{G}_{\rm PPMAP}$	$\mathcal{G}_{\rm MBB}$	$\mathcal{G}_{\rm PPMAP}$	$\mathcal{G}_{\rm MBB}$
160 µm	0.23	1.05	0.13	1.01
250 µm	0.11	1.02	0.10	0.92
350 µm	0.08	0.37	0.07	0.38
500 µm	0.08	0.09	0.08	0.10

PPMAP produces a good fit to the data in both the 160 µm and 250 µm bands in all regions of the observations, while the MBB technique significantly overestimates the contribution from the flux at shorter wavelengths. At 350 µm and 500 µm, the two techniques are more comparable, though PPMAP still performs better in the diffuse regions.

The Goodness of Fit parameter for each band and technique is presented in Table 5.6, for both the entire observable region, and for a 1 pc radius strip around the B211 and B213 sub-filaments. In all cases, PPMAP reproduces the observations better than the MBB fitting routine. This is particularly noticeable in the shorter wavelength bands and in the denser regions surrounding the filament.

5.4 Conclusions

I use PPMAP and *Herschel* observations that benefit from the final reduction pipeline to produce a dust model of the Taurus L1495/B213 complex. This gives an estimate of the H_2 column density, as inferred from dust column density with a gas-to-dust ratio of 100, at every sky position, and spanning 12 temperature bands and four opacity index bands. The results indicate that the FWHM and line density, μ, of the filament are smaller than previously published values. In addition, they also provide evidence that the temperature falls sharply within the filament structure, and that there is a shift in values of β between dust within the filament and dust in the surrounding cloud.

I conclude that much of the dust within the filament has a mean line-of-sight temperature $\leq$16 K, while the surrounding medium has a dust temperature of $\geq$16 K. Only a single region near to a Herbig Ae/Be star shows significant quantities of dust at temperatures above 18 K. The range of temperatures populated in the model is broader than those returned by standard MBB techniques.

Dust within the filament has a mean line-of-sight opacity index of $\beta \leq 1.5$, while the surrounding cloud generally displays $\beta \geq 1.7$. It is, therefore, likely that there is a change in the dust properties at the filament boundary, which could be due to changes such as those found in an accretion shock, or due to mantle growth around grains.

A median cut across the filament is well fit by a Plummer-like profile, with an exponent of $\bar{p} = 1.88$, and an inner radius of $\bar{r}_0 = 0.022$ pc. This gives an average $\mathrm{FWHM}_{\mathrm{PMP}}$ of the filament of 0.087 pc. While this appears to agree with previously published widths of 0.09 pc for the L1495/B213 complex, those widths are obtained by fitting a Gaussian profile to the inner portion of the filament. For comparison, I convert the Plummer-like FWHM to one for an equivalent Gaussian, which produces a value of $\mathrm{FWHM}_{\mathrm{GMP}} = 0.056$ pc, a reduction in width of almost 1/2.

The shallow Plummer-like exponent of $p \sim 2$ that is returned by fitting the median filament profile is likely a consequence of the smoothing of resolved sub-structure, and confusion between variations along the filament length. I find that fitting Plummer-like models to smaller bundles along the spine shows that a value of $p = 4$ produces a better fit to the data.

Additionally, I find that the line density of the filament has a median value of just 17.8 ± 4.4 $\mathrm{M}_{\odot}\,\mathrm{pc}^{-1}$, three times smaller than the $54\,\mathrm{M}_{\odot}\,\mathrm{pc}^{-1}$ published in Palmeirim et al. (2013). I assume the canonical value of the critical line density, as determined from a gas temperature of 10 K, and find only small, local sections of the filament are super-critical, and prone to collapse under gravity alone. These regions agree closely with the positions of pre-stellar cores, which suggests that local variations in density, rather than global ones, are responsible for determining where and how filaments fragment into cores.

Finally, I determine that PPMAP produces a much better fit to the observed data than typical MBB fitting techniques, and that the ability to distinguish dust temperatures along the line of sight is vital for obtaining an accurate column density of a region.

Chapter 6
The Ophiuchus L1688 and L1689 Clouds

In this chapter I present the results of applying the PPMAP column density estimation procedure to *Herschel* and SCUBA-2 observations of the L1688 and L1689 sub-regions of the Ophiuchus molecular cloud. I compare variations in the dust properties between the two sub-regions as revealed by PPMAP. I identify a network of filamentary structures within the sub-regions, and present a detailed analysis of their physical properties. I explore the distribution of mass within each of the sub-regions, and link it to the mass associated with prestellar cores and dense, compact clumps. I examine the impact of the S1 and HD147889 pre-main sequence stars on the filaments in the L1688 sub-region.

6.1 An Overview of the Ophiuchus Molecular Cloud

The Ophiuchus molecular cloud complex is a star-forming region commonly associated with the Gould Belt. As with the Taurus L1495/B213 complex, the Ophiuchus complex is estimated to lie at an average distance of ∼140 pc from the solar system (Mamajek 2008; Ortiz-León et al. 2018). Lynds (1962) classified a number of sub-regions within the complex, describing two large concentrations of mass (L1688 and L1689) and a number of additional, lower density streamers which extend eastwards from those clumps. Figure 6.1 presents a finding chart for the two mass concentrations. Recent VLBA and *Gaia* observations have verified the distance to the cloud complex, and have indicated that L1688 lies ∼5 pc to ∼10 pc closer than L1689 (138.4 pc for L1688, and 144.2 pc for L1689)(Ortiz-León et al. 2017; Ortiz-León et al. 2018).

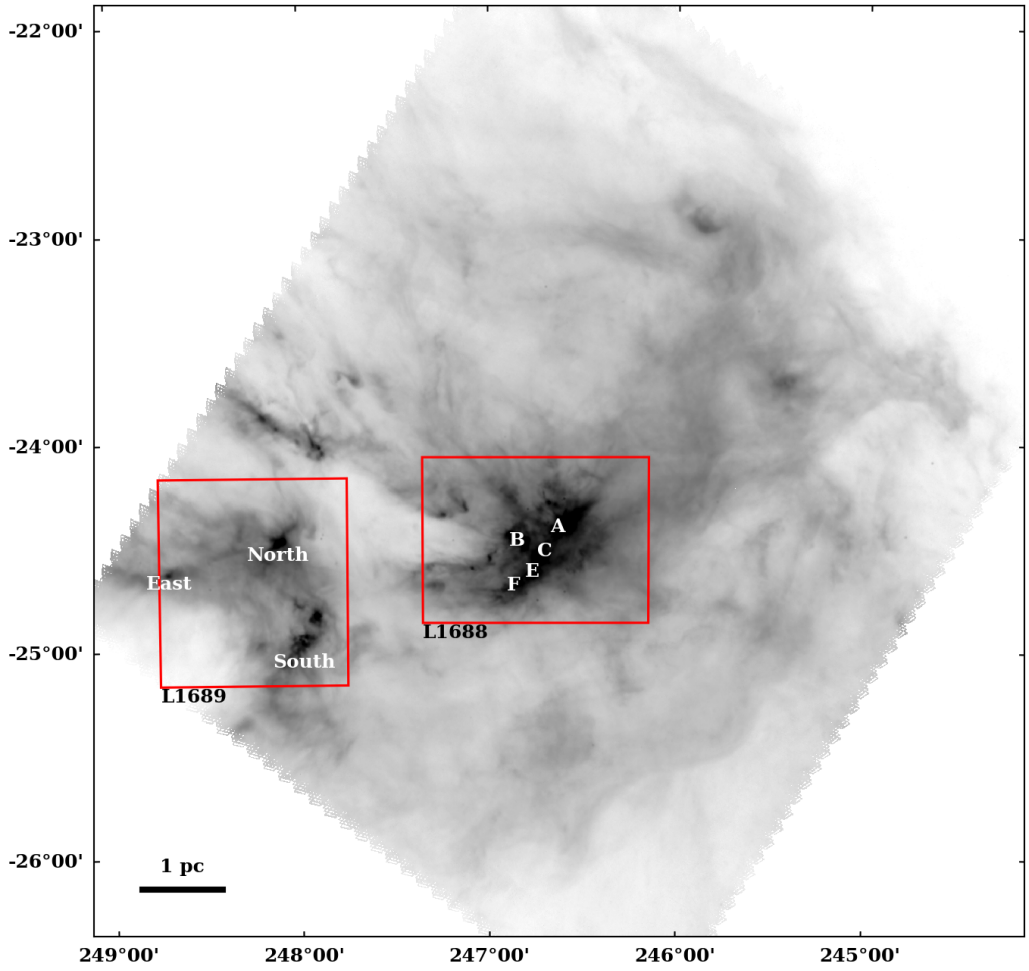

Figure 6.1. A finding chart of the Ophiuchus molecular cloud complex, indicating the different regions associated with the Lynds (1962) L1688 and L1689 catalogue dark nebulae. L1688 is further sub-divided into the clumps Oph A, Oph B, Oph C, Oph E, and Oph F, while L1689 is split into three regions, L1689-North, L1689-South, and L1689-East.

The large scale shape of the cloud complex is suspected to be largely due to feedback from the Upper Scorpius OB2 association (e.g., Loren and Wootten 1986; Motte, Andre, and Neri 1998), which is located west of the region, sweeping up material, enhancing the density of L1688 and L1689, and increasing their star-formation rates (particularly for the L1688 sub-region, Nutter, Ward-Thompson, and André 2006), while driving the low density streamers to the north and east. The L1688 and L1689 sub-regions themselves are typically subdivided into a number of visually distinct regions. Loren, Wootten, and Wilking (1990) identifies six dense gas clumps (Oph A to Oph F) within L1688, while L1689 is split into three clumps, which are given the identifiers L1689-East, L1689-North, and L1689-South (Loren, Wootten, and Wilking 1990; Pattle et al. 2015). These sub-divisions are indicated on Figure 6.1.

The streamer and hub nature of the cloud was first identified by Loren (1989), who indicated that the streamers and denser sub-regions resembled tangled cobwebs, while recent work has identified filaments within L1688 and L1689 (Ladjelate et al. 2020). Despite this, many studies of the Ophiuchus molecular cloud complex focused directly on the formation of pre- and protostellar cores without relating them to filaments, as typically done in other fields. These studies have indicated that L1688 has a higher star formation rate than L1689 (Nutter, Ward-Thompson, and André 2006; Pattle et al. 2015; Ladjelate et al. 2020), with L1689 presenting lower activity than many Gould Belt regions (André et al. 2010; Könyves et al. 2015). As with many nearby star forming regions, polarimetry data indicates a magnetic field which is initially parallel to low density striations in the dust, but which switches to being perpendicular to high density filaments, indicating that these structures may be being fed along magnetic field lines, as is proposed for the Taurus L1495/B213 complex (Soler 2019).

This thesis marks the first detailed investigation of the filament properties within the L1688 and L1689 sub-regions.

6.2 Observations of the Ophiuchus Molecular Cloud

The primary observations for the investigation of the Ophiuchus Molecular Cloud were five SPIRE/PACS Parallel observations, taken as part of the *Herschel* Gould Belt Survey in the PACS 70 µm and 160 µm, and SPIRE 250 µm, 350 µm and 500 µm bands. The observations comprised 10 individual scans, covering the areas shown in Figure 6.2.

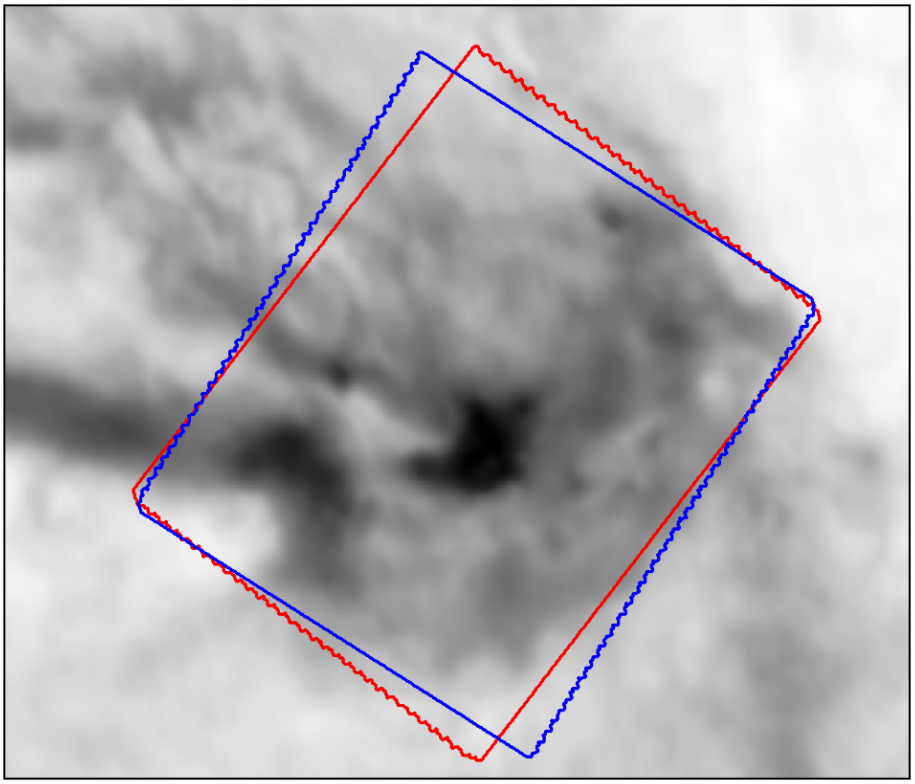

(a) PACS scan areas.

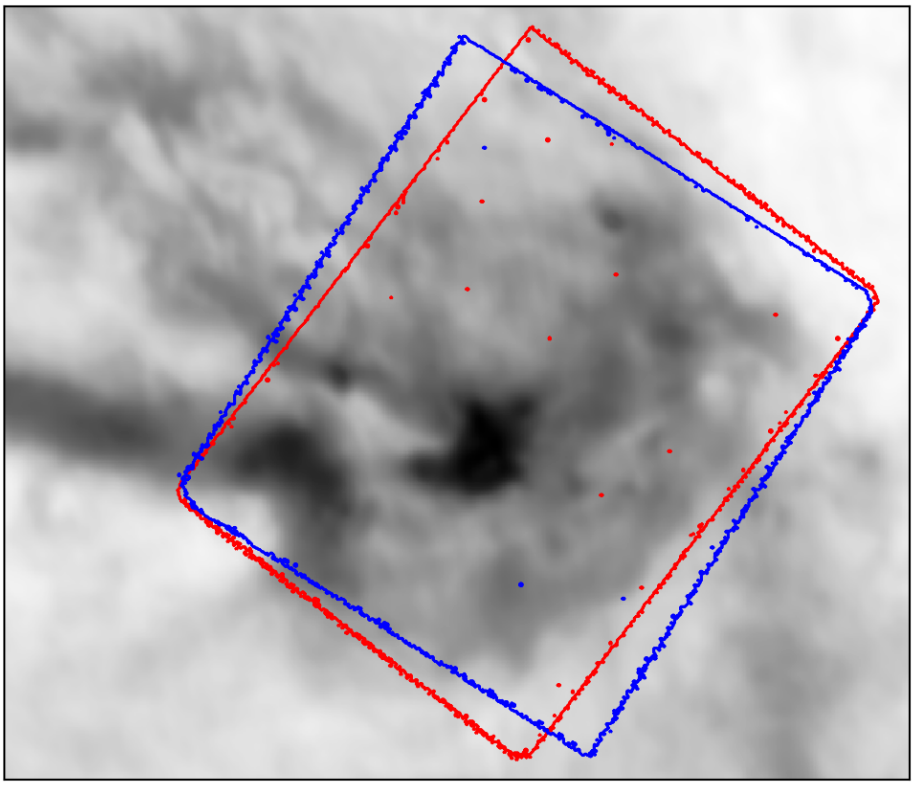

(b) SPIRE scan areas.

Figure 6.2. *Herschel* scan areas for the PACS and SPIRE observations of the Ophiuchus molecular cloud. Both images show nominal (red box, ObsID 1342205093), and orthogonal (blue box, ObsID 1342205094) scans. Background image taken from the *Planck* optical depth model of the region, at 5′ resolution (Planck Collaboration 2016d).

Unlike the L1495/B213 region, the Ophiuchus Molecular Cloud could be observed with a single pair of nominal (red) and orthogonal (blue) scans. The ObsIDs and scan dates are given in Table 6.1.

Table 6.1. The ObsIDs of the *Herschel* PACS and SPIRE scans of Ophiuchus, and their observation dates.

Scan Direction	ObsID	Date
PACS and SPIRE		
Nominal	1342205093	25/09/2010
Orthogonal	1342205094	25/09/2010

As with the L1495/B213 complex, the data reduction followed the method described in Chapter 2, Section 2.1.2; Zero-point corrections were determined and applied to the PACS band observations. Table 6.2 gives the offsets for the PACS and SPIRE bands.

Table 6.2. Zero-Point Offsets and regional Gaussian noise estimates for PACS, SPIRE and SCUBA-2 observations of Ophiuchus. I obtained the PACS and SCUBA-2 offsets through the procedure described in Chapter 2, Section 2.1.6, while SPIRE offsets were applied as part of the archive data reduction process to obtain Level 2 products. Gaussian noise was estimated through visual inspection of each band, as described below.

		L1688	L1689
Band	Offset (MJy/sr)	Noise (MJy/sr)	
PACS 70 µm	-8.4	15.0	8.45
PACS 160 µm	243.5	17.1	12.4
SPIRE 250 µm	93.0	14.0	5.80
SPIRE 350 µm	47.6	4.76	3.28
SPIRE 500 µm	18.1	2.08	1.46
SCUBA-2 850 µm	12.3	2.26	1.75

The SCUBA-2 850 µm supplementary observations were first published by Pattle et al. (2015), and have been supplied already reduced by Emily Drabek-Maunder. The observations are part of the JCMT Gould Belt Survey, and consist of seven 30′ diameter pointings, taken in the PONG1800 mapping mode. Reduction then follows the procedure described in Chapter 2, Section 2.1.3, with specific details published in Pattle et al. (2015). The reduced pointings are mosaicked together into a continuous region, the coverage of which is shown in Figure 6.3.

As previously discussed PPMAP produces artefacts around bright point sources

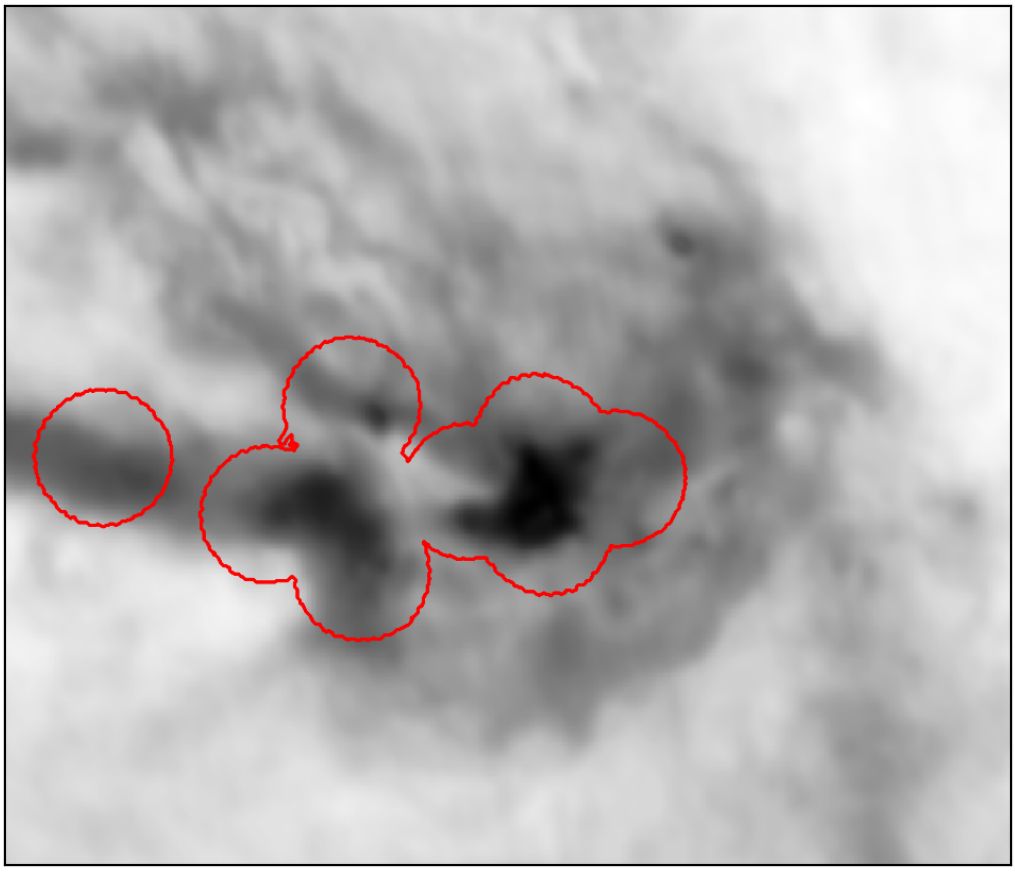

Figure 6.3. JCMT SCUBA-2 850 µm scan area for the composite observation of the Ophiuchus molecular cloud. The observations, taken as part of the JCMT Gould Belt Survey, were first published by Pattle et al. (2015), and were supplied by Emily Drabek-Maunder. Background image taken from the *Planck* optical depth model of the region, at 5′ resolution (Planck Collaboration 2016d).

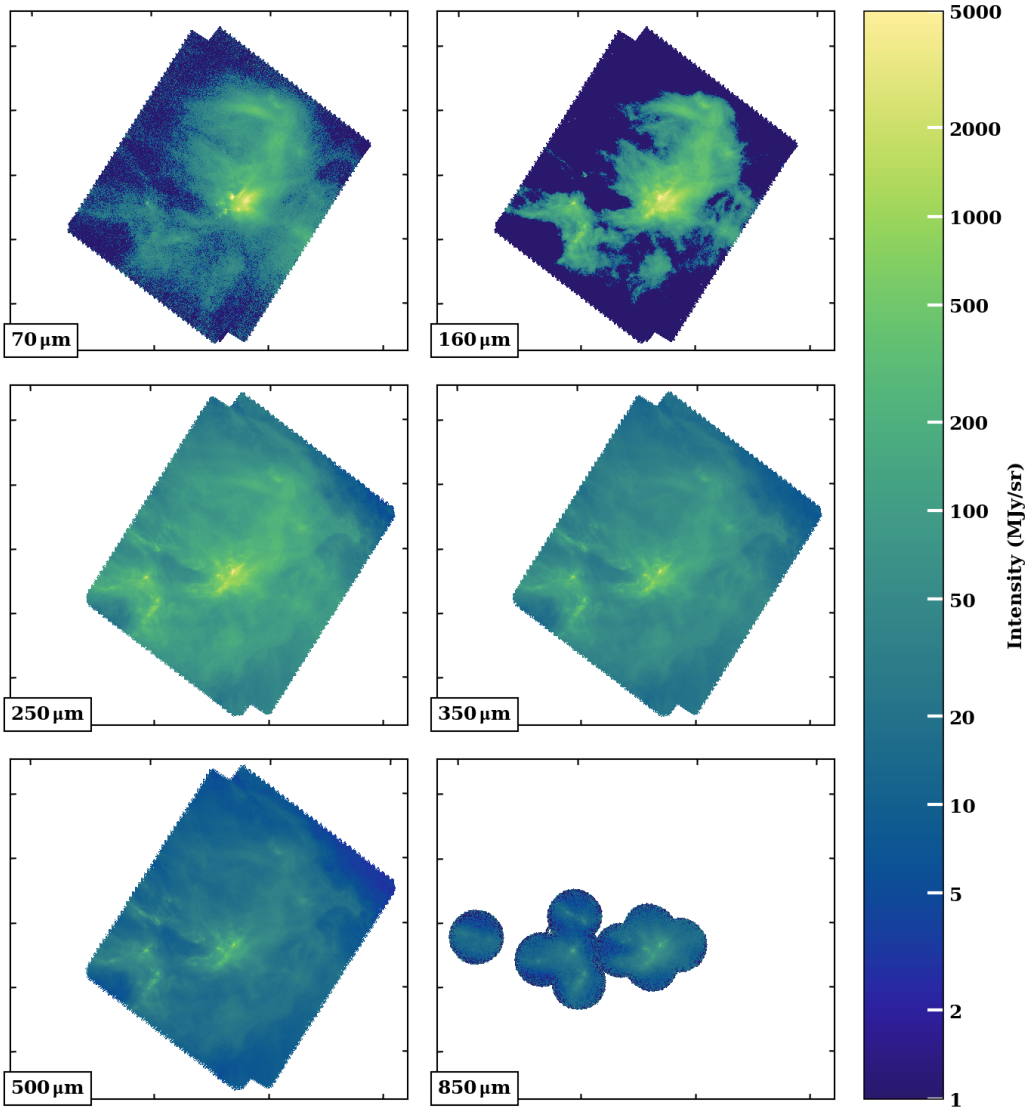

Figure 6.4. *Herschel* PACS 70 µm and 160 µm and SPIRE 250 µm, 350 µm and 500 µm observations, and JCMT SCUBA-2 850 µm observations of the Ophiuchus molecular cloud complex.

associated with 70 µm emission from optically thick objects. However, unlike the Taurus molecular cloud, extended emission from Ophiuchus dominates the artefacts in most regions. Therefore, I do not mask all protostellar sources in the observations. Figure 6.4 shows the reduced observations in each of the five *Herschel* bands and the single SCUBA-2 band at 70 µm, 160 µm, 250 µm, 350 µm, 500 µm and 850 µm, in a 6.2° by 5.3° region centred on $16^{\mathrm{h}}28^{\mathrm{m}}06.32^{\mathrm{s}}$, $-24°08'04.61''$ (247.026 370 4°, −24.134 614 26°), with a position angle of 0°.

6.2.1 Division into Sub-Regions

As PPMAP can take a long time to fit dust models to fields with large angular sizes, I define two sub-regions in the Ophiuchus observations which encompass the L1688 and L1689 structures. For each sub-region, I reproject the observations in each of the six bands to produce smaller intensity maps, which can then be passed to PPMAP. The L1688 observations cover a 1.2° by 0.8° field of view centred on $16^{\mathrm{h}}27^{\mathrm{m}}01.02^{\mathrm{s}}$, $-24°28'00.00''$ (246.750 000 0°, −24.466 666 6°). The L1689 observations cover a 1.0° by 1.0° area centred on $16^{\mathrm{h}}33^{\mathrm{m}}01.53^{\mathrm{s}}$, $-24°39'00.00''$ (248.250 000 0°, −24.666 666 6°). The sub-regions are shown in Figure 6.1.

A set of initial tests of PPMAP on the sub-regions had indicated that, while the artefacting due to point sources in L1688 did not greatly inhibit fitting the extended emission, two sources in L1689 prevented a reliable fit to the data. These sources are located at $16^{\mathrm{h}}32^{\mathrm{m}}00.96^{\mathrm{s}}$, $-24°56'42.00''$ and $16^{\mathrm{h}}32^{\mathrm{m}}22.56^{\mathrm{s}}$, $-24°28'33.60''$. I identify them in the literature as L1689-IRS6 (Greene et al. 1994), a Class I source, and *IRAS* 16293-2422 (Mundy et al. 1992), a binary/multiple Class 0 system. I mask both objects with a 40″ diameter circular patch in each of the input observations before conducting further PPMAP runs.

As previously stated PPMAP requires estimates of the noise level in each observation to produce good quality fits to the data. I follow the procedure for the L1495/B213 complex, identifying the standard deviation away from areas of bright structure in each observing band, within circular regions with angular radius ∼5′. The Ophiuchus estimates for each band and sub-region are given in Table 6.2.

6.3 PPMAP Analysis of Ophiuchus

For this investigation I choose to run PPMAP with a 14″ resolution (7″ Nyquist sample rate) to make the best use of the high resolution 70 µm and 850 µm bands.

I choose 12 logarithmically spaced temperature bins, 7.0 K, 8.4 K, 10.0 K, 12.0 K, 14.3 K, 17.1 K, 20.5 K, 24.5 K, 29.2 K, 35.0 K, 41.8 K and 50.0 K. The temperature range from 7.0 K to 50.0 K is wider than the one chosen for the L1495/B213 complex to account for the different dynamics in the region. The Ophiuchus cloud is known to be influenced by photodissociation regions (PDRs) produced by the S1 and HD147889 B-class pre-main sequence stars, and the more distant Upper Scorpius OB association. Thus, it is likely subject to greater heating than Taurus. PDRs are low density regions, which allow for high energy ultraviolet photons to propagate without being scattered or absorbed by dust grains. In turn, these photons dissociate complex

Table 6.3. The PPMAP input parameters for the L1688 and L1689 subregions. Parameters with list values are shown here separated by commas, but are to be separated by whitespace when running PPMAP. A description of each parameter is given in Chapter 3. The Herc850.txt colour correction table is given in Appendix A.

	L1688	L1689
Parameter	Value	
`gloncent`	246.75	248.25
`glatcent`	-24.466666	-24.6666666
`fieldsize`	1.2, 0.8	1.0, 1.0
`pixel`	7	
`dilution`	0.3	
`maxiteration`	10000	
`distance`	140.0	
`kappa300`	0.1	
`nbeta`	3	
`betagrid`	1.0, 1.5, 2.0	
`betaprior`	2.0, 0.25	
`Nt`	12	
`temperature`	7.0, 50.0	
`ncells`	40	
`noverlap`	20	
`ccfile`	Herc850.txt	
`nbands`	6	

molecules such as CO. In the case of S1 and HD147889, the PDRs are associated with HII regions created by the intense radiation fields from each object (Andre et al. 1988; Casassus et al. 2008). It is the radiation pressure from these ionised regions, together with strong winds from the OB association which serve to sweep up material in Ophiuchus, creating concentrations of dust and gas, and compressing the material when it becomes situated between any two of the sources. S1 lies a projected 0.07 pc to the North East of the central ridge of the nearest filamentary structure, while HD137889 lies 0.17 pc to the West (assuming a distance to L1688 of 140 pc).

I choose three linearly spaced β values, 1.0, 1.5, and 2.0. The decision to exclude a value at $\beta = 2.5$ is made after the L1495/B213 results indicate that the high-β band contains very little dust. I again impose a Gaussian prior on the β values with a mean of 2.0 and a standard deviation of 0.25. The full PPMAP input parameters for each sub-region are shown in Table 6.3.

The L1688 and L1689 results are produced by running PPMAP on the Super Computing Wales (SCW) HAWK super computer.

6.3.1 Basic PPMAP Products

As with my analysis of the Taurus L1495/B213 complex, the raw 4D data hypercubes for the L1688 and L1689 sub-fields are difficult to visualise. Therefore, I use a similar procedure to that discussed in Chapter 5 to reduce the dimensionality of the data hypercubes before presenting the data. The sub-fields are discussed separately.

6.3.1.1 L1688

For the L1688 sub-field I initially marginalise out the β dimension to produce a data cube of the H_2 column density in different line of sight temperature bins. This is shown in Figure 6.5. The conversion from PPMAP thermal-dust-emission derived optical depth to H_2 column density is again made with the assumption of a gas-to-dust ratio of 100, and a mean molecular H_2 weight of 2.8.

Figure 6.5 indicates that there is very little dust at $\leq$8.4 K, with only a few dense cores visible above the background level in the central and north-eastern portions of the sub-field. The dense, narrow, central spines of several filament-like structures can be seen to the east and centre of the image in the 10.0 K slice. These structures grow in width and mass through successive temperature slices up to the 14.3 K slice.

The intensity of the filamentary structures to the north east of L1688 rapidly decreases in successive temperature bands. They appear to contain very little dust in the 17.1 K slice, and are not visible at all in the 20.5 K band. This indicates that those structures remain relatively cold. The structures in the central region of the image persist strongly into the 17.1 K slice, but do not appear above the background at 20.5 K.

A single large filamentary structure can be seen spanning the region from the extreme south east, through the centre of the region, to the north west. However, its full extent is not visible in any single temperature slice. Instead, only the most south easterly portion ($\sim$0.5 pc) contains any significant quantity of dust at 14.3 K. The filament then appears to exhibit a strong temperature gradient along its length, as the 17.1 K, 20.5 K and 24.5 K bands appear to show the filament migrating to the north west of the sub-region. This does not show a true, spatial migration, but instead indicates that the dense dust within the filament is cooler to the south east, and hotter to the north west.

The temperature slices from 29.2 K to 50.0 K indicate two large regions of high temperature dust in the central and eastern portions of the sub-field. These regions are shown as voids in the column density at temperatures $\leq$24.5 K. These high temperature regions are likely due to PDRs associated with the S1 (central)

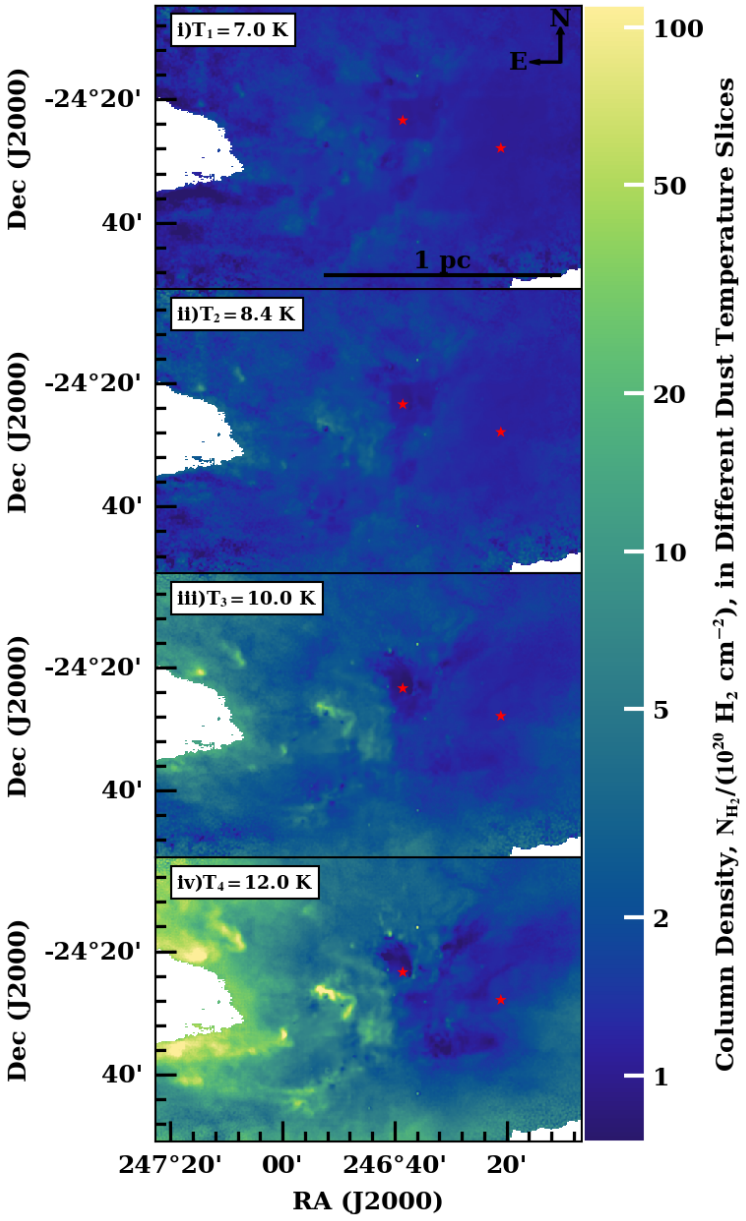

Figure 6.5. The distribution of dust, converted to H_2 column density, in 12 logarithmically spaced line of sight temperature bins for the L1688 sub-region. These maps are obtained by marginalising out the opacity index dimension of the PPMAP data hypercube. The red star markers indicate the positions of the S1 and HD147889 pre-main sequence stars.

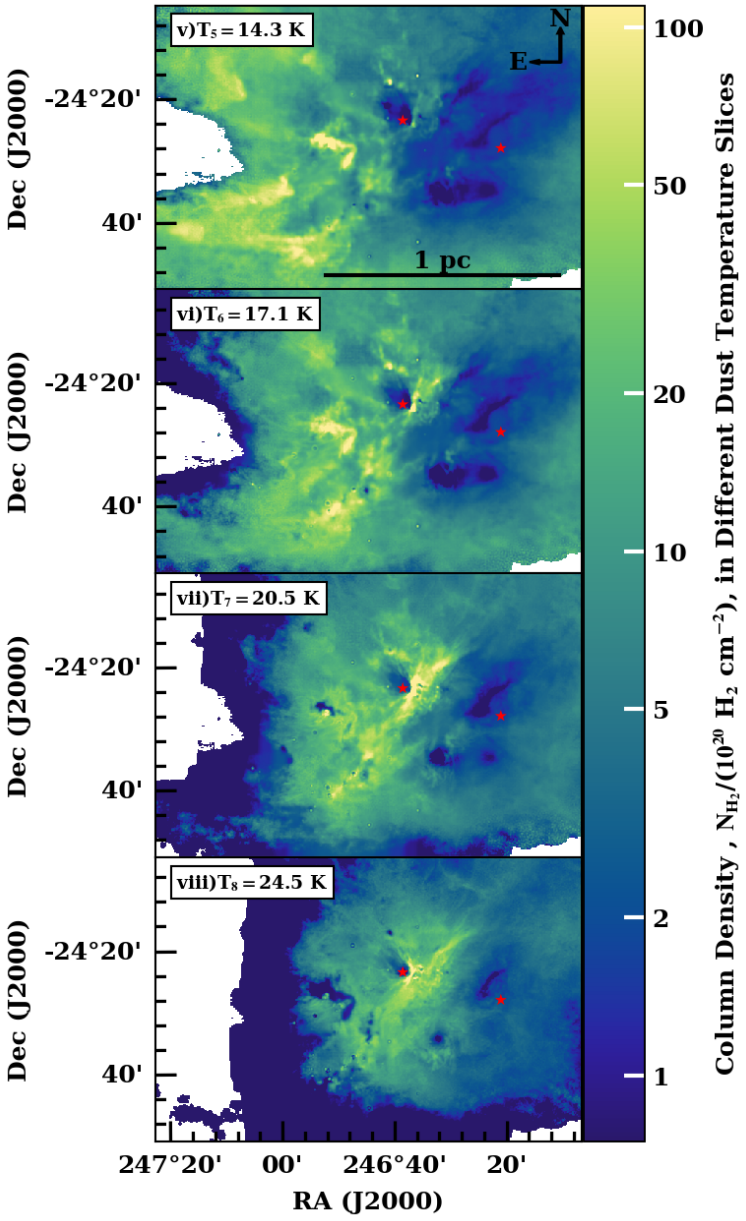

Figure 6.5 (cont.). The distribution of dust, converted to H_2 column density, in 12 logarithmically spaced line of sight temperature bins for the L1688 sub-region. These maps are obtained by marginalising out the opacity index dimension of the PPMAP data hypercube. The red star markers indicate the positions of the S1 and HD147889 pre-main sequence stars.

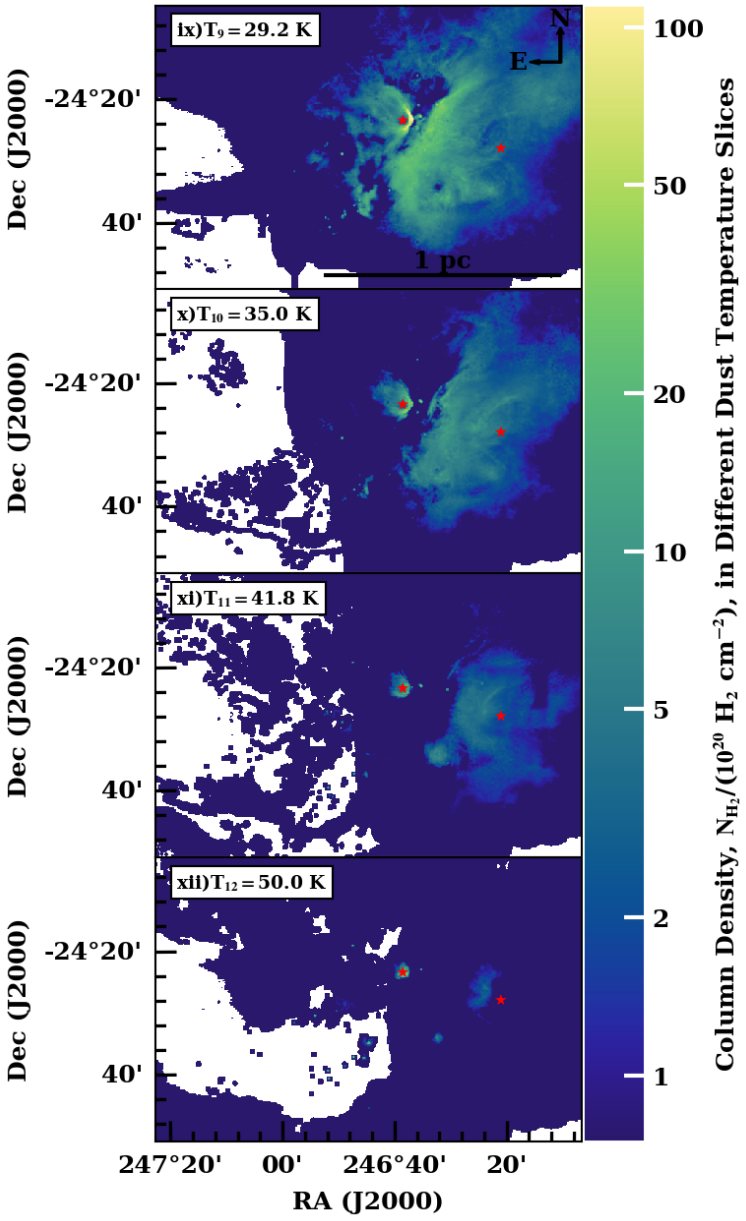

Figure 6.5 (cont.). The distribution of dust, converted to H_2 column density, in 12 logarithmically spaced line of sight temperature bins for the L1688 sub-region. These maps are obtained by marginalising out the opacity index dimension of the PPMAP data hypercube. The red star markers indicate the positions of the S1 and HD147889 pre-main sequence stars.

and HD147889 (eastern) pre-main sequence stars (shown as red stars in Figure 6.5). The influence of S1 and HD147889 are also likely to be the cause of the temperature gradient seen in the large filamentary structure previously discussed, and of the larger scale east/west temperature gradient across the sub-field.

Figure 6.6 shows the distribution of column density across the three β slices when I marginalise out the temperature dimension of the 4D data hypercube. As with Figure 6.5, the colour bar gives the column density of H_2 derived from the optical depth.

Dust with an opacity index of 1.0 is only present in the central region of L1688. The surrounding medium is instead comprised largely of dust contained within the $\beta = 1.5$ and $\beta = 2.0$ slices. The filamentary structures are most strongly traced by dust with $\beta = 1.5$, while only one of the structures is well traced in the $\beta = 1.0$ slice.

I note that dust in the PDR associated with HD147889 is better populated by dust in the $\beta = 2.0$ slice, while the S1 PDR appears to contain a high proportion of dust with $\beta = 1.5$.

The total column density map is shown in Figure 6.7. I obtain this map by marginalising out both the temperature and β dimensions from the 4D data hypercube. I apply the FilFinder algorithm (Koch and Rosolowsky 2015) to the total column density map to identify the filamentary structures observed in Figure 6.5. Figure 6.8 outlines the process of identifying and selecting the structures. FilFinder initially produces image masks of all potential filaments within a given field. I define a `glob_thresh` value of 80, and a `size_thresh` of 400. The `glob_thresh` variable excludes pixels from the mask with intensities below this value, while the `size_thresh` disregards masks with fewer than this number of pixels. I use FilFinder to extract filaments from the masks, trimming branches with a length <0.3 pc. Assuming a mean filament internal width of 0.1 pc, FilFinder will therefore only exclude branches with a minimum aspect ratio of 3.0 (Arzoumanian et al. 2011). All selected structures of this type are shown in Figure 6.8(b). I perform a selection cut, excluding filaments whose spine pixels have a median signal to noise value of < 5, and whose total length is <0.3 pc. This ensures that any selected filaments have a minimum aspect ratio of 3.0. The filaments that remain after this cut are shown in Figure 6.8(c). Finally, I identify the longest continuous path through each of the filaments, and give each one a classifier of the form f#, with the integer increasing from south to north. This final selection is shown in Figure 6.8(d). Figure 6.8(a) serves as a reference image, and is a duplicate of column density map shown in Figure 6.7.

Figure 6.9 shows the associated Point Process Statistical Degeneracy (PPSD) for the L1688 sub-region. The network of filamentary structures in L1688 have a

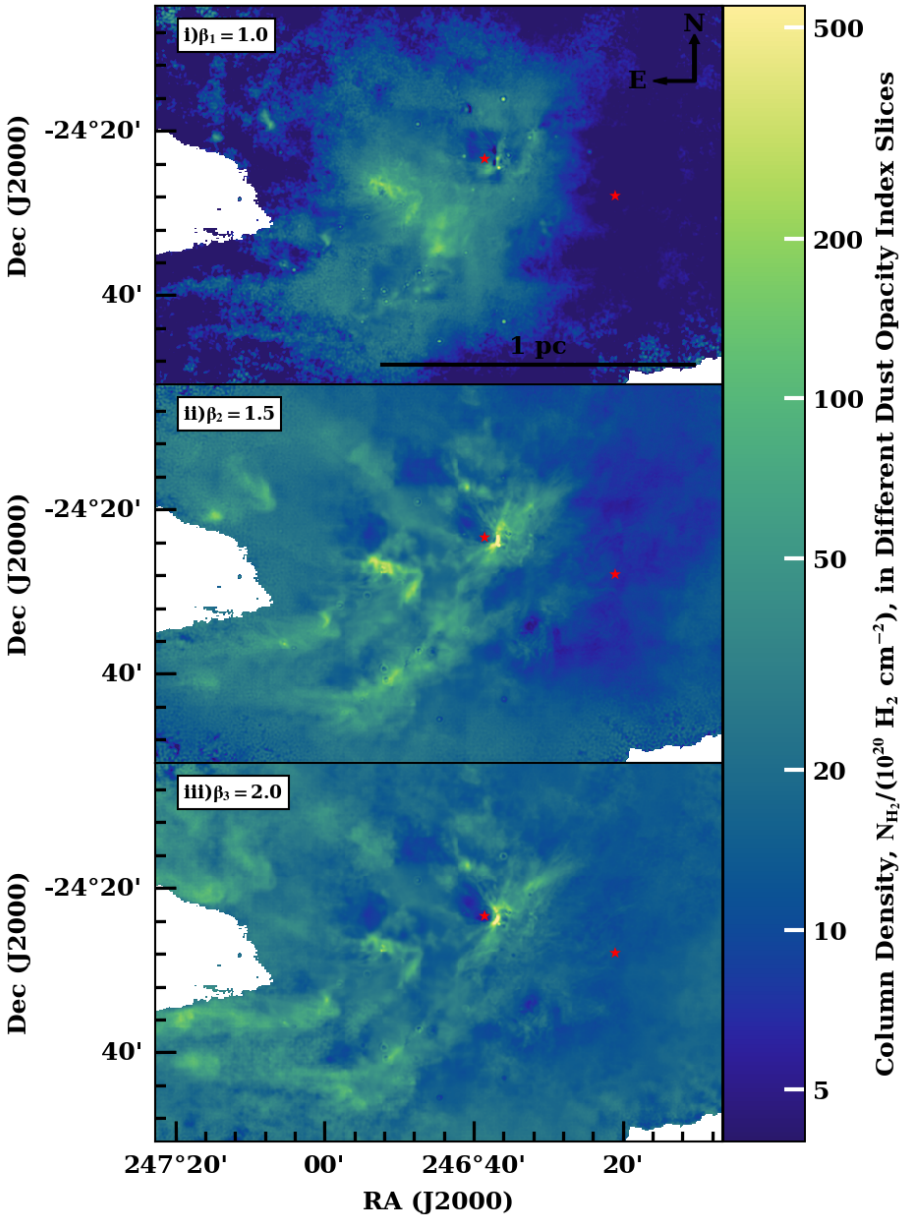

Figure 6.6. The distribution of dust, converted to H_2 column density, in three linearly spaced line of sight opacity index bins for the L1688 sub-region. These maps are obtained by marginalising out the temperature dimension of the PPMAP data hypercube. The red star markers indicate the positions of the S1 and HD147889 pre-main sequence stars.

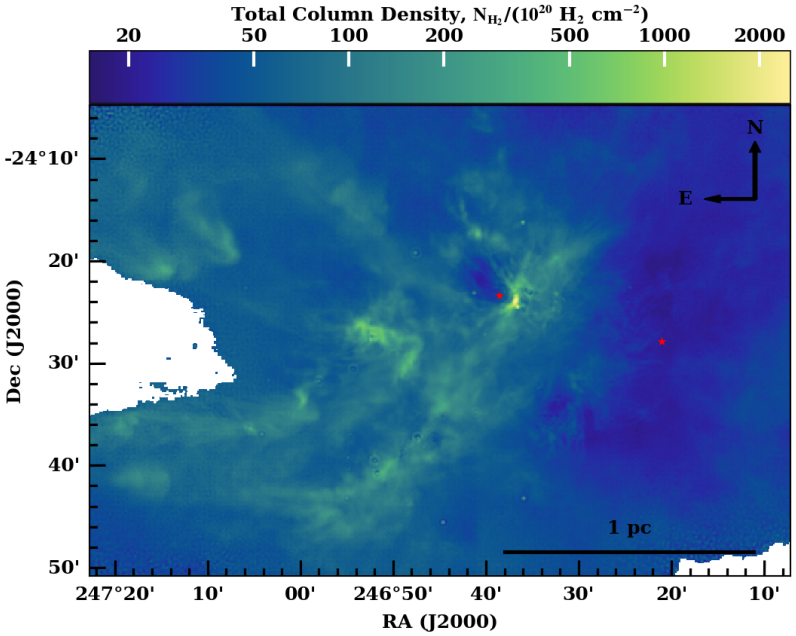

Figure 6.7. Total H_2 column density for L1688, derived from the PPMAP dust model. This map is obtained by marginalising out both the temperature and opacity index dimensions.

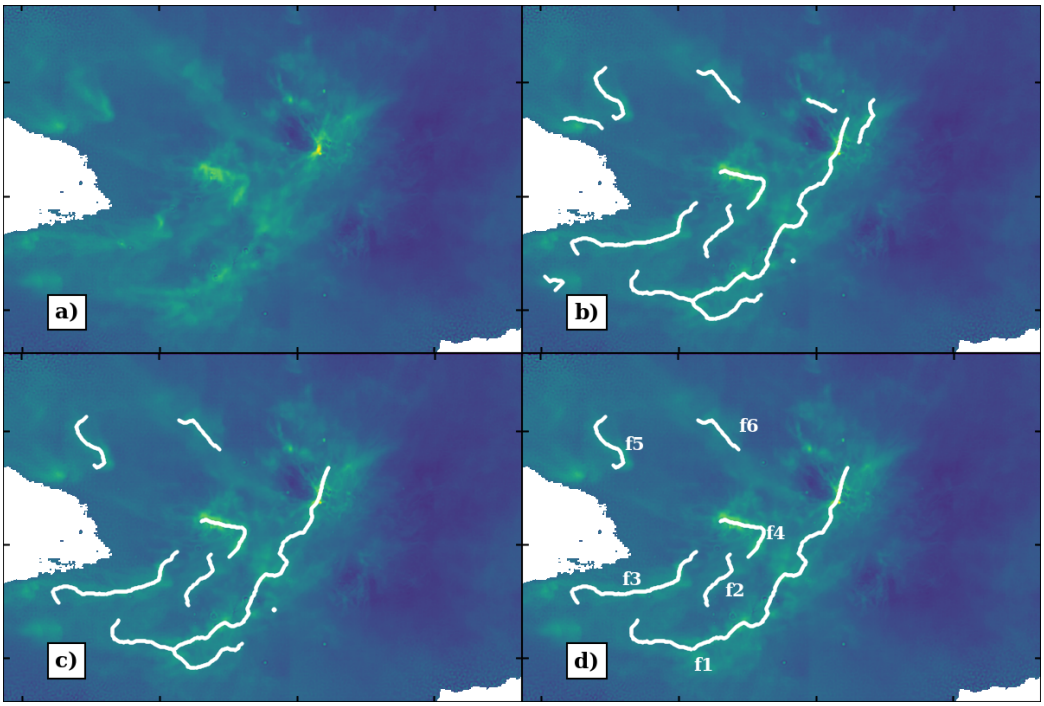

Figure 6.8. Diagram of the filament network in L1688 identified by FilFinder. Panel (b) shows all the filamentary structures after pruning branches with a length <0.3 pc, while panel (c) displays the subset of filaments with a longest path length >0.3 pc. Panel (d) shows the paths through each filament selected as the primary spine. Panel (a) is the column density map shown in Figure 6.7, and is included for reference. The column density map is also the background in the remaining panels, over which the filaments are plotted.

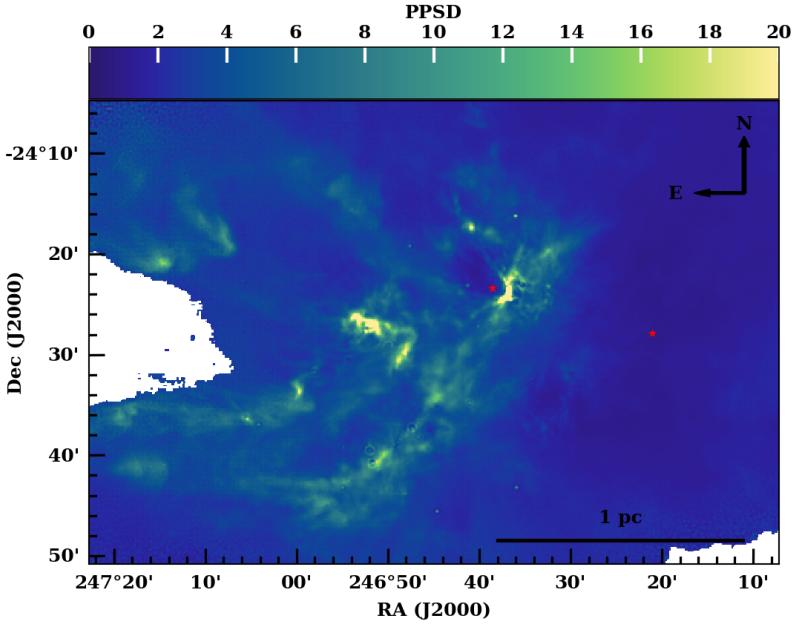

Figure 6.9. Map of the Point Process Statistical Degeneracy (PPSD, see Chapter 3, Section 3.1.4.3) for the L1688 sub-region. The uncertainty hypercube used to derive the map of PPSD is shown in Appendix B. The red stars indicate the positions of S1 and HD147889.

PPSD ≥ 5, and are, therefore, well constrained. The surrounding medium between the filaments is less well constrained, with a PPSD ~ 2. While the PDRs associated with S1 and HD147889 are comparatively poorly constrained when compared with the network of filaments, they still exceed a PPSD of 1, which indicates that the signal still dominates over the uncertainty inherent in the model.

Figure 6.10 and Figure 6.11 show the line of sight mean dust temperature, $\bar{T}_{\rm D}$, and the line of sight mean dust opacity index, $\bar{\beta}_{\rm D}$, respectively.

Figure 6.10 clearly indicates a temperature gradient from east to west within L1688, with the highest dust temperatures present in the PDRs around S1 and HD147889. Most of the filaments are not immediately identifiable from the mean dust temperature map, as they appear to have a similar mean temperature to their surroundings. f4 is a clear exception, appearing as a cold, <14 K region surrounded by warm, >17 K material. In contrast, Figure 6.11 does not indicate an east/west gradient in mean dust opacity index, $\bar{\beta}_{\rm D}$. Instead, dust with a lower mean opacity index (< 1.5) is concentrated in the centre of the region, with higher values of the opacity index in the surrounding medium. None of the previously identified filaments are clearly traced by variations in $\bar{\beta}_{\rm D}$. The PDRs are also not obviously traced by $\bar{\beta}$ variations, suggesting that they have little effect on the opacity index of the dust.

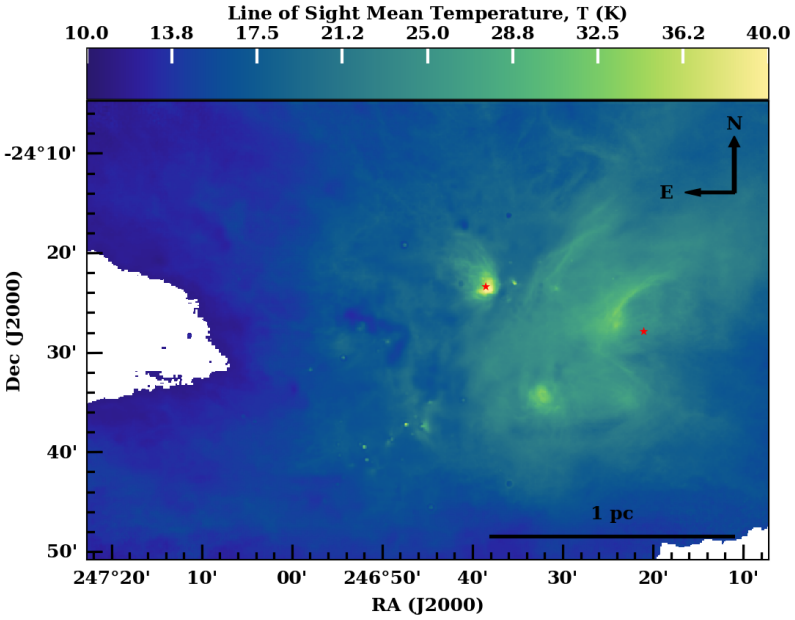

Figure 6.10. The mean line of sight dust temperature, $\bar{T}_{\rm D}$, at every pixel for L1688, obtained by marginalising out the opacity index dimension and then taking a weighted average of the temperature bins of the hypercube, with the H_2 column density in each bin as the weighting factor.

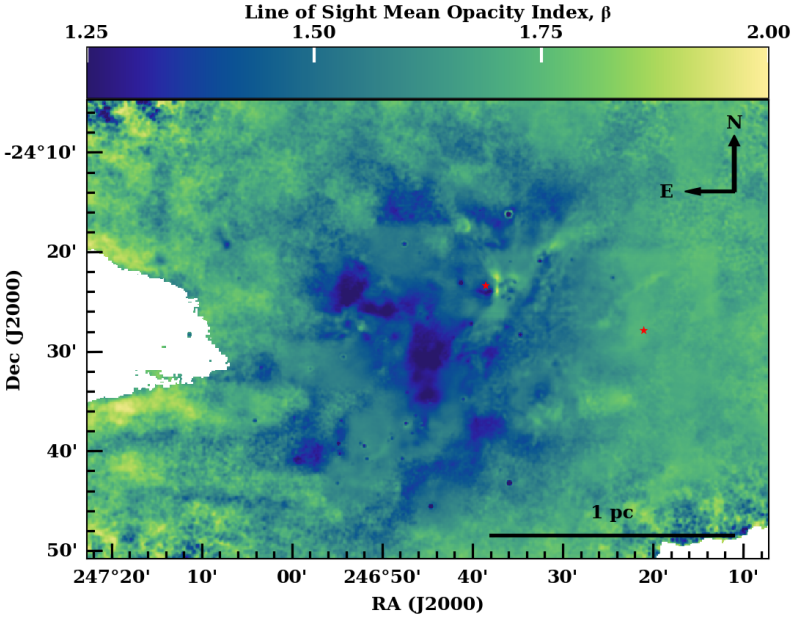

Figure 6.11. The mean line of sight dust opacity index, $\bar{\beta}_{\rm D}$, at every pixel for L1688, obtained by marginalising out the temperature dimension and then taking a weighted average of the opacity index bins of the hypercube, with the H_2 column density in each bin as the weighting factor.

6.3.1.2 L1689

Figure 6.12 shows the distribution of H_2 column density through the 12 dust temperature bands for the L1689 sub-field, after I marginalise out the β dimension.

Very little dust appears to occupy the lowest temperature bands in L1689, with only highly localised regions of diffuse material visible in Figure 6.12 at 8.4 K. These regions correspond well with the L1689 East, L1689 North, and L1689 South sub-clouds (Nutter, Ward-Thompson, and André 2006). The sub-clouds remain isolated in both the 10.0 K and 12.0 K slices, while the proportion of dust in each sub-cloud increases with an increase in temperature band when compared with lower bands.

A low density network of filamentary structures connecting the sub-clouds is visible in the 14.3 K and 17.1 K slices. The dust in the surrounding medium is mostly contained within these temperature slices.

L1689 East contains almost no dust at $\geq$20.5 K, while L1689 North and L1689 South remain connected by a large, diffuse cloud. This connecting cloud is not seen at 24.5 K. Instead, only two small, elongated structures are present in the slice. The northern most structure has a dense head around the masked source L1689-IRS6, and extends $\sim$0.5 pc to the south west. The southern structure has a semi-major axis $\sim$0.4 pc and runs south east to north west. It forms the southern edge of the L1689 South sub-cloud.

Very little dust is contained within slices with temperatures $\geq$29.2 K, and no further structures are visible.

When I instead marginalise out the β dimension, I produce Figure 6.13. All of the dust occupying the $\beta = 1.0$ slice is contained within the North, South and East sub-clouds of L1689. In contrast, the $\beta = 1.5$ and $\beta = 2.0$ slices contain dust more evenly distributed throughout the L1689 sub-region, with over-densities that more accurately trace the filamentary structure. These structures are more strongly traced at $\beta = 1.5$ than at $\beta = 2$, indicating that the denser, better shielded regions harbour the dust with the lowest opacity indices.

By marginalising out both the temperature and opacity index dimensions from the 4D data hypercube, I produce the total column density map, which is shown in Figure 6.14. As with the L1688 sub-region, I use FilFinder to identify filaments. All identified structures are shown in Figure 6.15(b), while only those with a total length in excess of 0.3 pc are indicated in 6.15(c). These are given identifiers following the convention derived for L1688 (shown in Figure 6.15(d)). The southward loop structure at the midpoint of f2 appears to trace a network of over-dense fragments, rather than a continuation of the filament. Therefore, I choose to exclude the loop, splitting the

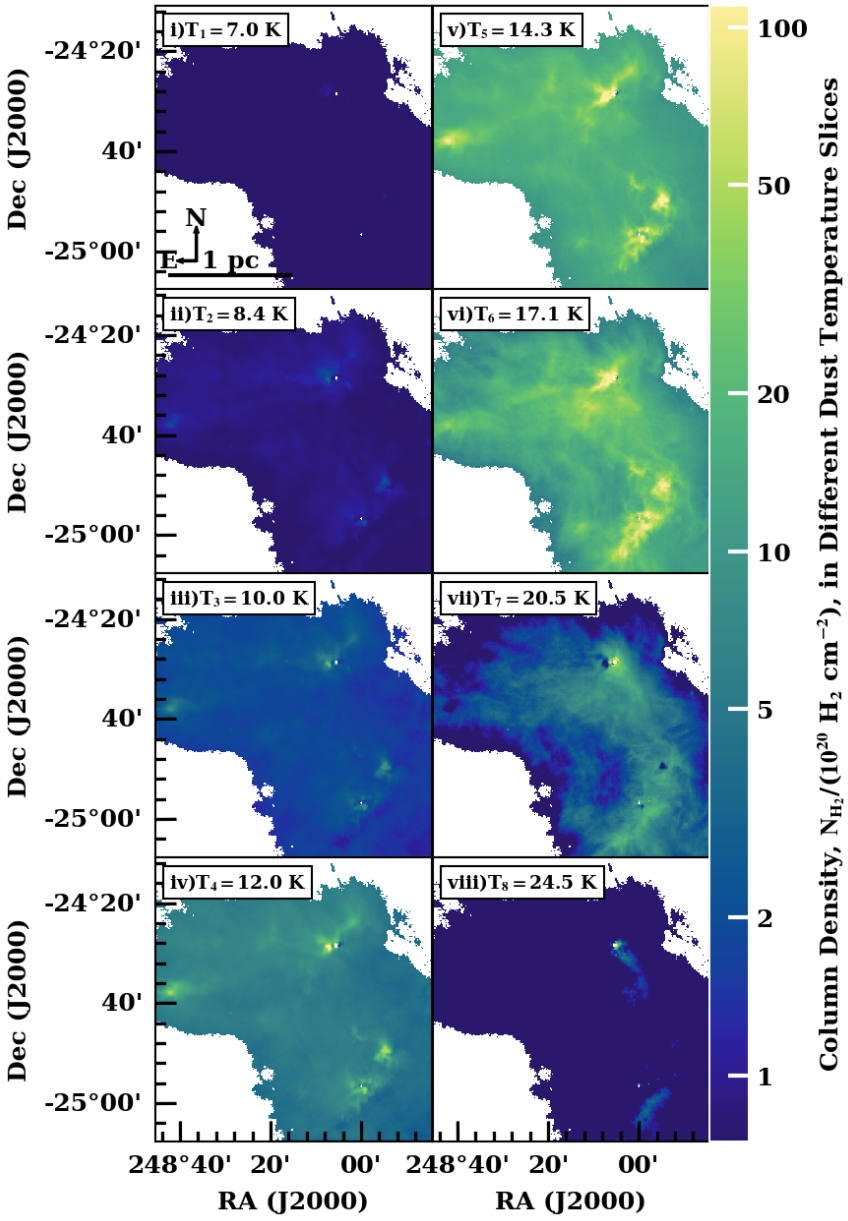

Figure 6.12. The distribution of dust, converted to H_2 column density, in 12 logarithmically spaced line of sight temperature bins for the L1689 sub-region, plotted for the eight lowest temperatures. These maps are obtained by marginalising out the opacity index dimension of the PPMAP data hypercube.

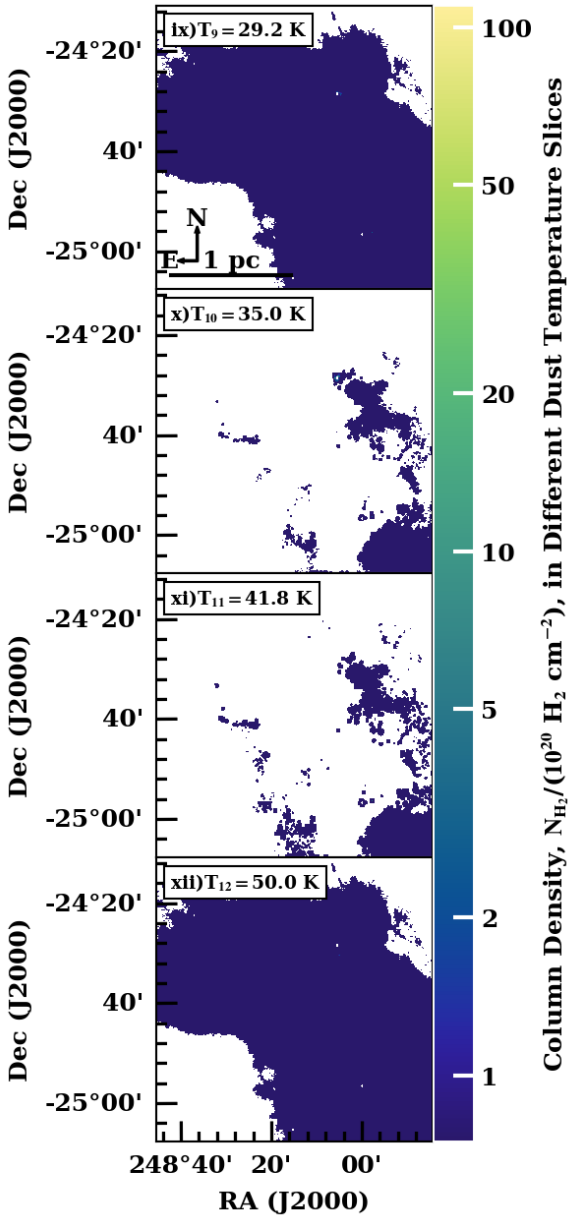

Figure 6.12 (cont.). The distribution of dust, converted to H_2 column density, in 12 logarithmically spaced line of sight temperature bins for the L1689 sub-region, plotted for the four highest temperatures. These maps are obtained by marginalising out the opacity index dimension of the PPMAP data hypercube.

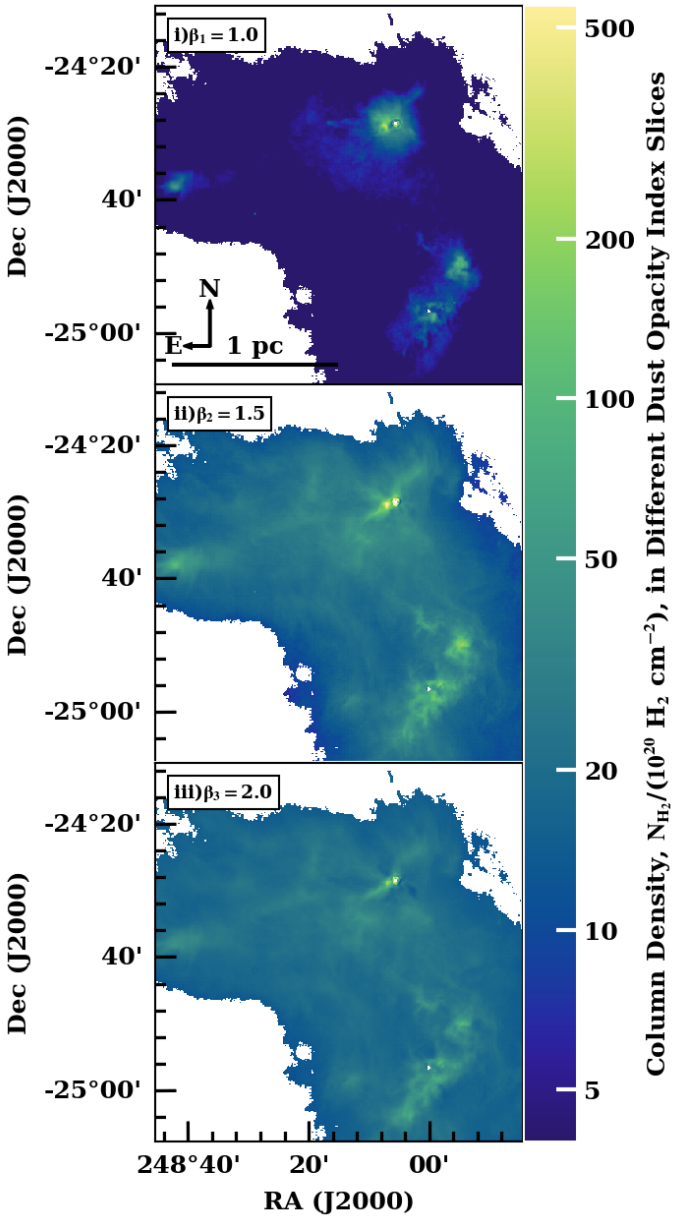

Figure 6.13. The distribution of dust, converted to H_2 column density, in three linearly spaced line of sight opacity index bins for the L1689 sub-region. These maps are obtained by marginalising out the temperature dimension of the PPMAP data hypercube.

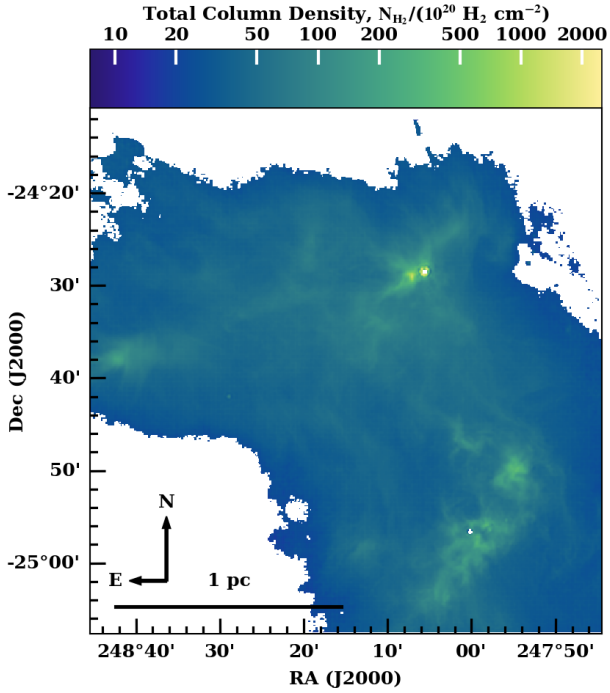

Figure 6.14. Total H_2 column density for L1689, derived from the PPMAP dust model. This map is obtained by marginalising out both the temperature and opacity index dimensions.

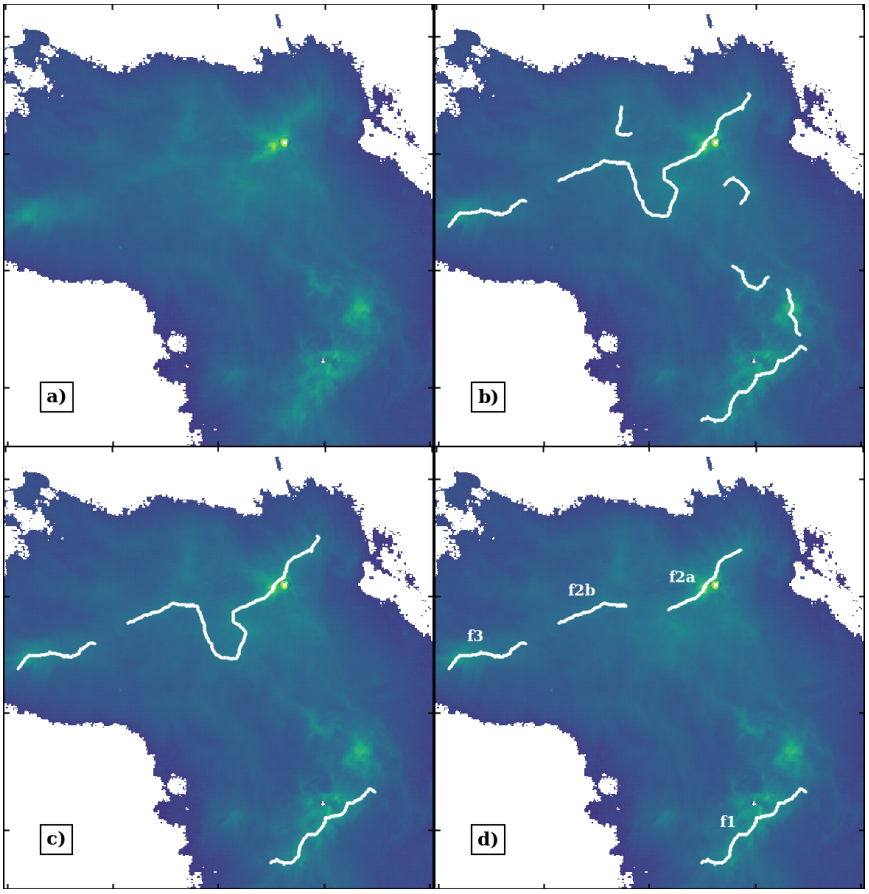

Figure 6.15. Diagram of the filament network in L1689 identified by FilFinder. Panel (b) shows all the filamentary structures after pruning branches with a length <0.3 pc, while panel (c) displays the subset of filaments with a longest path length >0.3 pc. Panel (d) shows the paths through each filament selected as the primary spine. Panel (a) is the column density map shown in Figure 6.7, and is included for reference. The column density map is also the background in the remaining panels, over which the filaments are plotted.

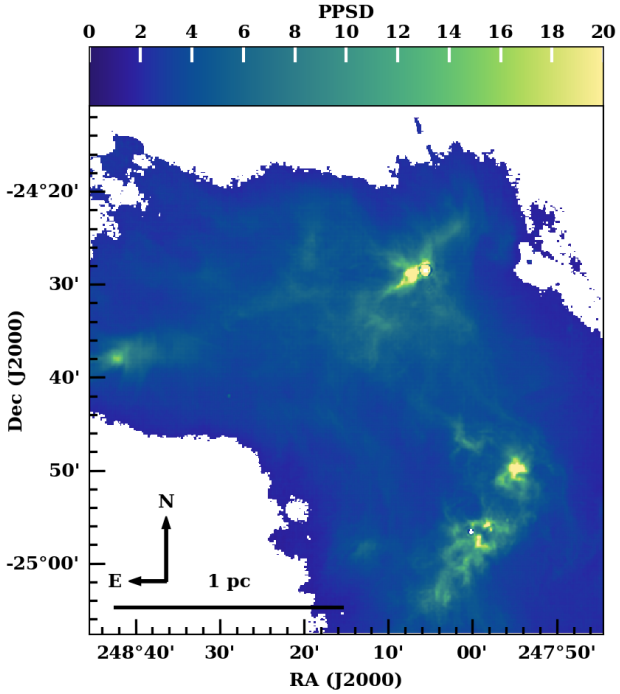

Figure 6.16. Map of the Point Process Statistical Degeneracy (PPSD, see Chapter 3, Section 3.1.4.3) for the L1689 sub-region. The uncertainty hypercube used to derive the map of PPSD is shown in Appendix B.

f2 filament into two, f2a and f2b, with similar orientations.

Figure 6.16 shows the associated PPSD for the L1689 sub-region. The prominent structures in L1689 have a PPSD ≥ 6, while the surroundings have a typical PPSD ~ 3, indicating that the model is generally well constrained. Only at the edges of the model does the PPSD fall to ~ 1, indicating it is less well constrained.

Figure 6.17 shows the mass weighted mean line of sight dust temperature, $\bar{T}_{\rm D}$ for L1689. The range of dust temperatures is much smaller than that observed in L1688. In addition, much of the complex variation shown in Figure 6.12 is lost. Figure 6.18 shows the mass weighted mean line of sight dust opacity index, $\bar{\beta}_{\rm D}$ for L1689. In contrast to Figure 6.17, the variation in dust opacity index is clearly visible, with the background value of $\bar{\beta}_{\rm D} \sim 1.75$, and falling sharply in the densest regions to $\bar{\beta}_{\rm D} \leq 1.25$.

6.3.1.3 Comparison of Column Density with *Planck* and 2MASS/NICER

To verify that the model produced by PPMAP for the L1688 and L1689 sub-regions provides an accurate estimate of the column density in the regions, I compare the sub-regions with column densities derived from the *Planck* dust models.

To derive the PPMAP-equivalent H_2 column density from the *Planck* dust models, I first equate equation 2.6 with equation 1.24, which produces

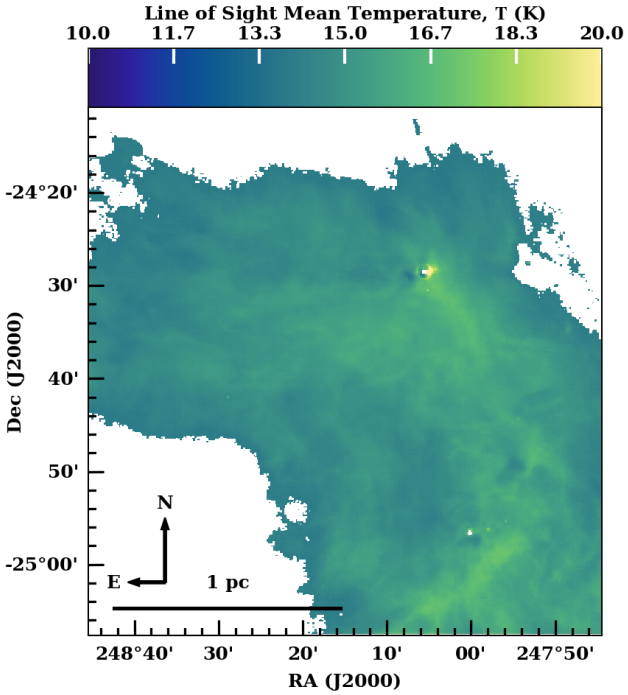

Figure 6.17. The mean line of sight dust temperature, $T_{\rm D}$, at every pixel for L1689, obtained by marginalising out the opacity index dimension and then taking a weighted average of the temperature bins of the hypercube, with the H_2 column density in each bin as the weighting factor.

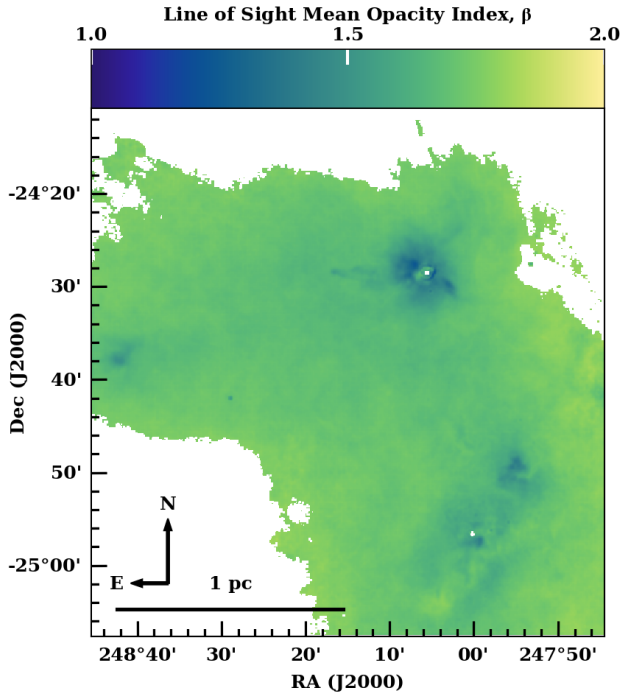

Figure 6.18. The mean line of sight dust opacity index, $\beta_{\rm D}$, at every pixel for L1689, obtained by marginalising out the temperature dimension and then taking a weighted average of the opacity index bins of the hypercube, with the H_2 column density in each bin as the weighting factor.

$$\Sigma_{\mathrm{H_2}} = \frac{\tau_{850\,\mu\mathrm{m}}}{\kappa_{300\,\mu\mathrm{m}}} \left(\frac{300\,\mu\mathrm{m}}{850\,\mu\mathrm{m}} \right)^{-\beta_{850\,\mu\mathrm{m}}} . \tag{6.1}$$

Values with the subscript 300 µm represent parameters which use the PPMAP assumptions of dust opacity, while those with subscript 850 µm are the parameters obtained from the *Planck* dust models. I convolve the PPMAP total column density map with a 5′ Gaussian kernel, which approximates the *Planck* beam profile. I reproject both the PPMAP column density, and the *Planck* derived column density onto the same pixel grid. I produce a median ratio between the PPMAP and *Planck* derived column densities of $\widetilde{\Sigma}_{PPMAP}/\widetilde{\Sigma}_{Planck} = 1.44$ for L1688, and $\widetilde{\Sigma}_{PPMAP}/\widetilde{\Sigma}_{Planck} = 1.31$ for L1689.

As a second method of verification, I convert the PPMAP column densities into visual extinction, A_v, and compare with A_v measurements derived from the 2MASS/NICER extinction maps (Juvela and Montillaud 2016). The two micron all sky survey (2MASS, Skrutskie et al. 2006) utilised autonomous telescopes to produce simultaneous maps of near infra-red (NIR) colour in the J (1.25 µm), H (1.65 µm), and K_s (2.17 µm) bands. The resolution of the maps is ∼1′ near the galactic plane but degrades near the galactic poles. The near infra-red colour excess revised (NICER Lombardi and Alves 2001) method was developed to convert NIR colour to NIR extinction for a few small regions, and was applied to the entire 2MASS data set to produce all sky 2MASS/NICER maps of extinction by Juvela and Montillaud (2016) with a 3′ resolution. These maps are publicly available*, and can be obtained with extinction scaled to A_J, A_H, or A_K.

I obtain 2MASS/NICER maps of A_K, covering the L1688 and L1689 subregions, and convert to an approximate map of A_V by multiplying the A_K maps by a factor of 8.93. This factor is consistent with the Rieke and Lebofsky (1985) reddening law, appropriate for 2MASS (Carpenter 2001; Lombardi, Alves, and Lada 2006). I convert the PPMAP column density maps to approximate A_V maps by assuming a column density to A_V conversion of $N_{\mathrm{H_2}} = 0.94 \times 10^{21} 1\,\mathrm{H_2\,cm^{-2}} A_V$ (Bohlin, Savage, and Drake 1978). The resultant maps of A_V derived from column density are then convolved with a 3′ Gaussian kernel, and both the 2MASS/NICER and PPMAP derived A_V maps are reprojected to the same pixel grid. As with the *Planck* column density comparison, I produce a median ratio of $\widetilde{A}_{V:PPMAP}/\widetilde{A}_{V:2MASS} = 0.83$ for L1688 and $\widetilde{A}_{V:PPMAP}/\widetilde{A}_{V:2MASS} = 1.17$ for L1689.

Therefore, I conclude that the PPMAP column density estimates are consistent with the 2MASS/NICER visual extinction maps to within 20%, though they produce

*https://www.interstellarmedium.org/Extinction/

a $\sim$ 35% over-estimate of the column density relative to the *Planck* dust models. However, given the large uncertainty in the value of the reference opacity, κ_0, the PPMAP models and the *Planck* models can still be considered in good agreement.

6.3.2 Comparison of the Large Scale Properties

To compare the large scale differences between the L1688 and L1689 sub-regions, I first produce a series of three-colour images from the column density cubes of each region. To create three-colour images of the variation in column density with temperature, I first marginalise out the β dimension of the 4D data hypercube. I then define a low temperature dust column density map, by summing over the 7.0 K, 8.4 K, 10.0 K, 12.0 K and 14.3 K bands, a mid temperature dust column density map comprised of the column density contained within the 17.1 K, 20.5 K and 24.5 K bands, and a high temperature dust column density map derived from the column density contained within the remaining 29.2 K, 35.0 K, 41.8 K and 50.0 K bands. This is done for both sub-regions. I utilise the `multicolorfits` tool (Cigan 2019) to convert the maps into three-colour images, assigning a different colour to each of the three temperature ranges. Standard three-colour image production assumes that the maximum and minimum of each component image is equivalent to the maxima and minima of the other images. However, in this instance the contribution to the total column density from the low, mid, and high temperature column density maps is not necessarily equal. Therefore, I normalise the relative intensity of each map to the total column density of the region. This ensures the total intensity contribution from each colour map is in proportion to its fraction of the total mass. The resultant images are shown in Figure 6.19 for the L1688 sub-region, and in Figure 6.20 for the L1689 sub-region.

The effect of the S1 and HD147889 can be clearly seen in Figure 6.19, with the dust contained within the high temperature regime ($T_D \geq 29.2$ K) clearly dominating the centre of the two PDRs. The upper portion of f1 passes between the two PDRs, and appears to contain dust which mostly occupies the mid temperature range (17.1 K $\leq T_D \leq$ 24.5 K. The remaining portion of f1, along with the other filaments, are mostly comprised of dust occupying the low temperature ($T_D \leq 14.3$ K) range. The largest contribution to the mass of the surrounding medium in the southern and eastern portions of the field is also found within the low temperature range, while the dust surrounding the PDRs occupies the middle temperature range.

In contrast, Figure 6.20 presents a picture of a comparatively quiescent field, with very little dust in the high temperature range. The dense clumps associated with

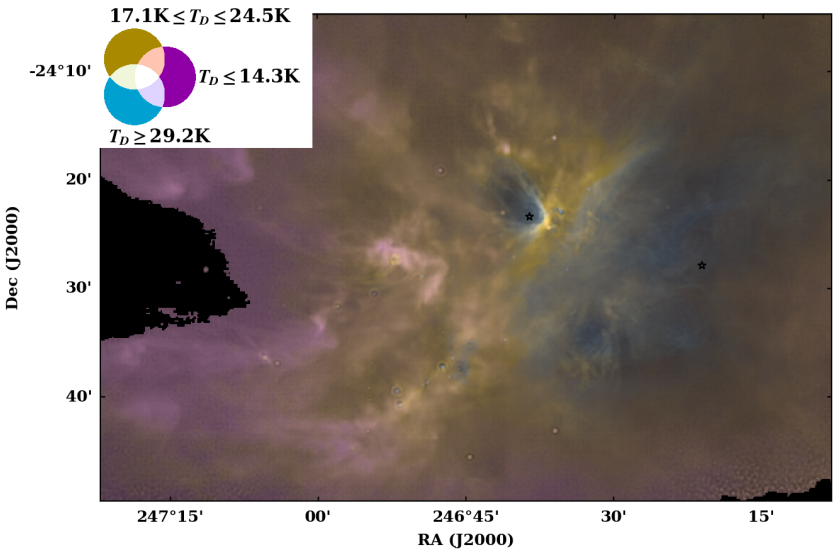

Figure 6.19. A three colour image of L1688, depicting the distribution of dust in three broad ranges covering multiple PPMAP temperature bands. The extent of the temperature ranges, and the associated colours, are shown in the diagram in the top left. The black star marks denote the positions of the S1 and HD147889 pre-main sequence stars.

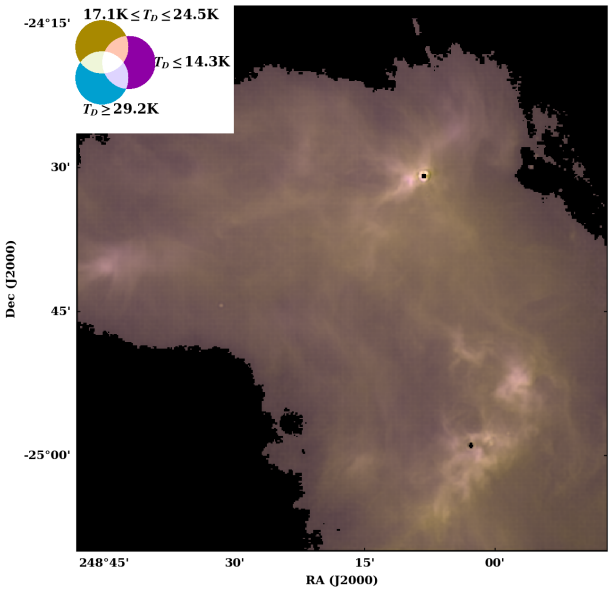

Figure 6.20. A three colour image of L1689, depicting the distribution of dust in three broad ranges covering multiple PPMAP temperature bands. The extent of the temperature ranges, and the associated colours, are shown in the diagram in the top left.

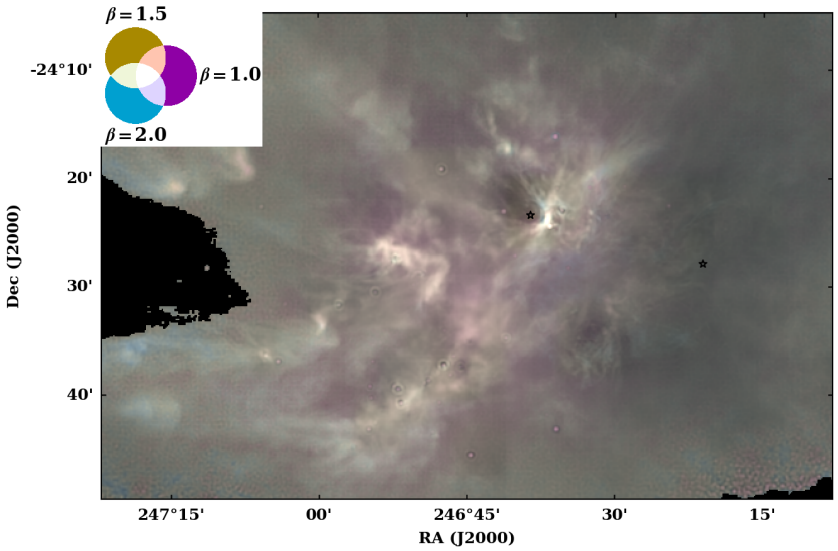

Figure 6.21. A three colour image of L1688, depicting the distribution of dust in the three PPMAP opacity index bands. The colours associated with each band are shown in the diagram in the top left. The black star marks denote the positions of the S1 and HD147889 pre-main sequence stars.

L1689 North, East, and South are dominated by dust in the low temperature range, while the network of connecting filamentary structures have a larger proportion of their mass contained within the mid temperature range. This is a view commonly associated with archetypal low mass star forming regions, with dense, cold filaments and clumps embedded in a warmer medium.

By marginalising out the temperature dimension from the 4D data hypercube of column densities, and repeating the method of generating the three-colour images, I produce comparison images of the column density variation with opacity index. As the hypercube only contains three β bands, I do not define a set of opacity index ranges, but instead allow each band to be wholly represented by a different colour. The resultant three-colour images are shown in Figure 6.21 for the L1688 sub-region, and in Figure 6.22 for the L1689 region.

The variations in the populations of dust with different opacity indices are broadly similar in both Figure 6.21 and 6.22. In the outer, diffuse medium surrounding each sub-region, the mass is dominated by dust with $\beta = 2.0$, with the opacity index falling towards the denser structures. When viewed as a composite three-colour image, as opposed to separate panels as with Figure 6.6, it is not possible to deduce an effect on the dust opacity index from the PDRs.

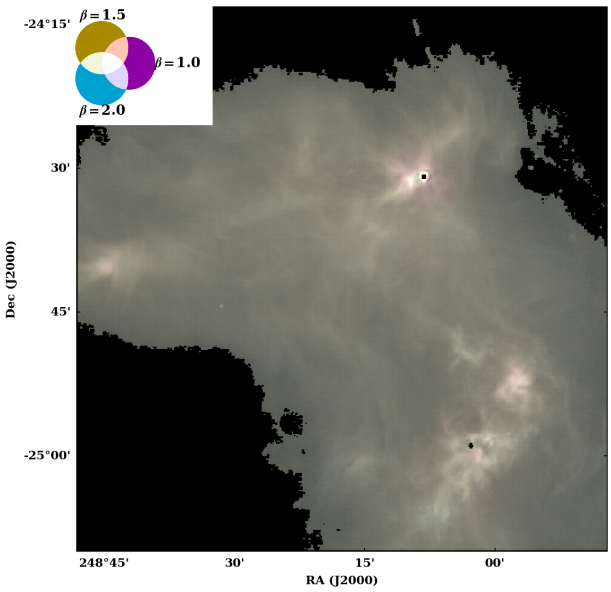

Figure 6.22. A three colour image of L1689, depicting the distribution of dust in the three PPMAP opacity index bands. The colours associated with each band are shown in the diagram in the top left.

To quantify the differences between L1688 and L1689 I first examine the mass distribution in each field. I convert the column density within the field of view of each model to a total mass of hydrogen through the equation

$$M_{\mathrm{H_2}} = \mathrm{N_{H_2}} \bar{m}_{\mathrm{H_2}} \cdot \Delta_{pix}^2, \tag{6.2}$$

where $\bar{m}_{\mathrm{H_2}}$ is the mean molecular mass of the gas, assuming a gas molecular gas fraction of 2.8, and Δ_{pix} is the pixel width in cm. The mean molecular mass has a value of $\bar{m}_{\mathrm{H_2}} = 1.68 \times 10^{-57}\,\mathrm{M_\odot}$. The total mass of $\mathrm{H_2}$ across the $5.74\,\mathrm{pc}^2$ field of view, derived from the PPMAP dust model of L1688, is $(650.7 \pm 0.4)\,\mathrm{M_\odot}$. The mass uncertainty is determined from the PPMAP uncertainty hypercube. The hypercube is flattened to produce a 2D column density uncertainty map by summing in quadrature along the temperature and opacity index dimensions as discussed in Chapter 3, Section 3.1.4.3. The flattened uncertainty map is then converted to a map of pixel mass uncertainty via equation 6.2. The pixel mass uncertainties are then summed in quadrature over the same area used to derive the mass. The average surface density of the observed region is $113.3\,\mathrm{M_\odot\,pc^{-2}}$. The total mass of the $5.96\,\mathrm{pc}^2$ model of the L1689 sub-region is $(395.4 \pm 0.3)\,\mathrm{M_\odot}$ giving an average surface density of $66.3\,\mathrm{M_\odot\,pc^{-2}}$. Therefore, L1688 is nearly 1.5 times as dense as L1689 over approximately the same extent as L1689.

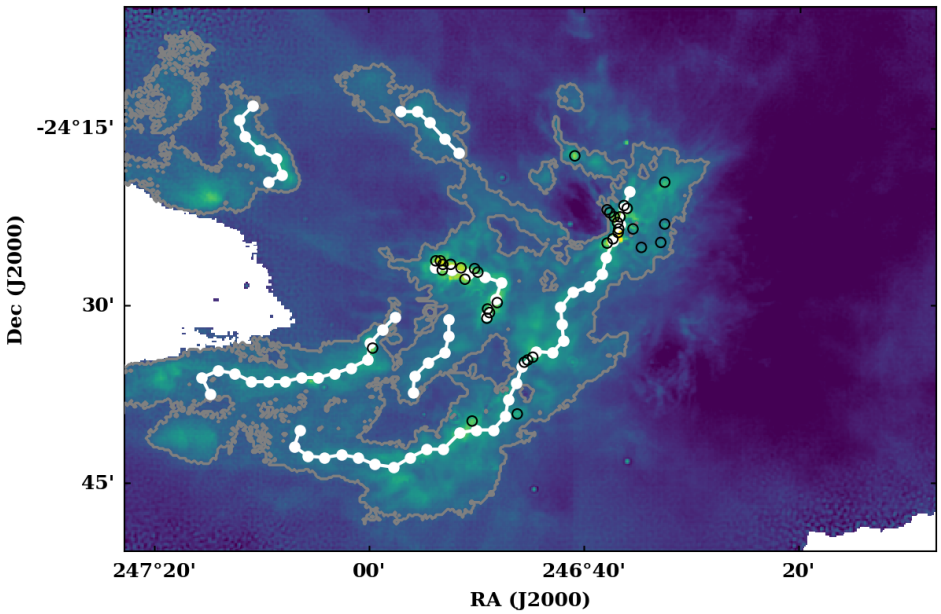

Figure 6.23. Map of the dense mass of L1688, bounded by the grey contours at $A_V > 7$ ($\Sigma > 7 \times 10^{21}\,\mathrm{H_2\,cm^{-2}}$). The centroid positions of the filament bundles are given by the filled white circles, with the filament spines traced by the white lines. The Pattle2015 core locations are shown as open black circles.

I note that these masses are likely lower bounds for the total masses of the sub-regions, as their boundaries are not well defined, and they likely extend beyond the edges of the models. A more robust measurement of cloud mass can be obtained from looking only at the mass of the dense gas contained within each sub-region. To obtain this I define a contour at the $7 \times 10^{21}\,\mathrm{H_2\,cm^{-2}}$ column density limit which corresponds to an approximate visual extinction of 7. This limit was chosen as $A_V = 7$ has been found to mark the transition between regions with low core forming efficiency and high core forming efficiency (André et al. 2010; Lada, Lombardi, and Alves 2010; Könyves et al. 2015). Therefore, it is a convenient transition point for defining the edge of an active star-forming GMC. The contoured regions marking this boundary for L1688 and L1689 are shown in grey in Figure 6.23 and Figure 6.24 respectively.

The mass of L1688 in the region above $A_v = 7$ is $(285.3 \pm 0.2)\,\mathrm{M_\odot}$ over an area of $1.2\,\mathrm{pc^2}$. L1689 has a total mass of $(88.5 \pm 0.1)\,\mathrm{M_\odot}$ distributed across a $0.37\,\mathrm{pc^2}$ region. Both sub-regions have a similar average surface density of dense gas within this regime ($239.0\,\mathrm{M_\odot\,pc^{-2}}$ for L1688 and $242.4\,\mathrm{M_\odot\,pc^{-2}}$ for L1689). I note that this is to be expected because the masses and areas are calculated based on the same threshold in column density in each sub-region. Instead, it is important to note that the dense gas accounts for 21% of the total area shown in Figure 6.23, while only

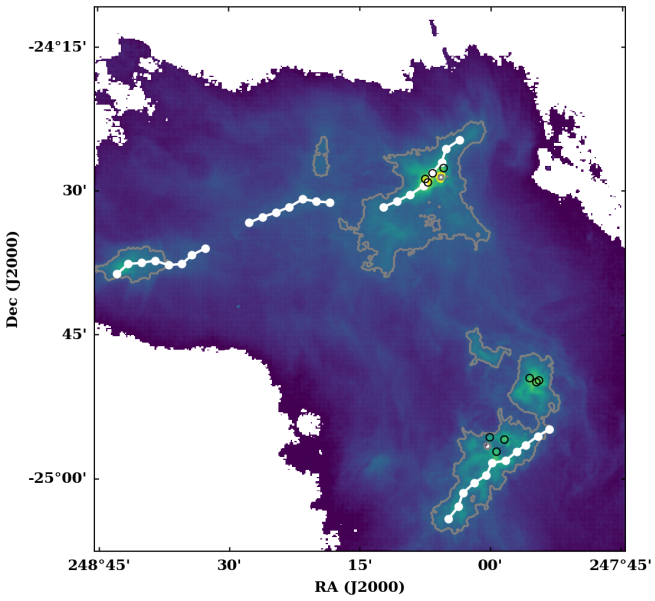

Figure 6.24. Map of the dense mass of L1689, bounded by the grey contours at $A_V > 7$ ($\Sigma > 7 \times 10^{21}\,\mathrm{H_2\,cm^{-2}}$). The centroid positions of the filament bundles are given by the filled white circles, with the filament spines traced by the white lines. The Pattle2015 core locations are shown as open black circles.

6% of the total area of Figure 6.24 is considered dense by the same metric. Thus, while the surface density of the dense gas is similar in both sub-regions, a much higher proportion of the totality of L1688 is dense, leading to the much higher average surface density across the full field of view.

6.3.2.1 Starless Core Distribution

To compare the evolutionary state of the two sub-regions, I analyse the distribution of starless cores contained within L1688 and L1689. I utilise the core catalogue published in Pattle et al. (2015). The catalogue contains both starless and protostellar cores, and covers several more sub-regions not analysed in this thesis. As previously discussed, PPMAP is unable to fit optically thick protostellar cores with central bright 70 µm sources. Therefore, I only select cores from the catalogue that are classified as starless, and which fall within the L1688 and L1689 sub-regions. The cores are plotted as black edged circles in Figure 6.23 and Figure 6.24.

I obtain masses for the cores by utilising the `photutils` Python package to apply an elliptical aperture at the centroid position of each one. The aperture semi-major and -minor axes and position angles are obtained from the catalogue. I convert the total column density map to a map of H_2 mass per pixel with equation 6.2, before

summing over the pixels within the aperture. Pixels which are bisected by the edge of the aperture have their mass contribution adjusted in proportion to how much of the pixel is within the ellipse. The mass uncertainty of each core is determined from the PPMAP uncertainty hypercube. The hypercube is flattened to produce a 2D column density uncertainty map by summing in quadrature along the temperature and opacity index dimensions as discussed in Chapter 3, Section 3.1.4.3. The flattened uncertainty map is then converted to a map of pixel mass uncertainty via equation 6.2. This map is then passed to `photutils`, which returns the uncertainty on the mass for each aperture. Table 6.4 displays the core centroid positions, masses, semi-major and minor axes, position angles, and the Pattle et al. (2015) identifiers for reference.

The L1688 sub-region contains 36 starless cores with a cumulative mass of $(20.93 \pm 0.04)\,\mathrm{M}_{\odot}$. They account for $\sim 3.2\%$ of the total mass, and $\sim 7.3\%$ of the mass of the dense portion of the cloud. In contrast, only 10 starless cores are located within L1689, totalling $(4.28 \pm 0.01)\,\mathrm{M}_{\odot}$. They make up $\sim 1.1\%$ of the total sub-region mass. However, this still accounts for $\sim 4.8\%$ of the total mass of the dense region. All the cores in both regions lie within the $A_V > 7$ boundary. This result suggests that core formation is more strongly dependent on the local surface density, and less dependent on total cloud mass. This is consistent with the findings presented by Ladjelate et al. (2020), and by Nutter, Ward-Thompson, and André (2006), though I note that the absolute percentages of cloud mass (or dense gas mass) bound in cores for L1688 and L1689 are markedly lower than that presented by Ladjelate et al. (2020). The absolute percentages are consistent with results presented by Nutter, Ward-Thompson, and André (2006). There are several potential factors contributing to this effect. For example, the full extent of the clouds is defined differently, the column density fitting methods are different, and the observation bands used to obtain the column density estimate are not the same. Furthermore, the core catalogue differs between these works, with Ladjelate et al. (2020) obtaining 142 cores, while Pattle et al. (2015) identify 46 cores. However, while the value of the core formation efficiency differs, the broad trends I observe agree well with existing literature; namely that as a fraction of total cloud mass, L1688 has a higher core formation efficiency than L1689, but the sub-regions have similar efficiencies at an $A_V > 7$.

To verify these results I produce an independent catalogue of compact objects. I apply a dendogram to the total column density maps of L1688 and L1689, with a minimum column density threshold set to five times the median uncertainty for each sub-region, a minimum difference between nested structures equal to the median uncertainty, and a minimum size of 10 pixels, equating to $\sim 0.0002\,\mathrm{pc}^2$ at the nominal cloud distance of 140 pc. The minimum column density threshold differs from that

Table 6.4. The positions, semi-major and semi-minor axes, PPMAP estimated mass, and position angles of the 46 starless cores in L1688 and L1689. The core positions, sizes and angles are taken from the catalogue presented by Pattle et al. (2015), as are the core identifiers, listed in column P15 ID.

L1688						
P15 ID	R.A. (°)	Dec. (°)	PPMAP Mass ($M_\odot$)	a $''$	b $''$	θ (°)
1	246.614	-24.398	1.96 ± 0.006	20.4	16.2	178.7
2	246.613	-24.393	1.28 ± 0.006	19.6	15.5	170.0
3	246.622	-24.407	1.55 ± 0.007	29.0	17.2	139.0
5	246.611	-24.376	0.88 ± 0.008	36.2	18.0	106.2
6	246.615	-24.384	1.16 ± 0.008	30.9	22.1	169.6
7	246.620	-24.376	0.64 ± 0.007	28.3	19.2	24.3
8	246.631	-24.413	0.69 ± 0.007	27.2	17.7	88.3
9	246.591	-24.393	0.29 ± 0.007	26.5	19.2	3.6
10	246.600	-24.364	0.44 ± 0.006	27.2	17.7	88.3
11	246.605	-24.360	0.19 ± 0.004	14.3	15.7	100.0
15	246.681	-24.290	0.56 ± 0.006	29.7	22.4	71.0
19	246.542	-24.327	0.24 ± 0.005	22.8	14.5	41.8
20	246.627	-24.370	0.36 ± 0.007	31.9	19.9	80.7
23	246.631	-24.366	0.24 ± 0.006	30.0	20.6	90.9
26	246.548	-24.412	0.17 ± 0.005	25.7	16.7	109.1
27	246.578	-24.419	0.11 ± 0.004	16.8	16.0	78.8
28	246.542	-24.386	0.23 ± 0.006	29.4	20.1	94.9
29	246.801	-24.497	0.62 ± 0.006	26.9	19.2	136.6
30	246.813	-24.511	0.57 ± 0.006	26.2	19.2	114.9
31	246.816	-24.506	0.28 ± 0.004	19.5	12.9	38.4
32	246.817	-24.519	0.35 ± 0.006	25.1	17.6	98.3
35	246.831	-24.454	0.48 ± 0.006	27.1	18.2	26.8
36	246.836	-24.449	0.43 ± 0.006	29.6	17.4	172.2
37	246.851	-24.464	0.34 ± 0.004	14.3	15.7	80.0
38	246.857	-24.448	0.91 ± 0.008	32.6	18.0	156.2
41	246.873	-24.443	0.91 ± 0.008	34.5	20.6	150.1
43	246.889	-24.438	0.88 ± 0.007	34.9	14.3	38.2
44	246.885	-24.443	1.16 ± 0.008	36.6	19.1	23.3
45	246.886	-24.451	0.53 ± 0.006	25.9	16.3	112.9
46	246.896	-24.438	0.38 ± 0.004	14.3	15.7	100.0
48	246.746	-24.574	0.50 ± 0.006	28.8	19.5	117.0
49	246.754	-24.578	0.27 ± 0.005	24.5	14.3	151.7
50	246.759	-24.581	0.32 ± 0.006	28.3	19.2	48.3
53	246.770	-24.654	0.27 ± 0.005	28.1	15.8	148.4
58	246.840	-24.664	0.22 ± 0.004	14.3	15.7	100.0
70	246.994	-24.561	0.50 ± 0.006	29.2	18.5	38.6

Table 6.4 (cont.). The positions, semi-major and semi-minor axes, PPMAP estimated mass, and position angles of the 46 starless cores in L1688 and L1689. The core positions, sizes and angles are taken from the catalogue presented by Pattle et al. (2015), as are the core identifiers, listed in column P15 ID.

L1689						
P15 ID	R.A. (°)	Dec. (°)	Mass ($M_\odot$)	a $''$	b $''$	θ (°)
75	247.988	-24.954	0.37 ± 0.004	28.3	19.2	65.7
78	247.973	-24.933	0.27 ± 0.003	22.8	14.5	158.2
79	248.001	-24.929	0.13 ± 0.002	14.3	15.7	86.2
80	247.907	-24.830	0.54 ± 0.004	29.2	18.5	161.4
81	247.912	-24.833	0.26 ± 0.003	14.3	15.7	80.0
82	247.925	-24.826	0.40 ± 0.004	28.1	16.1	109.9
84	248.120	-24.486	0.70 ± 0.003	14.3	15.7	80.0
86	248.125	-24.480	0.75 ± 0.004	23.5	14.3	44.7
87	248.111	-24.470	0.52 ± 0.005	25.6	21.4	23.6
88	248.090	-24.461	0.33 ± 0.004	22.1	18.8	74.3

used to estimate the boundary of the dense regions so as to avoid misidentifying small scale edge effects as objects.

The set of objects for each sub-region is then produced by selecting only the top level density structures, or leaves, of each dendogram, excluding any leaves which cover an area larger than $0.0079\,\mathrm{pc}^2$. This eliminates objects whose area on the sky is greater than that of a spherical core with a diameter of 0.1 pc. I note that the objects I have identified only represent dense, compact clumps and they have not been verified as starless cores. I identify 75 objects in L1688, and 20 in L1689. The objects are highlighted by black contours in Figure 6.25 and Figure 6.26.

The positions of the cores identified by Pattle et al. (2015) agree well with many of the objects identified in the dendogram, although many objects appear to be comprised of several overlapping cores. The dendogram also identifies many additional objects which do not have counterparts in the core catalogue. The total mass of the objects is $(54.1 \pm 0.8)\,M_\odot$, which accounts for 19.0% of the dense mass, and 8.3% of the total mass in L1688. The clump mass uncertainty was calculated in a method similar to that of the sub-region and dense gas mass uncertainties.

As with L1688 the core positions in L1689 agree well with several of the dense dendogram objects, with the dendogram identifying several additional compact objects. The combined L1689 object mass is $(18.9 \pm 0.3)\,M_\odot$, which accounts for 21.3% of the dense mass, and 4.8% of the total sub-region mass.

While the dendogram objects clearly account for a much larger percentage of the mass in both sub-regions, the results still appear to indicate that while the

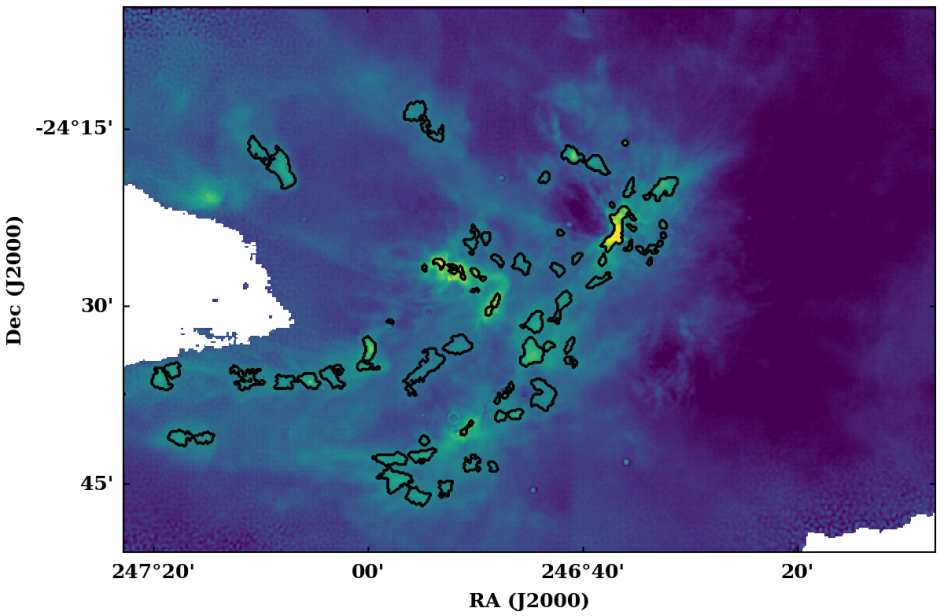

Figure 6.25. The set of dense objects detected in L1688 utilising a dendogram technique.

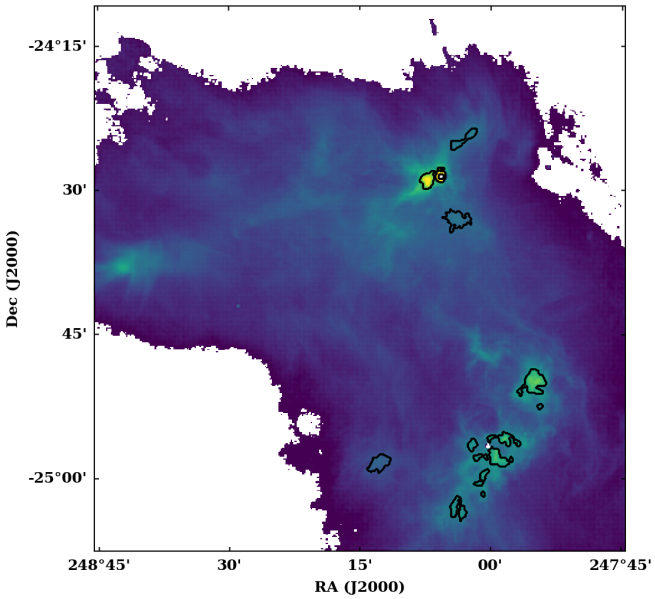

Figure 6.26. The set of dense objects detected in L1689 utilising a dendogram technique.

fraction of L1688 that is attributable to these structures is greater (by nearly a factor of two) than that of L1689, the fraction of the dense mass in objects is similar in both sub-region. This further suggests that global cloud mass does not directly influence core formation efficiency, but instead drives the formation of dense regions which, once they reach a given threshold, appear to have similar core formation efficiencies.

6.3.2.2 Filament Networks

To investigate the properties of the filaments identified in Section 6.3.1, I fit each filament with the FilChaP routine. I determine the local tangent to the filaments at every point along the spines by fitting adjacent spine points with a cubic polynomial and taking the derivative. From this I derive the perpendicular at each spine point, and take a slice in the data along the perpendicular out to 1 pc on either side of the filament. The slices are then passed to FilChaP which bundles neighbouring slices into contiguous groups of 12, and produces a local median filament profile located at the centre of each bundle. Therefore, the local median profiles are separated by $\sim$0.057 pc ($\sim$84″). The local median profile positions are indicated in Figure 6.23 and Figure 6.24 by the white points, while the filament shapes are approximately traced by the white connecting lines.

Each local median profile is independently fitted with a $p = 2$ Plummer-like function. FilChaP performs an automatic local background subtraction, and assumes the median profile can be fit by a symmetric function. The form of the Plummer-like function is identical to equation 5.6, with FilChaP returning values of the central column density, N_0, and the Plummer-like inner radius, r_0, for each local median profile position. r_0 is converted to a FWHM for a Plummer-like function through equation 5.3. The variation of these quantities along the filament lengths, along with other derived quantities for individual filaments, are discussed in detail in Section 6.3.3.

For each filament, I derive the total mass contained within the dense inner region within the FWHM. As the variation in r_0 and N_0 along the length of a filament is found to dominate over the uncertainty in either the column density map or the uncertainty in the fitting of the parameters for any given bundle, I utilise a bootstrapping method to determine the filament masses and associated uncertainties. For each local median profile, I draw random value of r_0 and N_0 from Gaussian distributions created from the previously fitted parameters. I then calculate the local line density for each local median profile using these randomly obtained parameters by employing equation 5.4, integrating out only to a distance of the FWHM. I then multiply each line mass by the nominal separation of the bundles, and sum the resulting values for

every bundle in a given filament. This produces a single value of the total filament mass. This process is repeated 10000 times, drawing a new set of r_0 and N^0 values for each of the local median profiles each time. Thus, a distribution of possible filament masses is constructed, from which I draw the median and MAD values.

In L1688 all the filaments lie wholly within the $A_V > 7$ contours (as shown in Figure 6.23). The inner filament regions have a mass of $(81.0 \pm 0.5)\,\mathrm{M}_\odot$ which accounts for $\sim 12.4\%$ of the total mass within the field of view, and $\sim 28.4\%$ of the mass of the dense gas. Figure 6.24 shows that, in L1689, while f1 and f2a (identified in Figure 6.15) are entirely enclosed by the $A_V > 7$ region, f2b and a portion of f3 extend beyond the contours into the more diffuse material. Therefore, when calculating the fraction of the dense gas in L1689 that is contained within the inner regions of the filaments, I exclude the mass contributions from the bundles that do not fall within the contours. The cumulative mass of the filaments in L1689 comes to $(42.2 \pm 0.3)\,\mathrm{M}_\odot$, accounting for $\sim 8.0\%$ of the total cloud mass. The filament mass excluding f2b and the low density portion of f3 is $(31.7 \pm 0.3)\,\mathrm{M}_\odot$, and accounts for $\sim 35.8\%$ of the dense gas mass.

6.3.3 Individual Filament Properties

The properties obtained from FilChaP for the filaments in the L1688 and L1689 sub-regions are shown by the coloured points for each of the local median profile locations in Figure 6.27 and Figure 6.28 respectively. In both Figures, panel (a) details the local measure of the FWHM, derived from the Plummer-like r_0 parameter. Panel (b) gives the central column density, N^0, while panel (c) shows the derived line mass, obtained by integrating the Plummer-like function at each bundle position with equation 5.4 out to 0.4 pc either side of the filament spine. Average parameter values are calculated for each filament by taking the median and MAD of each parameter for all the bundles in a given filament. These are presented in Table 6.5. An average value for each parameter is also calculated for each sub-region by considering all the bundles from each of the filaments within the sub-region boundaries.

Figure 6.27 indicates that the FWHM of the filaments in L1688 is generally drawn from a tight distribution around $\sim$0.1 pc. However, stark departures from this trend are present around the eastern ends of the f1 and f2 filaments, and in f5 and f6. f4 appears narrower than the other filaments, and indeed has the lowest median filament width, $\widetilde{\mathrm{FWHM}}_{f4} = 0.07 \pm 0.01$pc. f4 also has the highest median central column density, $\widetilde{N}_{0f4} = 222 \times 10^{20} \pm 62 \times 10^{20} \mathrm{H_2\,cm^{-2}}$. The bundles in f1 directly between the S1 and HD147889 are narrower than the remaining filament, and also have a higher

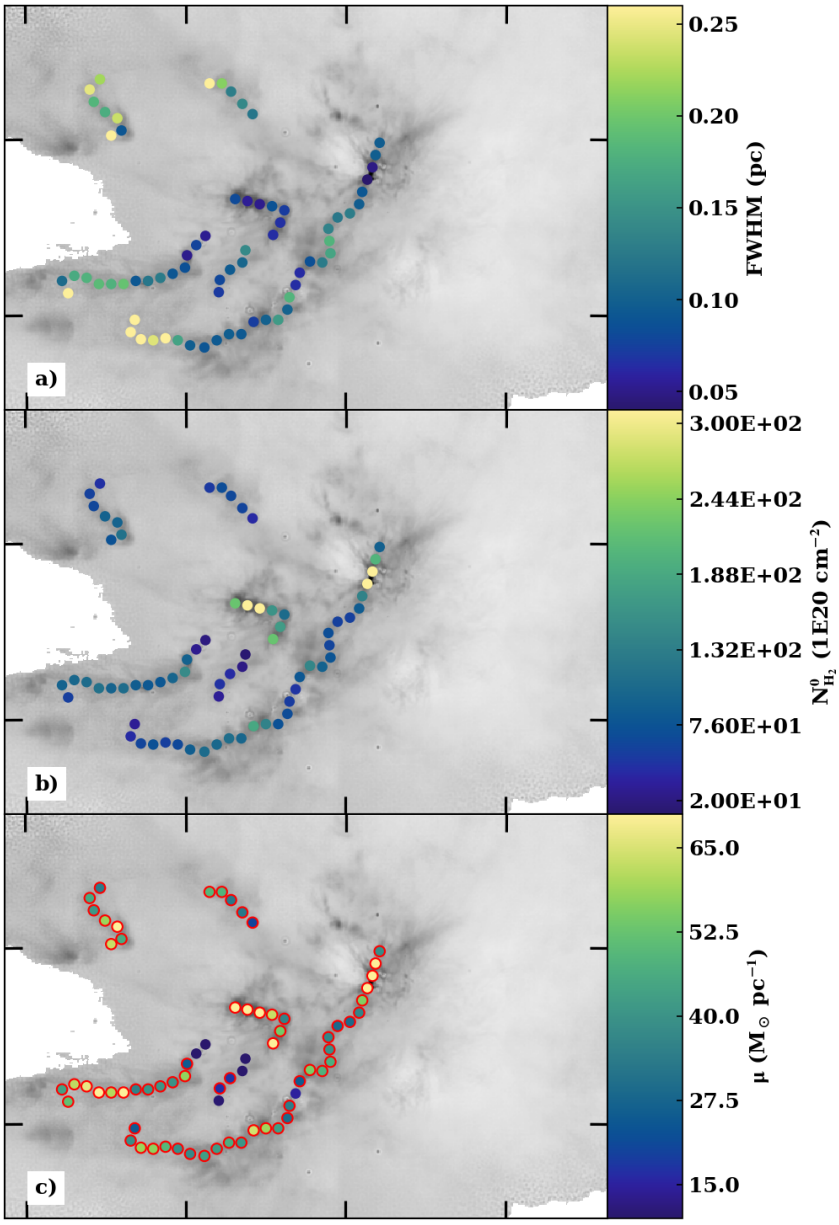

Figure 6.27. Results from L1688 of using the FilChaP algorithm to investigate variations in (a) FWHM, (b) central column density N_0, and (c) line density, μ. The value of each parameter is given by the colour of each circle. Red outlines around circles in (c) indicate bundles with a value of μ that exceeds the nominal critical line density $\mu_c = 16.2\ \mathrm{M}_\odot\,\mathrm{pc}^{-1}$, for a gas with a temperature of 10 K.

Table 6.5. The properties of each of the filaments identified in the L1688 and L1689 sub-regions. $N^0_{H_2}$, FWHM and μ are length averaged median values.

L1688							
Fil	N_0 (10^{20} $H_2\,cm^{-2}$)	FWHM (10^{-1} pc)	μ ($M_\odot\,pc^{-1}$)	Length (pc)	Mass ($M_\odot$)	$\frac{M_{cores}}{M_{fil}}$	N_{cores}
f1	81.3±3.6	1.00±0.04	42.4±1.4	1.76	36.1±0.5	0.32	18
f2	31.0±1.7	0.95±0.02	10.5±1.4	0.28	1.4±0.1	0.0	0
f3	94.7±1.9	1.21±0.08	43.6±4.5	0.81	17.8±0.4	0.03	1
f4	222.7±9.4	0.66±0.02	70.1±5.9	0.35	10.1±0.4	0.77	13
f5	75.2±2.8	2.21±0.06	46.0±4.7	0.35	10.4±0.2	0.0	0
f6	61.1±1.2	1.39±0.03	32.8±5.7	0.24	5.3±0.1	0.0	0
L1689							
Fil	N_0 (10^{20} $H_2\,cm^{-2}$)	FWHM (10^{-1} pc)	μ ($M_\odot\,pc^{-1}$)	Length (pc)	Mass ($M_\odot$)	$\frac{M_{cores}}{M_{fil}}$	N_{cores}
f1	85.8±3.0	1.58±0.08	46.9±3.5	0.61	14.2±0.3	0.05	2
f2a	78.8±3.7	0.98±0.07	41.3±4.4	0.46	10.0±0.2	0.23	4
f2b	27.2±0.6	3.15±0.08	23.8±1.3	0.36	7.1±0.2	0.0	0
f3	53.8±2.9	2.60±0.03	45.4±4.4	0.42	10.9±0.2	0.0	0

central column density, indicating that they may be experiencing compression from the two PDRs. The line mass of all the filaments varies between $5.3\,M_\odot\,pc^{-1}$ and $136.8\,M_\odot\,pc^{-1}$. The compressed bundles in f1 have line masses of $117.1\,M_\odot\,pc^{-1}$ and $136.8\,M_\odot\,pc^{-1}$. f4 has the highest median line mass at $71.0\,M_\odot\,pc^{-1}$.

By taking the nominal density threshold for thermally supercritical gas at 10 K, $16.2\,M_\odot\,pc^{-1}$, I can infer which parts of the filaments are likely unable to support themselves against gravitational collapse with thermal pressure alone. I mark these super-critical bundles with a red outline in Figure 6.27. I find that very few regions of the L1688 filaments can be described as sub-critical by this metric. However, I note that the mean dust temperature in L1688 is higher than 10 K, and given the presence of the two PDRs, the true gas temperature also likely exceeds this value. Therefore, the critical threshold of $16.2\,M_\odot\,pc^{-1}$ is likely an extreme lower limit.

The filaments in L1688 have a median width of $\widetilde{\text{FWHM}}_{L1688} = (0.11 \pm 0.04)$ pc, with an average uncertainty on a single width measurement of 0.007 pc. The median value for the filament central column density, $\widetilde{N_{0\,L1688}} = (8.4 \pm 2.6) \times 10^{21}$ $H_2\,cm^{-2}$, with an average individual bundle uncertainty of 0.2×10^{21} $H_2\,cm^{-2}$. The median line mass, $\widetilde{\mu}_{L1688} = 43 \pm 14$ $M_\odot\,pc^{-1}$.

By associating the starless cores with individual filaments, I can determine which filaments are more readily forming stars. For each of the 36 cores in L1688, I determine the distance to the nearest spine point on any filament. Cores are associated with the filament which contains the nearest bundle if this distance is less than the

0.1 pc median FWHM for L1688. By this metric, only three of the filaments contain associated cores: f1, f2 and f4. f2 contains only a single core, while f1 contains 18 and f4 contains 13. One core is not associated with any of the identified filaments. However, I note that it does reside in a filamentary spur to the north of the S1 PDR, which is initially detected by FilFinder, but is rejected from the final sample as its length does not exceed 0.3 pc.

The mass of cores accounts for $\sim 25\%$ of the total mass of filaments in L1688. The mass of each filament which is bound in the cores is given in Table 6.5.

In L1689 filaments f1, f2a, and the section of f3 that falls within the $A_V > 7$ contour display a similar distribution of widths to the filaments in L1688. However, f2b and the diffuse region of f3 have much larger widths. In both f1 and f2a the sections of the filaments near the masked protostars both appear pinched, with narrower widths when compared to the other segments in the filaments. The median width of f2b is three times greater than that of f2a, and twice the median width of f1. In addition, f2b and f3 have lower median central column density values ($\widetilde{N_{0f3}} = (54 \pm 19) \times 10^{20} \mathrm{H_2\,cm^{-2}}$ and $\widetilde{N_{0f2b}} = (27 \pm 4) \times 10^{20} \mathrm{H_2\,cm^{-2}}$ respectively) than those of f1 and f2b ($\widetilde{N_{0f1}} = (85 \pm 19) \times 10^{20} \mathrm{H_2\,cm^{-2}}$ and $\widetilde{N_{0f2a}} = (79 \pm 24) \times 10^{20} \mathrm{H_2\,cm^{-2}}$). The variation in column density along the length of the filaments is relatively smooth, with the exception of the squeezed bundles near *IRAS* 16293-2422. These bundle points display an increase in column density of approximately a factor of five.

The L1689 median filament width, $\widetilde{\mathrm{FWHM}}_{L1689}$, is (0.19 ± 0.08) pc, with an average uncertainty on an estimate from an individual bundle of 0.007 pc. The median filament width in L1689 is nearly twice the median filament width in L1688. However, this estimate of median width includes the contributions from the low density, more diffuse sections of f3 and f2b, which have a much wider profile, as shown in Table 6.5. By excluding these low density structures, the median filament width for L1689 is (0.14 ± 0.05) The median value for the filament central column density, $\widetilde{N_{0L1689}} = (6.8 \pm 3.3) \times 10^{21}$ $\mathrm{H_2\,cm^{-2}}$, with an average uncertainty of 0.1×10^{21} $\mathrm{H_2\,cm^{-2}}$. If I again exclude the contribution from filament f2b and the low density tail of f3, the median central column density for the filaments in L1689 rises to $(8.3 \pm 2.5) \times 10^{21}\,\mathrm{H_2\,cm^{-2}}$.

By assuming the same critical density threshold as L1688, the filaments in L1689 are super-critical at all points. Here too, I assume the value for the critical density to be a lower limit, as the dust in L1689 appears to be hotter than 10 K, indicating this may also be true for the gas. However, L1689 is much less strongly heated than L1688.

The median line mass for the filaments in L1689 is $\widetilde{\mu}_{L1689} = 43 \pm 12\ \mathrm{M_\odot\,pc^{-1}}$. This value also includes the contributions from the low density portion of f3, and from

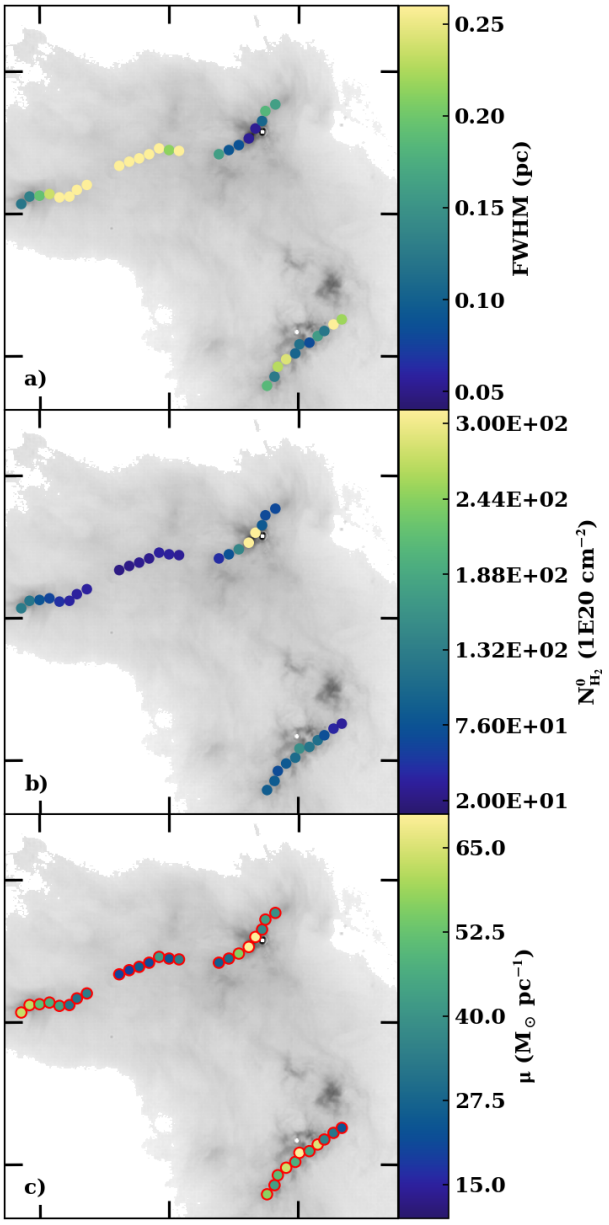

Figure 6.28. Results from L1689 of using the FilChaP algorithm to investigate variations in (a) FWHM, (b) central column density N_0, and (c) line density, μ. The value of each parameter is given by the colour of each circle. Red outlines around circles in (c) indicate bundles with a value of μ that exceeds the nominal critical line density $\mu_c = 16.2\ \mathrm{M}_\odot\,\mathrm{pc}^{-1}$, for a gas with a temperature of 10 K.

the f2b sub-filament. By excluding these low density filament sections, I estimate a median line density of $45 \pm 12\,\mathrm{M_\odot\,pc^{-1}}$.

As with L1688, I attempt to associate the cores within L1689 with parent filaments. Four of the 10 cores are not associated with any filaments, while two are associated with f1, and the remaining four are part of f2a. The f1 and f2a cores are clustered near the masked protostars. The cores account for $\sim 13\%$ of the total filament mass in L1689.

6.3.3.1 The Effect of S1 and HD147889 on L1688 f1

As discussed in Section 6.3.1, the PPMAP data hypercube for L1688 indicates that the north west portion of the f1 filament is being impacted by its proximity to the PDRs produced by S1 and HD147889. To investigate this, I first define the straight line directly connecting S1 and HD147889. I make the assumption that this connecting line represents the axis of strongest combined influence between the two pre-main sequence stars.

Figure 6.29 shows the position of the filament spine points in relation to S1 and HD147889 (indicated by the blue star markers). For each spine point along the L1688 f1 filament I record the column density, line of sight mean dust temperature and line of sight mean dust opacity index. I also calculate the shortest distance from the point to the S1-HD147889 axis. Figure 6.30, Figure 6.31 and Figure 6.32 show plots of the spine point column density, temperature, and opacity index respectively as a function of this distance. In all cases, the black markers in the Figures indicate spine points located to the south east of the S1-HD147889 axis, while the black-edged, grey markers indicate spine points that lie to the north west. Markers with a red boarder highlight spine points at the positions of local maxima in the column density.

The relationship shown in Figure 6.30 displays an initially sharp decrease in the column density of the filament spine with distance from the S1-HD147889 axis. The fall in surface density, of more than an order of magnitude, persists from the peak near the S1-HD147889 axis, out to 0.2 pc, and is seen to both the north west and the south east. While the north west spur of f1 then terminates at $\sim$0.2 pc, the south east region retains an approximately constant column density over its remaining extent out to a projected distance of 1 pc from the axis. The peak in column density occurs at the point closest to the S1-HD147889 axis, indicating that this region is likely being compressed by the two sources.

Two secondary peaks in column density occur at 0.5 pc and 0.8 pc from the axis. By comparing Figure 6.29 with Figure 6.23, it can be seen that these secondary maxima corrispond with the positions of several of the identified pre-stellar cores

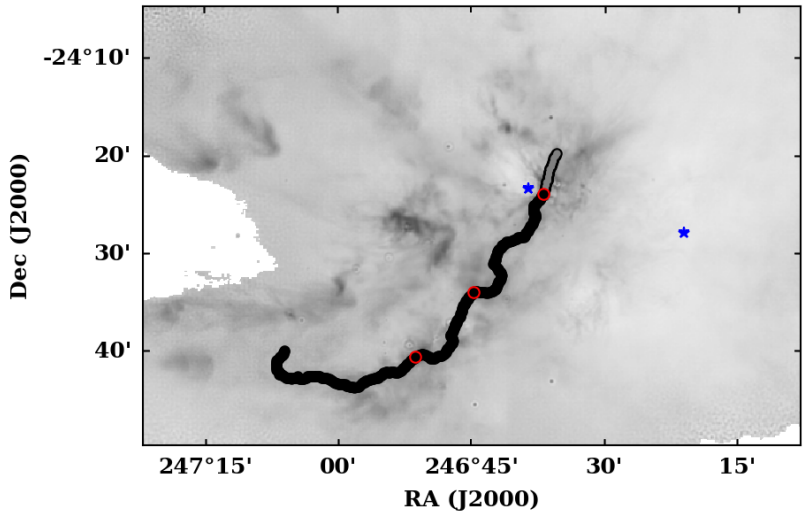

Figure 6.29. The spine of the L1688 f1 filament with respect to the pre-main sequence stars, S1 and HD147889 (blue star markers). The solid black line represents the portion of the spine to the south east of an axis drawn directly between the stars, while the grey line represents the portion of the filament to the north west of this axis. Red outlines indicate local maxima in the column density of the spine.

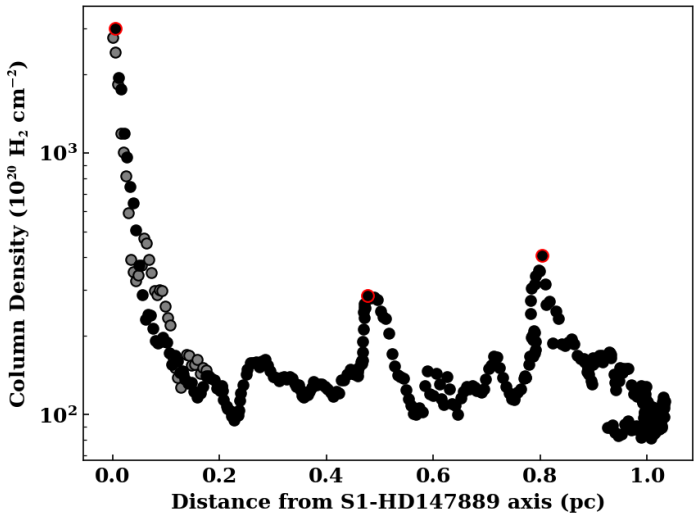

Figure 6.30. Variations in column density at each spine point along L1688 f1, with distance from the axis defined between S1 and HD147889. The black markers are taken from spine points to the south east of the axis, while the grey markers are from spine points to the north west of the axis. The markers with red outlines highlight the spine points at local maxima. The error bars show the total column density uncertainty derived from the PPMAP uncertainty data-hypercube.

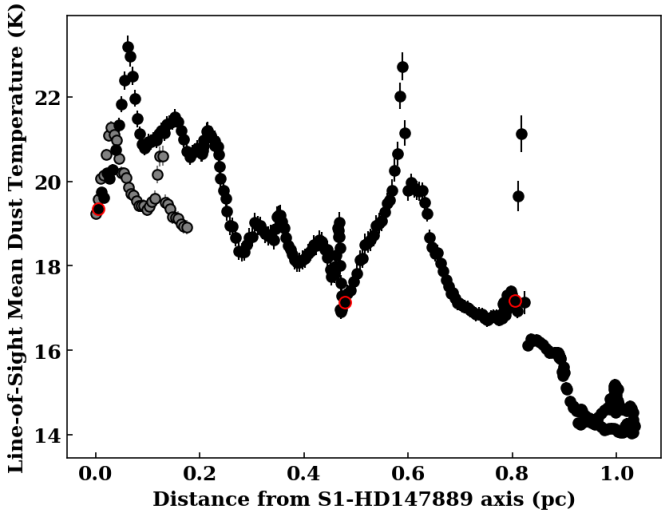

Figure 6.31. Variations in mean line of sight dust temperature at each spine point along L1688 f1, with distance from the axis defined between S1 and HD147889. The black markers are taken from spine points to the south east of the axis, while the grey markers are from spine points to the north west of the axis. The markers with red outlines correspond to spine points at local maxima in the column density. The error bars show the associated error-on-the-mean for each of the mean dust temperatures.

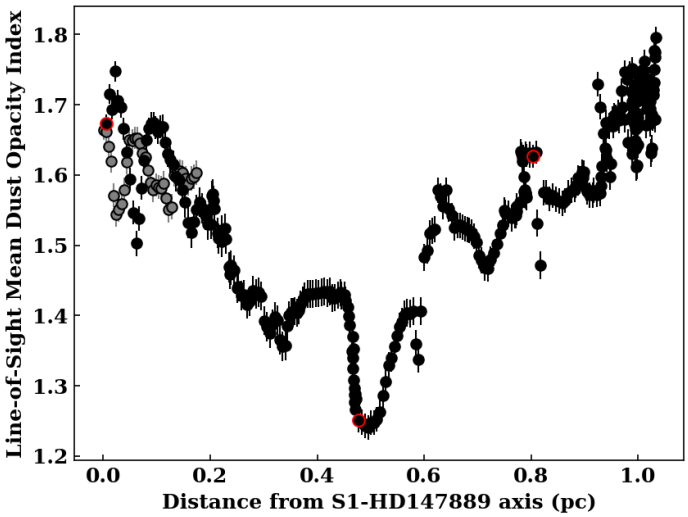

Figure 6.32. Variations in mean line of sight dust opacity index, β, at each spine point along L1688 f1, with distance from the axis defined between S1 and HD147889. The black markers are taken from spine points to the south east of the axis, while the grey markers are from spine points to the north west of the axis. The markers with red outlines correspond to spine points at local maxima in the column density. The error bars show the associated error-on-the-mean for each of the mean opacity indices.

obtained from the Pattle et al. (2015) catalogue.

Figure 6.31 shows a decrease in the line of sight mean dust temperature with distance from the axis at each of the spine points. In contrast to the column density, the decrease in dust temperature is approximately linear over the 1.0 pc distance range. The spine points associated with the column density maxima are located at local minima in temperature. The temperature peaks sharply to either side of these points, with the south eastern side of these regions experiencing the greatest increase in temperature. The anti-correlation between column density and temperature in this instance is consistent with a view of young sites of active star formation becoming denser and colder than the surrounding medium as they contract and become more optically thick to the ambient radiation field. The rise in temperature to either side of these regions can potentially be explained by heating from more massive, faster forming proto-stars which warm the edges of these dense regions.

There is no equivalent fall in the value of the dust opacity index with distance seen in Figure 6.32. Similarly, there is no apparent correlated trend in the dust opacity index at the positions of the column density maxima at 0.005 pc and 0.8 pc. However, as with temperature, the local column density maxima at 0.5 pc from the axis coincides with a minimum in the dust opacity index. At present, there is no clear explanation for this phenomenon, though as the dust temperature and opacity index exhibit similar trends at this location, the temperature-β anti-correlation can be ruled out as a cause.

6.3.4 Comparison with *Herschel* Observations

To ensure that the PPMAP column density hypercubes of the regions are a good fit to the data, I perform the flux recovery tests outlined in Chapter 4 and Chapter 5. I first produce maps of column density for both the L1688 and L1689 regions by conducting a MBB fitting routine on the 160 µm to 500 µm observations, with the Palmeirim et al. (2013) resolution recovery technique, using a fixed value of $\beta = 2$.

I then recover *Herschel*-like and SCUBA-2-like observations from the PPMAP and MBB products with the method described in Chapter 4. Unlike the L1495 tests, I generate recovered observations for all six bands (70 µm to 850 µm) from both the PPMAP and MBB products, despite only four bands being used to generate the MBB maps. This allows me to ensure PPMAP is a good fit to the data over all observation bands. I note, therefore, that the 70 µm and 850 µm observations recovered from the MBB products are not necessarily expected to be good fits to the true *Herschel*

observations.

Figure 6.33 and Figure 6.34 show the recovered observations from both PPMAP and the MBB technique for all observation bands alongside the true observations for L1688 and L1689 respectively. Even neglecting the artefacts present in the MBB recovered observations, it is clear that PPMAP produces a better fit to the background medium than the MBB technique, though both methods perform well in the more dense regions. As expected, this is particularly true for the 70 µm and 850 µm bands, which are not available to the MBB fitting algorithm. The same trend is seen in Figure 6.34 for the L1689 region, with PPMAP more accurately recovering extended emission. Both techniques encounter problems with areas of low true emission in the 160 µm band. The black contour is plotted over the recovered and true 160 µm observations, highlighting the region where the true *Herschel* observation has a value of 52.0 MJy sr^{-1}. This threshold represents the value below which lies the lowest quartile of emission. Within this contour, both fitting techniques perform well at recovering the true emission. However, the lower signal to noise outside of this contour contributes to PPMAP greatly overestimating, and the MBB technique underestimating, the true emission.

Table 6.6 presents the Goodness of Fit parameter, $\mathcal{G}$ (defined in equation 4.4 in Chapter 4, Section 4.0.1.2), for each of the recovered observations for the L1688 and L1689 sub-regions. In L1688, PPMAP produces a better fit to the true observations in all bands except the 160 µm and 500 µm band, though both methods perform reasonably well across all bands. The Goodness of Fit is much better for PPMAP than the MBB technique in L1689, with the exception of the 160 µm band, where the effects of PPMAP overestimating the contribution from the lowest quartile of emission dominate the parameter calculation. When the lowest quartile of emission is excluded from the calculation of $\mathcal{G}$, indicated in the Table by the 160_C µm band, PPMAP and the MBB technique perform equally well.

As the poor fit to the lowest quartile of emission only affects the edges of the map, and a small area of low density material near the centre, while much of the analysis takes place away from these zones, I find PPMAP produces a model that is generally a good fit to the input observations for both regions across all bands. This fit is comparable to or better than the fit produced by a MBB technique across bands common to both algorithms, and benefits from the added bands at 70 µm and 850 µm.

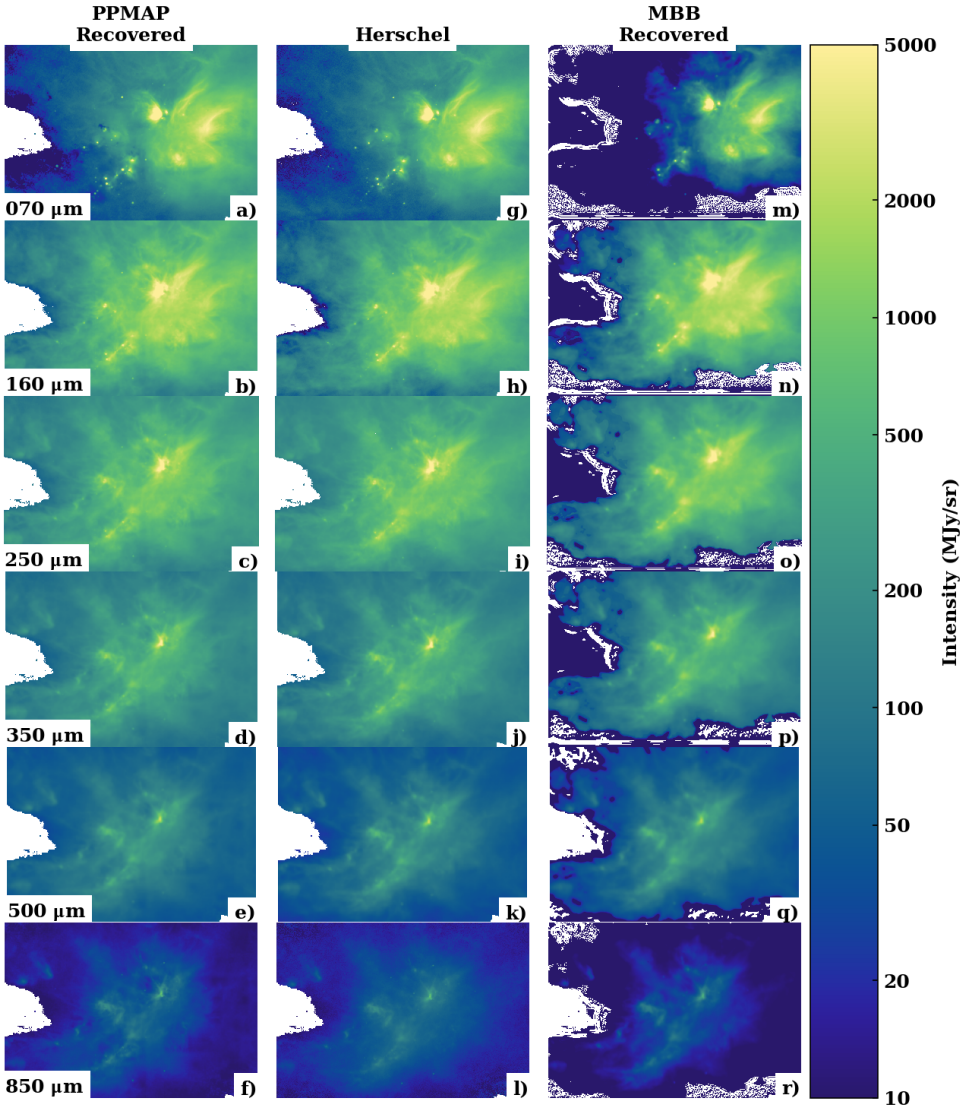

Figure 6.33. A comparison of recovered intensity from the PPMAP dust model of L1688, presented as synthetic observations (left), with the true *Herschel* and SCUBA-2 observations used to derive the model (middle). A further comparison with intensity recovered from a MBB fitting technique (right) provides a reference for the standard method. The images are compared across six bands (70 µm to 850 µm), and share a common intensity colour scale.

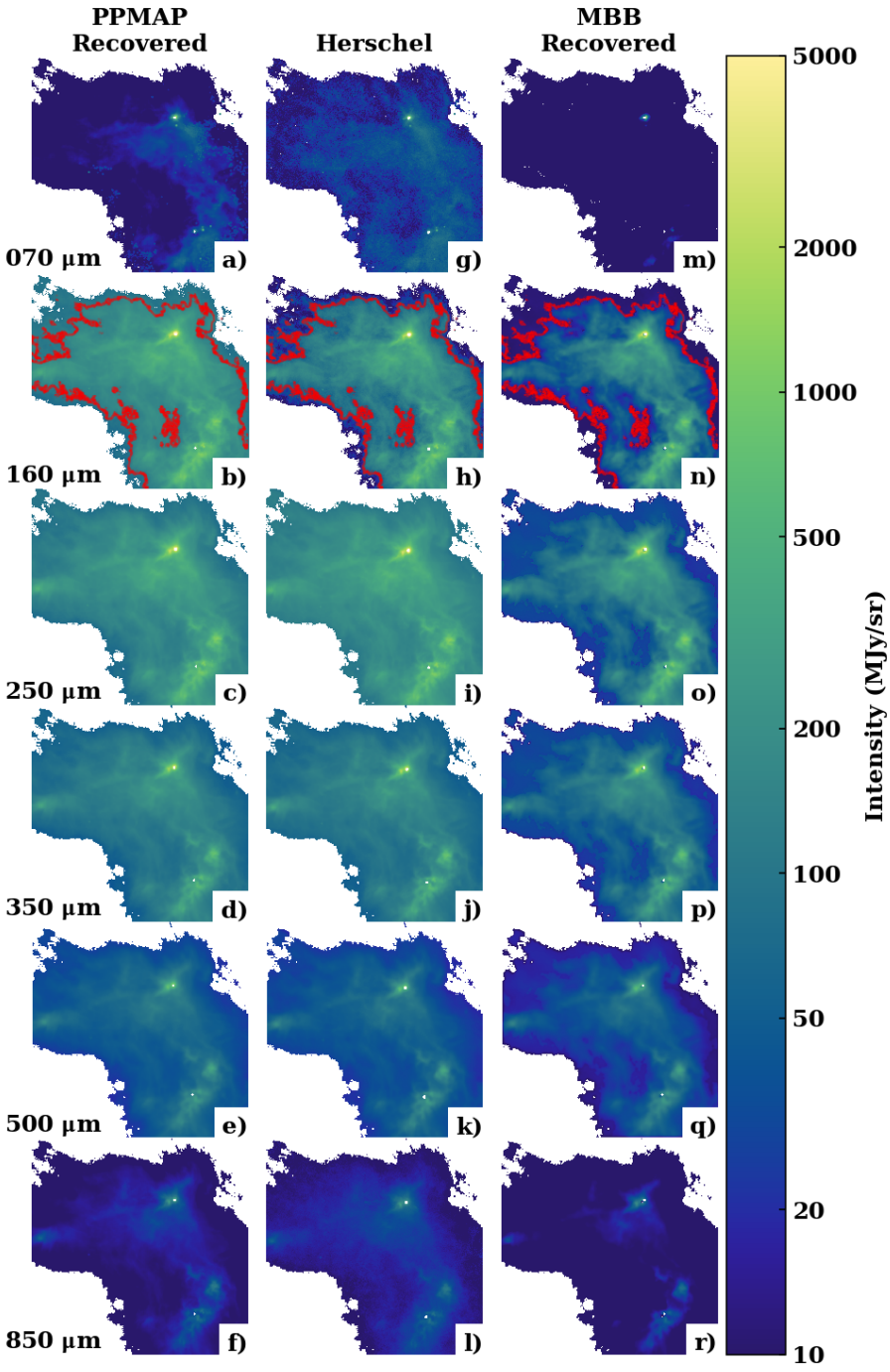

Figure 6.34. A comparison of recovered intensity from the PPMAP dust model of L1689, presented as synthetic observations (left), with the true *Herschel* and SCUBA-2 observations used to derive the model (middle). A further comparison with intensity recovered from a MBB fitting technique (right) provides a reference for the standard method. The images are compared across six bands (70 µm to 850 µm), and share a common intensity colour scale. The red contour on the images for the 160 µm band are drawn at the level of the lowest quartile of emission from the *Herschel* observation, and act as a method of excluding the edges and a low signal to noise region of the models, which are subject to poor fitting.

Table 6.6. Goodness of Fit parameter, $\mathcal{G}$, for synthetic observations recovered from the models produced by PPMAP and a MBB fitting technique for the L1688 and L1689 sub-regions. The row for band 160_C µm gives the Goodness of Fit parameters for L1689 within a contour excluding the edges and a low signal to noise region of the observations. This contour is at the level of the lowest quartile of emission in the *Herschel* 160 µm observation.

	L1688	
Band	$\mathcal{G}_{\rm PPMAP}$	$\mathcal{G}_{\rm MBB}$
70 µm	0.21	0.61
160 µm	0.29	0.21
250 µm	0.19	0.30
350 µm	0.20	0.25
500 µm	0.28	0.21
850 µm	0.32	0.53
	L1689	
Band	$\mathcal{G}_{\rm PPMAP}$	$\mathcal{G}_{\rm MBB}$
70 µm	0.57	0.97
160 µm	19.76	1.96
160_C µm	0.50	0.50
250 µm	0.18	0.57
350 µm	0.17	0.43
500 µm	0.28	0.31
850 µm	0.32	0.56

6.4 Conclusions

I utilise the PPMAP algorithm to produce a dust model from *Herschel* and SCUBA-2 observations of the L1688 and L1689 sub-regions of the molecular cloud. This produces an estimate of the H_2 column density, as inferred from the dust optical depth, assuming a gas-to-dust ratio of 100 at every sky position, and assuming that the dust can be represented by 12 temperature bands and three opacity index bands. The dust model is found to be consistent both with column density derived from the *Planck* all sky dust model (which has a value of $\widetilde{\Sigma}_{PPMAP}/\widetilde{\Sigma}_{\rm Planck} = 1.44$ for L1688, and 1.31 for L1689), and the 2MASS/NICER (with $A_{V:PPMAP}/A_{V:2MASS} = 0.83$ for L1688, and 1.17 for L1689).

The dust models indicate that both sub-regions are highly sub-structured and fragmented. The areas of the models covering the two sub-regions are similar (5.74 $\rm pc^2$ for L1688, and 5.96 $\rm pc^2$ for L1689, assuming a distance of 140 pc). L1688 is more massive, with a total mass contained within the model of $(650.7 \pm 0.4)\,\rm M_\odot$, while L1689 contains just $(395.4 \pm 0.3)\,\rm M_\odot$ of material. The proportion of the total model area in each sub-region which has a visual extinction greater than $A_V = 7$ ($7 \times 10^{21}\,\rm H_2\,cm^{-2}$) is much greater for L1688 (21%) than for L1689 (6%). The total mass of dense material for the two sub-regions of $(258.3 \pm 0.2)\,\rm M_\odot$ and $(88.5 \pm 0.1)\,\rm M_\odot$, respectively. A

Table 6.7. A summary table of the mass distributions associated with different structures in the L1688 and L1689 sub-regions.

	L1688	L1689
General Properties		
Dust Model Area	5.74 pc^2	5.96 pc^2
Total Mass in Model	650.7±0.4M$_\odot$	395.4±0.3M$_\odot$
Mass of Dense Material ($A_V \geq 7$)	285.3±0.2M$_\odot$	88.5±0.1M$_\odot$
Area Percentage of Dense Material ($A_V \geq 7$)	21%	6%
Mass Percentage of Dense Material ($A_v \geq 7$)	43%	22%
Starless Cores		
Number of Pattle Cores	36	10
Mass of Pattle Cores	20.93±0.04M$_\odot$	4.28±0.01M$_\odot$
Percentage of Total Mass in Pattle Cores	3.2%	1.1%
Percentage of Dense Mass in Pattle Cores	7.3%	4.8%
Number of Dendogram Clumps	75	20
Mass of Dendogram Clumps	54.1±0.8M$_\odot$	18.9±0.3M$_\odot$
Percentage of Total Mass in Dendogram Cores	8.3%	4.8%
Percentage of Dense Mass in Dendogram Cores	19.0%	21.3%
Filament Properties		
Mass of Inner Portion of Filaments	81.1±0.5M$_\odot$	42.2±0.3M$_\odot$
Percentage of Total Mass in Inner Filaments	12.4%	8.0%
Percentage of Dense Mass in Inner Filaments	28.4%	35.8%

summary of the mass distributions of the sub-regions, as well as the mass distributions of smaller structures contained within the sub-regions, is given in Table 6.7.

The distribution of the dust with different temperatures also differs between the two sub-regions. The dense structures in L1689 are mostly composed of material with a dust temperature between 10.0 K and 17.1 K, while the diffuse surrounding medium comprises dust which occupies the temperature range 14.3 K and 20.5 K. Very little dust is found in the L1689 dust model with temperatures above 24.5 K. The L1688 dust model presents a strong temperature gradient from east to west, with significant quantities of dust occupying the 29.2 K and 35.0 K band. Two low density PDRs blown by the stars contain dust at 41.8 K over a large area, with smaller areas of dust at 50.0 K. In contrast, both sub-regions exhibit similar variations in dust opacity index, with dense structures containing dust in all three opacity index bands, while dust in the diffuse surrounding medium is mostly contained within the $\beta = 1.5$ and $\beta = 2.0$ bands.

I utilise the starless core catalogue produced by Pattle et al. (2015) to estimate the mass of 36 cores in L1688, and ten cores in L1689. All the cores in both sub-regions are located in areas with $A_V \geq 7$. The total mass of cores in L1688 is 20.9 M$_\odot$,

and the mass of the cores in L1689 is $4.3\,M_\odot$. While this accounts for 3.2% of the total mass of the L1688 dust model and only 1.1% of the total mass of L1689, the cores in each region make up a roughly similar proportion of the dense material, at 7.3% and 4.8% respectively. The star formation efficiencies as measured over the entirety of each sub-region is three times larger in L1688 than L1689. However, the proportion of the mass of the dense material in each sub-region associated with cores is much closer ($\sim$ 1.5 times higher in L1688). I therefore propose that the star formation efficiency is not directly bound to the total mass of the parent cloud. Instead, once dense structures form, star formation progresses with similar efficiency across all such structures. It is differences in the properties of, and influences on, parent clouds that govern the rate of formation of these dense structures, and drive apparent differences in global star formation efficiency.

To verify this result I produce a catalogue of dense clumps for both regions via a dendogram method. The clumps each have a maximum area less than $0.0079\,pc^2$ (the projected area of a spherical object with a 0.1 pc diameter). The position of the starless cores from the Pattle et al. (2015) catalogue agree well with several of the dense clumps identified in the dendogram, though the cores are not uniquely associated with clumps, and many identified clumps do not have an associated starless core. Therefore the clumps should be considered a loose proxy for the star formation efficiency, indicating structures which could fragment, or have fragmented into one or more starless cores. I identify 75 dense clumps in L1688, with a total mass of $54.1\,M_\odot$ accounting for 19.0% of the dense material by mass, and 8.3% of the total mass. In L1689, I identify 20 dense clumps, with a combined mass of $18.9\,M_\odot$, which equates to 21.3% of the mass of the dense material, and 4.8% of the total mass. These figures are consistent with the hypothesis that dense regions fragment into cores with comparable efficiency, and that differences in sub-region and cloud star formation efficiencies are a consequence of clouds forming $A_V > 7$ structures at different rates.

I apply the FilFinder algorithm to the sub-regions, and identify six filaments within L1688, and three filaments in L1689. I split one filament in L1689 into two due to the algorithm tracing a structure at the midpoint that does not appear to be part of the filament. I take perpendicular slices in the column density at each spine point along the filament, and use FilChaP to bundle the slices in groups of 12, and return a median column density profile at 0.057 pc intervals along each of the filament spines. FilChaP fits an axially symmetric Plummer-like function with a $p = 2$ exponent to each of the median profiles, and performs an automatic background subtraction. FilChaP returns a fitted value of the central column density, N_0, and the inner radius, r_0 (which I convert into a measure of the FWHM of the Plummer-like function) for each

median profile. I estimate the mass contained within the inner portion of each filament by integrating the Plummer-like functions out to their FWHM to produce an estimate of the inner line density at each bundle centroid position, and then integrating these values along each filament. I find that in L1688, the filaments have a total inner mass of $(81.1 \pm 0.5)\,M_\odot$, and account for 12.4% of the total sub-region mass, and 28.4% of the dense mass. The filaments in L1689 have a combined inner mass of $(49.8 \pm 0.3)\,M_\odot$, and make up 12.6% of the total sub-region mass. By excluding the parts of the filaments in L1689 which fall outside the $A_V \geq 7$ material, I calculate the proportion of the dense mass of L1689 bound in the filamentary structures is 35.8%.

This result is at odds with that produced by the analysis of the full sub-regions the cores and dense clumps. As summarised in Table 6.7, while the proportion of the mass of cores in L1688 is approximately a factor three higher than the proportion of the mass of cores in L1689, the proportion of the dense material in each region which is bound in cores is much closer. The same is true of the dense clumps identified via the dendogram analysis. However, the mass of material of L1688 associated with the inner portions of the filaments is only ~ 1.5 times larger than that of L1689, while the proportion of the dense material associated with filament sis actually higher for L1689 than L1688.

The filaments in L1688 have a median width of 0.11 ± 0.04 pc, a median central column density of $(8.4 \pm 2.6) \times 10^{21}\,H_2\,cm^{-2}$, and a median line density of $43 \pm 14\,M_\odot\,pc^{-1}$. In L1689, the median width is 0.19 ± 0.08 pc, the median central column density is $(6.8 \pm 3.3) \times 10^{21}\,H_2\,cm^{-2}$, and the median line density is $43 \pm 12\,M_\odot\,pc^{-1}$. However, the f2b sub-filament, and a portion of the f3 filament in L1689 are much more diffuse than the other filaments, with a greater median width. By excluding sub-filament f2b and the low density portion of f3, the median values for the remaining filaments in L1689 are $\widetilde{\text{FWHM}} = 0.14 \pm 0.05$ pc, $\widetilde{N_0} = (8.3 \pm 2.5) \times 10^{21}\,H_2\,cm^{-2}$, and $\widetilde{\mu} = 45 \pm 12\,M_\odot\,pc^{-1}$.

I attempt to associate each of the starless cores from the Pattle et al. (2015) catalogue with a filament, by identifying the closest filament to each core. Cores further than 0.1 pc from the filaments are deemed not to have an association with any filament. I then calculate the proportion of the mass of each filament that is contained within its associated cores. In L1688, the f1 filament has 18 associated cores, making up 32% of its mass. The f3 filament has a single associated core, which accounts for 3% of its mass, while the f4 filament has 13 associated cores, which containing 77% of its mass. In L1689, f1 has two associated cores, comprising 5% of its mass, while f2a is associated with four cores, which make up 23% of its mass.

The f1 filament in L1688 is the longest filament in either sub-region, running

1.76 pc. The dust model indicates that it has a significant temperature gradient along its length, with the hottest region coinciding with the most dense region, directly between the PDRs associated with S1 and HD147889. To investigate the impact of these PDRs on the filament, I define an axis between the two parent stars, and calculate the distance of each spine point along the filament to this axis. From this I am able to plot the value of the column density, mean line of sight dust temperature, and mean line of sight dust opacity index as a function of distance from the axis. I deduce that the two PDRs are causing significant heating and squeezing, with both temperature and density falling off rapidly with increasing distance from the axis. This is likely the trigger for the formation of a cluster of cores directly between the two stars. Two local maxima in the column density at $\sim$0.5 pc and $\sim$0.8 pc from the axis coincide with the locations of smaller core clusters, and have accompanying local peaks in temperature. The temperature peaks are offset from the column density peaks by a small distance, which is likely evidence that the edges of these regions are strongly heated, while the inner, denser portions are better shielded and thus colder. There is no systematic variation in the dust opacity index with distance from the axis.

Chapter 7
Summary and Future Work

In this chapter I summarise the key points and results from Chapters 4 to 6, which constitute the original work in this thesis. In particular I emphasise the advances in our understanding of filament structure and properties, and their role in mediating star formation, and I establish the PPMAP algorithm as a powerful tool for analysing far infrared and sub-millimetre observations of dusty star forming regions.

I also outline areas of potential future work to place PPMAP in the public domain and extend the scope of this research programme.

7.1 Testing PPMAP

In Chapter 4 I carry out a series of tests with real and synthetic data to verify that PPMAP is able to accurately produce four dimensional models of the column density of dusty objects as a function of line of sight dust temperature and dust opacity index. I derive synthetic specific intensity maps at 160 µm, 250 µm, 350 µm and 500 µm from the PPMAP column density data hypercube produced from *Herschel* observations of the Taurus L1495/B213 star forming complex. These synthetic maps are convolved with the beam profiles of the corresponding *Herschel* observing bands to produce simulated *Herschel*-like observations.

I visually compare the simulated observations with the true observations used to derive the PPMAP model, and with similarly produced synthetic observations derived from a MBB fitting routine applied to the same set of observations. In addition, I derive a "goodness of fit" parameter to quantify how well the synthetic observations match the true observations. I find that while the synthetic observations from both PPMAP and the MBB fitting routine closely match the *Herschel* observations at 350 µm and 500 µm, PPMAP is much more accurate in estimating the contribution

from the 160 µm and 250 µm bands, with the MBB fitting technique tending to overestimate the contribution from the background at shorter wavelengths.

In Chapter 6, I perform a similar flux recovery test on dust models of regions in the Ophiuchus molecular cloud. This produces similar results, although in this case the MBB fitting routine underestimates the contribution from the background at short wavelengths. I also note that the edges of the PPMAP maps can be subject to high uncertainty due to both boundary effects during the fitting procedure, and increased measurement noise at the edges of scan regions in the input observations. This can negatively impact the accuracy of estimation of the contribution from the observing bands. This effect is particularly apparent for the 160 µm band in the L1689 sub-region.

To verify that the algorithm is able to accurately recover the mass of an astrophysical object, I produce a PPMAP column density hypercube from synthetic observations of a model filament. The filament is axially symmetric, and has a Plummer-like radial density profile. The filament has a uniform opacity index of 2, and a temperature profile given by an inverse Plummer-like function. The filament is placed in a diffuse background with uniform column density, dust temperature and opacity index. I find that PPMAP produces an estimate of the total mass of the synthetic filament which is 7% larger than the true mass. In contrast, a MBB fitting technique applied to the same set of synthetic observations underestimates the mass, recovering only 70% of the total column density through the spine of the filament.

In order to ensure that PPMAP can accurately probe dust temperature and dust opacity index simultaneously, I produce a series of PPMAP hypercubes from synthetic observations of four model filaments. All the model filaments have a Plummer-like radial density profile identical to the model filament described above. The filaments are constructed such that there is a pair of "cold" (10 K to 20 K) filaments with correlated and anti-correlated dust temperature and dust opacity index profiles, and a pair of "hot" (20 K to 30 K) filaments with correlated and anti-correlated dust temperature and dust opacity index profiles. The synthetic observations of these filaments are produced at 70 µm, 160 µm, 250 µm, 350 µm, 500 µm and 850 µm, and are convolved with the appropriate *Herschel* and SCUBA-2 beam profiles. The results indicate that PPMAP is able to lift the dust temperature and dust opacity index degeneracy provided it has observations which probe sufficiently far into the Rayleigh-Jeans tail of a modified black body function. This can be achieved with only the *Herschel* bands for dust temperatures in the range of 20 K to 30 K, or for structures with dust temperatures between 10 K and 20 K with a combination of both *Herschel* observing bands and SCUBA-2 850 µm observations.

7.2 Dust Temperature and Dust Opacity Index Variations

In Chapter 5 and Chapter 6, I present the results of applying the PPMAP algorithm to *Herschel* and SCUBA-2 observations of the Taurus L1495/B213 and the Ophiuchus L1688 and L1689 star forming complexes.

In both the Taurus L1495/B213 complex and the Ophiuchus sub-regions, the dust in the more diffuse background clouds mainly occupies the dust opacity index bands where $\beta \geq 1.5$. While the more dense clumps and filamentary structures also contain large reservoirs of dust at these higher opacity indexes, their central regions contain significant quantities of dust which occupies the $\beta = 1.0$ PPMAP band. The presence of dust with a lower opacity index in the better shielded regions of the dense structures may be an indicator of grain growth or other physical or chemical changes to the dust structure.

In the L1495/B213 complex and the L1689 sub-region, the lower density background clouds contain very little cold dust. The dust that is present is found to predominantly occupy the warm (>12 K) PPMAP dust temperature bands. The dust occupying the low temperature bands ($\leq$12 K) is almost exclusively found in the centres of dense clumps and filaments. These structures also contains large reservoirs of dust in the warm bands. This dust is likely to be in outer envelopes or sheaths, or is found near sources of local heating.

The variations in dust temperature in the L1688 sub-region present a more confused picture. The influence of the nearby Upper Scorpious OB association, and pre-main sequence stars S1 and HD147889, produce strong heating effects. This leads to a sharp temperature gradient across the region. Therefore, the diffuse background material and the dense structures in the West of the sub-region are significantly warmer than those in the East. Despite this, inspection of the column density in the PPMAP dust temperature bands reveals that the centres of dense structures harbour colder dust than their local surroundings.

Dense structures in the PPMAP dust models of Taurus and Ophiuchus are found to have lower column densities and higher mean line of sight temperatures compared with estimates produced by single-temperature MBB fitting techniques. This effect is due to single-temperature MBB fitting techniques confusing the contribution to the total emission from less dense, warmer material with the contribution from more dense, colder material along the line of sight. This is a consequence of requiring all emission along the line of sight to come from material with a single temperature. PPMAP overcomes this problem by distributing the dust into different

line of sight temperature bins. PPMAP is therefore able to disentangle the contribution from different dust populations, and reveal the presence of warm dust in dense structures.

7.3 Filament properties

In the PPMAP dust models of Taurus and the Ophiuchus, I identify several filamentary structures. I present the analysis of the properties Taurus B211/B213 filament in Chapter 5, and compare the results to those presented by Palmeirim et al. (2013). In Chapter 6, I identify several filamentary structures in both the L1688 and L1689 sub-regions of Ophiuchus, and present the first systematic investigation of their properties.

7.3.1 Length Averaged Properties of the B211/B213 Filament

To investigate the properties of the Taurus L1495/B213 complex, I produce a length averaged median profile of the B211/B213 filament. I achieve this by taking a series of profiles of the column density perpendicular to the spine of the filament at 0.004 pc intervals along its length, out to a distance of 1 pc either side of the spine. I then take the median value of the column density at evenly spaced values of the impact parameter from the spine. To this median profile, I fit a Plummer-like function. I do not perform a background subtraction, and do not require that the function be symmetric, though the function is continuous across the filament spine. This allows for simultaneous fitting of the central column density, N_0, and independent values of the inner width, r_0, Plummer-like exponent, p, and background N_B, for the North and South side of the filament.

The average of the North and South Plummer-like exponents is $\bar{p} = 1.88 \pm 0.05$, which is consistent with the results published by Palmeirim et al. (2013). I recover a value of $N_0 = (6.38 \pm 0.09) \times 10^{21}\,\mathrm{H_2\,cm^{-2}}$, and an average value of $\bar{r}_0 = 0.022 \pm 0.002$ pc, which are both significantly lower than the values reported by Palmeirim et al. (2013).

An estimate of the inner width of the filament is produced by utilising $\bar{r_0}$ and $\bar{p}$ to calculate the FWHM of the fitted Plummer-like function. I estimate the width of the B211/B213 filament to be 0.087 pc. This is approximately half the width reported by Palmeirim et al. (2013), and at the extreme lower end of the distribution of filament widths presented by Arzoumanian et al. (2019) when adjusted for differences in the fitting techniques.

7.3.2 Comparison of Filament Properties between Taurus and Ophiuchus

I analyse variations in filament properties along the length of identified filaments in both Taurus and Ophiuchus with the FilChaP algorithm. FilChaP splits the filament into a series of perpendicular bundled profiles, performs a background subtraction, and fits a symmetric Plummer-like $p = 2$ function to each bundle with N_0 and r_0 as free parameters.

The filament width and central column density is found to vary significantly along the length of each filament in both Taurus and Ophiuchus. The median filament width in L1495 is (0.08 ± 0.02) pc. The average uncertainty of a single estimate of the width at a point along the spine is just 0.005 pc, half an order of magnitude smaller than the variation in the distribution of all width estimates along the filament spine. As with the length averaged fit, the median of the distribution of widths estimated at points along the filament spine is much less than the width reported by Palmeirim et al. (2013). In L1688 I recover a median filament width of (0.11 ± 0.04) pc, while in L1689, the median filament width is (0.19 ± 0.08) pc. While this is nearly two times larger than the median width of the filaments in L1688, and more than twice the median width of the B211/B213 filament, the 0.19 pc median width in L1689 includes the contributions from filament f2b and a section of filament f3 (see Figure 6.15 in Chapter 6). These structures are less dense and significantly wider than the other filaments within the region. If they are excluded from the analysis, the median width of the remaining filaments in L1689 is (0.14 ± 0.05) pc.

The median of the mixed distribution of the filament bundle widths from all the regions is (0.10 ± 0.04) pc. As discussed in Chapter 5, this is the median width of the FWHM of the Plummer-like profiles fitted to the filament bundles. By converting to the FWHM of an equivalent Gaussian profile fitted to the inner regions ($b \leq r_0$) of the bundles, I obtain a median Gaussian width of (0.071 ± 0.026) pc. This is somewhat lower than the median filament width of 0.09 pc reported by Arzoumanian et al. (2019).

I use the N_0 and r_0 values of the fitted bundles to calculate the local line density at points along each of the filaments. In the L1495/B213 complex, I estimate a median line density of $(17.8 \pm 4.4)\,\mathrm{M_\odot\,pc^{-1}}$. This is close to the critical line density of $16.2\,\mathrm{M_\odot\,pc^{-1}}$, assuming a gas temperature of 10 K. This result is inconsistent with the B211/B213 filament being globally super-critical as concluded by Palmeirim et al. (2013). I do, however, find that the positions of starless cores (taken from Marsh et al. 2016), correlate with locally super-critical bundles along the filament.

In contrast, I find the median filament line densities in L1688 and L1689 to be $(43 \pm 14)\,M_\odot\,pc^{-1}$ and $(43 \pm 12)\,M_\odot\,pc^{-1}$ respectively. These values are much higher than the median line density I observe in the L1495/B213 complex. While this indicates that the filaments are super-critical as they have line densities that greatly exceed $16.2\,M_\odot\,pc^{-1}$, I note that the the gas temperature here may be higher than 10 K due to the local feedback. If the gas is as 25 K, the critical line density is $43\,M_\odot\,pc^{-1}$.

I also use FilChaP to fit the bundles of the B211/B213 filament with $p = 4$ Plummer-like functions. I find that the $p = 4$ Plummer-like functions produce a better fit to the data than the $p = 2$ Plummer-like profiles. This indicates that the B211/B213 filament might be closer to the hydrostatic equalibrium solution for an isothermal filament derived by Ostriker (1964), and that the shallower $p = 2$ profile may be a consequence of averaging over resolved substructure along the length of the filament.

7.4 Measurements of Mass Distribution in Ophiuchus

To compare the L1688 and L1689 sub-regions, I analyse the mass distribution of different structures contained within them. I find that while the area covered by the dust models is approximately the same ($5.74\,pc^2$ for L1688 and $5.96\,pc^2$ for L1689), the L1688 model contains ~ 1.5 times more mass than the L1689 model ($(650.7 \pm 0.4)\,M_\odot$ and $(395.4 \pm 0.3)\,M_\odot$, respectively). I estimate the percentage of dense material in the sub-fields by defining a contour at $7 \times 10^{21}\,H_2\,cm^{-2}$. This is equivalent to a visual extinction of $A_V = 7$, which has been shown to mark the transition between low core formation efficiency and high core formation efficiency (e.g. André et al. 2010). The dense material accounts for 21% of the area of the L1688 model, while the dense material in L1689 covers only 6% of the model area.

I utilise the catalogue produced by Pattle et al. (2015) to locate starless cores within the two sub-regions. I determine the masses of the cores by performing aperture photometry on maps of H_2 column density derived using PPMAP. I find that the 36 cores located within L1688 have a total mass of $(20.93 \pm 0.04)\,M_\odot$, while the 10 cores in L1689 have a total mass of $(4.28 \pm 0.01)\,M_\odot$. The cores account for 3.2% of the total mass and 7.3% of the dense ($A_V \geq 7$) mass of L1688, and 1.1% of the total mass and 4.8% of the dense mass of L1689. The percentage of sub-region mass

contained within cores is three times larger in L1688 than L1689. However, the percentage of the dense mass contained within cores in L1688 is only 1.5 times larger. This finding is consistent with similar analyses conducted by Ladjelate et al. (2020) and Nutter, Ward-Thompson, and André (2006).

As an independent verification of these findings, I utilise dendograms to identify a series of dense, compact objects in the L1688 and L1689 dust models. Each of the objects had an upper size threshold of $0.0079\,\mathrm{pc}^2$. This threshold equates to the cross-sectional area of a spherical core with a diameter of 0.1 pc. I identify 75 dense objects in L1688 with a total mass of $(54.1 \pm 0.8)\,\mathrm{M}_\odot$, which accounts for 8.3% of the total mass of the model, and 19.0% of the dense material. In L1689, I identify 20 dense objects with a total mass of $(18.9 \pm 0.3)\,\mathrm{M}_\odot$. Therefore the dense objects in L1689 make up 4.8% of the total model mass, and 21.3% of the total mass. As with the Pattle et al. (2015) core catalogue, the proportion of total model mass contained within the dense objects is larger (by nearly a factor of two) for L1688 than for L1689, while the fraction of dense material associated with the objects is much lower (and nearly equal across the two sub-regions). This suggests that global cloud mass does not directly affect core formation efficiency, but instead drives the formation of dense regions. These regions, once they achieve a density $\geq 7 \times 10^{21}\,\mathrm{H_2\,cm^{-2}}$, form starless cores with similar core formation efficiencies.

I also determine the mass contained within the inner portion of each of the filaments identified in the two sub-regions. I limit my mass estimates to the inner portions of the filaments as it facilitates a comparison between the filaments and the dense ($A_V \geq 7$) material. I find the filaments in L1688 have a total inner mass of $(81.1 \pm 0.5)\,\mathrm{M}_\odot$, which accounts for 12.4% of the total model mass. All of the filaments in L1688 lie fully within the $A_V = 7$ contour. Therefore, they account for 28.4% of the mass of the dense material. The total inner mass of the L1689 filaments is $(49.8 \pm 0.3)\,\mathrm{M}_\odot$. The inner portions of the filaments therefore make up 12.6% of the total mass of the sub-region. Unlike L1688, the filaments in L1689 do not all lie within the dense material. Therefore, I exclude the f2b filament and a portion of the f3 filament before comparing the filament inner mass with the mass of the dense material. The remaining filaments make up 35.8% of the dense material.

7.5 Impacts of Feedback on L1688 Filament f1

I investigate the effect of the S1 and HD147889 pre-main sequence stars on the f1 filament in L1688. I plot the H_2 column density, dust temperature, and dust opacity index of the spine points along f1 as a function of their distance from the

axis which connects the two pre-main sequence stars. The column density and dust temperature both peak near to the axis itself, and fall off rapidly with distance from the axis. Therefore, I deduce that S1 and HD147889 are responsible for significant squeezing and heating of the filament. This region between the PDRs blown by the stars harbours a large number of starless cores. This might indicate that the impact of the stars has led to an increase in core formation rate. The f1 filament shows two local maxima in the column density and dust temperature at 0.5 pc and 0.8 pc from the S1-HD147889 axis. Both local maxima coincide with the positions of groups of starless cores. In each case, the peak temperature is offset from the peak column density. This suggests that the outer edges of the denser regions are being heated, but the inner portions of these regions are colder due to shielding. I am unable to find a correlation between dust opacity index and distance from the S1-HD147889 axis.

7.6 Future Work

This thesis showcases the ability of PPMAP to produce column density maps of star forming regions without degrading the resolution of the finest resolution observations, and highlights variations in the dust opacity index and dust temperature both in the plane of the sky and along the line of sight. I use PPMAP to produce detailed studies of the filamentary structures in two different environments within the Gould Belt star forming clouds, and to probe their temperature and density structure and dust properties with significantly more discrimination than previously adopted analyses. At this stage, several areas of further study present themselves.

7.6.1 Developing PPMAP for the Astronomy Community

This thesis constitutes a successful pilot study and validation of the PPMAP-based analysis methodology. If applied systematically to nearby star forming clouds, it has the potential to bring about a major advance in the diagnostic capabilities of multi-band dust continuum observation, and in our understanding of how filamentary structure mediates star formation. In addition, PPMAP has been successfully applied to both extragalactic environments (Marsh et al. 2018; Whitworth et al. 2019) and supernova remnants (Chawner et al. 2019).

However, while PPMAP is a powerful tool, installation, set-up and use of the algorithm is difficult. This limits usability to a small subset of people who are

already experienced with its operation. Furthermore, there is no documentation for the algorithm, nor any publicly available tests or examples.

I would develop PPMAP into a user-friendly, well documented tool, and place it in the public domain. As part of this process, I would refine the tests presented in Chapter 4 into a series of working examples which demonstrate the functionality, robustness, and limitations of the algorithm. I would also develop a new test, comprising a series of uniform discs of gas and dust, with differing column densities and dust temperatures (and potentially opacity indices). The discs would be tuned to probe the 70 µm optically thick boundary. By producing synthetic observations of an array of these discs (each separated from its neighbour by a small distance), I could produce PPMAP models of temperature and column density. Thus I could construct a correction table based on these two parameters, allowing optical depth issues to be corrected by post-processing procedures.

While PPMAP already includes beam profiles and colour correction factors for the *Herschel* and SCUBA-2 observing bands, I would create a number of complementary scripts to allow users to create observation beam profiles and colour correction factors for other instruments. I would also continue to develop the functionality of the preMAP and PPMAP algorithms. These developments would expand the capabilities of PPMAP, allowing for use of colour corrections dependent on both dust temperature and dust opacity index, and enabling the user to select both logarithmic and linear discrete dust temperature scales. An extensive installation and user manual would allow PPMAP to be compiled and run on a wide array of supercomputing clusters, and aid in the production and interpretation of the results. This would pave the way for PPMAP to become a standard alternative to the traditional MBB-based analysis methodologies.

7.6.2 Continued Analysis of L1495 and Oph

The analysis in this thesis focused primarily on the B211/B213 filament in Taurus, and the L1688 and L1689 sub-fields of Ophiuchus. An obvious first step in extending this work would be to study the complex head region of L1495 and the network of diffuse structures and cores which extend beyond the head to the West of the region. In addition, the investigation of Ophiuchus should be extended to cover the L1709 structure, which lies North of L1689, and North East of L1688, and appears to be composed of a single, isolated filament similar to B211/B213, which is more quiescent than either L1688 or L1689 (see Figure 7.1).

In addition, I would revisit the core formation efficiency investigation, utilising

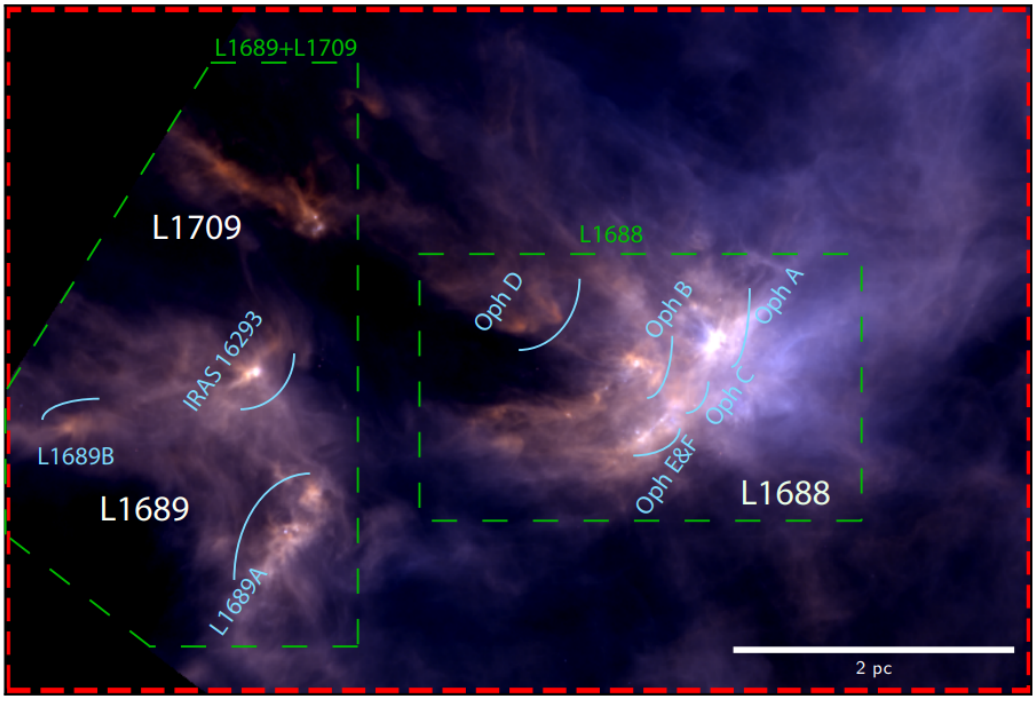

Figure 7.1. A three colour image of the Ophiuchus star forming cloud showing the position of the L1709 structure in relation to the L1688 and L1689 sub-fields. Image credit Ladjelate et al. (2020).

the Ladjelate et al. (2020) core catalogue, allowing for a more direct comparison with their results.

Polarimitary studies show that magnetic fields play an important role in the evolution of filament structure. In the L1495/B213 complex, for example, the background magnetic field lies perpendicular to the primary B211/B213 filament, and parallel to diffuse striations which appear to be feeding mateiral onto the main filamentary structure (Palmeirim et al. 2013). This change in the orientation of structures relative to the magnetic field appears to coincide with the transition in dust opacity index from higher values in low-density structures to lower values in high-density structures. I would use the high resolution PPMAP dust models to analyse the relative orientation of structure in Taurus and Ophiuchus with respect to the background magnetic field, and attempt to link the magnetic field to variations in the line of sight dust opacity index and dust temperature. This would likely require new polarimitary data to be taken with, for instance, the Pol-2 instrument on the JCMT. This investigation would also involve producing a new model of the L1495/B213 complex at the higher 14″ resolution used to create the Ophiuchus dust models. Quantifying the filament orientation in Ophiuchus would also enable further analysis of the impacts of the Upper Scopius OB association on the evolution of L1688 and L1689.

It is also important to conduct a more in-depth core analysis of the regions, to

better determine how the large scale structures are linked to prestellar and protostellar cores. Such an analysis would examine the core spacing and try to determine the characteristic length scale of fragmentation along the filaments with the FragMent algorithm (Clarke et al. 2019). However, this and other core studies will have to involve either a modification of PPMAP to attempt to resolve the artefacts caused by optically thick cores with bright central 70 µm sources, or else a better pipeline for masking those sources which does not cause such severe data loss from the filament structure.

7.6.3 Extension to Other Gould Belt Fields

The L1495/B213 complex and Ophiuchus cover only a small subset of the environments within the Gould Belt. In future studies, I would apply PPMAP to the remaining Gould Belt star forming regions. This would allow for high resolution comparisons of filament and cloud dust properties spanning a large range of cloud properties. The active formation of massive stars in Orion A, for example, will provide a particularly important contrast in terms of environment with the low mass star forming L1495/B213 complex.

These investigations would aim to utilise ArTéMiS 350 µm and 450 µm observations from the 12 m diameter APEX telescope to improve the resolution of the *Herschel* SPIRE observations by up to a factor of three. As ArTéMiS is ground based, feathering the observations with similar *Herschel* bands will be required to recover the extended emission. This is easily achieved for the 350 µm band, which is common to both ArTéMiS and SPIRE. The 450 µm band does not have a direct *Herschel* counterpart. However, 450 µm SCUBA-2 observations have been successfully feathered with SPIRE 500 µm observations by Matt Smith (in prep.), indicating that a similar process could be used here.

With the increase in resolution that this would facilitate, any resolved filament sub-structure revealed by PPMAP could be compared with the studies of velocity coherent fibres (see e.g. Hacar et al. 2013; Henshaw et al. 2017; Hacar, Tafalla, and Alves 2017; Hacar et al. 2018) to identify if a correlation exists between the structures.

7.6.4 Probing Dust Opacity Index Variations with NIKA 2, MUSCAT, and TolTEC

Chapter 4 has shown that while PPMAP is able to lift the degeneracy between estimates of dust temperature and dust opacity if it is supplied with sufficiently long

wavelength observations. The results presented in this thesis have shown that high column density regions can harbour reservoirs of dust with low opacity indices. To better explore this result, future studies of star forming regions should include not just SCUBA-2 850 µm data, but also 1.1 mm observations from the NIKA2 (Adam et al. 2018) instrument on the 30 m diameter IRAM telescope, or from the MUSCAT (Castillo-Dominguez et al. 2018) and TolTEC (Bryan 2018) instruments due to begin operation shortly on the 50 m diameter Large Millimetre Array. Delivery and installation of TolTEC is expected to be operational by the latter part of 2020. MUSCAT delivery has been postponed due to the outbreak of the SARS-CoV-2 virus and subsequent global COVID 19 pandemic (WHO 2020). As with SCUBA-2 and ArTéMiS, 1.1 mm observations would be feathered with a corresponding observing band from a space-borne telescope; in this case, the 1 mm band on *Planck*.

TolTEC will be particularly useful, as it is sensitive to the polarisation angle of the incoming light, allowing it to complement studies of the magnetic fields performed with the JCMT Pol-2 instrument.

Appendix A
PPMAP colour correction tables

This appendix presents the colour correction factors for the *Herschel* instruments and the SCUBA-2 850 µm as a function of dust temperature. The tables are generated via the method described in Chapter 2, section 2.2. The colour correction factors are utilised by PPMAP in the estimation of accurate column density distributions as described in Chapter 3, Section 3.1.3.

Table A.1. The `Herschel.txt` table of colour correction factors utilised by PPMAP to produce column density models.

Temp	Colour Correction Factors				
(K)	70 µm	160 µm	250 µm	350 µm	500 µm
5	0.00545	0.33405	0.88318	0.98683	1.04955
6	0.03217	0.53344	0.95294	1.01432	1.06084
7	0.09056	0.70145	0.99104	1.02526	1.06074
8	0.17397	0.82788	1.01143	1.02835	1.05637
9	0.27008	0.91693	1.02173	1.02767	1.05064
10	0.36847	0.97685	1.02622	1.02520	1.04474
11	0.46235	1.01555	1.02733	1.02198	1.03915
12	0.54804	1.03933	1.02646	1.01851	1.03403
13	0.62400	1.05277	1.02447	1.01506	1.02943
14	0.69004	1.05915	1.02188	1.01176	1.02531
15	0.74673	1.06076	1.01899	1.00866	1.02164
16	0.79495	1.05916	1.01599	1.00580	1.01836
17	0.83573	1.05545	1.01300	1.00315	1.01542
18	0.87006	1.05040	1.01009	1.00073	1.01277
19	0.89889	1.04451	1.00729	0.99850	1.01039

Continued on next page

Table A.1 – *Continued from previous page*

Temp	Colour Correction Factors				
(K)	70 µm	160 µm	250 µm	350 µm	500 µm
20	0.92304	1.03817	1.00463	0.99646	1.00824
21	0.94323	1.03160	1.00212	0.99458	1.00629
22	0.96009	1.02499	0.99975	0.99286	1.00451
23	0.97413	1.01846	0.99753	0.99127	1.00289
24	0.98580	1.01207	0.99544	0.98980	1.00140
25	0.99546	1.00587	0.99348	0.98845	1.00003
26	1.00345	0.99991	0.99165	0.98719	0.99877
27	1.01000	0.99418	0.98992	0.98603	0.99760
28	1.01535	0.98871	0.98831	0.98494	0.99652
29	1.01968	0.98349	0.98679	0.98393	0.99551
30	1.02315	0.97851	0.98536	0.98299	0.99458
31	1.02588	0.97378	0.98402	0.98210	0.99370
32	1.02799	0.96927	0.98275	0.98128	0.99289
33	1.02957	0.96499	0.98156	0.98050	0.99212
34	1.03070	0.96092	0.98043	0.97977	0.99140
35	1.03145	0.95705	0.97937	0.97908	0.99073
36	1.03188	0.95336	0.97836	0.97843	0.99009
37	1.03203	0.94986	0.97740	0.97782	0.98949
38	1.03195	0.94652	0.97650	0.97724	0.98892
39	1.03167	0.94335	0.97564	0.97669	0.98838
40	1.03122	0.94032	0.97482	0.97617	0.98787
41	1.03064	0.93744	0.97405	0.97568	0.98739
42	1.02994	0.93468	0.97331	0.97521	0.98693
43	1.02913	0.93205	0.97260	0.97476	0.98649
44	1.02825	0.92954	0.97193	0.97433	0.98607
45	1.02730	0.92714	0.97129	0.97393	0.98567
46	1.02629	0.92485	0.97068	0.97354	0.98529
47	1.02525	0.92265	0.97009	0.97317	0.98493
48	1.02416	0.92055	0.96953	0.97281	0.98458
49	1.02305	0.91853	0.96899	0.97248	0.98425
50	1.02192	0.91659	0.96848	0.97215	0.98393
51	1.02078	0.91474	0.96798	0.97184	0.98363
52	1.01962	0.91296	0.96751	0.97154	0.98333

Continued on next page

Table A.1 – *Continued from previous page*

Temp	Colour Correction Factors				
(K)	70 µm	160 µm	250 µm	350 µm	500 µm
53	1.01846	0.91124	0.96705	0.97125	0.98305
54	1.01730	0.90960	0.96661	0.97097	0.98278
55	1.01615	0.90801	0.96619	0.97071	0.98252
56	1.01499	0.90649	0.96578	0.97045	0.98227
57	1.01385	0.90502	0.96539	0.97021	0.98203
58	1.01271	0.90360	0.96501	0.96997	0.98180
59	1.01158	0.90224	0.96465	0.96974	0.98157
60	1.01047	0.90092	0.96430	0.96952	0.98135
61	1.00937	0.89965	0.96396	0.96930	0.98115
62	1.00829	0.89842	0.96363	0.96910	0.98094
63	1.00721	0.89724	0.96331	0.96890	0.98075
64	1.00616	0.89609	0.96301	0.96870	0.98056
65	1.00512	0.89498	0.96271	0.96852	0.98037
66	1.00410	0.89391	0.96242	0.96834	0.98020
67	1.00309	0.89287	0.96214	0.96816	0.98002
68	1.00210	0.89187	0.96187	0.96799	0.97986
69	1.00113	0.89089	0.96161	0.96783	0.97970
70	1.00018	0.88995	0.96136	0.96767	0.97954
71	0.99924	0.88903	0.96111	0.96751	0.97939
72	0.99832	0.88815	0.96087	0.96736	0.97924
73	0.99741	0.88728	0.96064	0.96721	0.97909
74	0.99653	0.88645	0.96041	0.96707	0.97895
75	0.99566	0.88563	0.96019	0.96693	0.97882
76	0.99480	0.88484	0.95998	0.96680	0.97869
77	0.99396	0.88408	0.95977	0.96667	0.97856
78	0.99314	0.88333	0.95957	0.96654	0.97843
79	0.99234	0.88260	0.95937	0.96642	0.97831
80	0.99155	0.88190	0.95918	0.96630	0.97819
81	0.99077	0.88121	0.95900	0.96618	0.97808
82	0.99001	0.88054	0.95881	0.96606	0.97796
83	0.98926	0.87989	0.95864	0.96595	0.97785
84	0.98853	0.87925	0.95846	0.96584	0.97775
85	0.98781	0.87863	0.95830	0.96574	0.97764

Continued on next page

Table A.1 – *Continued from previous page*

Temp	Colour Correction Factors				
(K)	70 µm	160 µm	250 µm	350 µm	500 µm
86	0.98711	0.87803	0.95813	0.96563	0.97754
87	0.98642	0.87744	0.95797	0.96553	0.97744
88	0.98574	0.87687	0.95781	0.96543	0.97734
89	0.98508	0.87631	0.95766	0.96534	0.97725
90	0.98443	0.87576	0.95751	0.96524	0.97715
91	0.98379	0.87523	0.95737	0.96515	0.97706
92	0.98316	0.87470	0.95722	0.96506	0.97697
93	0.98255	0.87420	0.95708	0.96497	0.97689
94	0.98194	0.87370	0.95695	0.96489	0.97680
95	0.98135	0.87321	0.95681	0.96480	0.97672
96	0.98077	0.87274	0.95668	0.96472	0.97664
97	0.98020	0.87227	0.95656	0.96464	0.97656
98	0.97964	0.87182	0.95643	0.96456	0.97648
99	0.97909	0.87137	0.95631	0.96448	0.97640
100	0.97855	0.87094	0.95619	0.96441	0.97633
101	0.97802	0.87051	0.95607	0.96433	0.97626
102	0.97750	0.87010	0.95596	0.96426	0.97619
103	0.97699	0.86969	0.95585	0.96419	0.97612
104	0.97649	0.86929	0.95574	0.96412	0.97605
105	0.97600	0.86890	0.95563	0.96405	0.97598
106	0.97552	0.86852	0.95552	0.96398	0.97591
107	0.97504	0.86814	0.95542	0.96392	0.97585
108	0.97457	0.86778	0.95532	0.96385	0.97578
109	0.97412	0.86742	0.95522	0.96379	0.97572
110	0.97367	0.86706	0.95512	0.96373	0.97566
111	0.97322	0.86672	0.95502	0.96367	0.97560
112	0.97279	0.86638	0.95493	0.96361	0.97554
113	0.97236	0.86604	0.95484	0.96355	0.97548
114	0.97194	0.86572	0.95475	0.96349	0.97543
115	0.97153	0.86539	0.95466	0.96344	0.97537
116	0.97112	0.86508	0.95457	0.96338	0.97531
117	0.97072	0.86477	0.95448	0.96333	0.97526
118	0.97033	0.86447	0.95440	0.96327	0.97521

Continued on next page

Table A.1 – *Continued from previous page*

Temp	Colour Correction Factors				
(K)	70 µm	160 µm	250 µm	350 µm	500 µm
119	0.96994	0.86417	0.95432	0.96322	0.97516
120	0.96956	0.86388	0.95424	0.96317	0.97510
121	0.96919	0.86359	0.95416	0.96312	0.97505
122	0.96882	0.86331	0.95408	0.96307	0.97500
123	0.96846	0.86303	0.95400	0.96302	0.97496
124	0.96810	0.86276	0.95392	0.96297	0.97491
125	0.96775	0.86249	0.95385	0.96292	0.97486
126	0.96741	0.86223	0.95378	0.96288	0.97481
127	0.96707	0.86197	0.95370	0.96283	0.97477
128	0.96674	0.86171	0.95363	0.96278	0.97472
129	0.96641	0.86146	0.95356	0.96274	0.97468
130	0.96608	0.86122	0.95349	0.96270	0.97464
131	0.96576	0.86097	0.95343	0.96265	0.97459
132	0.96545	0.86074	0.95336	0.96261	0.97455
133	0.96514	0.86050	0.95329	0.96257	0.97451
134	0.96484	0.86027	0.95323	0.96253	0.97447
135	0.96454	0.86005	0.95316	0.96249	0.97443
136	0.96424	0.85982	0.95310	0.96245	0.97439
137	0.96395	0.85960	0.95304	0.96241	0.97435
138	0.96366	0.85939	0.95298	0.96237	0.97431
139	0.96338	0.85917	0.95292	0.96233	0.97427
140	0.96310	0.85896	0.95286	0.96229	0.97424
141	0.96283	0.85876	0.95280	0.96226	0.97420
142	0.96256	0.85855	0.95275	0.96222	0.97416
143	0.96229	0.85835	0.95269	0.96218	0.97413
144	0.96203	0.85816	0.95263	0.96215	0.97409
145	0.96177	0.85796	0.95258	0.96211	0.97406
146	0.96151	0.85777	0.95252	0.96208	0.97402
147	0.96126	0.85758	0.95247	0.96204	0.97399
148	0.96101	0.85739	0.95242	0.96201	0.97396
149	0.96077	0.85721	0.95237	0.96198	0.97392
150	0.96053	0.85703	0.95232	0.96195	0.97389

Table A.2. The `Herc850.txt` table of colour correction factors utilised by PPMAP to produce column density models.

Temp	Colour Correction Factors					
(K)	70 µm	160 µm	250 µm	350 µm	500 µm	850 µm
5	0.00545	0.33405	0.88318	0.98683	1.04955	1.00000
6	0.03217	0.53344	0.95294	1.01432	1.06084	1.00000
7	0.09056	0.70145	0.99104	1.02526	1.06074	1.00000
8	0.17397	0.82788	1.01143	1.02835	1.05637	1.00000
9	0.27008	0.91693	1.02173	1.02767	1.05064	1.00000
10	0.36847	0.97685	1.02622	1.02520	1.04474	1.00000
11	0.46235	1.01555	1.02733	1.02198	1.03915	1.00000
12	0.54804	1.03933	1.02646	1.01851	1.03403	1.00000
13	0.62400	1.05277	1.02447	1.01506	1.02943	1.00000
14	0.69004	1.05915	1.02188	1.01176	1.02531	1.00000
15	0.74673	1.06076	1.01899	1.00866	1.02164	1.00000
16	0.79495	1.05916	1.01599	1.00580	1.01836	1.00000
17	0.83573	1.05545	1.01300	1.00315	1.01542	1.00000
18	0.87006	1.05040	1.01009	1.00073	1.01277	1.00000
19	0.89889	1.04451	1.00729	0.99850	1.01039	1.00000
20	0.92304	1.03817	1.00463	0.99646	1.00824	1.00000
21	0.94323	1.03160	1.00212	0.99458	1.00629	1.00000
22	0.96009	1.02499	0.99975	0.99286	1.00451	1.00000
23	0.97413	1.01846	0.99753	0.99127	1.00289	1.00000
24	0.98580	1.01207	0.99544	0.98980	1.00140	1.00000
25	0.99546	1.00587	0.99348	0.98845	1.00003	1.00000
26	1.00345	0.99991	0.99165	0.98719	0.99877	1.00000
27	1.01000	0.99418	0.98992	0.98603	0.99760	1.00000
28	1.01535	0.98871	0.98831	0.98494	0.99652	1.00000
29	1.01968	0.98349	0.98679	0.98393	0.99551	1.00000
30	1.02315	0.97851	0.98536	0.98299	0.99458	1.00000
31	1.02588	0.97378	0.98402	0.98210	0.99370	1.00000
32	1.02799	0.96927	0.98275	0.98128	0.99289	1.00000
33	1.02957	0.96499	0.98156	0.98050	0.99212	1.00000
34	1.03070	0.96092	0.98043	0.97977	0.99140	1.00000
35	1.03145	0.95705	0.97937	0.97908	0.99073	1.00000

Continued on next page

Table A.2 – *Continued from previous page*

Temp	Colour Correction Factors					
(K)	70 µm	160 µm	250 µm	350 µm	500 µm	850 µm
36	1.03188	0.95336	0.97836	0.97843	0.99009	1.00000
37	1.03203	0.94986	0.97740	0.97782	0.98949	1.00000
38	1.03195	0.94652	0.97650	0.97724	0.98892	1.00000
39	1.03167	0.94335	0.97564	0.97669	0.98838	1.00000
40	1.03122	0.94032	0.97482	0.97617	0.98787	1.00000
41	1.03064	0.93744	0.97405	0.97568	0.98739	1.00000
42	1.02994	0.93468	0.97331	0.97521	0.98693	1.00000
43	1.02913	0.93205	0.97260	0.97476	0.98649	1.00000
44	1.02825	0.92954	0.97193	0.97433	0.98607	1.00000
45	1.02730	0.92714	0.97129	0.97393	0.98567	1.00000
46	1.02629	0.92485	0.97068	0.97354	0.98529	1.00000
47	1.02525	0.92265	0.97009	0.97317	0.98493	1.00000
48	1.02416	0.92055	0.96953	0.97281	0.98458	1.00000
49	1.02305	0.91853	0.96899	0.97248	0.98425	1.00000
50	1.02192	0.91659	0.96848	0.97215	0.98393	1.00000
51	1.02078	0.91474	0.96798	0.97184	0.98363	1.00000
52	1.01962	0.91296	0.96751	0.97154	0.98333	1.00000
53	1.01846	0.91124	0.96705	0.97125	0.98305	1.00000
54	1.01730	0.90960	0.96661	0.97097	0.98278	1.00000
55	1.01615	0.90801	0.96619	0.97071	0.98252	1.00000
56	1.01499	0.90649	0.96578	0.97045	0.98227	1.00000
57	1.01385	0.90502	0.96539	0.97021	0.98203	1.00000
58	1.01271	0.90360	0.96501	0.96997	0.98180	1.00000
59	1.01158	0.90224	0.96465	0.96974	0.98157	1.00000
60	1.01047	0.90092	0.96430	0.96952	0.98135	1.00000
61	1.00937	0.89965	0.96396	0.96930	0.98115	1.00000
62	1.00829	0.89842	0.96363	0.96910	0.98094	1.00000
63	1.00721	0.89724	0.96331	0.96890	0.98075	1.00000
64	1.00616	0.89609	0.96301	0.96870	0.98056	1.00000
65	1.00512	0.89498	0.96271	0.96852	0.98037	1.00000
66	1.00410	0.89391	0.96242	0.96834	0.98020	1.00000
67	1.00309	0.89287	0.96214	0.96816	0.98002	1.00000
68	1.00210	0.89187	0.96187	0.96799	0.97986	1.00000

Continued on next page

Table A.2 – *Continued from previous page*

Temp	Colour Correction Factors					
(K)	70 µm	160 µm	250 µm	350 µm	500 µm	850 µm
69	1.00113	0.89089	0.96161	0.96783	0.97970	1.00000
70	1.00018	0.88995	0.96136	0.96767	0.97954	1.00000
71	0.99924	0.88903	0.96111	0.96751	0.97939	1.00000
72	0.99832	0.88815	0.96087	0.96736	0.97924	1.00000
73	0.99741	0.88728	0.96064	0.96721	0.97909	1.00000
74	0.99653	0.88645	0.96041	0.96707	0.97895	1.00000
75	0.99566	0.88563	0.96019	0.96693	0.97882	1.00000
76	0.99480	0.88484	0.95998	0.96680	0.97869	1.00000
77	0.99396	0.88408	0.95977	0.96667	0.97856	1.00000
78	0.99314	0.88333	0.95957	0.96654	0.97843	1.00000
79	0.99234	0.88260	0.95937	0.96642	0.97831	1.00000
80	0.99155	0.88190	0.95918	0.96630	0.97819	1.00000
81	0.99077	0.88121	0.95900	0.96618	0.97808	1.00000
82	0.99001	0.88054	0.95881	0.96606	0.97796	1.00000
83	0.98926	0.87989	0.95864	0.96595	0.97785	1.00000
84	0.98853	0.87925	0.95846	0.96584	0.97775	1.00000
85	0.98781	0.87863	0.95830	0.96574	0.97764	1.00000
86	0.98711	0.87803	0.95813	0.96563	0.97754	1.00000
87	0.98642	0.87744	0.95797	0.96553	0.97744	1.00000
88	0.98574	0.87687	0.95781	0.96543	0.97734	1.00000
89	0.98508	0.87631	0.95766	0.96534	0.97725	1.00000
90	0.98443	0.87576	0.95751	0.96524	0.97715	1.00000
91	0.98379	0.87523	0.95737	0.96515	0.97706	1.00000
92	0.98316	0.87470	0.95722	0.96506	0.97697	1.00000
93	0.98255	0.87420	0.95708	0.96497	0.97689	1.00000
94	0.98194	0.87370	0.95695	0.96489	0.97680	1.00000
95	0.98135	0.87321	0.95681	0.96480	0.97672	1.00000
96	0.98077	0.87274	0.95668	0.96472	0.97664	1.00000
97	0.98020	0.87227	0.95656	0.96464	0.97656	1.00000
98	0.97964	0.87182	0.95643	0.96456	0.97648	1.00000
99	0.97909	0.87137	0.95631	0.96448	0.97640	1.00000
100	0.97855	0.87094	0.95619	0.96441	0.97633	1.00000
101	0.97802	0.87051	0.95607	0.96433	0.97626	1.00000

Continued on next page

Table A.2 – *Continued from previous page*

Temp	Colour Correction Factors					
(K)	70 µm	160 µm	250 µm	350 µm	500 µm	850 µm
102	0.97750	0.87010	0.95596	0.96426	0.97619	1.00000
103	0.97699	0.86969	0.95585	0.96419	0.97612	1.00000
104	0.97649	0.86929	0.95574	0.96412	0.97605	1.00000
105	0.97600	0.86890	0.95563	0.96405	0.97598	1.00000
106	0.97552	0.86852	0.95552	0.96398	0.97591	1.00000
107	0.97504	0.86814	0.95542	0.96392	0.97585	1.00000
108	0.97457	0.86778	0.95532	0.96385	0.97578	1.00000
109	0.97412	0.86742	0.95522	0.96379	0.97572	1.00000
110	0.97367	0.86706	0.95512	0.96373	0.97566	1.00000
111	0.97322	0.86672	0.95502	0.96367	0.97560	1.00000
112	0.97279	0.86638	0.95493	0.96361	0.97554	1.00000
113	0.97236	0.86604	0.95484	0.96355	0.97548	1.00000
114	0.97194	0.86572	0.95475	0.96349	0.97543	1.00000
115	0.97153	0.86539	0.95466	0.96344	0.97537	1.00000
116	0.97112	0.86508	0.95457	0.96338	0.97531	1.00000
117	0.97072	0.86477	0.95448	0.96333	0.97526	1.00000
118	0.97033	0.86447	0.95440	0.96327	0.97521	1.00000
119	0.96994	0.86417	0.95432	0.96322	0.97516	1.00000
120	0.96956	0.86388	0.95424	0.96317	0.97510	1.00000
121	0.96919	0.86359	0.95416	0.96312	0.97505	1.00000
122	0.96882	0.86331	0.95408	0.96307	0.97500	1.00000
123	0.96846	0.86303	0.95400	0.96302	0.97496	1.00000
124	0.96810	0.86276	0.95392	0.96297	0.97491	1.00000
125	0.96775	0.86249	0.95385	0.96292	0.97486	1.00000
126	0.96741	0.86223	0.95378	0.96288	0.97481	1.00000
127	0.96707	0.86197	0.95370	0.96283	0.97477	1.00000
128	0.96674	0.86171	0.95363	0.96278	0.97472	1.00000
129	0.96641	0.86146	0.95356	0.96274	0.97468	1.00000
130	0.96608	0.86122	0.95349	0.96270	0.97464	1.00000
131	0.96576	0.86097	0.95343	0.96265	0.97459	1.00000
132	0.96545	0.86074	0.95336	0.96261	0.97455	1.00000
133	0.96514	0.86050	0.95329	0.96257	0.97451	1.00000
134	0.96484	0.86027	0.95323	0.96253	0.97447	1.00000

Continued on next page

Table A.2 – *Continued from previous page*

Temp	Colour Correction Factors					
(K)	70 µm	160 µm	250 µm	350 µm	500 µm	850 µm
135	0.96454	0.86005	0.95316	0.96249	0.97443	1.00000
136	0.96424	0.85982	0.95310	0.96245	0.97439	1.00000
137	0.96395	0.85960	0.95304	0.96241	0.97435	1.00000
138	0.96366	0.85939	0.95298	0.96237	0.97431	1.00000
139	0.96338	0.85917	0.95292	0.96233	0.97427	1.00000
140	0.96310	0.85896	0.95286	0.96229	0.97424	1.00000
141	0.96283	0.85876	0.95280	0.96226	0.97420	1.00000
142	0.96256	0.85855	0.95275	0.96222	0.97416	1.00000
143	0.96229	0.85835	0.95269	0.96218	0.97413	1.00000
144	0.96203	0.85816	0.95263	0.96215	0.97409	1.00000
145	0.96177	0.85796	0.95258	0.96211	0.97406	1.00000
146	0.96151	0.85777	0.95252	0.96208	0.97402	1.00000
147	0.96126	0.85758	0.95247	0.96204	0.97399	1.00000
148	0.96101	0.85739	0.95242	0.96201	0.97396	1.00000
149	0.96077	0.85721	0.95237	0.96198	0.97392	1.00000
150	0.96053	0.85703	0.95232	0.96195	0.97389	1.00000

Appendix B
PPMAP uncertainty maps

This appendix presents the uncertainty on the PPMAP models for the Taurus L1495/B213 complex (presented in Chapter 5) and the Ophiuchus L1688 and L1689 sub-regions (presented in Chapter 6). An explanation of how the uncertainty is calculated for a PPMAP model is given in Chapter 3, Section 3.1.3.

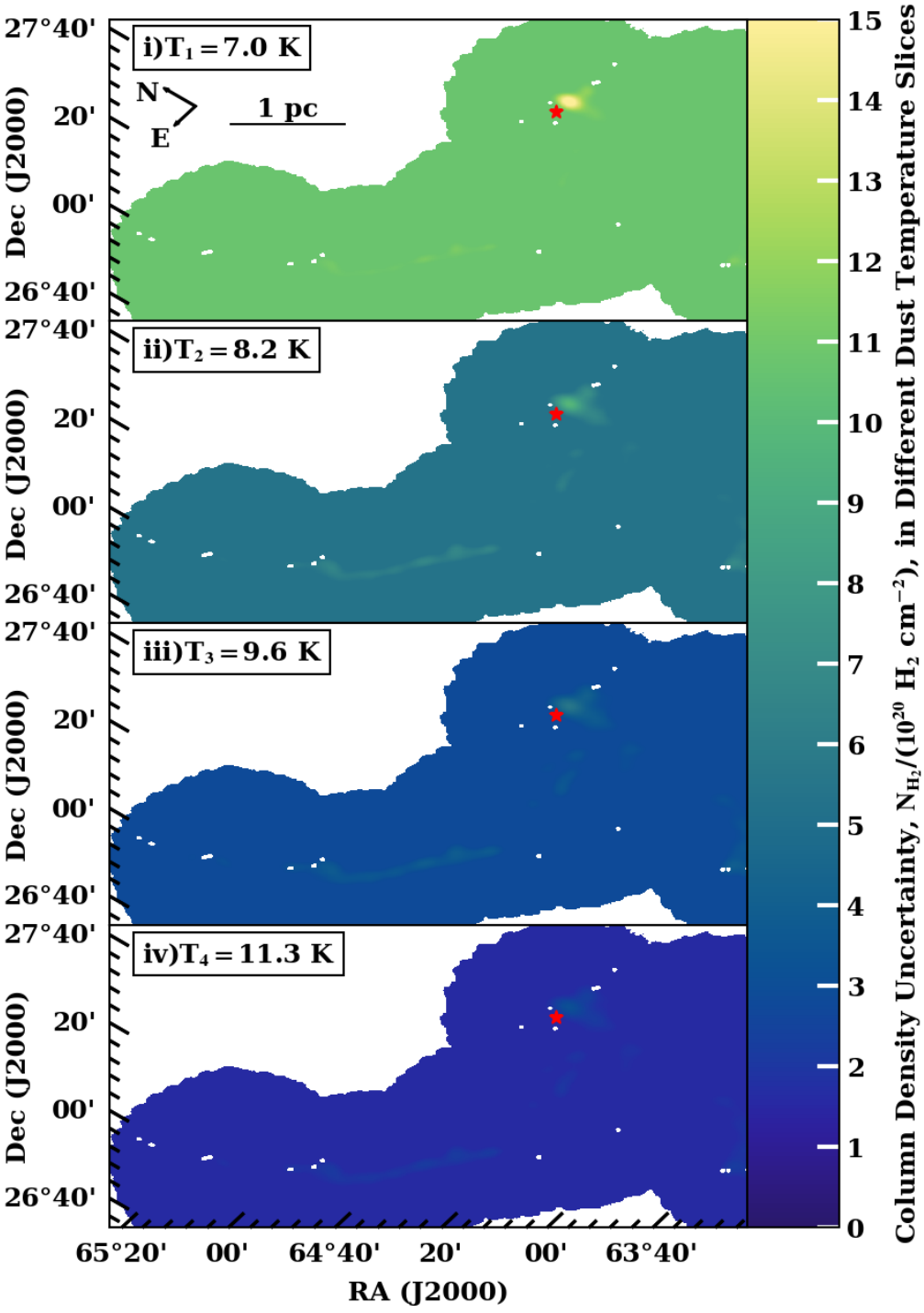

Figure B.1. The uncertainty in the H_2 column density model, in 12, logarithmically spaced line of sight temperature bins for the L1495/B213 complex. These maps are obtained by marginalising out the opacity index dimension of the PPMAP hypercube.

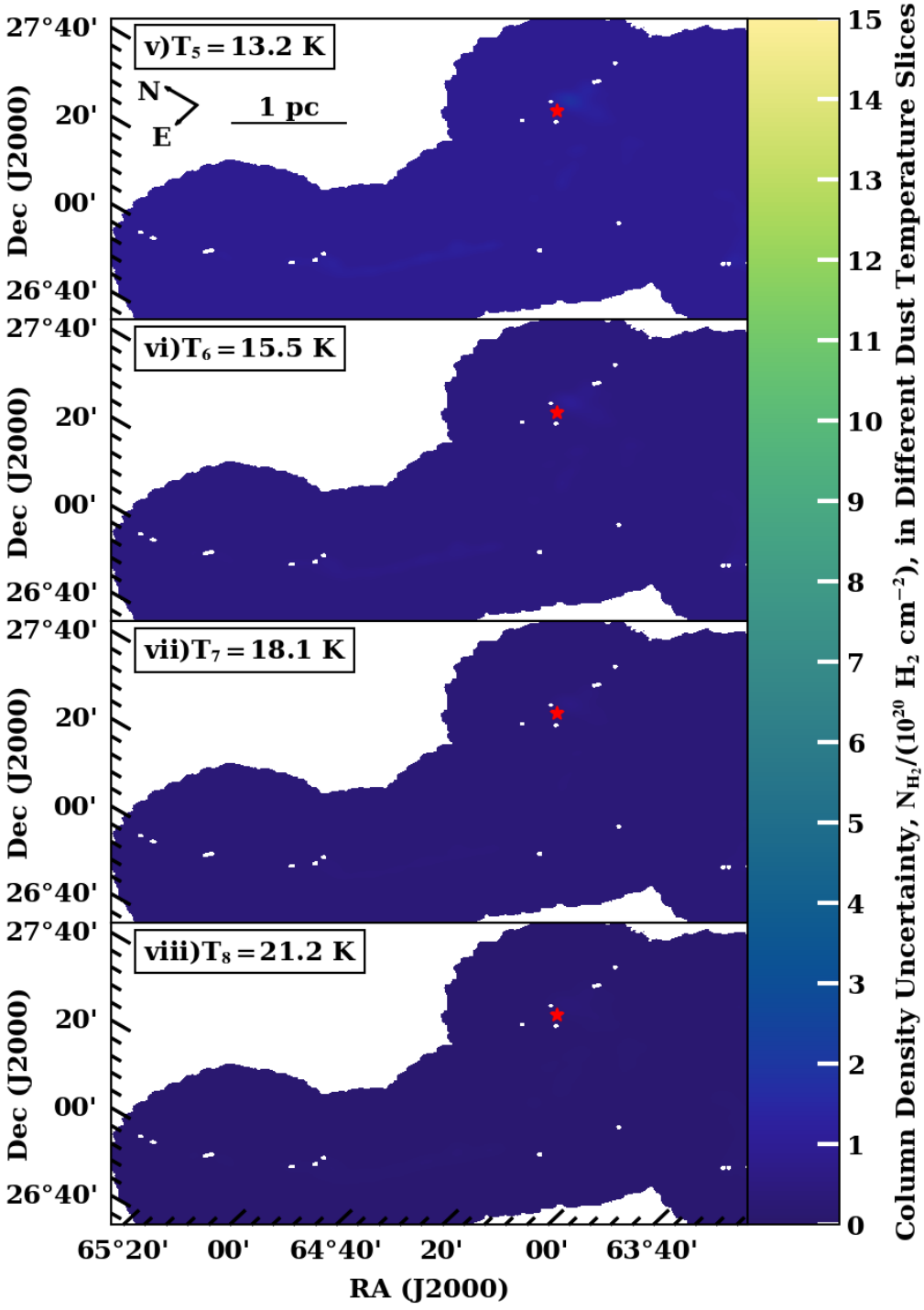

Figure B.1 (cont.). The uncertainty in the H_2 column density model, in 12, logarithmically spaced line of sight temperature bins for the L1495/B213 complex. These maps are obtained by marginalising out the opacity index dimension of the PPMAP hypercube.

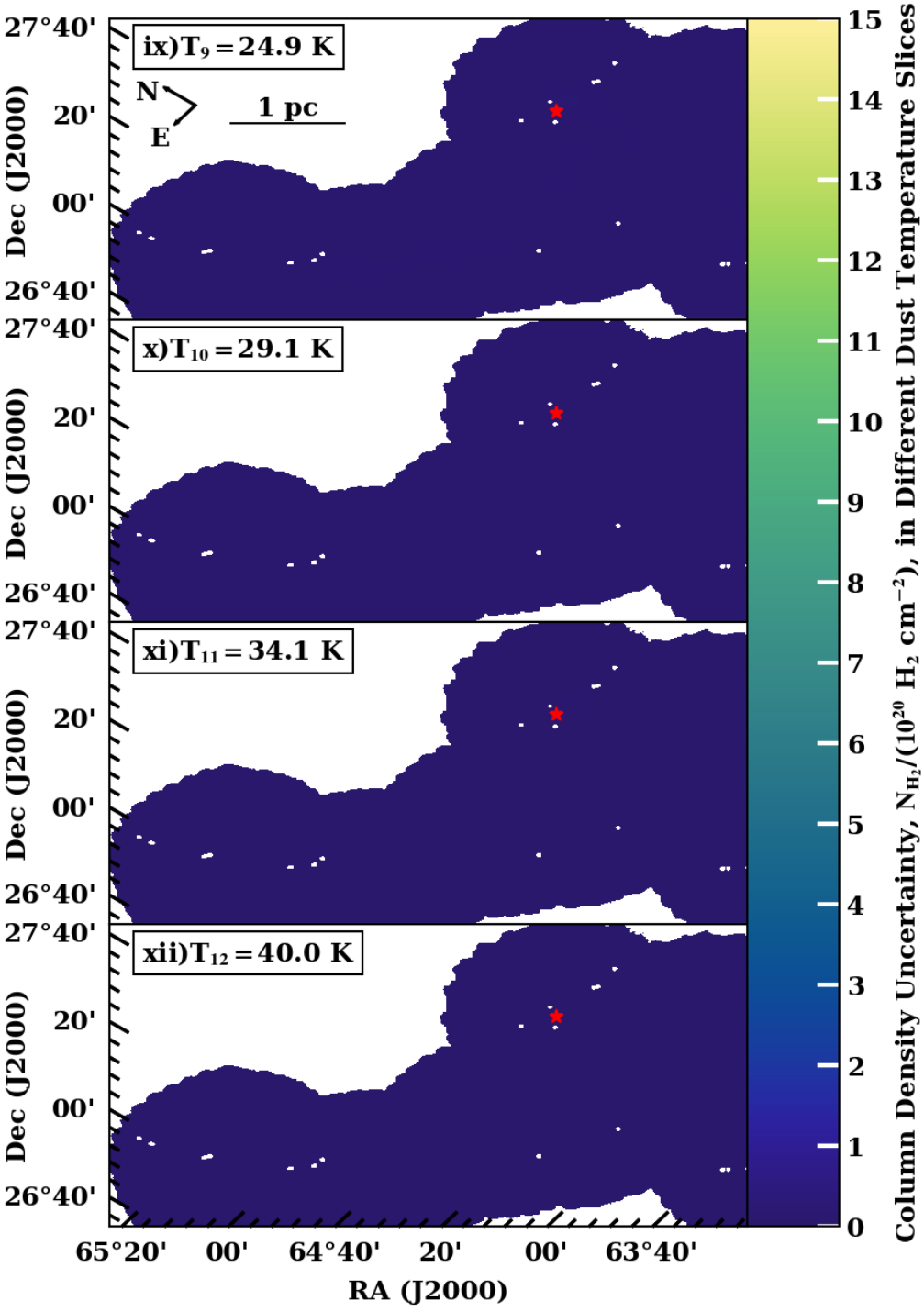

Figure B.1 (cont.). The uncertainty in the H_2 column density model, in 12, logarithmically spaced line of sight temperature bins for the L1495/B213 complex. These maps are obtained by marginalising out the opacity index dimension of the PPMAP hypercube.

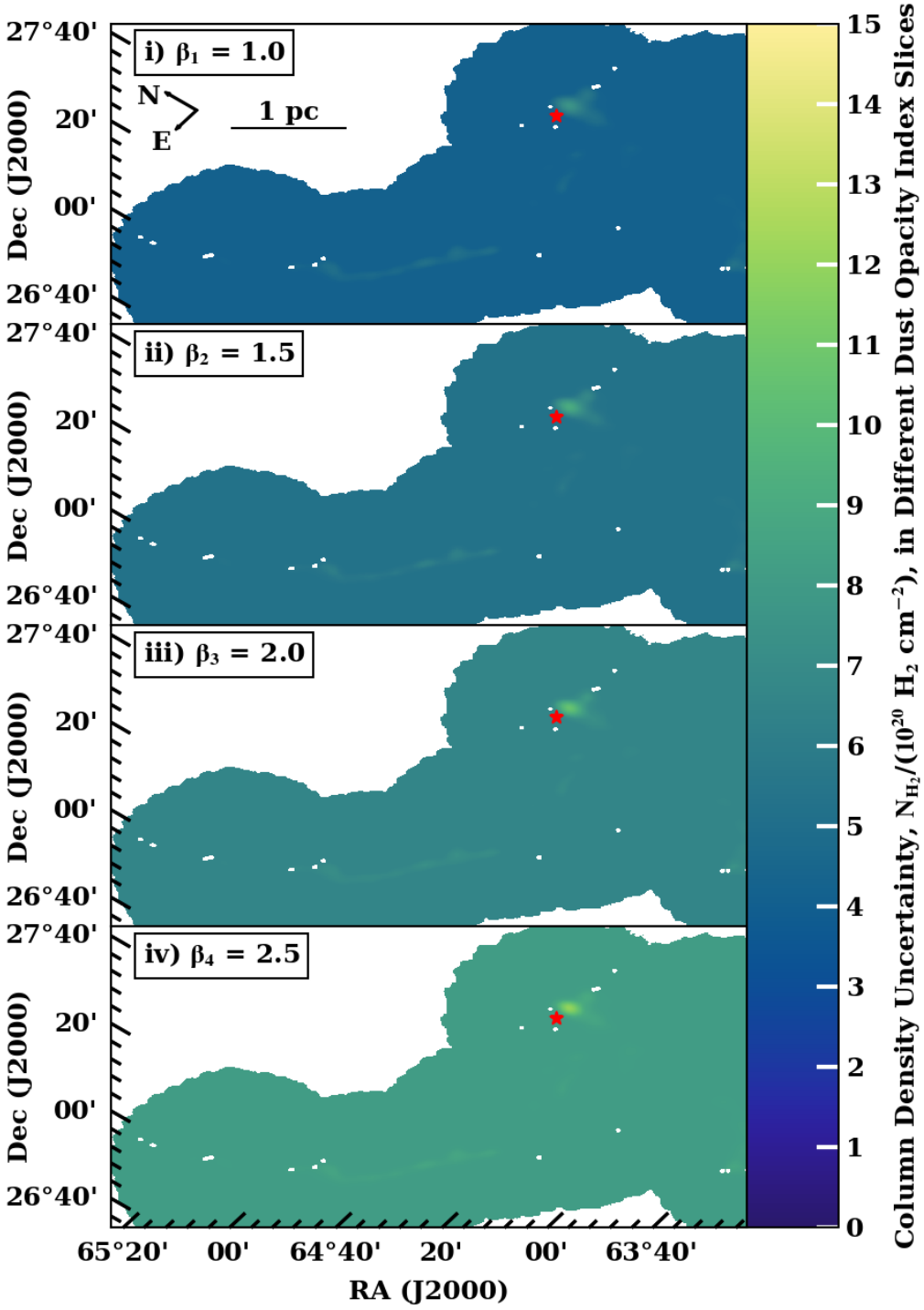

Figure B.2. The uncertainty in the H_2 column density model, in 4 linearly spaced line of sight opacity index bins for the L1495/B213 complex. These maps are obtained by marginalising out the temperature dimension of the PPMAP hypercube.

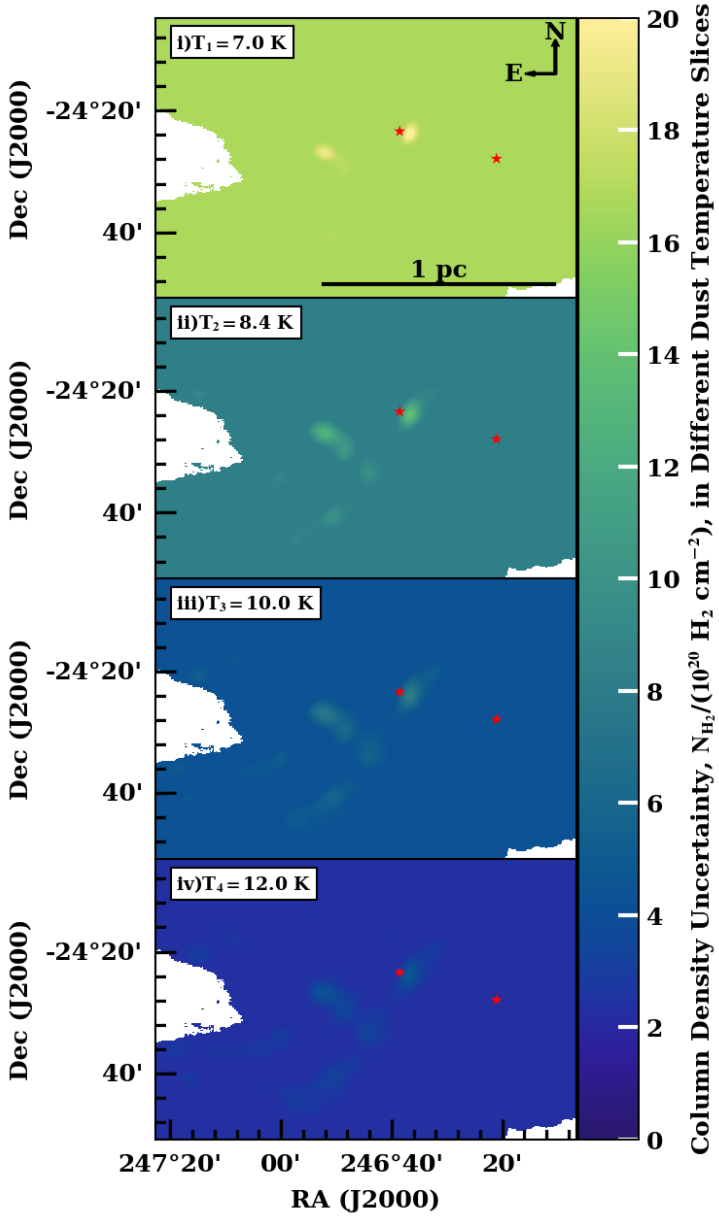

Figure B.3. The uncertainty in the H_2 column density model, in 12 logarithmically spaced line of sight temperature bins for the L1688 sub-region. These maps are obtained by marginalising out the opacity index dimension of the PPMAP data hypercube. The red star markers indicate the positions of the S1 and HD147889 pre-main sequence stars.

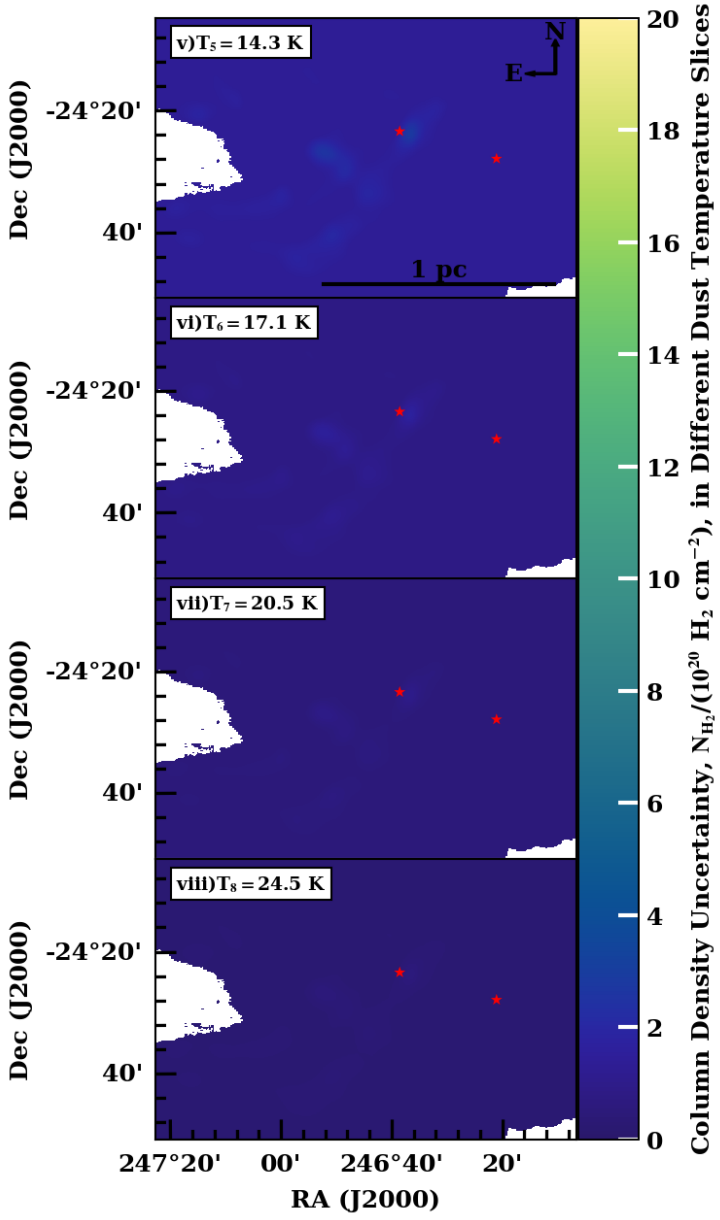

Figure B.3 (cont.). The uncertainty in the H_2 column density model, in 12 logarithmically spaced line of sight temperature bins for the L1688 sub-region. These maps are obtained by marginalising out the opacity index dimension of the PPMAP data hypercube. The red star markers indicate the positions of the S1 and HD147889 pre-main sequence stars.

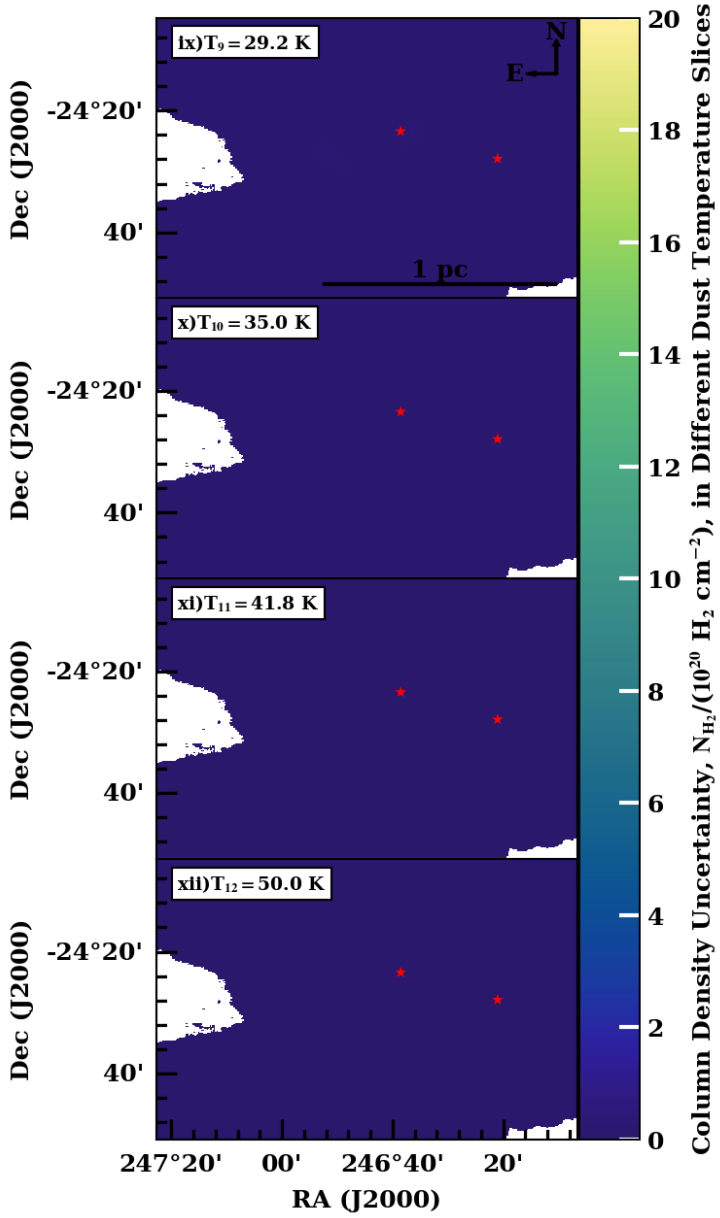

Figure B.3 (cont.). The uncertainty in the H_2 column density model, in 12 logarithmically spaced line of sight temperature bins for the L1688 sub-region. These maps are obtained by marginalising out the opacity index dimension of the PPMAP data hypercube. The red star markers indicate the positions of the S1 and HD147889 pre-main sequence stars.

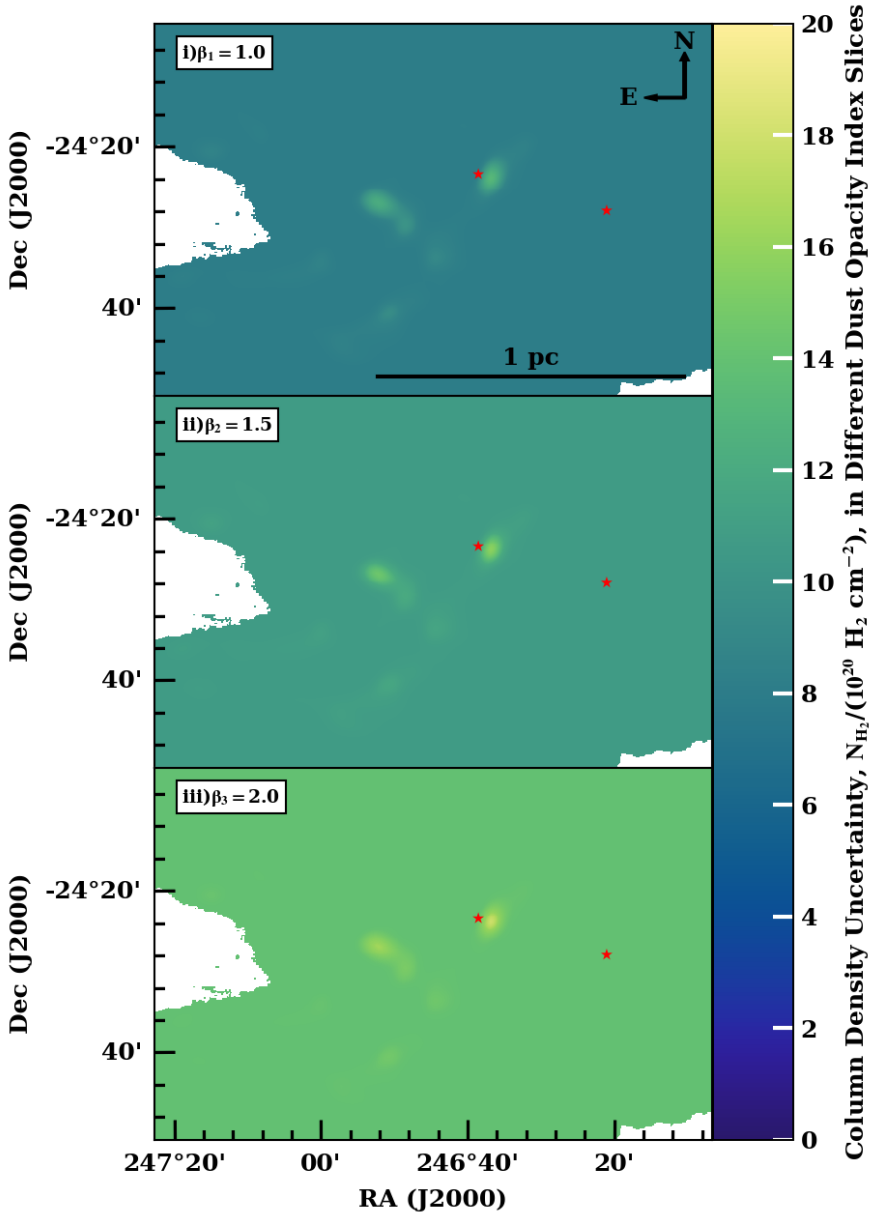

Figure B.4. The uncertainty in the H_2 column density model, in three linearly spaced line of sight opacity index bins for the L1688 sub-region. These maps are obtained by marginalising out the temperature dimension of the PPMAP data hypercube. The red star markers indicate the positions of the S1 and HD147889 pre-main sequence stars.

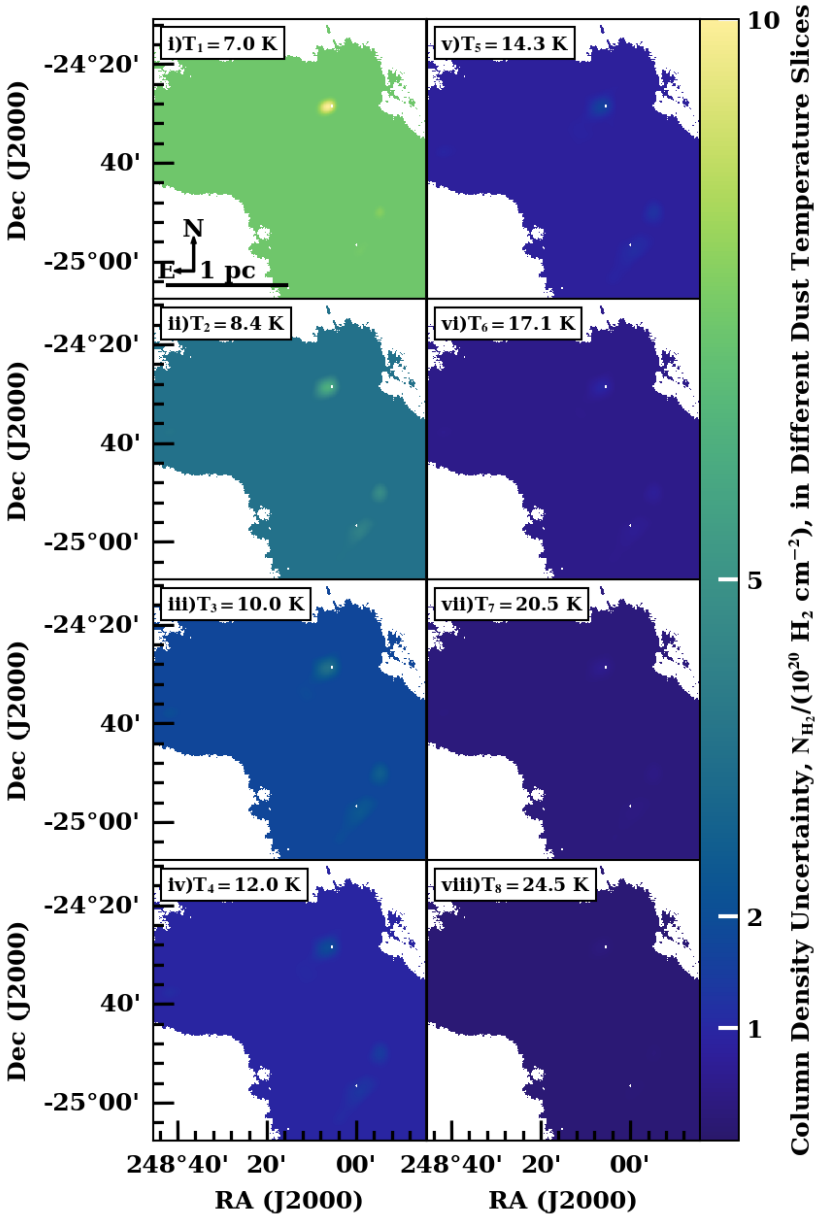

Figure B.5. The uncertainty in the H_2 column density model, in 12 logarithmically spaced line of sight temperature bins for the L1689 sub-region, plotted for the eight lowest temperatures. These maps are obtained by marginalising out the opacity index dimension of the PPMAP data hypercube.

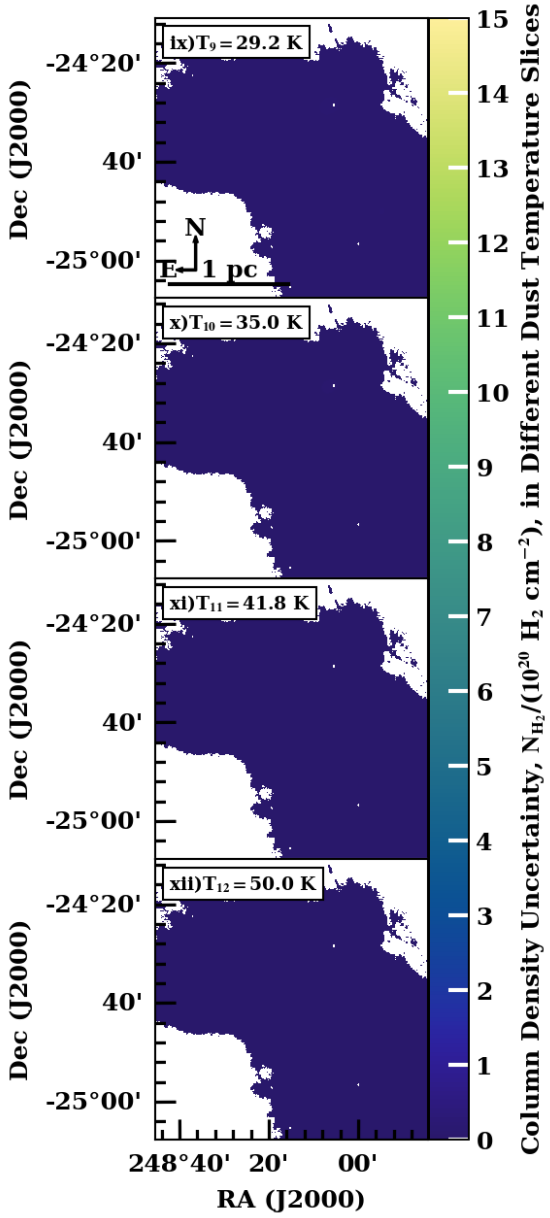

Figure B.5 (cont.). The uncertainty in the H_2 column density model, in 12 logarithmically spaced line of sight temperature bins for the L1689 sub-region, plotted for the four highest temperatures. These maps are obtained by marginalising out the opacity index dimension of the PPMAP data hypercube.

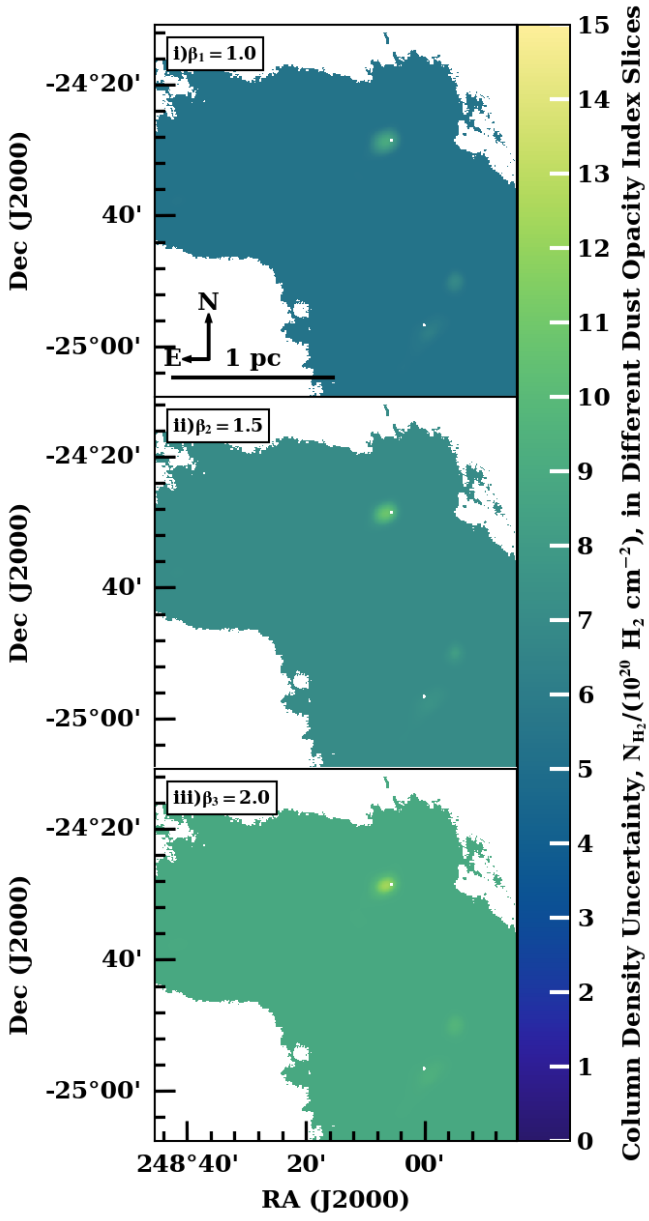

Figure B.6. The uncertainty in the H_2 column density model, in three linearly spaced line of sight opacity index bins for the L1689 sub-region. These maps are obtained by marginalising out the temperature dimension of the PPMAP data hypercube.

Bibliography

Abreu-Vicente, J. et al. (Aug. 2017). "Fourier-Space Combination of Planck and Herschel Images". In: *Astronomy & Astrophysics* 604, A65, A65. DOI: 10.1051/0004-6361/201628891.

Adam, R. et al. (Jan. 2018). "The NIKA2 Large-Field-of-View Millimetre Continuum Camera for the 30 m IRAM Telescope". In: *Astronomy & Astrophysics* 609, A115. ISSN: 0004-6361, 1432-0746. DOI: 10.1051/0004-6361/201731503. URL: https://www.aanda.org/10.1051/0004-6361/201731503 (visited on 04/28/2020).

Agladze, N. I., A. J. Sievers, S. A. Jones, J. M. Burlitch, and S. V. W. Beckwith (May 1996). "Laboratory Results on Millimeter-Wave Absorption in Silicate Grain Materials at Cryogenic Temperatures". In: *The Astrophysical Journal* 462, p. 1026. ISSN: 0004-637X, 1538-4357. DOI: 10.1086/177217. URL: http://adsabs.harvard.edu/doi/10.1086/177217 (visited on 04/14/2020).

Alves, João et al. (Feb. 2020). "A Galactic-Scale Gas Wave in the Solar Neighbourhood". In: *Nature* 578.7794, pp. 237–239. ISSN: 0028-0836, 1476-4687. DOI: 10.1038/s41586-019-1874-z. URL: http://www.nature.com/articles/s41586-019-1874-z (visited on 04/14/2020).

Andre, P., D. Ward-Thompson, and M. Barsony (May 2000). "From Prestellar Cores to Protostars: The Initial Conditions of Star Formation". In: *Protostars and Planets IV*. Ed. by V. Mannings, A. P. Boss, and S. S. Russell, p. 59.

Andre, P., D. Ward-Thompson, and F. Motte (Oct. 1996). "Probing the Initial Conditions of Star Formation: The Structure of the Prestellar Core L 1689B." In: *Astronomy & Astrophysics* 314, pp. 625–635.

André, P. et al. (July 2010). "From Filamentary Clouds to Prestellar Cores to the Stellar IMF: Initial Highlights from the Herschel Gould Belt Survey". In: *Astronomy & Astrophysics* 518, L102, p. L102. DOI: 10.1051/0004-6361/201014666.

André, P. et al. (July 2016). "Characterizing Filaments in Regions of High-Mass Star Formation: High-Resolution Submilimeter Imaging of the Massive Star-Forming Complex NGC 6334 with ArTéMiS". In: *Astronomy & Astrophysics* 592, A54, A54. DOI: 10.1051/0004-6361/201628378.

Andre, Philippe, Thierry Montmerle, Eric D. Feigelson, Peter C. Stine, and Karl-Ludwig Klein (Dec. 1988). "A Young Radio-Emitting Magnetic b Star in the Rho Ophiuchi Cloud". In: *The Astrophysical Journal* 335, p. 940. DOI: 10.1086/166979.

Andre, Philippe, Derek Ward-Thompson, and Mary Barsony (Mar. 1993). "Submillimeter Continuum Observations of Rho Ophiuchi A - The Candidate Protostar VLA 1623 and Prestellar Clumps". In: *The Astrophysical Journal* 406, p. 122. ISSN: 0004-637X, 1538-4357. DOI: 10.1086/172425. URL: http://adsabs.harvard.edu/doi/10.1086/172425 (visited on 04/14/2020).

Aristotle (c. 350 BCE). *Meteorologica*.

Arzoumanian, D. et al. (May 2011). "Characterizing Interstellar Filaments with Herschel in IC 5146". In: *Astronomy & Astrophysics* 529, L6, p. L6. DOI: 10.1051/0004-6361/201116596.

Arzoumanian, D. et al. (Jan. 2019). "Characterizing the Properties of Nearby Molecular Filaments Observed with Herschel". In: *Astronomy & Astrophysics* 621, A42, A42. DOI: 10.1051/0004-6361/201832725.

Ballesteros-Paredes, J. (Oct. 11, 2006). "Six Myths on the Virial Theorem for Interstellar Clouds". In: *Monthly Notices of the Royal Astronomical Society* 372.1, pp. 443–449. ISSN: 0035-8711, 1365-2966. DOI: 10.1111/j.1365-2966.2006.10880.x. URL: https://academic.oup.com/mnras/article-lookup/doi/10.1111/j.1365-2966.2006.10880.x (visited on 04/13/2020).

Ballesteros-Paredes, Javier, Lee Hartmann, and Enrique Vazquez-Semadeni (Dec. 10, 1999). "Turbulent Flow–Driven Molecular Cloud Formation: A Solution to the Post–T Tauri Problem?" In: *The Astrophysical Journal* 527.1, pp. 285–297. ISSN: 0004-637X, 1538-4357. DOI: 10.1086/308076. URL: http://stacks.iop.org/0004-637X/527/i=1/a=285 (visited on 04/13/2020).

Barnard, E. E. (Jan. 1910). "On a Great Nebulous Region and the Question of Absorbing Matter in Space and the Transparency of the Nebulae." In: *The Astrophysical Journal* 31, p. 8. ISSN: 0004-637X, 1538-4357. DOI: 10.1086/141719. URL: http://adsabs.harvard.edu/doi/10.1086/141719 (visited on 04/13/2020).

Barnard, Edward Emerson (1927). *Catalogue of 349 Dark Objects in the Sky*. University of Chicago Press.

Bate, Matthew R., Terrence S. Tricco, and Daniel J. Price (Jan. 1, 2014). "Collapse of a Molecular Cloud Core to Stellar Densities: Stellar-Core and Outflow Formation in Radiation Magnetohydrodynamic Simulations". In: *Monthly Notices of the Royal Astronomical Society* 437.1, pp. 77–95. ISSN: 0035-8711, 1365-2966. DOI: 10.1093/mnras/stt1865. URL: http://academic.oup.com/mnras/article/437/1/77/993807/Collapse-of-a-molecular-cloud-core-to-stellar (visited on 04/14/2020).

Beichman, C A, G Neugebauer, H J Habing, P E Clegg, and T J Chester (July 2002a). *IRAS Explanatory Supplement*. URL: https://irsa.ipac.caltech.edu/IRASdocs/exp.sup/.

Beichman, Charles A., Daniel R. Coulter, Chris Lindensmith, and Peter R. Lawson (Dec. 1, 2002b). "Selected Mission Architectures For The Terrestrial Planet Finder (TPF): Large, Medium, and Small". In: *Proceedings of the SPIE*. Astronomical Telescopes and Instrumentation. Ed. by Alan M. Dressler. Waikoloa, Hawai'i, United States, p. 115. DOI: 10.1117/12.461532. URL: http://proceedings.spiedigitallibrary.org/proceeding.aspx?doi=10.1117/12.461532 (visited on 03/10/2020).

Bekki, Kenji (Sept. 1, 2009). "Dark Impact and Galactic Star Formation: Origin of the Gould Belt". In: *Monthly Notices of the Royal Astronomical Society: Letters* 398.1, pp. L36–L40. ISSN: 17453925, 17453933. DOI: 10.1111/j.1745-3933.2009.00702.x. URL: https://academic.oup.com/mnrasl/article-lookup/doi/10.1111/j.1745-3933.2009.00702.x (visited on 04/14/2020).

Bergin, Edwin A. and Mario Tafalla (Sept. 2007). "Cold Dark Clouds: The Initial Conditions for Star Formation". In: *Annual Review of Astronomy and Astrophysics* 45.1, pp. 339–396. ISSN: 0066-4146, 1545-4282. DOI: 10.1146/annurev.astro.45.071206.100404. URL: http://arxiv.org/abs/0705.3765 (visited on 04/13/2020).

Bernard, J. -Ph. et al. (July 2010). "Dust Temperature Tracing the ISRF Intensity in the Galaxy". In: *Astronomy & Astrophysics* 518, L88, p. L88. DOI: 10.1051/0004-6361/201014540.

Berry, D. S. (Apr. 2015). "FellWalker-A Clump Identification Algorithm". In: *Astronomy and Computing* 10, pp. 22–31. DOI: 10.1016/j.ascom.2014.11.004.

Beuther, H. et al. (Dec. 2015). "Filament Fragmentation in High-Mass Star Formation". In: *Astronomy & Astrophysics* 584, A67. ISSN: 0004-6361, 1432-0746. DOI: 10.1051/0004-6361/201527108. URL: http://www.aanda.org/10.1051/0004-6361/201527108 (visited on 04/13/2020).

Bianchi, S. et al. (Oct. 2, 2018). "The Fraction of Bolometric Luminosity Absorbed by Dust in DustPedia Galaxies". In: *Astronomy & Astrophysics*. DOI: 10.1051/0004-6361/201833699. URL: http://arxiv.org/abs/1810.01208 (visited on 07/01/2020).

Bobylev, V. V. (Nov. 22, 2014). "The Gould Belt". In: *Astrophysics*. ISSN: 0571-7256, 1573-8191. DOI: 10.1007/s10511-014-9360-7. URL: http://link.springer.com/10.1007/s10511-014-9360-7 (visited on 04/14/2020).

Bohlin, R. C., B. D. Savage, and J. F. Drake (Aug. 1978). "A Survey of Interstellar H I from L-Alpha Absorption Measurements. II". In: *The Astrophysical Journal* 224, p. 132. ISSN: 0004-637X, 1538-4357. DOI: 10.1086/156357. URL: http://adsabs.harvard.edu/doi/10.1086/156357 (visited on 03/02/2020).

Bonnell, Ian A., Matthew R. Bate, and Stephen G. Vine (Aug. 2003). "The Hierarchical Formation of a Stellar Cluster". In: *Monthly Notices of the Royal Astronomical Society* 343.2, pp. 413–418. ISSN: 0035-8711, 1365-2966. DOI: 10.1046/j.1365-8711.2003.06687.x. URL: https://academic.oup.com/mnras/article-lookup/doi/10.1046/j.1365-8711.2003.06687.x (visited on 04/13/2020).

Bryan, Sean (Jan. 25, 2018). "The Toltec Camera For The Lmt Telescope". In: *Zendo*. DOI: 10.5281/ZENODO.1159073. URL: https://zenodo.org/record/1159073 (visited on 04/28/2020).

Buckle, J. V. et al. (May 2015). "The JCMT Gould Belt Survey: SCUBA-2 Observations of Circumstellar Discs in l 1495". In: *Monthly Notices of the Royal Astronomical Society* 449.3, pp. 2472–2488. DOI: 10.1093/mnras/stv438.

Cardelli, Jason A., Geoffrey C. Clayton, and John S. Mathis (Oct. 1989). "The Relationship between Infrared, Optical, and Ultraviolet Extinction". In: *The Astrophysical Journal* 345, p. 245. ISSN: 0004-637X, 1538-4357. DOI: 10.1086/167900. URL: http://adsabs.harvard.edu/doi/10.1086/167900 (visited on 05/04/2020).

Carpenter, John M. (May 2001). "Color Transformations for the 2MASS Second Incremental Data Release". In: *The Astronomical Journal* 121.5, pp. 2851–2871. ISSN: 00046256. DOI: 10.1086/320383. URL: http://stacks.iop.org/1538-3881/121/i=5/a=2851 (visited on 03/02/2020).

Casali, M. M. (Nov. 1986). "Near-Infrared Observations of BOK Globules." In: *Monthly Notices of the Royal Astronomical Society* 223, pp. 341–352. DOI: 10.1093/mnras/223.2.341.

Casassus, Simon et al. (Dec. 2008). "Centimetre-Wave Continuum Radiation from the ρ Ophiuchi Molecular Cloud". In: *Monthly Notices of the Royal Astronomical Society* 391.3, pp. 1075–1090. DOI: 10.1111/j.1365-2966.2008.13954.x.

Casey, Caitlin M., Desika Narayanan, and Asantha Cooray (Aug. 2014). "Dusty Star-Forming Galaxies at High Redshift". In: *Physics Report* 541, pp. 45–161. DOI: 10.1016/j.physrep.2014.02.009.

Castillo-Dominguez, E. et al. (Dec. 2018). "Mexico-UK Sub-Millimeter Camera for Astronomy". In: *Journal of Low Temperature Physics* 193.5-6, pp. 1010–1015. ISSN: 0022-2291, 1573-7357. DOI: 10.1007/s10909-018-2018-9. URL: http://link.springer.com/10.1007/s10909-018-2018-9 (visited on 04/28/2020).

Chandrasekhar, S. (1960). *Radiative Transfer*.

Chapin, Edward L. et al. (Apr. 2013). "SCUBA-2: Iterative Map-Making with the Sub-Millimetre User Reduction Facility". In: *Monthly Notices of the Royal Astronomical Society* 430.4, pp. 2545–2573. DOI: 10.1093/mnras/stt052.

Chawner, H et al. (Feb. 11, 2019). "A Catalogue of Galactic Supernova Remnants in the Far-Infrared: Revealing Ejecta Dust in Pulsar Wind Nebulae". In: *Monthly Notices of the Royal Astronomical Society* 483.1, pp. 70–118. ISSN: 0035-8711, 1365-2966. DOI: 10.1093/mnras/sty2942. URL: https://academic.oup.com/mnras/article/483/1/70/5151342 (visited on 05/07/2020).

Cigan, Phil (Sept. 2019). "MultiColorFits: Colorize and Combine Multiple Fits Images for Visually Aesthetic Scientific Plots". In: *Astrophysics Source Code Library*, ascl:1909.002, ascl:1909.002.

Clark, P. C. and I. A. Bonnell (Jan. 11, 2004). "Star Formation in Transient Molecular Clouds". In: *Monthly Notices of the Royal Astronomical Society* 347.2, pp. L36–L40. ISSN: 0035-8711, 1365-2966. DOI: 10.1111/j.1365-2966.2004.07377.x. URL: https://academic.oup.com/mnras/article-lookup/doi/10.1111/j.1365-2966.2004.07377.x (visited on 04/13/2020).

Clark, Paul C., Ian A. Bonnell, Hans Zinnecker, and Matthew R. Bate (May 2005). "Star Formation in Unbound Giant Molecular Clouds: The Origin of OB Associations?" In: *Monthly Notices of the Royal Astronomical Society* 359.3, pp. 809–818. ISSN: 00358711, 13652966. DOI: 10.1111/j.1365-2966.2005.08942.x. URL: https://academic.oup.com/mnras/article-lookup/doi/10.1111/j.1365-2966.2005.08942.x (visited on 04/13/2020).

Clarke, S. D., A. P. Whitworth, A. Duarte-Cabral, and D. A. Hubber (June 2017). "Filamentary Fragmentation in a Turbulent Medium". In: *Monthly Notices of the Royal Astronomical Society* 468, pp. 2489–2505. DOI: 10.1093/mnras/stx637.

Clarke, S. D., A. P. Whitworth, and D. A. Hubber (May 2016). "Perturbation Growth in Accreting Filaments". In: *Monthly Notices of the Royal Astronomical Society* 458, pp. 319–324. DOI: 10.1093/mnras/stw407.

Clarke, S. D., G. M. Williams, J. C. Ibáñez-Mejía, and S. Walch (Apr. 11, 2019). "Determining the Presence of Characteristic Fragmentation Length-Scales in Filaments". In: *Monthly Notices of the Royal Astronomical Society* 484.3, pp. 4024–4045. ISSN: 0035-8711, 1365-2966. DOI: 10.1093/mnras/stz248. URL: http://arxiv.org/abs/1901.06205 (visited on 04/28/2020).

Clarke, S. D. et al. (Sept. 2018). "Synthetic C18O Observations of Fibrous Filaments: The Problems of Mapping from PPV to PPP". In: *Monthly Notices of the Royal Astronomical Society* 479, pp. 1722–1746. DOI: 10.1093/mnras/sty1675.

Comeron, F. and J. Torra (Jan. 1994). "The Origin of the Gould Belt by the Impact of a High Velocity Cloud on the Galactic Disk." In: *Astronomy & Astrophysics* 281, pp. 35–45.

Commerçon, B., E. Audit, G. Chabrier, and J.-P. Chièze (June 2011). "Physical and Radiative Properties of the First-Core Accretion Shock". In: *Astronomy & Astrophysics* 530, A13. ISSN: 0004-6361, 1432-0746. DOI: 10.1051/0004-6361/201016213. URL: http://www.aanda.org/10.1051/0004-6361/201016213 (visited on 04/14/2020).

De Graauw, Th. et al. (July 2010). "The Herschel-Heterodyne Instrument for the Far-Infrared (HIFI)". In: *Astronomy & Astrophysics* 518, L6, p. L6. DOI: 10.1051/0004-6361/201014698.

Dempsey, J. T. et al. (Apr. 2013). "SCUBA-2: On-Sky Calibration Using Submillimetre Standard Sources". In: *Monthly Notices of the Royal Astronomical Society* 430.4, pp. 2534–2544. DOI: 10.1093/mnras/stt090.

Demyk, K. et al. (Jan. 2013). "FIR and Submm Optical Properties of Astrophysically Relevant Minerals". In: *Proceedings of the Life Cycle of Dust in the Universe: Observations*, p. 44.

Dib, Sami, C. Jakob Walcher, Mark Heyer, Edouard Audit, and Laurent Loinard (Sept. 21, 2009). "The Orientations of Molecular Clouds in the Outer Galaxy: Evidence for the Scale of the Turbulence Driver?" In: *Monthly Notices of the Royal Astronomical Society* 398.3, pp. 1201–1206. ISSN: 00358711, 13652966. DOI: 10.1111/j.1365-2966.2009.15201.x. URL: https://academic.oup.com/mnras/article-lookup/doi/10.1111/j.1365-2966.2009.15201.x (visited on 04/13/2020).

Dickey, J. M., Y. Terzian, and E. E. Salpeter (Jan. 1978). "Galactic Neutral Hydrogen Emission-Absorption Observations from Arecibo". In: *The Astrophysical Journal Supplement Series* 36, p. 77. ISSN: 0067-0049, 1538-4365. DOI: 10.1086/190492. URL: http://adsabs.harvard.edu/doi/10.1086/190492 (visited on 04/10/2020).

Dobbs, Clare L. (Mar. 11, 2015). "The Interstellar Medium and Star Formation on Kpc Size Scales". In: *Monthly Notices of the Royal Astronomical Society* 447.4, pp. 3390–3401. ISSN: 1365-2966, 0035-8711. DOI: 10.1093/mnras/stu2585. URL: http://academic.oup.com/mnras/article/447/4/3390/1747462/The-interstellar-medium-and-star-formation-on-kpc (visited on 04/13/2020).

Dobson, Trevor (2015). *Whateye Image*. URL: https://petapixel.com/assets/uploads/2015/04/whateye.jpg (visited on 09/30/2020).

Drabek-Maunder, E., J. Hatchell, J. V. Buckle, J. Di Francesco, and J. Richer (Mar. 21, 2016). "The JCMT Gould Belt Survey: Understanding the Influence of Outflows on Gould Belt Clouds". In: *Monthly Notices of the Royal Astronomical Society: Letters* 457.1, pp. L84–L88. ISSN: 1745-3925, 1745-3933. DOI: 10.1093/mnrasl/slv202. URL: https://academic.oup.com/mnrasl/article-lookup/doi/10.1093/mnrasl/slv202 (visited on 04/13/2020).

Drabek-Maunder, Emily (2017). In:

— (2019). In:

Duarte-Cabral, Ana and C. L. Dobbs (Oct. 1, 2017). "The Evolution of Giant Molecular Filaments". In: *Monthly Notices of the Royal Astronomical Society* 470.4, pp. 4261–4273. ISSN: 0035-8711, 1365-2966. DOI: 10.1093/mnras/stx1524. URL: https://academic.oup.com/mnras/article/470/4/4261/3871368 (visited on 04/13/2020).

Dunne, L. and S. A. Eales (Nov. 1, 2001). "The SCUBA Local Universe Galaxy Survey - II. 450- m Data: Evidence for Cold Dust in Bright IRAS Galaxies". In: *Monthly Notices of the Royal Astronomical Society* 327.3, pp. 697–714. ISSN: 0035-8711, 1365-2966. DOI: 10.1046/j.1365-8711.2001.04789.x. URL: https://academic.oup.com/mnras/article-lookup/doi/10.1046/j.1365-8711.2001.04789.x (visited on 04/13/2020).

Dunne, L. et al. (Oct. 21, 2011). "Herschel-ATLAS: Rapid Evolution of Dust in Galaxies over the Last 5 Billion Years: Evolution of Dust Mass". In: *Monthly Notices of the Royal Astronomical Society* 417.2, pp. 1510–1533. ISSN: 00358711. DOI: 10.1111/j.1365-2966.2011.19363.x. URL: https://academic.oup.com/

mnras/article-lookup/doi/10.1111/j.1365-2966.2011.19363.x (visited on 04/13/2020).

Dunne, Loretta, Stephen Eales, Rob Ivison, Haley Morgan, and Mike Edmunds (July 2003). "Type II Supernovae as a Significant Source of Interstellar Dust". In: *Nature* 424.6946, pp. 285–287. ISSN: 0028-0836, 1476-4687. DOI: 10.1038/nature01792. URL: http://www.nature.com/articles/nature01792 (visited on 04/13/2020).

Dwek, E. and J. M. Scalo (July 1980). "The Evolution of Refractory Interstellar Grains in the Solar Neighborhood". In: *The Astrophysical Journal* 239, p. 193. ISSN: 0004-637X, 1538-4357. DOI: 10.1086/158100. URL: http://adsabs.harvard.edu/doi/10.1086/158100 (visited on 04/13/2020).

Dwek, Eli (July 10, 1998). "The Evolution of the Elemental Abundances in the Gas and Dust Phases of the Galaxy". In: *The Astrophysical Journal* 501.2, pp. 643–665. ISSN: 0004-637X, 1538-4357. DOI: 10.1086/305829. URL: http://stacks.iop.org/0004-637X/501/i=2/a=643 (visited on 04/10/2020).

East Asian Observatory (2010). *Cryostatic Window, Filter and Dichroic Specification and Measurements*. URL: https://www.easobservatory.org/jcmt/insturmentation/continuum/scuba-2/filters/ (visited on 07/16/2019).

— (2017). *Image 7441*. URL: eaobservatory.org/jcmt/public/gallery/images/img_7441/ (visited on 07/16/2019).

Elias, J. H. (Sept. 1978). "A Study of the Taurus Dark Cloud Complex." In: *The Astrophysical Journal* 224, pp. 857–872. DOI: 10.1086/156436.

Elmegreen, Bruce G. (Feb. 10, 2000). "Star Formation in a Crossing Time". In: *The Astrophysical Journal* 530.1, pp. 277–281. ISSN: 0004-637X, 1538-4357. DOI: 10.1086/308361. URL: http://stacks.iop.org/0004-637X/530/i=1/a=277 (visited on 04/13/2020).

Enoch, Melissa L. et al. (Sept. 2008). "The Mass Distribution and Lifetime of Prestellar Cores in Perseus, Serpens, and Ophiuchus". In: *The Astrophysical Journal* 684.2, pp. 1240–1259. DOI: 10.1086/589963.

Exter, K. (2017). "The PACS Handbook". In: *Herschel Explanatory Supplement* III.

Federrath, Christoph (Mar. 21, 2016). "On the Universality of Interstellar Filaments: Theory Meets Simulations and Observations". In: *Monthly Notices of the Royal Astronomical Society* 457.1, pp. 375–388. ISSN: 0035-8711, 1365-2966. DOI: 10.1093/mnras/stv2880. URL: https://academic.oup.com/mnras/article-lookup/doi/10.1093/mnras/stv2880 (visited on 04/13/2020).

Ferrarotti, A. S. and H.-P. Gail (Feb. 2006). "Composition and Quantities of Dust Produced by AGB-Stars and Returned to the Interstellar Medium". In: *Astronomy & Astrophysics* 447.2, pp. 553–576. ISSN: 0004-6361, 1432-0746. DOI: 10.1051/0004-6361:20041198. URL: http://www.aanda.org/10.1051/0004-6361:20041198 (visited on 04/13/2020).

Ferriere, Katia (Aug. 20, 1998). "The Hot Gas Filling Factor in Our Galaxy". In: *The Astrophysical Journal* 503.2, pp. 700–716. ISSN: 0004-637X, 1538-4357. DOI: 10.1086/306003. URL: http://stacks.iop.org/0004-637X/503/i=2/a=700 (visited on 04/10/2020).

Field, G. B., D. W. Goldsmith, and H. J. Habing (Mar. 1969). "Cosmic-Ray Heating of the Interstellar Gas". In: *The Astrophysical Journal* 155, p. L149. ISSN: 0004-637X, 1538-4357. DOI: 10.1086/180324. URL: http://adsabs.harvard.edu/doi/10.1086/180324 (visited on 04/13/2020).

Fischera, J. and P. G. Martin (June 2012). "Physical Properties of Interstellar Filaments". In: *Astronomy & Astrophysics* 542, A77, A77. DOI: 10.1051/0004-6361/201218961.

Galli, Phillip A. B. et al. (May 21, 2018). "The Gould's Belt Distances Survey (GOBELINS). IV. Distance, Depth and Kinematics of the Taurus Star-Forming Region". In: *The Astrophysical Journal* 859.1, p. 33. ISSN: 1538-4357. DOI: 10.3847/1538-4357/aabf91. URL: http://arxiv.org/abs/1805.09357 (visited on 07/21/2020).

Geis, N. and D. Lutz (Mar. 8, 2010). "Herschel/PACS Modelled Point-Spread Functions". In: *Herschel Explanatory Supplement* 2.0.

Giardino, G., F. Favata, G. Micela, and F. Reale (Jan. 2004). "A Large X-Ray Flare from the Herbig Ae Star V892 Tau". In: *Astronomy & Astrophysics* 413, pp. 669–679. DOI: 10.1051/0004-6361:20034151.

Gómez, Gilberto C. and Enrique Vázquez-Semadeni (Aug. 6, 2014). "Filaments in Simulations of Molecular Cloud Formation". In: *The Astrophysical Journal* 791.2, p. 124. ISSN: 1538-4357. DOI: 10.1088/0004-637X/791/2/124. URL: https://iopscience.iop.org/article/10.1088/0004-637X/791/2/124 (visited on 04/13/2020).

Gould, Benjamin Apthorp (Jan. 1879). "Uranometria Argentina : Brillantez y Posicion de Las Estrellas Fijas, Hasta La Septima Magnitud, Comprendidas Dentro de Cien Grados Del Polo Austral : Con Atlas". In: *Resultados del Observatorio Nacional Argentino* 1.

Greene, Thomas P., Bruce A. Wilking, Philippe Andre, Erick T. Young, and Charles J. Lada (Oct. 1994). "Further Mid-Infrared Study of the Rho Ophiuchi Cloud

Young Stellar Population: Luminosities and Masses of Pre–Main-Sequence Stars". In: *The Astrophysical Journal* 434, p. 614. DOI: 10.1086/174763.

Griffin, M. J. (2007). "SPIRE Sensitivity Models". In: *Research Report SPIRE-QMW-NOT-000642*. SPIRE Consortium. Rutherford Appleton Laboratory, Harwell, UK.

Griffin, M. J. et al. (July 2010). "The Herschel-SPIRE Instrument and Its in-Flight Performance". In: *Astronomy & Astrophysics* 518, L3, p. L3. DOI: 10.1051/0004-6361/201014519.

Gritschneder, Matthias, Thorsten Naab, Stefanie Walch, Andreas Burkert, and Fabian Heitsch (Mar. 20, 2009). "Driving Turbulence and Triggering Star Formation by Ionizing Radiation". In: *The Astrophysical Journal* 694.1, pp. L26–L30. ISSN: 0004-637X, 1538-4357. DOI: 10.1088/0004-637X/694/1/L26. URL: http://arxiv.org/abs/0901.2113 (visited on 04/13/2020).

Großschedl, Josefa E. et al. (Nov. 2018). "3D Shape of Orion A from *Gaia* DR2". In: *Astronomy & Astrophysics* 619, A106. ISSN: 0004-6361, 1432-0746. DOI: 10.1051/0004-6361/201833901. URL: https://www.aanda.org/10.1051/0004-6361/201833901 (visited on 04/13/2020).

Hacar, A., M. Tafalla, and J. Alves (Oct. 2017). "Fibers in the NGC 1333 Proto-Cluster". In: *Astronomy & Astrophysics* 606, A123. ISSN: 0004-6361, 1432-0746. DOI: 10.1051/0004-6361/201630348. URL: http://www.aanda.org/10.1051/0004-6361/201630348 (visited on 04/13/2020).

Hacar, A., M. Tafalla, J. Kauffmann, and A. Kovács (June 2013). "Cores, Filaments, and Bundles: Hierarchical Core Formation in the L1495/B213 Taurus Region". In: *Astronomy & Astrophysics* 554, A55, A55. DOI: 10.1051/0004-6361/201220090.

Hacar, A. et al. (Mar. 2018). "An ALMA Study of the Orion Integral Filament. I. Evidence for Narrow Fibers in a Massive Cloud". In: *Astronomy & Astrophysics* 610, A77, A77. DOI: 10.1051/0004-6361/201731894.

Hartmann, Lee, Javier Ballesteros-Paredes, and Edwin A. Bergin (Dec. 2001). "Rapid Formation of Molecular Clouds and Stars in the Solar Neighborhood". In: *The Astrophysical Journal* 562.2, pp. 852–868. ISSN: 0004-637X, 1538-4357. DOI: 10.1086/323863. URL: https://iopscience.iop.org/article/10.1086/323863 (visited on 05/08/2020).

Heitsch, F. (June 2013a). "Gravitational Infall onto Molecular Filaments". In: *The Astrophysical Journal* 769, 115, p. 115. DOI: 10.1088/0004-637X/769/2/115.

Heitsch, Fabian (Oct. 2013b). "Gravitational Infall onto Molecular Filaments. II. Externally Pressurized Cylinders". In: *The Astrophysical Journal* 776.1, 62, p. 62. DOI: 10.1088/0004-637X/776/1/62.

Heitsch, Fabian, Javier Ballesteros-Paredes, and Lee Hartmann (Oct. 20, 2009). "Gravitational Collapse and Filament Formation: Comparison with the Pipe Nebula". In: *The Astrophysical Journal* 704.2, pp. 1735–1742. ISSN: 0004-637X, 1538-4357. DOI: 10.1088/0004-637X/704/2/1735. URL: https://iopscience.iop.org/article/10.1088/0004-637X/704/2/1735 (visited on 04/13/2020).

Heitsch, Fabian, Lee W. Hartmann, Adrianne D. Slyz, Julien E. G. Devriendt, and Andreas Burkert (Feb. 10, 2008). "Cooling, Gravity, and Geometry: Flow-driven Massive Core Formation". In: *The Astrophysical Journal* 674.1, pp. 316–328. ISSN: 0004-637X, 1538-4357. DOI: 10.1086/523697. URL: http://stacks.iop.org/0004-637X/674/i=1/a=316 (visited on 04/13/2020).

Hennebelle, Patrick (Aug. 2013). "On the Origin of Non-Self-Gravitating Filaments in the ISM". In: *Astronomy & Astrophysics* 556, A153. ISSN: 0004-6361, 1432-0746. DOI: 10.1051/0004-6361/201321292. URL: http://www.aanda.org/10.1051/0004-6361/201321292 (visited on 04/13/2020).

Henshaw, J. D. et al. (Jan. 1, 2017). "Unveiling the Early-Stage Anatomy of a Protocluster Hub with ALMA". In: *Monthly Notices of the Royal Astronomical Society: Letters* 464.1, pp. L31–L35. ISSN: 1745-3925, 1745-3933. DOI: 10.1093/mnrasl/slw154. URL: https://academic.oup.com/mnrasl/article-lookup/doi/10.1093/mnrasl/slw154 (visited on 04/13/2020).

Herschel, Sir John Frederick William (1847). *Results of Astronomical Observations Made during the Years 1834, 5, 6, 7, 8, at the Cape of Good Hope; Being the Completion of a Telescopic Survey of the Whole Surface of the Visible Heavens, Commenced in 1825.*

Hildebrand, R. H. (Sept. 1983). "The Determination of Cloud Masses and Dust Characteristics from Submillimetre Thermal Emission". In: *Quarterly Journal of the Royal Astronomical Society* 24, p. 267.

Hill, T. et al. (Sept. 2011). "Filaments and Ridges in Vela C Revealed by *Herschel* : From Low-Mass to High-Mass Star-Forming Sites". In: *Astronomy & Astrophysics* 533, A94. ISSN: 0004-6361, 1432-0746. DOI: 10.1051/0004-6361/201117315. URL: http://www.aanda.org/10.1051/0004-6361/201117315 (visited on 04/13/2020).

Holland, W. S. et al. (Apr. 2013). "SCUBA-2: The 10 000 Pixel Bolometer Camera on the James Clerk Maxwell Telescope". In: *Monthly Notices of the Royal Astronomical Society* 430, pp. 2513–2533. DOI: 10.1093/mnras/sts612.

Hollenbach, David and E. E. Salpeter (Jan. 1971). "Surface Recombination of Hydrogen Molecules". In: *The Astrophysical Journal* 163, p. 155. ISSN: 0004-637X, 1538-4357. DOI: 10.1086/150754. URL: http://adsabs.harvard.edu/doi/10.1086/150754 (visited on 04/13/2020).

Howard, A. D. P. et al. (Oct. 2019). "L1495 Revisited: A PPMAP View of a Star-Forming Filament". In: *Monthly Notices of the Royal Astronomical Society* 489.1, pp. 962–976. DOI: 10.1093/mnras/stz2234.

Inutsuka, S.-I. and S. M. Miyama (Apr. 1992). "Self-Similar Solutions and the Stability of Collapsing Isothermal Filaments". In: *The Astrophysical Journal* 388, pp. 392–399. DOI: 10.1086/171162.

Jeans, James Hopwood (1928). *Astronomy and Cosmogony*.

Jenkins, Edward B. (1987). "Element Abundances in the Interstellar Atomic Material". In: *Interstellar Processes*. Ed. by David J. Hollenbach and Harley A. Thronson. Vol. 134. Astrophysics and Space Science Library. Dordrecht: Springer Netherlands, pp. 533–559. ISBN: 978-90-277-2485-4 978-94-009-3861-8. DOI: 10.1007/978-94-009-3861-8_20. URL: http://link.springer.com/10.1007/978-94-009-3861-8_20 (visited on 04/13/2020).

Juvela, M. and J. Montillaud (Jan. 2016). "Allsky NICER and NICEST Extinction Maps Based on the 2MASS Near-Infrared Survey". In: *Astronomy & Astrophysics* 585, A38, A38. DOI: 10.1051/0004-6361/201425112.

Kelsall, T. et al. (Nov. 1998). "The COBE Diffuse Infrared Background Experiment Search for the Cosmic Infrared Background. II. Model of the Interplanetary Dust Cloud". In: *The Astrophysical Journal* 508.1, pp. 44–73. DOI: 10.1086/306380.

Kim, Sang-Hee and P. G. Martin (Aug. 1994). "The Size Distribution of Interstellar Dust Particles as Determined from Polarization: Infinite Cylinders". In: *The Astrophysical Journal* 431, p. 783. ISSN: 0004-637X, 1538-4357. DOI: 10.1086/174529. URL: http://adsabs.harvard.edu/doi/10.1086/174529 (visited on 04/13/2020).

Klessen, R. S. and P. Hennebelle (Sept. 2010). "Accretion-Driven Turbulence as Universal Process: Galaxies, Molecular Clouds, and Protostellar Disks". In: *Astronomy & Astrophysics* 520, A17. ISSN: 0004-6361, 1432-0746. DOI: 10.1051/0004-6361/200913780. URL: http://www.aanda.org/10.1051/0004-6361/200913780 (visited on 04/13/2020).

Koch, E. W. and E. W. Rosolowsky (Oct. 2015). "Filament Identification through Mathematical Morphology". In: *Monthly Notices of the Royal Astronomical Society* 452, pp. 3435–3450. DOI: 10.1093/mnras/stv1521.

Könyves, V. et al. (July 2010). "The Aquila Prestellar Core Population Revealed by *Herschel*". In: *Astronomy & Astrophysics* 518, p. L106. ISSN: 0004-6361, 1432-0746. DOI: 10.1051/0004-6361/201014689. URL: http://www.aanda.org/10.1051/0004-6361/201014689 (visited on 04/13/2020).

Könyves, V. et al. (Dec. 2015). "A Census of Dense Cores in the Aquila Cloud Complex: SPIRE/PACS Observations from the Herschel Gould Belt Survey". In: *Astronomy & Astrophysics* 584, A91, A91. DOI: 10.1051/0004-6361/201525861.

Kulkarni, Shrinivas R. and Carl Heiles (1987). "The Atomic Component". In: *Interstellar Processes*. Ed. by David J. Hollenbach and Harley A. Thronson. Vol. 134. Astrophysics and Space Science Library. Dordrecht: Springer Netherlands, pp. 87–122. ISBN: 978-90-277-2485-4 978-94-009-3861-8. DOI: 10.1007/978-94-009-3861-8_5. URL: http://link.springer.com/10.1007/978-94-009-3861-8_5 (visited on 04/13/2020).

Lada, Charles J. (Jan. 1987). "Star Formation: From OB Associations to Protostars." In: *Star Forming Regions*. Ed. by Manuel Peimbert and Jun Jugaku. Vol. 115. IAU Symposium, p. 1.

Lada, Charles J., Elizabeth A. Lada, Dan P. Clemens, and John Bally (1994). "Mapping Dust Extinction with IR Cameras". In: *Infrared Astronomy with Arrays*. Ed. by Ian S. McLean. Vol. 190. Astrophysics and Space Science Library. Dordrecht: Springer Netherlands, pp. 473–480. ISBN: 978-94-010-4466-0 978-94-011-1070-9. DOI: 10.1007/978-94-011-1070-9_141. URL: http://link.springer.com/10.1007/978-94-011-1070-9_141 (visited on 04/13/2020).

Lada, Charles J., Marco Lombardi, and João F. Alves (Nov. 2010). "On the Star Formation Rates in Molecular Clouds". In: *The Astrophysical Journal* 724.1, pp. 687–693. DOI: 10.1088/0004-637X/724/1/687.

Ladjelate, Bilal et al. (Jan. 2020). "The Herschel View of the Dense Core Population in the Ophiuchus Molecular Cloud". In: *Astronomy & Astrophysics*, arXiv:2001.11036, arXiv:2001.11036.

Lamarre, J. -M. et al. (Sept. 2010). "Planck Pre-Launch Status: The HFI Instrument, from Specification to Actual Performance". In: *Astronomy & Astrophysics* 520, A9, A9. DOI: 10.1051/0004-6361/200912975.

Larson, R. B. (Aug. 1, 1969a). "Numerical Calculations of the Dynamics of a Collapsing Proto-Star*". In: *Monthly Notices of the Royal Astronomical Society* 145.3, pp. 271–295. ISSN: 0035-8711, 1365-2966. DOI: 10.1093/mnras/145.3.271.

URL: https://academic.oup.com/mnras/article-lookup/doi/10.1093/mnras/145.3.271 (visited on 04/14/2020).

Larson, R. B. (Aug. 1, 1969b). "The Emitted Spectrum of a Proto-Star". In: *Monthly Notices of the Royal Astronomical Society* 145.3, pp. 297–308. ISSN: 0035-8711, 1365-2966. DOI: 10.1093/mnras/145.3.297. URL: https://academic.oup.com/mnras/article-lookup/doi/10.1093/mnras/145.3.297 (visited on 04/14/2020).

Leitherer, Claus, Carmelle Robert, and Laurent Drissen (Dec. 1992). "Deposition of Mass, Momentum, and Energy by Massive Stars into the Interstellar Medium". In: *The Astrophysical Journal* 401, p. 596. ISSN: 0004-637X, 1538-4357. DOI: 10.1086/172089. URL: http://adsabs.harvard.edu/doi/10.1086/172089 (visited on 04/13/2020).

Lomax, O., A. P. Whitworth, and A. Cartwright (Dec. 11, 2013). "The Intrinsic Shapes of Starless Cores in Ophiuchus". In: *Monthly Notices of the Royal Astronomical Society* 436.3, pp. 2680–2688. ISSN: 1365-2966, 0035-8711. DOI: 10.1093/mnras/stt1764. URL: http://academic.oup.com/mnras/article/436/3/2680/1261811/The-intrinsic-shapes-of-starless-cores-in (visited on 04/14/2020).

Lombardi, M. and J. Alves (Oct. 2001). "Mapping the Interstellar Dust with Near-Infrared Observations: An Optimized Multi-Band Technique". In: *Astronomy & Astrophysics* 377.3, pp. 1023–1034. ISSN: 0004-6361, 1432-0746. DOI: 10.1051/0004-6361:20011099. URL: http://www.aanda.org/10.1051/0004-6361:20011099 (visited on 03/02/2020).

Lombardi, M., J. Alves, and C. J. Lada (Aug. 2006). "2MASS Wide Field Extinction Maps: I. The Pipe Nebula". In: *Astronomy & Astrophysics* 454.3, pp. 781–796. ISSN: 0004-6361, 1432-0746. DOI: 10.1051/0004-6361:20042474. URL: http://www.aanda.org/10.1051/0004-6361:20042474 (visited on 03/02/2020).

Lombardi, Marco, Hervé Bouy, João Alves, and Charles J. Lada (June 2014). "Herschel-Planck Dust Optical-Depth and Column-Density Maps. I. Method Description and Results for Orion". In: *Astronomy & Astrophysics* 566, A45, A45. DOI: 10.1051/0004-6361/201323293.

Loren, R. B. and A. Wootten (July 1986). "A Massive Prestellar Molecular Core and Adjacent Compression Front in the Rho Ophiuchi Cloud". In: *The Astrophysical Journal* 306, p. 142. ISSN: 0004-637X, 1538-4357. DOI: 10.1086/164327. URL: http://adsabs.harvard.edu/doi/10.1086/164327 (visited on 03/03/2020).

Loren, Robert B. (Mar. 1989). "The Cobwebs of Ophiuchus. I - Strands of (C-13)O - The Mass Distribution". In: *The Astrophysical Journal* 338, p. 902. ISSN: 0004-637X, 1538-4357. DOI: 10.1086/167244. URL: http://adsabs.harvard.edu/doi/10.1086/167244 (visited on 03/04/2020).

Loren, Robert B., Alwyn Wootten, and Bruce A. Wilking (Dec. 1990). "Cold DCO(+) Cores and Protostars in the Warm Rho Ophiuchi Cloud". In: *The Astrophysical Journal* 365, p. 269. ISSN: 0004-637X, 1538-4357. DOI: 10.1086/169480. URL: http://adsabs.harvard.edu/doi/10.1086/169480 (visited on 03/03/2020).

Lynds, Beverly T. (May 1962). "Catalogue of Dark Nebulae." In: *The Astrophysical Journal Supplement Series* 7, p. 1. DOI: 10.1086/190072.

Mamajek, E.E. (Jan. 2008). "On the Distance to the Ophiuchus Star-Forming Region". In: *Astronomische Nachrichten* 329.1, pp. 10–14. ISSN: 00046337, 15213994. DOI: 10.1002/asna.200710827. URL: http://doi.wiley.com/10.1002/asna.200710827 (visited on 03/03/2020).

Marsh, K A, A P Whitworth, M W L Smith, O Lomax, and S A Eales (Nov. 1, 2018). "Dust in the Eye of Andromeda". In: *Monthly Notices of the Royal Astronomical Society* 480.3, pp. 3052–3061. ISSN: 0035-8711, 1365-2966. DOI: 10.1093/mnras/sty2037. URL: https://academic.oup.com/mnras/article/480/3/3052/5060786 (visited on 05/07/2020).

Marsh, K. A., A. P. Whitworth, and O. Lomax (Dec. 2015). "Temperature as a Third Dimension in Column-Density Mapping of Dusty Astrophysical Structures Associated with Star Formation". In: *Monthly Notices of the Royal Astronomical Society* 454, pp. 4282–4292. DOI: 10.1093/mnras/stv2248.

Marsh, K. A. et al. (June 2016). "A Census of Dense Cores in the Taurus L1495 Cloud from the Herschel". In: *Monthly Notices of the Royal Astronomical Society* 459, pp. 342–356. DOI: 10.1093/mnras/stw301.

Marsh, Kenneth A., Thangasamy Velusamy, and Brent Ware (Nov. 2006). "Point Process Algorithm: A New Bayesian Approach for Planet Signal Extraction with the Terrestrial Planet Finder-Interferometer". In: *The Astrophysical Journal* 132.5, pp. 1789–1795. DOI: 10.1086/507676.

Masunaga, Hirohiko and Shu-ichiro Inutsuka (Mar. 2000). "A Radiation Hydrodynamic Model for Protostellar Collapse. II. The Second Collapse and the Birth of a Protostar". In: *The Astrophysical Journal* 531.1, pp. 350–365. ISSN: 0004-637X, 1538-4357. DOI: 10.1086/308439. URL: http://stacks.iop.org/0004-637X/531/i=1/a=350 (visited on 04/14/2020).

Matsuura, M. et al. (June 21, 2009). "The Global Gas and Dust Budget of the Large Magellanic Cloud: AGB Stars and Supernovae, and the Impact on

the ISM Evolution". In: *Monthly Notices of the Royal Astronomical Society* 396.2, pp. 918–934. ISSN: 00358711, 13652966. DOI: 10.1111/j.1365-2966.2009.14743.x. URL: https://academic.oup.com/mnras/article-lookup/doi/10.1111/j.1365-2966.2009.14743.x (visited on 04/13/2020).

Matsuura, M. et al. (Sept. 2, 2011). "Herschel Detects a Massive Dust Reservoir in Supernova 1987A". In: *Science* 333.6047, pp. 1258–1261. ISSN: 0036-8075, 1095-9203. DOI: 10.1126/science.1205983. URL: https://www.sciencemag.org/lookup/doi/10.1126/science.1205983 (visited on 04/13/2020).

McCray, Richard and Minas Kafatos (June 1987). "Supershells and Propagating Star Formation". In: *The Astrophysical Journal* 317, p. 190. ISSN: 0004-637X, 1538-4357. DOI: 10.1086/165267. URL: http://adsabs.harvard.edu/doi/10.1086/165267 (visited on 04/13/2020).

McKee, C. F. and J. P. Ostriker (Nov. 1977). "A Theory of the Interstellar Medium - Three Components Regulated by Supernova Explosions in an Inhomogeneous Substrate". In: *The Astrophysical Journal* 218, p. 148. ISSN: 0004-637X, 1538-4357. DOI: 10.1086/155667. URL: http://adsabs.harvard.edu/doi/10.1086/155667 (visited on 04/10/2020).

McMullin, J. P., B. Waters, D. Schiebel, W. Young, and K. Golap (2007). *Astronomical Data Analysis Software and Systems XVI*. Ed. by R. A. Shaw, F. Hill, and D. J. Bell. ASP.

Men'shchikov, A. et al. (July 2010). "Filamentary Structures and Compact Objects in the Aquila and Polaris Clouds Observed by *Herschel*". In: *Astronomy & Astrophysics* 518, p. L103. ISSN: 0004-6361, 1432-0746. DOI: 10.1051/0004-6361/201014668. URL: http://www.aanda.org/10.1051/0004-6361/201014668 (visited on 04/13/2020).

Mie, Gustav (1908). "Beiträge zur Optik trüber Medien, speziell kolloidaler Metallösungen". In: *Annalen der Physik* 330.3, pp. 377–445. ISSN: 00033804, 15213889. DOI: 10.1002/andp.19083300302. URL: http://doi.wiley.com/10.1002/andp.19083300302 (visited on 04/13/2020).

Miville-Deschênes, M. -A. et al. (July 2010). "Herschel-SPIRE Observations of the Polaris Flare: Structure of the Diffuse Interstellar Medium at the Sub-Parsec Scale". In: *Astronomy & Astrophysics* 518, L104, p. L104. DOI: 10.1051/0004-6361/201014678.

Miville-Deschênes, Marc-Antoine and Guilaine Lagache (Apr. 2005). "IRIS: A New Generation of IRAS Maps". In: *The Astronomical Journal* 157.2, pp. 302–323. DOI: 10.1086/427938.

Miyama, S. M., S. Narita, and C. Hayashi (Nov. 1, 1987). "Fragmentation of Isothermal Sheet-Like Clouds. I: Solutions of Linear and Second-Order Perturbation Equations". In: *Progress of Theoretical Physics* 78.5, pp. 1051–1064. ISSN: 0033-068X, 1347-4081. DOI: 10.1143/PTP.78.1051. URL: https://academic.oup.com/ptp/article-lookup/doi/10.1143/PTP.78.1051 (visited on 04/13/2020).

Morton, D. C. et al. (May 1973). "Spectrophotometric Results from the Copernicus Satellite. II. Composition of Interstellar Clouds". In: *The Astrophysical Journal* 181, p. L103. ISSN: 0004-637X, 1538-4357. DOI: 10.1086/181195. URL: http://adsabs.harvard.edu/doi/10.1086/181195 (visited on 04/13/2020).

Motte, F. and P. André (Jan. 2001). "The Circumstellar Environment of Low-Mass Protostars: A Millimeter Continuum Mapping Survey". In: *Astronomy & Astrophysics* 365, pp. 440–464. DOI: 10.1051/0004-6361:20000072.

Motte, F., P. Andre, and R. Neri (Aug. 1998). "The Initial Conditions of Star Formation in the Rho Ophiuchi Main Cloud: Wide-Field Millimeter Continuum Mapping". In: *Astronomy & Astrophysics* 336, pp. 150–172.

Müller, T., D. Cesarsky, and AOT WG (2011). "SPIRE PACS Parallel Observers' Manual". In: *Herschel Explanatory Supplement*.

Müller, T., K. Okumura, and U. Klass (2011). "PACS Photometer Passbands and Colour Correction Factors for Various Source SEDs". In: *Nasa Herschel Science Center*.

Mundy, Lee G., Alwyn Wootten, Bruce A. Wilking, Geoffrey A. Blake, and Anneila I. Sargent (Jan. 1992). "IRAS 16293-2422: A Very Young Binary System?" In: *The Astrophysical Journal* 385, p. 306. DOI: 10.1086/170939.

Nakamura, Fumitaka and Zhi-Yun Li (Nov. 2008). "Magnetically Regulated Star Formation in Three Dimensions: The Case of the Taurus Molecular Cloud Complex". In: *The Astrophysical Journal* 687, pp. 354–375. DOI: 10.1086/591641.

Neugebauer, G. et al. (Mar. 1984). "The Infrared Astronomical Satellite (IRAS) Mission." In: *The Astrophysical Journal* 278, pp. L1–L6. DOI: 10.1086/184209.

Newville, Matthew, Till Stensitzki, Daniel B. Allen, and Antonino Ingargiola (Sept. 2014). "LMFIT: Non-Linear Least-Square Minimization and Curve-Fitting for Python". In: *Zendo*. DOI: 10.5281/zenodo.11813.

Nutter, D., D. Ward-Thompson, and P. André (June 2006). "A SCUBA Survey of L1689 - the Dog That Didn't Bark". In: *Monthly Notices of the Royal Astronomical Society* 368.4, pp. 1833–1842. DOI: 10.1111/j.1365-2966.2006.10249.x.

Onishi, Toshikazu, Akira Mizuno, Akiko Kawamura, Kengo Tachihara, and Yasuo Fukui (Aug. 2002). "A Complete Search for Dense Cloud Cores in Taurus". In: *The Astrophysical Journal* 575, pp. 950–973. DOI: 10.1086/341347.

Ortiz-León, Gisela N. et al. (Jan. 10, 2017). "The Gould's Belt Distances Survey (GOBELINS). I. Trigonometric Parallax Distances and Depth of the Ophiuchus Complex". In: *The Astrophysical Journal* 834.2, p. 141. ISSN: 1538-4357. DOI: 10.3847/1538-4357/834/2/141. URL: http://stacks.iop.org/0004-637X/834/i=2/a=141?key=crossref.c71145071e6b873bb209a30d66d5a9fb (visited on 03/03/2020).

Ortiz-León, Gisela N. et al. (Dec. 19, 2018). "Gaia -DR2 Confirms VLBA Parallaxes in Ophiuchus, Serpens, and Aquila". In: *The Astrophysical Journal* 869.2, p. L33. ISSN: 2041-8213. DOI: 10.3847/2041-8213/aaf6ad. URL: https://iopscience.iop.org/article/10.3847/2041-8213/aaf6ad (visited on 03/03/2020).

Ostriker, J. (Oct. 1964). "The Equilibrium of Polytropic and Isothermal Cylinders." In: *The Astrophysical Journal* 140, p. 1056. DOI: 10.1086/148005.

Palmeirim, P. et al. (Feb. 2013). "Herschel View of the Taurus B211/3 Filament and Striations: Evidence of Filamentary Growth?" In: *Astronomy & Astrophysics* 550, A38, A38. DOI: 10.1051/0004-6361/201220500.

Panopoulou, G. V., I. Psaradaki, R. Skalidis, K. Tassis, and J. J. Andrews (Apr. 2017). "A Closer Look at the 'characteristic' Width of Molecular Cloud Filaments". In: *Monthly Notices of the Royal Astronomical Society* 466, pp. 2529–2541. DOI: 10.1093/mnras/stw3060.

Panopoulou, G. V., I. Psaradaki, and K. Tassis (Oct. 21, 2016). "The Magnetic Field and Dust Filaments in the Polaris Flare". In: *Monthly Notices of the Royal Astronomical Society* 462.2, pp. 1517–1529. ISSN: 0035-8711, 1365-2966. DOI: 10.1093/mnras/stw1678. URL: https://academic.oup.com/mnras/article-lookup/doi/10.1093/mnras/stw1678 (visited on 04/13/2020).

Panopoulou, G. V., K. Tassis, P. F. Goldsmith, and M. H. Heyer (Nov. 1, 2014). "13CO Filaments in the Taurus Molecular Cloud". In: *Monthly Notices of the Royal Astronomical Society* 444.3, pp. 2507–2524. ISSN: 0035-8711, 1365-2966. DOI: 10.1093/mnras/stu1601. URL: http://academic.oup.com/mnras/article/444/3/2507/1060709/13CO-filaments-in-the-Taurus-molecular-cloud (visited on 04/13/2020).

Pattle, K. et al. (June 2015). "The JCMT Gould Belt Survey: First Results from the SCUBA-2 Observations of the Ophiuchus Molecular Cloud and a Virial

Analysis of Its Prestellar Core Population". In: *Monthly Notices of the Royal Astronomical Society* 450.1, pp. 1094–1122. DOI: 10.1093/mnras/stv376.

Pattle, Kate et al. (June 2018). "First Observations of the Magnetic Field inside the Pillars of Creation: Results from the BISTRO Survey". In: *The Astrophysical Journal Letters* 860.1, L6, p. L6. DOI: 10.3847/2041-8213/aac771.

Perrot, C. A. and I. A. Grenier (June 2003). "3D Dynamical Evolution of the Interstellar Gas in the Gould Belt". In: *Astronomy & Astrophysics* 404.2, pp. 519–531. ISSN: 0004-6361, 1432-0746. DOI: 10.1051/0004-6361:20030477. URL: http://www.aanda.org/10.1051/0004-6361:20030477 (visited on 04/14/2020).

Phillips, Robin (Oct. 2002). *The James Clerk Maxwell Telescope (JCMT): A Brief Overview*. URL: www.jach.hawaii.edu/JACpublic/JCMT/About_JCMT/about_jcmt.html.

Pilbratt, G. L. et al. (July 2010). "Herschel Space Observatory. An ESA Facility for Far-Infrared and Submillimetre Astronomy". In: *Astronomy & Astrophysics* 518, L1, p. L1. DOI: 10.1051/0004-6361/201014759.

Planck Collaboration (Nov. 2014). "Planck 2013 Results. XIV. Zodiacal Emission". In: *Astronomy & Astrophysics* 571, A14, A14. DOI: 10.1051/0004-6361/201321562.

— (Sept. 2016a). "Planck 2015 Results. VII. High Frequency Instrument Data Processing: Time-Ordered Information and Beams". In: *Astronomy & Astrophysics* 594, A7, A7. DOI: 10.1051/0004-6361/201525844.

— (Sept. 2016b). "Planck 2015 Results. VIII. High Frequency Instrument Data Processing: Calibration and Maps". In: *Astronomy & Astrophysics* 594, A8, A8. DOI: 10.1051/0004-6361/201525820.

— (Sept. 2016c). "Planck 2015 Results. XXVI. The Second Planck Catalogue of Compact Sources". In: *Astronomy & Astrophysics* 594, A26, A26. DOI: 10.1051/0004-6361/201526914.

— (Dec. 2016d). "Planck Intermediate Results. XLVIII. Disentangling Galactic Dust Emission and Cosmic Infrared Background Anisotropies". In: *Astronomy & Astrophysics* 596, A109, A109. DOI: 10.1051/0004-6361/201629022.

— (July 2018a). "Planck 2018 Results. I. Overview and the Cosmological Legacy of Planck". In: *arXiv e-prints*, arXiv:1807.06205, arXiv:1807.06205.

— (2018b). *The 2018 Instrument Model*. URL: https://wiki.cosmos.eas.int/planck-legacy-archive/index.php/The_RIMO (visited on 07/16/2019).

Planck Collaboration et al. (Apr. 2014). "Planck Intermediate Results. XIV. Dust Emission at Millimetre Wavelengths in the Galactic Plane". In: *Astronomy & Astrophysics* 564, A45. ISSN: 0004-6361, 1432-0746. DOI: 10.1051/0004-

6361/201322367. URL: http://arxiv.org/abs/1307.6815 (visited on 03/30/2020).

Planck Collaboration et al. (Feb. 2016a). "*Planck* Intermediate Results: XXXII. The Relative Orientation between the Magnetic Field and Structures Traced by Interstellar Dust". In: *Astronomy & Astrophysics* 586, A135. ISSN: 0004-6361, 1432-0746. DOI: 10.1051/0004-6361/201425044. URL: http://www.aanda.org/10.1051/0004-6361/201425044 (visited on 04/13/2020).

Planck Collaboration et al. (Feb. 2016b). "*Planck* Intermediate Results: XXXV. Probing the Role of the Magnetic Field in the Formation of Structure in Molecular Clouds". In: *Astronomy & Astrophysics* 586, A138. ISSN: 0004-6361, 1432-0746. DOI: 10.1051/0004-6361/201525896. URL: http://www.aanda.org/10.1051/0004-6361/201525896 (visited on 04/13/2020).

Poglitsch, A. et al. (July 2010). "The Photodetector Array Camera and Spectrometer (PACS) on the Herschel Space Observatory". In: *Astronomy & Astrophysics* 518, L2, p. L2. DOI: 10.1051/0004-6361/201014535.

Polychroni, D. et al. (Oct. 25, 2013). "Two Mass Distributions in the L1641 Molecular Clouds: The *Herschel* Connection of Dense Cores and Filaments in Orion A". In: *The Astrophysical Journal* 777.2, p. L33. ISSN: 2041-8205, 2041-8213. DOI: 10.1088/2041-8205/777/2/L33. URL: https://iopscience.iop.org/article/10.1088/2041-8205/777/2/L33 (visited on 04/13/2020).

Pon, A., D. Johnstone, and F. Heitsch (Oct. 20, 2011). "Modes of Star Formation in Finite Molecular Clouds". In: *The Astrophysical Journal* 740.2, p. 88. ISSN: 0004-637X, 1538-4357. DOI: 10.1088/0004-637X/740/2/88. URL: https://iopscience.iop.org/article/10.1088/0004-637X/740/2/88 (visited on 04/14/2020).

Popescu, Cristina C. and Richard J. Tuffs (Sept. 2002). "The Percentage of Stellar Light Re-Radiated by Dust in Late-Type Virgo Cluster Galaxies". In: *Monthly Notices of the Royal Astronomical Society* 335.2, pp. L41–L44. ISSN: 0035-8711, 1365-2966. DOI: 10.1046/j.1365-8711.2002.05881.x. URL: https://academic.oup.com/mnras/article-lookup/doi/10.1046/j.1365-8711.2002.05881.x (visited on 04/13/2020).

Poppel, W. (Jan. 1997). "The Gould Belt System and the Local Interstellar Medium". In: *Fundamentals of Cosmic Physics* 18, pp. 1–271.

Porras, Alicia et al. (Oct. 2003). "A Catalog of Young Stellar Groups and Clusters within 1 Kiloparsec of the Sun". In: *The Astronomical Journal* 126.4, pp. 1916–1924. ISSN: 0004-6256, 1538-3881. DOI: 10.1086/377623. URL: http://stacks.iop.org/1538-3881/126/i=4/a=1916 (visited on 04/14/2020).

Preibisch, Th., V. Ossenkopf, H. W. Yorke, and Th. Henning (Nov. 1993). "The Influence of Ice-Coated Grains on Protostellar Spectra." In: *Astronomy & Astrophysics* 279, pp. 577–588.

Punanova, A. et al. (Sept. 2018). "Kinematics of Dense Gas in the L1495 Filament". In: *Astronomy & Astrophysics* 617, A27, A27. DOI: 10.1051/0004-6361/201731159.

Ragan, S. E. et al. (Aug. 2014). "Giant Molecular Filaments in the Milky Way". In: *Astronomy & Astrophysics* 568, A73. ISSN: 0004-6361, 1432-0746. DOI: 10.1051/0004-6361/201423401. URL: http://www.aanda.org/10.1051/0004-6361/201423401 (visited on 04/13/2020).

Rebull, L. M. et al. (Feb. 2010). "The Taurus Spitzer Survey: New Candidate Taurus Members Selected Using Sensitive Mid-Infrared Photometry". In: *The Astrophysical Journal Supplement Series* 186, pp. 259–307. DOI: 10.1088/0067-0049/186/2/259.

Remazeilles, Mathieu, Jacques Delabrouille, and Jean-François Cardoso (Nov. 2011). "Foreground Component Separation with Generalized Internal Linear Combination". In: *Monthly Notices of the Royal Astronomical Society* 418.1, pp. 467–476. DOI: 10.1111/j.1365-2966.2011.19497.x.

Reynolds, R. J., N. C. Sterling, and L. M. Haffner (Sept. 10, 2001). "Detection of a Large Arc of Ionized Hydrogen Far above the Cassiopeia OB6 Association: A Superbubble Blowout into the Galactic Halo?" In: *The Astrophysical Journal* 558.2, pp. L101–L104. ISSN: 0004637X. DOI: 10.1086/323638. URL: https://iopscience.iop.org/article/10.1086/323638 (visited on 04/10/2020).

Richardson, J. M. and K. A. Marsh (1987). "Acoustical Imaging and Point Process". In: *Acoustical Imaging* 17, pp. 615–633.

— (1992). "Point-Process Theory and the Surveillance of Many Objects". In: *Maximum Entropy and Bayesian Methods. Fundamental Theories of Physics (an International Book Series on the Fundamental Theories of Physics: Their Clarification, Development and Application)*. Ed. by Neudorfer P.O. Smith C.R. Erickson G.J. Vol. 50. Dordrecht: Springer.

Rieke, G. H. and M. J. Lebofsky (Jan. 1985). "The Interstellar Extinction Law from 1 to 13 Microns". In: *The Astrophysical Journal* 288, p. 618. ISSN: 0004-637X, 1538-4357. DOI: 10.1086/162827. URL: http://adsabs.harvard.edu/doi/10.1086/162827 (visited on 03/02/2020).

Robitaille, Thomas P. (Apr. 2017). "A Modular Set of Synthetic Spectral Energy Distributions for Young Stellar Objects". In: *Astronomy & Astrophysics* 600,

A11. ISSN: 0004-6361, 1432-0746. DOI: 10.1051/0004-6361/201425486. URL: http://arxiv.org/abs/1703.05765 (visited on 08/05/2020).

Robitaille, Thomas P., Barbara A. Whitney, Remy Indebetouw, and Kenneth Wood (Apr. 2007). "Interpreting Spectral Energy Distributions from Young Stellar Objects. II. Fitting Observed SEDs Using a Large Grid of Pre-Computed Models". In: *The Astrophysical Journal Supplement Series* 169.2, pp. 328–352. ISSN: 0067-0049, 1538-4365. DOI: 10.1086/512039. URL: http://arxiv.org/abs/astro-ph/0612690 (visited on 08/05/2020).

Robitaille, Thomas P., Barbara A. Whitney, Remy Indebetouw, Kenneth Wood, and Pia Denzmore (Dec. 2006). "Interpreting Spectral Energy Distributions from Young Stellar Objects. I. A Grid of 200,000 YSO Model SEDs". In: *The Astrophysical Journal Supplement Series* 167.2, pp. 256–285. ISSN: 0067-0049, 1538-4365. DOI: 10.1086/508424. URL: http://arxiv.org/abs/astro-ph/0608234 (visited on 08/05/2020).

Roman-Duval, Julia et al. (Feb. 18, 2016). "Distribution and Mass of Diffuse and Dense CO Gas in the Milky Way". In: *The Astrophysical Journal* 818.2, p. 144. ISSN: 1538-4357. DOI: 10.3847/0004-637X/818/2/144. URL: https://iopscience.iop.org/article/10.3847/0004-637X/818/2/144 (visited on 04/10/2020).

Roy, A. et al. (June 2019). "How the Power Spectrum of Dust Continuum Images May Hide the Presence of a Characteristic Filament Width". In: *Astronomy & Astrophysics* 626, A76. ISSN: 0004-6361, 1432-0746. DOI: 10.1051/0004-6361/201832869. URL: https://www.aanda.org/10.1051/0004-6361/201832869 (visited on 04/13/2020).

Sargent, Benjamin A. et al. (June 10, 2010). "The Mass-Loss Return from Evolved Stars to the Large Magellanic Cloud. II. Dust Properties for Oxygen-Rich Asymptotic Giant Branch Stars". In: *The Astrophysical Journal* 716.1, pp. 878–890. ISSN: 0004-637X, 1538-4357. DOI: 10.1088/0004-637X/716/1/878. URL: https://iopscience.iop.org/article/10.1088/0004-637X/716/1/878 (visited on 04/13/2020).

Schisano, E. et al. (July 23, 2014). "The Identification of Filaments on Far-Infrared and Submillimeter Images: Morphology, Physical Conditions and Relation with Star Formation of Filamentary Structure". In: *The Astrophysical Journal* 791.1, p. 27. ISSN: 0004-637X, 1538-4357. DOI: 10.1088/0004-637X/791/1/27. URL: https://iopscience.iop.org/article/10.1088/0004-637X/791/1/27 (visited on 04/13/2020).

Schlegel, David J., Douglas P. Finkbeiner, and Marc Davis (June 1998). "Maps of Dust Infrared Emission for Use in Estimation of Reddening and Cosmic Microwave Background Radiation Foregrounds". In: *The Astrophysical Journal* 500.2, pp. 525–553. DOI: 10.1086/305772.

Schmalzl, M. et al. (Dec. 2010). "Star Formation in the Taurus Filament L1495: From Dense Cores to Stars". In: *The Astrophysical Journal* 725, pp. 1327–1336. DOI: 10.1088/0004-637X/725/1/1327.

Schneider, S. and B. G. Elmegreen (Sept. 1979). "A Catalog of Dark Globular Filaments". In: *The Astrophysical Journal Supplement Series* 41, p. 87. ISSN: 0067-0049, 1538-4365. DOI: 10.1086/190609. URL: http://adsabs.harvard.edu/doi/10.1086/190609 (visited on 04/13/2020).

Seo, Y. M. et al. (June 2015). "An Ammonia Spectral Map of the L1495-B218 Filaments in the Taurus Molecular Cloud. I. Physical Properties of Filaments and Dense Cores". In: *The Astrophysical Journal* 805, 185, p. 185. DOI: 10.1088/0004-637X/805/2/185.

Shapley, H. (June 1919). "Studies Based on the Colors and Magnitudes in Stellar Clusters. XII. Remarks on the Arrangement of the Sidereal Universe." In: *The Astrophysical Journal* 49, p. 311. ISSN: 0004-637X, 1538-4357. DOI: 10.1086/142469. URL: http://adsabs.harvard.edu/doi/10.1086/142469 (visited on 04/14/2020).

Shimajiri, Y. et al. (Mar. 2019). "Probing Accretion of Ambient Cloud Material into the Taurus B211/B213 Filament". In: *Astronomy & Astrophysics* 623, A16. ISSN: 0004-6361, 1432-0746. DOI: 10.1051/0004-6361/201834399. URL: https://www.aanda.org/10.1051/0004-6361/201834399 (visited on 04/13/2020).

Shu, F. H., F. C. Adams, and S. Lizano (Jan. 1987). "Star Formation in Molecular Clouds: Observation and Theory." In: *Annual Review of Astronomy and Astrophysics* 25, pp. 23–81. DOI: 10.1146/annurev.aa.25.090187.000323.

Skrutskie, M. F. et al. (Feb. 2006). "The Two Micron All Sky Survey (2MASS)". In: *The Astronomical Journal* 131.2, pp. 1163–1183. ISSN: 0004-6256, 1538-3881. DOI: 10.1086/498708. URL: http://stacks.iop.org/1538-3881/131/i=2/a=1163 (visited on 03/02/2020).

Smith, Matt (2017). In:

Smith, Matthew (Jan. 17, 2013). "The Herschel Perspective On Nearby Galaxies". In: *Cardiff University*. In collab. with Stephen Eales and Jonathan Davies. DOI: 10.5281/ZENODO.1244777. URL: https://zenodo.org/record/1244777 (visited on 04/13/2020).

Smith, R. J., S. C. O. Glover, and R. S. Klessen (Dec. 2014). "On the Nature of Star-Forming Filaments - I. Filament Morphologies". In: *Monthly Notices of the Royal Astronomical Society* 445, pp. 2900–2917. DOI: 10.1093/mnras/stu1915.

Soler, Juan D. (Sept. 2019). "Using Herschel and Planck Observations to Delineate the Role of Magnetic Fields in Molecular Cloud Structure". In: *Astronomy & Astrophysics* 629, A96, A96. DOI: 10.1051/0004-6361/201935779.

Sousbie, T. (June 2011). "The Persistent Cosmic Web and Its Filamentary Structure - I. Theory and Implementation". In: *Monthly Notices of the Royal Astronomical Society* 414.1, pp. 350–383. DOI: 10.1111/j.1365-2966.2011.18394.x.

Sousbie, T., C. Pichon, and H. Kawahara (June 2011). "The Persistent Cosmic Web and Its Filamentary Structure - II. Illustrations". In: *Monthly Notices of the Royal Astronomical Society* 414.1, pp. 384–403. DOI: 10.1111/j.1365-2966.2011.18395.x.

Spitzer, Lyman (1978). *Physical Processes in the Interstellar Medium*. New York: Wiley. 318 pp. ISBN: 978-0-471-02232-9.

Stahler, Steven W and Francesco Palla (2005). *The Formation of Stars*. Weinheim: Wiley-VCH. ISBN: 978-3-527-61867-5. URL: http://www3.interscience.wiley.com/cgi-bin/homepage/?isbn=9783527618675 (visited on 04/13/2020).

Strom, K. M. and S. E. Strom (Mar. 1994). "A Multiwavelength Study of Star Formation in the L1495E Cloud in Taurus". In: *The Astrophysical Journal* 424, pp. 237–256. DOI: 10.1086/173886.

Stutz, Amelia M. et al. (Mar. 22, 2013). "A *Herschel* and APEX Census of the Reddest Sources in Orion: Searching for the Youngest Protostars". In: *The Astrophysical Journal* 767.1, p. 36. ISSN: 0004-637X, 1538-4357. DOI: 10.1088/0004-637X/767/1/36. URL: https://iopscience.iop.org/article/10.1088/0004-637X/767/1/36 (visited on 04/14/2020).

Suri, S. T. et al. (Jan. 2019). "The CARMA-NRO Orion Survey: The Filamentary Structure as Seen in C18O Emission". In: *arXiv e-prints*, arXiv:1901.00176, arXiv:1901.00176.

Suri, Sümeyye (2019). In:

Tafalla, M. and A. Hacar (Feb. 2015). "Chains of Dense Cores in the Taurus L1495/B213 Complex". In: *Astronomy & Astrophysics* 574, A104, A104. DOI: 10.1051/0004-6361/201424576.

Tauber, J. A. et al. (Sept. 2010). "Planck Pre-Launch Status: The Planck Mission". In: *Astronomy & Astrophysics* 520, A1, A1. DOI: 10.1051/0004-6361/200912983.

Tavakoli, Maryam (July 25, 2012). "Three Dimensional Distribution of Atomic Hydrogen in the Milky Way". In: *arXiv e-prints*. URL: http://arxiv.org/abs/1207.6150 (visited on 04/10/2020).

Taylor, David K., R. L. Dickman, and N. Z. Scoville (Apr. 1987). "Molecular Clouds and the Gould Belt". In: *The Astrophysical Journal* 315, p. 104. ISSN: 0004-637X, 1538-4357. DOI: 10.1086/165117. URL: http://adsabs.harvard.edu/doi/10.1086/165117 (visited on 04/14/2020).

Testi, L. et al. (2014). "Dust Evolution in Protoplanetary Disks". In: *Protostars and Planets VI*. University of Arizona Press. ISBN: 978-0-8165-3124-0. DOI: 10.2458/azu_uapress_9780816531240-ch015. URL: http://muse.jhu.edu/books/9780816598762/9780816598762-22.pdf (visited on 04/14/2020).

Tielens, A. G. G. M. and L. J. Allamandola (1987). "Composition, Structure, and Chemistry of Interstellar Dust". In: *Interstellar Processes*. Ed. by David J. Hollenbach and Harley A. Thronson. Vol. 134. Astrophysics and Space Science Library. Dordrecht: Springer Netherlands, pp. 397–470. ISBN: 978-90-277-2485-4 978-94-009-3861-8. DOI: 10.1007/978-94-009-3861-8_16. URL: http://link.springer.com/10.1007/978-94-009-3861-8_16 (visited on 04/14/2020).

Valtchanov, I. (2017). "SPIRE Handbook v3.1". In: *Herschel Explanatory Supplement* IV.

Van Dishoeck, Ewine F. and John H. Black (Nov. 1988). "The Photodissociation and Chemistry of Interstellar CO". In: *The Astrophysical Journal* 334, p. 771. ISSN: 0004-637X, 1538-4357. DOI: 10.1086/166877. URL: http://adsabs.harvard.edu/doi/10.1086/166877 (visited on 04/13/2020).

Van Dishoeck, Ewine F. and Geoffrey A. Blake (Sept. 1998). "Chemical Evolution of Star-Forming Regions". In: *Annual Review of Astronomy and Astrophysics* 36.1, pp. 317–368. ISSN: 0066-4146, 1545-4282. DOI: 10.1146/annurev.astro.36.1.317. URL: http://www.annualreviews.org/doi/10.1146/annurev.astro.36.1.317 (visited on 04/13/2020).

Van Steenberg, Michael E. and J. Michael Shull (July 1988). "Galactic Interstellar Abundance Surveys with IUE. III - Silicon, Manganese, Iron, Sulfur, and Zinc". In: *The Astrophysical Journal* 330, p. 942. ISSN: 0004-637X, 1538-4357. DOI: 10.1086/166525. URL: http://adsabs.harvard.edu/doi/10.1086/166525 (visited on 04/13/2020).

Vazquez-Semadeni, Enrique, Thierry Passot, and Annick Pouquet (Mar. 1995). "A Turbulent Model for the Interstellar Medium. 1: Threshold Star Formation and Self-Gravity". In: *The Astrophysical Journal* 441, p. 702. ISSN: 0004-637X,

1538-4357. DOI: 10.1086/175393. URL: http://adsabs.harvard.edu/doi/10.1086/175393 (visited on 04/13/2020).

Viaene, S. et al. (Feb. 2016). "The Bolometric and UV Attenuation in Normal Spiral Galaxies of the *Herschel* Reference Survey". In: *Astronomy & Astrophysics* 586, A13. ISSN: 0004-6361, 1432-0746. DOI: 10.1051/0004-6361/201527586. URL: http://www.aanda.org/10.1051/0004-6361/201527586 (visited on 04/13/2020).

Wang, Ke et al. (July 11, 2015). "Large-Scale Filaments Associated with Milky Way Spiral Arms". In: *Monthly Notices of the Royal Astronomical Society* 450.4, pp. 4043–4049. ISSN: 1365-2966, 0035-8711. DOI: 10.1093/mnras/stv735. URL: http://academic.oup.com/mnras/article/450/4/4043/989841/Largescale-filaments-associated-with-Milky-Way (visited on 04/13/2020).

Wang, Ke et al. (Sept. 8, 2016). "A Census of Large-Scale (¿10 Pc), Velocity-Coherent, Dense Filaments in the Northern Galactic Plane: Automated Identification Using Minimum Spanning Tree". In: *The Astrophysical Journal Supplement Series* 226.1, p. 9. ISSN: 1538-4365. DOI: 10.3847/0067-0049/226/1/9. URL: https://iopscience.iop.org/article/10.3847/0067-0049/226/1/9 (visited on 04/13/2020).

Ward-Thompson, D. et al. (Aug. 2007). "The James Clerk Maxwell Telescope Legacy Survey of Nearby Star-Forming Regions in the Gould Belt". In: *The Publications of the Astronomical Society of the Pacific* 119, pp. 855–870. DOI: 10.1086/521277.

Ward-Thompson, D. et al. (Nov. 2016). "The JCMT and Herschel Gould Belt Surveys: A Comparison of SCUBA-2 and Herschel Data of Dense Cores in the Taurus Dark Cloud L1495". In: *Monthly Notices of the Royal Astronomical Society* 463, pp. 1008–1025. DOI: 10.1093/mnras/stw1978.

Ward-Thompson, Derek and Anthony P. Whitworth (2015). *An Introduction to Star Formation*. Cambridge: Cambridge University Press. ISBN: 978-0-511-97402-1.

Whalen, Anthony D. (1971). *Detection of Signals in Noise*. Electrical Science Series. New York: Academic Press. 411 pp. ISBN: 978-0-12-744850-3.

Wheelock, S. et al. (July 2002). "IRAS Sky Survey Atlas Explanatory Supplement". In: *NASA/IPAC Infrared Science Archive*. URL: https://irsa.ipac.caltech.edu/IRASdocs/issa.exp.sup/.

Whitworth, A P et al. (Nov. 11, 2019). "The Dust in M31". In: *Monthly Notices of the Royal Astronomical Society* 489.4, pp. 5436–5452. ISSN: 0035-8711, 1365-2966.

DOI: 10.1093/mnras/stz2166. URL: https://academic.oup.com/mnras/article/489/4/5436/5549520 (visited on 05/07/2020).

Whitworth, A. P. (May 11, 2016). "A Ram-Pressure Threshold for Star Formation". In: *Monthly Notices of the Royal Astronomical Society* 458.2, pp. 1815–1832. ISSN: 0035-8711, 1365-2966. DOI: 10.1093/mnras/stw442. URL: https://academic.oup.com/mnras/article-lookup/doi/10.1093/mnras/stw442 (visited on 04/13/2020).

Whitworth, A. P. and S. E. Jaffa (Mar. 2018). "A Simple Approach to CO Cooling in Molecular Clouds". In: *Astronomy & Astrophysics* 611, A20, A20. DOI: 10.1051/0004-6361/201731871.

Whitworth, A. P. and D. Ward-Thompson (Jan. 2001). "An Empirical Model for Protostellar Collapse". In: *The Astrophysical Journal* 547, pp. 317–322. DOI: 10.1086/318373.

WHO (Mar. 11, 2020). *WHO Director-General's Opening Remarks at the Media Briefing on COVID-19 - 11 March 2020*. URL: https://web.archive.org/web/20200311212521/https://www.who.int/dg/speeches/detail/who-director-general-s-opening-remarks-at-the-media-briefing-on-covid-19---11-march-2020 (visited on 04/28/2020).

Zucker, Catherine et al. (July 15, 2019). "A Large Catalog of Accurate Distances to Local Molecular Clouds: The Gaia DR2 Edition". In: *The Astrophysical Journal* 879.2, p. 125. ISSN: 1538-4357. DOI: 10.3847/1538-4357/ab2388. URL: http://arxiv.org/abs/1902.01425 (visited on 07/21/2020).